GENERAL ATOMIC

GA-A13444
UC-77

HTGR FUELS AND CORE DEVELOPMENT PROGRAM

QUARTERLY PROGRESS REPORT FOR THE PERIOD ENDING MAY 31, 1975

Prepared under
Contract AT(04-3)-167
Project Agreement No. 17
for the
San Francisco Operations Office
U.S. Energy Research and Development Administration

GENERAL ATOMIC PROJECT 3224
(FORMERLY 0317)

DATE PUBLISHED
JUNE 30, 1975

DISCLAIMER

QUARTERLY REPORT SERIES

GA-4072-December, 1962, through February, 1963
GA-4350-March, 1963, through May, 1963
GA-4569-June, 1963, through August, 1963
GA-4937-September, 1963, through November, 1963
GA-5104-December, 1963, through February, 1964
GA-5366-March, 1964, through May, 1964
GA-5618-June, 1964, through August, 1964
GA-5866-September, 1964, through November, 1964
GA-6113-December, 1964, through February, 1965
GA-6418-March, 1965, through May, 1965
GA-6671-June, 1965, through August, 1965
GA-6869-September, 1965, through November, 1965
GA-7010-December, 1965, through February, 1966
GA-7181-March, 1966, through May, 1966
GA-7396-June, 1966, through August, 1966
GA-7553-September, 1966, through November, 1966
GA-7801-December, 1966, through February, 1967
GA-7981-March, 1967, through May, 1967
GA-8200-June, 1967, through August, 1967
GA-8356-September, 1967, through November, 1967
GA-8530-December, 1967, through February, 1968
GA-8662-March, 1968, through May, 1968
GA-8860-June, 1968, through August, 1968
GA-9090-September, 1968, through November, 1968
GA-9227-December, 1968, through February, 1969
GA-9372-March, 1969, through May, 1969
GA-9660-June, 1969, through August, 1969
GA-9815-September, 1969, through November, 1969
GA-9944-December, 1969, through February, 1970
GA-10088-March, 1970, through May, 1970
GA-10288-June, 1970, through August, 1970
GA-10399-September, 1970, through November, 1970
GA-10501-December, 1970, through February, 1971
GA-10661-March, 1971, through May, 1971
Gulf-GA-A10784-June, 1971, through August, 1971
Gulf-GA-A10930-September, 1971, through November, 1971
Gulf-GA-A10999-December, 1971, through February, 1972
Gulf-GA-A12150-March, 1972, through May, 1972
Gulf-GA-A12222-June, 1972, through August, 1972
Gulf-GA-A12422-September, 1972, through November, 1972
Gulf-GA-A12515-December, 1972, through February, 1973
Gulf-GA-12599-March, 1973, through May, 1973
Gulf-GA-A12725-June, 1973, through August, 1973
Gulf-GA-A12818-September, 1973, through November, 1973
GA-A12916-December, 1973, through February, 1974
GA-A13030-March, 1974, through May, 1974
GA-A13126-June, 1974, through August, 1974
GA-A13253-September, 1974, through November, 1974
GA-A13353-December, 1974, through February, 1975

ABSTRACT

This publication continues the quarterly report series on the HTGR Fuels and Core Development Program. The Program covers items of the base technology of the High-Temperature Gas-Cooled Reactor (HTGR) system. The development of the HTGR system will, in part, meet the greater national objective of more effective and efficient utilization of our national resources. The work reported here includes studies of reactions between core materials and coolant impurities, basic fission product transport mechanisms, core graphite development and testing, the development and testing of recyclable fuel systems, and physics and fuel management studies. Materials studies include irradiation capsule tests of both fuel and graphite. Experimental procedures and results are discussed and, where appropriate, the data are presented in tables, graphs, and photographs. More detailed descriptions of experimental work are presented in topical reports; these are listed at the end of the report.

INTRODUCTION

This report covers the work performed by the General Atomic Company under U.S. Atomic Energy Commission Contract AT(04-3)-167, Project Agreement No. 17. This Project Agreement calls for support of basic technology associated with the fuels and core of the gas-cooled, nuclear power reactor systems. The program is based on the concept of the High-Temperature Gas-Cooled Reactor (HTGR) developed by the General Atomic Company.

Large HTGR systems will be placed in operation starting in the early 1980's following the operation of the 330-MW(e) prototype in 1975. Characteristics of these advanced systems include:

1. A single-phase gas coolant allowing generation of high-temperature, high-pressure steam with consequent high-efficiency energy conversion and low thermal discharge.

2. A prestressed concrete reactor vessel (PCRV) offering advantages in field construction, primary system integrity, and stressed member inspectability.

3. Graphite core material assuring high-temperature structural strength, large temperature safety margins, and good neutron economy.

4. Thorium fuel cycle leading to U-233 fuel which allows good utilization of nuclear resources and minimum demands on separative work.

CONTENTS

FIGURES

TABLES

TASK 4 (189a 13114)

FISSION PRODUCT MECHANISMS

FISSION GAS RELEASE STUDIES

Fission gas release (Kr-85m R/B) data have been measured for failed reference fertile particles. The R/B data were derived from TRIGA tests on fuel rods irradiated in the P13P capsule. These fuel rods contained reference fertile particles (BISO ThO_2 particles irradiated to 0.9 to 1.9% FIMA burnup) and fissile particles (TRISO UO_2 and $(Th,U)O_2$ particles irradiated to 50 to 62% FIMA burnup). Prior to this work, essentially no R/B data were available for failed BISO ThO_2 particles.

Earlier studies (Ref. 4-1) provided R/B data for failed reference fissile particles [TRISO coated particles with melted UC_2 (VSM) kernels] and failed development reference fissile particles [TRISO coated particles with weak-acid-resin (WAR) UC_2 kernels].

As pointed out in the previous Quarterly Progress Report (Ref. 4-1), fission gas release (R/B) data for failed particles are important for use in calculating the inventory (circulating activity) of gaseous (krypton and xenon) nuclides in the primary coolant of HTGR systems. The primary circuit inventory is presently calculated using the RAD computer code, developed at GA. Required input data include fission gas release data, fission product decay rates, helium coolant purification rates, etc. Sources of fission gas release are heavy metal contamination in the fuel rod and fuel particles with failed coatings.

The fuel rods irradiated in the P13P capsule contained BISO ThO_2 particles with known coating failure fractions and thus were suitable for use in measuring R/B data for failed reference fertile particles. The

BISO coating failure, as described in Ref. 4-2, was attributed to irradiation instability of a highly anisotropic layer in the outer pyrocarbon coating or instability of high density outer PyC coatings applied at relatively low coating rates.

Additional experiments to provide R/B data for failed fertile particles are planned. These experiments involve TRIGA tests on laser-failed* BISO ThO_2 particles irradiated in the P13R and P13S capsules. These fertile particles will be available for testing when postirradiation examination (PIE) of fuel from the two irradiation tests is resumed. This PIE work was delayed because of higher priority PIE work on the P13Q capsule.

Experimental

Fission gas release measurements on the fuel rods were performed using a standard procedure, which involves irradiating fuel rod or particle samples in a TRIGA reactor, trapping the released fission gases, and gamma-counting the traps. The gamma-counting and calculations are done by use of a Sigma II analyzer-computer. The test yields a direct measure of the R/B value at 1100°C for 4.4-hr Kr-85m, which is taken to be the reference noble gas nuclide.

The rod (or particle) sample is placed inside a special graphite crucible. The crucible is inserted into a King furnace mounted in the TRIGA Mark I reactor. The furnace is purged with helium, and the crucible is heated to 1100°C. The TRIGA King furnace facility is described in Ref. 4-3. With helium sweeping through the furnace, the sample is irradiated for one-half hour at a power level sufficient to yield about 10^{14} fissions per fuel rod. During the irradiation period, the sweep gas, which contains the fission gases escaping from the crucible, is purged into a liquid-nitrogen-cooled charcoal trap. After irradiation, the trap is removed and gamma-counted using a lithium-drifted germanium detector in conjunction with the Sigma II analyzer-computer.

*Laser-failed particles are made, as described in Ref. 4-1, by laser-drilling pinholes into the coatings of otherwise intact particles.

The fractional release (R/B) values for Kr-85m (or other noble gas nuclide) are calculated from the released activity and the birth activity as determined from the TRIGA reactor power level, fissionable heavy metal loading, and elapsed TRIGA irradiation time. The calculation is performed using appropriate codes stored in the Sigma II computer. In the calculation, the measured activity (counts per minute) in the trap is compared to that for a trap run with a known uranium standard in the reactor. The Sigma II computer code FISSIN was used to calculate the end-of-irradiation heavy metal loadings. A steady-state correction factor was not applied in the R/B calculation.*

Results

Table 4-1 shows the rods and particles tested, the observed failure fractions, and the observed Kr-85m R/B values for the fuel rods tested. (Descriptions of the rod samples and particles are given in Ref. 4-2, Table 9-1.) The fuel particle failure fractions shown in Table 4-1 were determined by examination of metallographic specimens of the rods prepared after the nondestructive fission gas release tests were completed. The rods irradiated in capsule cell 2 (samples 2A-9, 2B-18, and 2D-10) showed failure fractions approaching 1.0 for the fertile particles. This particular batch of fertile particles, used in all three rods tested in cell 2 and in the two rods tested in cell 4 (samples 4B-17 and 4D-3), had high density OPyC coatings applied at low coating rates. This contributed to the high coating failure. The cell 2 rods, compared to the cell 4 rods, were irradiated at higher temperatures and to higher burnups (see Ref. 4-2), and thus exhibited higher failure fractions. The fissile particles in all six rods tested did not fail to a measurable degree; thus, the fission gas release observed was attributed to the fertile particles.

*A steady-state correction is applied in some cases because during the one-half hour irradiation the level of Kr-85m in the sweep gas does not reach equilibrium. Tests show that the steady-state correction is required for unirradiated fuel particles but is not required for fuel particles previously irradiated to several percent burnup.

TABLE 4-1
FISSION GAS RELEASE (R/B) DATA FOR FAILED FERTILE PARTICLES IN FUEL RODS IRRADIATED IN CAPSULE P13P

Rod Sample No.	Fissile Particle			Fertile Particle			Rod Kr-85m R/B[b] at 1100°C	Kr-85m $(R/B)_f$[c] at 1100°C
	Type	Burnup (% FIMA)	Failed Fraction[a]	Type	Burnup (% FIMA)	Failed Fraction[a]		
2A-9	UO_2 TRISO	61	0	ThO_2 BISO	1.8	0.833	1.1×10^{-3}	1.3×10^{-3}
2B-18	UO_2 TRISO	62	0	ThO_2 BISO	1.9	0.962	1.4×10^{-3}	1.5×10^{-3}
2D-10	$(Th,U)O_2$ TRISO	62	0	ThO_2 BISO	1.9	0.970	1.7×10^{-3}	1.8×10^{-3}
4B-17	UO_2 TRISO	52	0	ThO_2 BISO	1.1	0.228	1.7×10^{-4}	7.5×10^{-4}
4D-3	UO_2 TRISO	50	0	ThO_2 BISO	0.9	0.007	1.2×10^{-5}	1.7×10^{-3}
5A-8	UO_2 TRISO	50	0	ThO_2 BISO	0.9	0.007	5.2×10^{-5}	7.4×10^{-3}
								2.4×10^{-3} avg

[a] Fraction of failed particles based on visual stereomicroscopic examination of metallographic section of fuel rod after R/B test. No failures were detected for the fissile particles.

[b] The steady-state correction was not applied to the R/B data because the particles were previously irradiated to appreciable burnup. These R/B values differ from those in Table 9-1, Ref. 4-2 because of revised U loadings.

[c] $(R/B)_f$ = R/B observed/failed fraction.

The average $(R/B)_f$* for BISO ThO_2 particles, i.e., the ratio of the observed R/B to the failed fraction, was determined to be approximately 2×10^{-3}, as shown in Table 4-1. This is in accord with the average $(R/B)_f$ value of 5×10^{-3} found for failed particles constrained in fuel rods (Ref. 4-4, Table 1). The earlier study found that a constrained failed particle configuration, i.e., cracked coatings held in place around the kernel by surrounding fuel rod matrix material, will exhibit a lower R/B than loose failed particles. The average $(R/B)_f$ value of 2×10^{-3} is also in accord with R/B values ranging from 2.6×10^{-3} to 9.7×10^{-3} found for laser-failed fissile (BISO coated UC_2) particles (Ref. 4-1).

FISSION METAL RELEASE STUDIES

Annealing tests have been performed to measure the release of cesium from bare kernels of ThO_2. The data derived from these tests are important in reactor analyses for the calculation of cesium release from intact BISO particles and from failed particles. The experimental procedure for conducting these tests has been described in detail previously (Ref. 4-5).

The kernel diffusion data obtained thus far are summarized in Table 4-2. The listed values of D' were calculated according to the equation $D' = \pi(f_1 - f_2)^2/36(t_1 - t_2)$, where D' is the reduced diffusion coefficient given by the ratio of D/a^2, a is the radius of the equivalent sphere of the particle or grain through which diffusion occurs, f is the fractional release, and t is the corresponding time. Most of the anneals have been at temperature for about 600 hr, but even for this time interval, the fractional release of Cs is found to be generally less than 2%. To improve the accuracy of the measurement of cesium released, the annealing experiments are being continued.

At the lower temperatures, 1000° to 1300°C, some of the cesium released from the bare kernels has been found to be deposited on the Ta containment

*$(R/B)_f$ = R/B for fuel particles with failed coatings.

TABLE 4-2
DATA FOR CESIUM DIFFUSION IN ThO_2 KERNELS

Capsule:	HB-1
Particle Batch No.:	4222-02-101
Kernel Diameter:	492 μm
Estimated Fast Fluence:	$\sim 3.1 \times 10^{21}$ n/cm^2
Estimated Thermal Fluence:	$\sim 2.4 \times 10^{21}$ n/cm^2
Kernel Density:	9.86 g/cm^3

Sample No.	Irradiation Temp (°C)	Burnup (% FIMA)	Annealing Temp (°C)	D' (sec^{-1})	D (cm^2/sec)
5787-16	<700	0.9	1300	1.3×10^{-12}	7.8×10^{-16}
-17	↓	↓	1300	8.3×10^{-13}	5.0×10^{-16}
-18			1200	1.7×10^{-14}	1.0×10^{-17}
-19			1200	2.2×10^{-14}	1.4×10^{-17}
-20			1000	4.3×10^{-14}	2.6×10^{-17}
-21			1000	1.2×10^{-14}	7.0×10^{-18}
-22			1400	8.8×10^{-13}	5.4×10^{-16}
-23			1400	2.4×10^{-13}	1.5×10^{-16}
-24	↓	↓	1300	8.8×10^{-13}	5.4×10^{-16}

tube as well as on the copper plated cold finger (see diagram of the containment tube and cold finger in Ref. 4-5). During the initial stages of the anneal, more cesium is deposited on the Ta containment tube than on the cold finger, but after 100 to 300 hr, the amount of cesium deposited on the Ta containment tube remains constant. Thus, in computing the D' values, release fractions obtained after about 300 hr are used.

To compare the present results with previous (Ref. 4-2) diffusion coefficients for cesium in kernels as derived from postirradiation annealing experiments on intact BISO coated kernels, the reduced diffusion coefficients listed in Table 4-2 have been converted to diffusion coefficients by using the kernel radius as previously calculated (Ref. 4-2). The comparison is shown in Fig. 4-1. The solid curve is the least-squares straight line previously derived (Ref. 4-2) for the coated particle data; the dashed line is the corresponding fit for the data of Table 4-2. In the mutual temperature range, diffusion coefficients from the bare kernel data are about an order of magnitude smaller than those from anneals of coated particles. There are, however, differences in the two sets of data with regard to experimental conditions and kernel composition. The coated particles experienced burnups ranging from 1.4 to 13% FIMA and include kernels of ThO_2 as well as ThC_2, $(Th,U)O_2$, and $(Th,U)C_2$. The bare ThO_2 kernels experienced burnups of only 0.9% FIMA.

From an examination of the coated particle diffusion coefficients (Ref. 4-2), no clear dependence on FIMA or kernel composition is evident in the data; however, the data show a large scatter. Thus, dependence on FIMA and kernel composition cannot be ruled out on the basis of the data in Fig. 4-1 to account for the differences in the data sets of Fig. 4-1. Experiments with bare kernels as a function of FIMA would aid in clarifying the bases of the observed differences.

DIFFUSION STUDIES

An earlier quarterly report (Ref. 4-6) described the beginning of the present study of the transport of cesium through graphite with the purpose

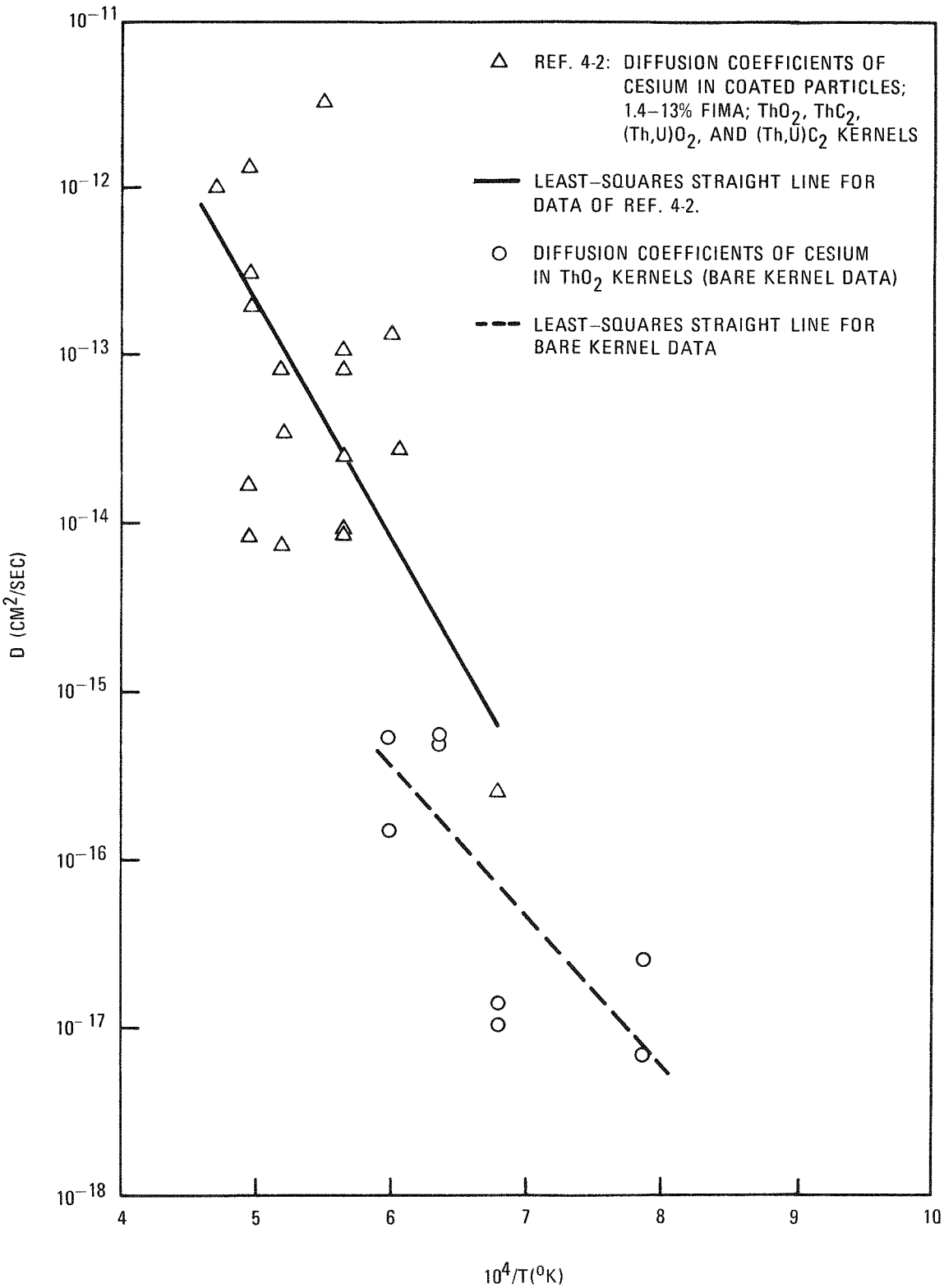

Fig. 4-1. Diffusion coefficients of cesium in kernels

of supplying dependable data for use in calculating cesium release from HTGR fuel elements. The basic method described in the earlier report continues to be developed and seems promising.

The underlying idea is to have a source of tracer cesium and a good sink for it separated by a leak-tight barrier of the studied graphite. If this assembly is also isolated against outside contamination then, after annealing for a known time at a known temperature, the activity of the sink measures the amount of cesium that has permeated through the barrier under these conditions. In addition, the activity of the barrier measures its overall takeup of the cesium and, if desired, a profile can be obtained to show the distribution within the barrier.

The parts of the assembly are shown in Fig. 4-2. Typically the rod and the skirt as well as the caps are made of char-loaded, i.e., highly sorptive, graphite and serve as source and sink, respectively. The sleeve and the plugs are of the graphite studied. The rod fits rather loosely in the sleeve, but the plugs are press-fitted into the sleeve and the caps are press-fitted into the skirt. Radio-autographs of the plugs and the skirt show that these press-fits are effective in preventing any significant leakage of the cesium. (When the fit is loose, considerable cesium travels through the joint.) Thus, a leak-tight envelope is placed around the source and is in turn surrounded by a leak-tight sink.

The assembly is placed in a char-loaded crucible to prevent any contamination from the outside and then annealed in a controlled atmosphere in a quartz tube.

As mentioned in Ref. 4-6, the effectiveness of the sink was determined by conducting comparative experiments in which the sleeve itself was char-loaded and acted as the sink so that there was no resistance (normally supplied by the sleeve of ordinary graphite) between source and sink. The amount of cesium transported under these conditions at lower temperature (860°C) was always 10 to 20 times that transported through the resistance.

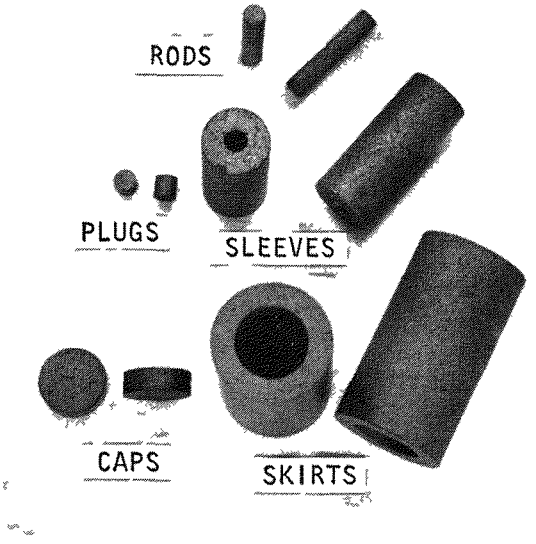

Fig. 4-2. Parts of assembly for diffusion studies

Hence, the sink and source together offered at most about 5% of the resistance of the normal sleeve, which is negligible.

The normal expectation would be that once steady state is reached, as shown by constant loading of the sleeve, successive experiments, each with a fresh sink but the same source and sleeve, would give identical results if one takes into consideration counting errors and the slow depletion of the source. As mentioned previously, this turned out to be far from the real situation, and much effort has been, and is still being, expended to approach the "normal" expectation. The situation still is that two or more experiments annealed together vary in quite satisfactory unison from anneal to anneal, but the variation of their average from one anneal to another supposedly identical anneal is considerably wider.

As already mentioned, an important source of variation was in the nature of the atmosphere present during annealing. In the presence of carbon monoxide or impure helium, i.e., slightly oxidizing atmospheres, transport was much higher than in the presence of hydrogen or under continuous evacuation. Hence all experiments are currently done in 0.1 atm of a buffer mixture of 10% CO in H_2, which gives about the same results as pure hydrogen but should be less influenced by degassing impurities. In order to reduce the effect of the latter, the quartz tube is evacuated and refilled twice with this mixture at room temperature, than again at 500°C, and finally at the temperature of the experiment. The temperatures are changed by inserting the tube into a tube furnace preheated to a slightly higher temperature so that thermal equilibrium is attained in less than 10 min. However, the first thorough evacuation to less than 0.1 μm Hg at a new temperature sometimes takes longer.

It was verified that transport is not enhanced significantly by evacuation and introduction of the gas; repeating this procedure every 15 min during a 2-hr anneal led to no noticeable increase in transport.

Another variation was traced to the fact that fresh sources, especially if prepared in niobium crucibles that prevent the loss of cesium during

annealing of the char-loaded rod with the cesium oxalate (36 to 72 hr at 1100°C in the mixed CO/H_2 atmosphere), are apparently not at equilibrium and contain some cesium of much higher chemical activity, which gives rise to increased transport during initial experiments. Hence sources are now "conditioned" by an experiment leading to some 20 to 30% depletion prior to undertaking a measurement.

An additional problem has been identified recently and has not as yet been eliminated. During the first few minutes of an experiment a significant transport of cesium occurs, which can amount to about 50% of the total during a 2-hr anneal at 860°C and about 25% of the total at 1100°C. This transport occurs above 500°C, is independent of evacuation and gas replacement, is not very reproducible, and is higher when the source is present than when it is omitted and transport is from the sleeve. Clearly this initial "burst" is an artifact. Until a technique for avoiding it is found, its effect can be minimized by accepting only the results of longer experiments, e.g., $\geq$6 hr, to which its contribution is minor.

Figure 4-3 shows the experimental results obtained to date. The solid points represent data obtained in the longer experiments. The Greek letters next to the solid points show which source-sleeve combinations were the same and the Roman letters show which anneals were the same. For historical reasons, there is no cross comparison as yet between temperatures for the same assemblies. A variance analysis of these scant data indicates that differences between samples (source and sleeve) contribute a standard error of some 23%, differences between annealing conditions (including the remnants of the "burst" effect) some 18%, and counting, etc., some 3.5%, giving a total standard error of some 34%. This is indeed close to the standard deviation from the best straight line shown in Fig. 4-3, which is 37%.

Shorter (2-hr) experiments are shown in Fig. 4-3 by open circles. The scatter in these data is much larger and the data points are higher. Similar short experiments performed with a 1000-times-higher cesium concentration are shown by open squares. These data points are clearly higher. The few

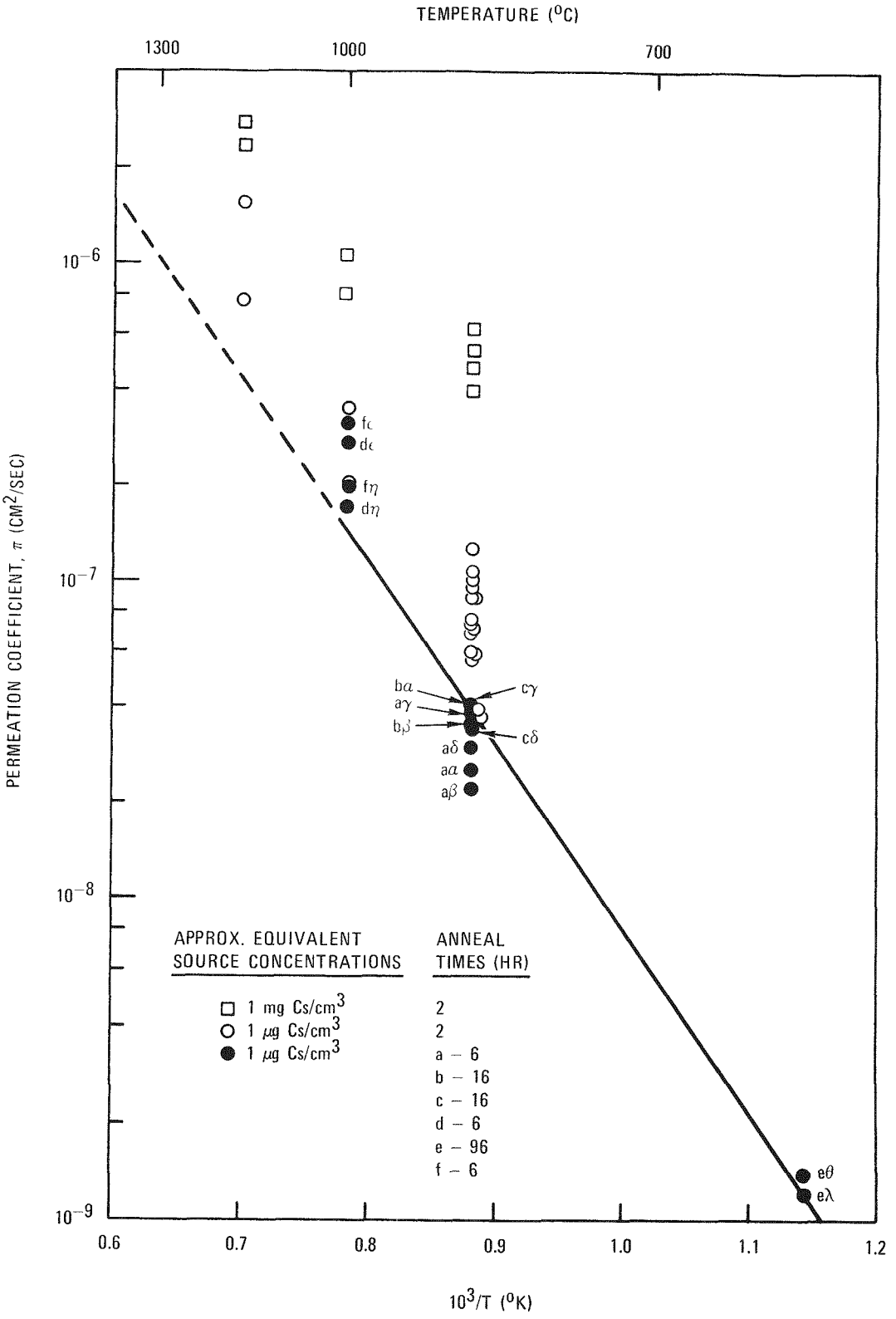

Fig. 4-3. Permeability coefficients as defined in text for cesium in H-451 graphite. Solid data points denote the more reliable experiments of 6 hr or more. Greek letters identify individual source-sleeve combinations and Roman letters identify anneals.

points at 1150°C are even more uncertain than the rest. Here the rapid permeation seems to saturate the sink as evidenced by an increase in the loading of the sleeve, which is lost within a short time of contact with a fresh sleeve at 860°C. This would indicate that the points should be somewhat higher than shown. On the other hand, they already appear to be above the value expected by extrapolation from lower temperatures. Clearly, additional work is required in this region.

The quantity plotted in Fig. 4-3 is a permeability coefficient defined in principle as follows:

$$J = \pi \frac{\Delta C}{\Delta x} \quad ,$$

where J is the flux per unit surface and unit time and ΔC is the concentration difference between the source and the sink separated by a sample thickness Δx. It is thus analogous to a diffusion coefficient for steady-state transport.

In practice, several modifications had to be introduced. As indicated above, the sink concentration is justifiably taken as equivalent to zero. Since the source is a different, highly sorptive graphite, its concentration has been divided by an estimate of its higher sorptivity relative to the graphite, namely, a factor of 10. To avoid any contamination by leaks, only the skirt part of the sink is counted; the geometric factor of the sleeve [equivalent to area/thickness or $2L/\ln(a/b)$, where L is the length of the cylinder and a and b are its radii] is 11.2 based on L = 2 cm, which is a compromise between the lengths of 2.22 cm for the skirt and 1.59 cm for the source. Thus, the expression used is

$$\pi = \frac{Q}{11.2t\ (S/10)} \quad ,$$

where Q is the activity of the skirt (μCi) after the anneal of duration t (sec) and S is the activity of the source per unit volume ($\mu Ci/cm^3$). Or, more conveniently,

$$\pi = 3.0 \times 10^{-5} \frac{Q}{sh} \left(\frac{cm^2}{sec}\right) \quad ,$$

where h is the duration of the experiment (hr), S is the source activity (μCi), and Q is the sink activity after the experiment (μCi). (The source volume is 0.12 cm^3, and its activity is of the order of 100 μCi.)

In the above discussion, loading of the sleeve was not included as the loading process was covered in Ref. 4-1.

VAPOR PRESSURE STUDIES

Cesium Sorption Isotherms on Irradiated H-451 Graphite

Isotherms for cesium sorption on irradiated near-isotropic (H-451) graphite have been obtained. The graphite sample was irradiated to a fluence of 3.4×10^{21} n/cm^2 at a temperature of 980°C.

The sorption measurements were made using the mass spectrometric - Knudsen cell method, which has previously been described (Refs. 4-7 through 4-9). In this method a sample of the graphite with sorbed metal is placed in a molybdenum Knudsen cell, which is a sealed cell with a small orifice. The cell is heated at a series of temperatures and the effusion of the metal vapor from the cell is monitored, as a function of temperature and time, by ionizing a portion of the effusant and measuring the intensity of the ion beam. The effusion of the metal vapor from the cell is a negligible perturbation to the equilibrium between the sorbed and vapor concentrations of the metal during the measurements at a fixed temperature. The vapor and sorbed concentrations of the metal are determined from a knowledge of the initial and final quantities of sorbate and the time profile of effusing metal. Initially, the metal is in the form of the nitrate, and a preliminary heating of the nitrate impregnated graphite in the cell converts the sorbate to metal. In the usual method, the graphite is in the form of a powder with particles having diameters in the range of 44 to 74 μm.

The isotherm derived for the irradiated H-451 graphite is compared with the isotherm for unirradiated H-451 graphite in Fig. 4-4 for a temperature of 1360°K. Isotherms for unirradiated H-451 graphite are presented in Ref. 4-5. The comparison is similar at other temperatures between 1100° and 1500°K. At all values of the vapor pressure shown in Fig. 4-4, the sorptivity of the irradiated graphite is greater than that of the unirradiated graphite by factors as large as 10. The increase in sorptivity with irradiation is greater at smaller vapor pressures. For both sets of data shown in Fig. 4-4, the representation for the higher sorbate concentrations can be made with the Freundlich sorption isotherm and for the lower sorbate concentrations, with the Henrian sorption isotherm (a description of the two types of isotherms is given in Ref. 4-10). The transition from the sorbate concentration range in which the Freundlich sorption isotherm represents the data to that range in which the Henrian isotherm is the preferred description occurs at nearly the same vapor pressure for both the irradiated and unirradiated graphite isotherms. The sorbate concentrations at the transition are, from Fig. 4-4, about 0.16 and 1 mg Cs/g graphite for the unirradiated and irradiated graphite isotherms, respectively. The ratio of the sorbate concentration for irradiated to unirradiated graphite is essentially the same for isotherms covering the temperature range between 1100° and 1500°K.

With the determination of the cesium sorption isotherms on irradiated, near-isotropic (H-451) graphite, the planned work on cesium sorption on near-isotropic graphite has been completed.

Strontium Sorption Isotherms on Fuel Rod Matrix

Measurements of the strontium sorption isotherms on the fuel rod matrix material M-205 have been completed. The material M-205 is the near-reference fuel rod matrix material for the large HTGR and is very similar to the matrix material used in Fort St. Vrain fuel rods. Thus, the present experimental results serve as the basis for the reference strontium sorption isotherms for the fuel rod matrix. Another feature of the present results

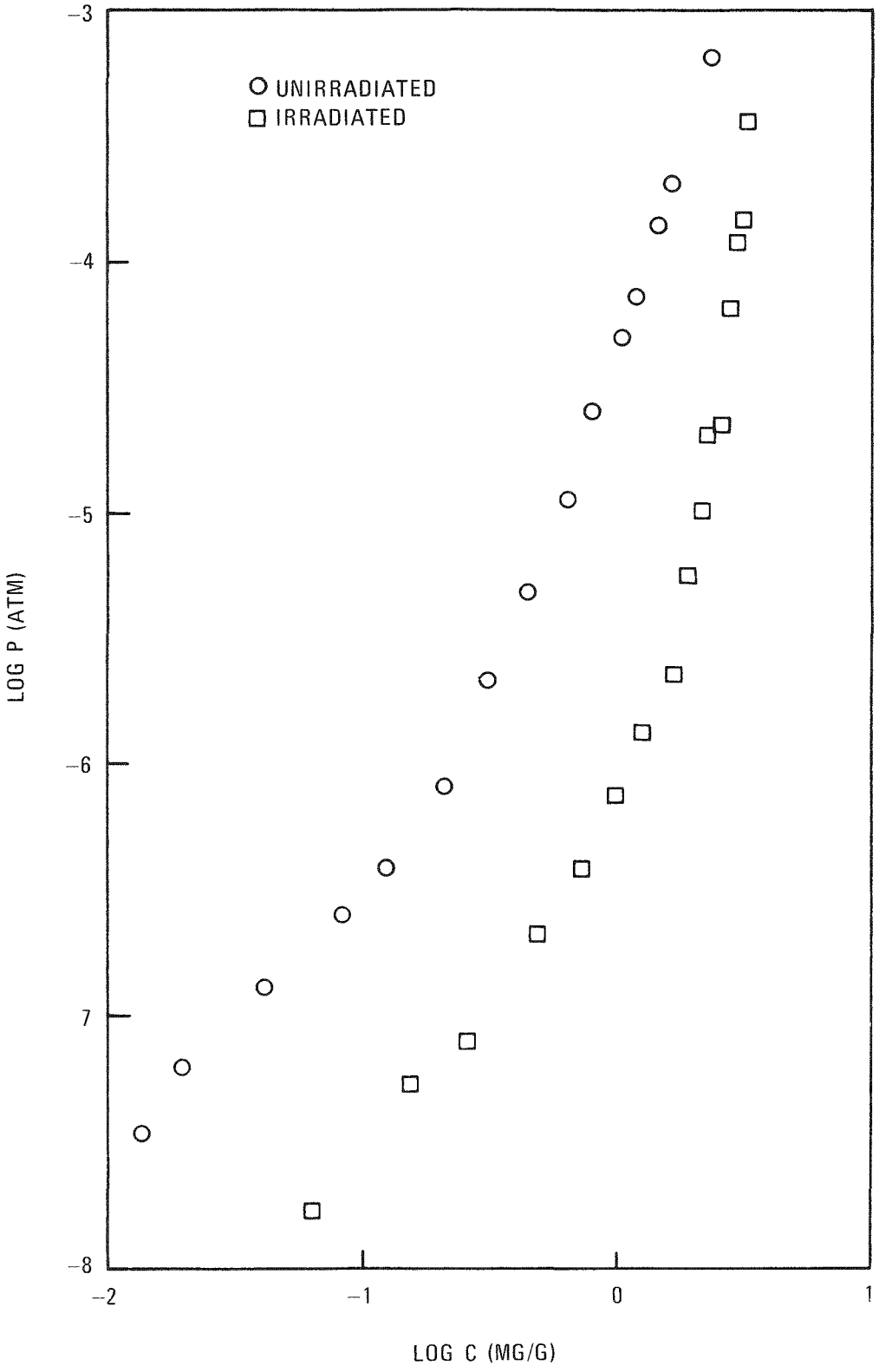

Fig. 4-4. Cesium sorption isotherms at 1360°K for irradiated and unirradiated H-451 graphite

is the first extension of the measurements to the range of low sorbate concentrations where the Henrian isotherm is appropriate to represent the data.

The measurements were made using the mass spectrometric - Knudsen cell method as described above. Isotherms derived from the measurements are shown in Fig. 4-5 at 1800°K for two runs. The sorbate concentrations are based on a molecular weight of 87.6 g/mole for strontium. Table 4-3 gives the heat of adsorption, temperature range, and sorbate concentration for each determination. For run number 1, the 11 data points in Fig. 4-5 corresponding to the highest vapor pressures were based on extrapolations of the data to 1800°K from temperatures below 1750°K; for run number 2, only the two data points corresponding to the highest vapor pressures were so obtained.

The data of Fig. 4-5 clearly demonstrate a transition to the Henrian isotherm region for sorbate concentrations below 30 μmole Sr/g matrix. In the mutual concentration range of the two runs, the agreement of the data is to within a factor of four in vapor pressure. The previously selected reference isotherm (Ref. 4-10) is also shown in Fig. 4-5. The agreement is very satisfactory in view of the fact that the previously selected reference curve was chosen on the basis of the similarity of the composition of the Fort St. Vrain matrix material, for which sorption measurements were then available, and the reference matrix material, M-205.* It should also be noted that the previously selected reference isotherm was assigned a transition concentration, i.e., sorbate concentration at which the isotherm description is changed from Freundlich to Henrian, on the basis of the vapor pressure corresponding to the transition concentration of the reference graphite isotherm (Ref. 4-10). According to Fig. 4-5, this procedure yielded essentially correct transition concentrations for the materials.

*The major difference between the Fort St. Vrain matrix material and M-205 is that coal tar pitch, Grade 15v, was used to formulate the former material while petroleum pitch, Grade A240, was used in the latter material. Also, the M-205 fuel rod material contains about 2% more graphite and roughly twice as much sulfur as the Fort St. Vrain material.

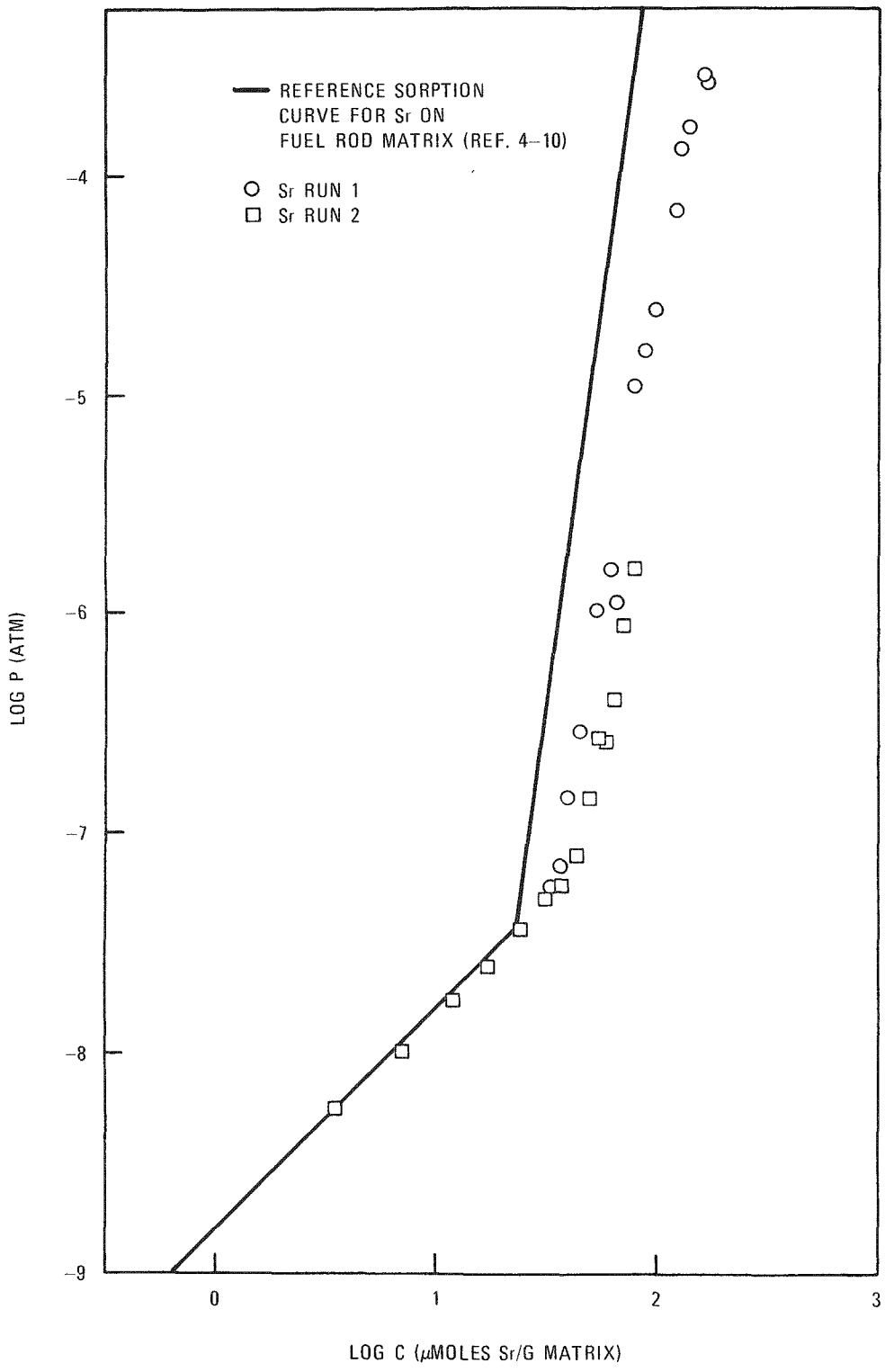

Fig. 4-5. Strontium sorption isotherms at 1800°K on fuel rod matrix material

TABLE 4-3
HEATS OF ADSORPTION FOR STRONTIUM ON FUEL ROD MATRIX MATERIAL (M-205)

Run No.	Determination No.	ΔH (kcal/mole)	Temperature Range (°K)	Sorbate Concentration (μmole Sr/g material)
1	1	80.2 ± 2.6	1296-1437	173
	2	73.9 ± 1.6	1327-1447	163
	3	77.2 ± 1.4	1327-1473	154
	4	75.7 ± 2.2	1352-1503	141
	5	78.7 ± 2.1	1324-1526	130
	6	73.4 ± 1.8	1364-1585	122
	7	71.7 ± 2.0	1419-1620	102
	8	75.5 ± 2.0	1453-1649	90.1
	9	77.7 ± 2.0	1503-1579	80.5
	10	83.1 ± 3.4	1551-1719	67.4
	11	86.2 ± 2.1	1610-1764	61.8
	12	85.0 ± 0.7	1649-1829	53.5
	13	84.9 ± 3.0	1704-1889	44.7
	14	93.9 ± 2.3	1759-1904	40.4
	15	99.9 ± 3.5	1769-1899	37.4
	16	98.6 ± 5.5	1789-1919	34.3
2	1	103.7 ± 4.7	1553-1663	78.5
	2	98.8 ± 2.2	1578-1753	77.8
	3	97.8 ± 2.3	1608-1818	72.7
	4	109.2 ± 1.6	1673-1868	65.6
	5	109.1 ± 1.9	1678-1883	60.0
	6	108.8 ± 2.8	1713-1903	55.2
	7	111.4 ± 4.9	1758-1953	49.4
	8	114.8 ± 3.9	1748-1948	43.2
	9	122.6 ± 3.3	1773-1948	37.5
	10	116.2 ± 2.8	1793-1978	31.0
	11	120.3 ± 2.4	1783-1988	24.2
	12	128.8 ± 4.0	1808-1993	17.4
	13	125.9 ± 2.6	1808-1998	11.9
	14	126.5 ± 2.3	1823-2013	7.18
	15	130.8 ± 2.3	1813-2008	3.45

The 1200°K isotherms for material M-205 are shown in Fig. 4-6 along with the corresponding, previously selected, isotherm (Ref. 4-10). The data in Fig. 4-6 were obtained by extrapolation of the results of runs 1 and 2; the extent of this extrapolation is indicated by the data of Table 4-3. The comparison of the 1200°K isotherms with the previously selected isotherm (Ref. 4-10) again indicates agreement.

The uncertainties associated with the heats of adsorption given in Table 4-3 are the standard deviations of the mean from the least-squares fit to the curves of log P versus 1/T, where P is the vapor pressure in atm and T is the temperature in °K. As expected, the heats of adsorption increase with a decrease in sorbate concentration and appear to have reached a region of constant value in run 2 in the range between 125 and 131 kcal/mole.

TRAFIC CODE DEVELOPMENT

Development of the TRAFIC code has achieved a significant milestone in that the first operational version is now complete. TRAFIC is being developed, as a fast-running replacement for FIPER, for use in calculating the release of metallic fission products from HTGR fuel elements.

The operational version of TRAFIC reads an input data tape prepared by a proprietary core performance code named TREVER. The input tape contains fuel temperatures, fuel failure fractions, and a number of other thermal and/or physics parameters as functions of time for a large number of spatial positions in the core. TRAFIC automatically processes this tape for all space points. It then sorts and processes the local fuel block release values to obtain results categorized by total core, core segment, and reload. The work performed during the quarter is summarized below.

The TREVER tape version of TRAFIC has undergone a thorough reprogramming and cleanup. The purpose of this work has been to:

1. Improve the calculational efficiency of the program.

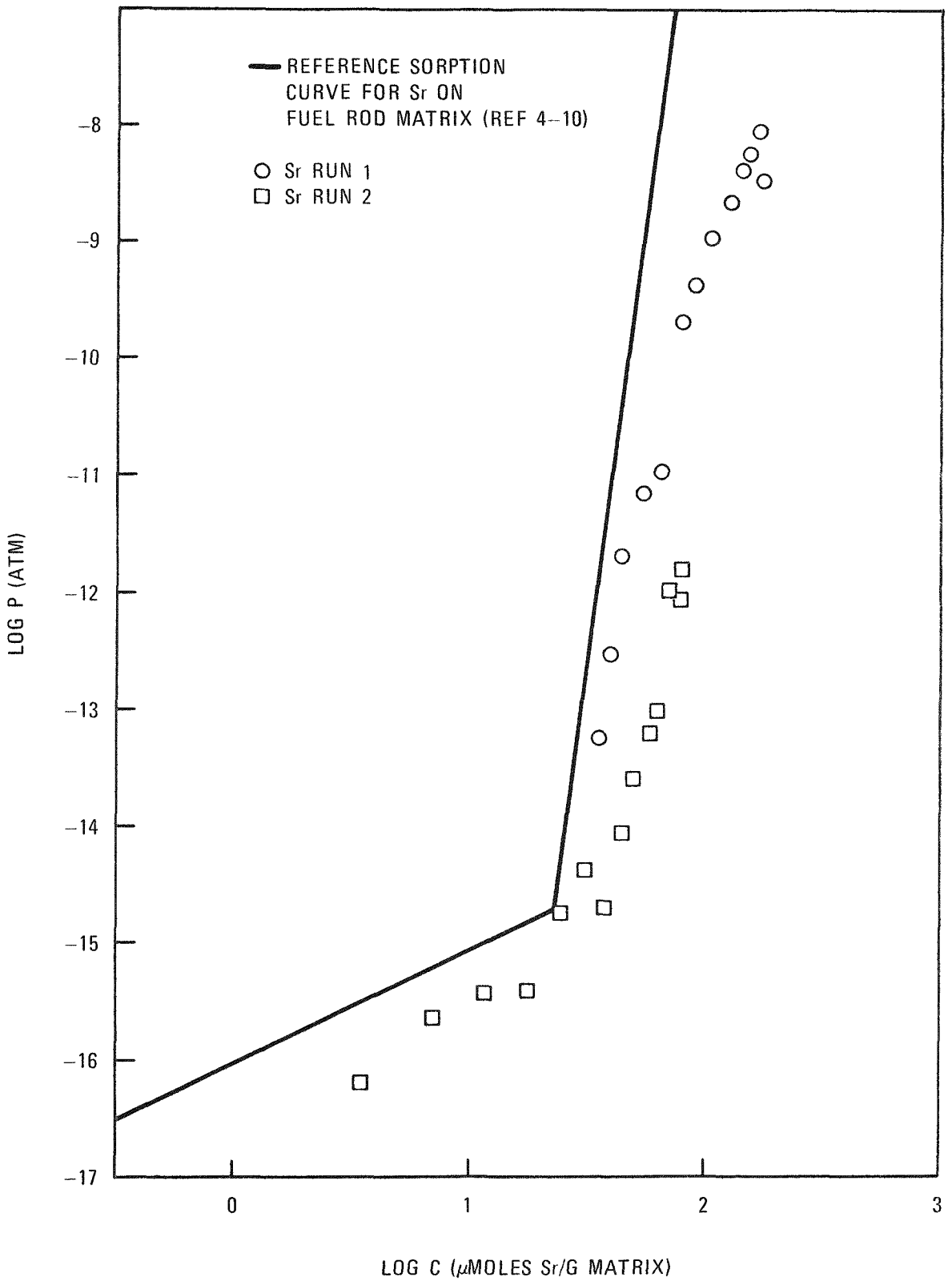

Fig. 4-6. Strontium sorption isotherms at 1200°K on fuel rod matrix material

2. Remove nonconvergence and numerical stability difficulties previously encountered.

3. Provide an independent check that the solution algorithm is correctly programmed.

4. Generalize the program to accept problem-dependent parameters from input cards rather than have them initialized as built-in data.

5. Clean up and simplify the program logic.

6. Document the program with descriptive comments throughout the coding.

7. Modularize the metallic fission product transport solution as a subroutine.

This work has been completed, and all the objectives have been realized. The major improvements to TRAFIC can be summarized as follows:

1. The present version of TRAFIC, compared to the older version, runs 4.9 times faster with printout (1.4 sec versus 6.9 sec per location analyzed) and 8.5 times faster without printout (0.73 sec versus 6.2 sec).

2. The present version of TRAFIC requires 40% less program storage (8,040 words versus 13,470 words) and 78% less data storage (5,610 words versus 25,820 words for a representative problem) at execution. The reduction in variable storage was made possible through reprogramming many dimensioned variables as simple variables.

3. The previous (5 x 5) system of equations has been reduced to a (2 x 2) system of equations for solution by the subroutine VECTIT.

This was made possible by the fact that three of the original five equations are linear in their unknowns.

4. Roundoff errors were detected in a few of the equation coefficients for very small times. These caused small negative concentrations early in life, but they had no significant effect on the final results. The problem was eliminated by replacing the series solution by a fitted quadratic polynomial for short times.

5. A new method for projecting the solution in time was developed. This gives a much more accurate first guess and significantly reduces the number of iterations required.

6. A number of minor errors in the earlier coding were corrected.

The present version of TRAFIC has been tested in comparison with the older version by doing a column-averaged strontium release calculation at high and low power locations. Results before the error corrections [item (6) above] were identical within the accuracy of the convergency tolerance. After the error corrections it was found that short time releases were significantly higher but that the accumulated error was reduced to a few percent in the fourth year of irradiation.

FISSION PRODUCT TRANSPORT CODE VALIDATION PROGRAM

The objectives and schedule for work on validation of fission product transport codes and input data have been formulated with the issuance of the "Planning Guide for Validation of Fission Product Transport Codes" (Ref. 4-11). This document serves as a supplementary document to the "HTGR National Fission Product and Coolant Chemistry Program Plan" (in review) and as lead document for proposed validation studies. A summary of the validation program plan was presented in a previous quarterly report (Ref. 4-12).

Data are being collected for use in the various code and data validation tests, and work plans are being prepared for each test. Considerable effort has been expended on fundamental review studies and code familiarization for engineers and scientists assigned to the code validation subtask.

TRITIUM TRANSPORT DATA REVIEW

A review of tritium behavior in HTGR systems is nearly complete. The purpose of this review, which is in the form of a topical report, is to examine all the available data relevant to tritium production and migration in HTGRs in order to decide if adequate data exist to predict with sufficient confidence the level of tritium release to the environment from large HTGR plants.

The transport of tritium from the reactor into the environment via the secondary coolant may be considered to depend upon five main processes:

1. The production of tritium in the reactor.

2. The release by diffusion of tritium into the primary coolant from reactor materials in which it is borne.

3. The retention of tritium on reactor core materials by recoil and by chemisorption.

4. The removal of tritium by the reactor coolant purification and recovery system.

5. The tritium permeation rate through the steam generator tube materials.

Processes (1) through (4) determine the tritium concentration in the primary coolant, which in turn provides the driving force for tritium permeation of the superheater steam tubes.

Conclusions from the review are:

1. More accurate prediction of tritium behavior in HTGRs is needed.

2. Calculation of the amount of tritium produced in HTGR fuel is uncertain because not enough is known about the influence of flux energy spectrum, enrichment, and type of fuel on the tritium fission yield.

3. Lithium impurity levels for reference fuel rod matrix and graphite materials need to be determined (see following section). These impurity levels often border on the limit of analytical detection; nonetheless, they give rise to the production of substantial quantities of tritium.

4. More needs to be known about the release (especially long-term release) of tritium from intact and failed reference fuel particles.

5. The tritium retention characteristics of reference matrix and graphite materials need to be determined.

6. More needs to be known about the effect of oxide films on the permeation of tritium through steam generator tubes.

7. Tritium chemisorbs on graphite but the extent to which this occurs in the radiation field of an HTGR is not certain.

The main conclusion to be drawn from the above items is that there is not yet enough information on tritium behavior to determine with adequate confidence whether or not tritium release levels for the large HTGR plants will be within the limit of 3 mrem/yr (for the liquid effluent) as fixed by the final version of 10 CFR 50, Appendix I. In accord with this conclusion, laboratory work to determine the retention of tritium in reference fuel and graphite materials has been initiated.

LITHIUM CONTENT OF CORE MATERIALS

The lithium content of reference and near-reference fuel rod matrix and near-isotropic graphite samples has been measured; however, the results are questionable because round-robin lithium determinations, made a GA and ORNL, do not agree. This study was undertaken to provide more accurate input data for use in calculating the production of tritium in large HTGRs.

In preparation for this work, an analytical method based on atomic absorption was developed for the determination of lithium in graphite at levels below about 0.05 ppm. This method is described in Ref. 4-1.

The round-robin study consists of lithium determinations at GA and ORNL (and possibly other laboratories) on companion samples of graphite cut from the same graphite specimen. The analytical techniques utilized are atomic absorption (Ref. 4-1) at GA and spark mass spectrometry at ORNL.

The lithium content values for the six graphite samples tested range from <10 ppb to 70 ppb as determined at GA and <5 ppb on all six samples as determined at ORNL.

It is concluded that additional work is required to resolve the discrepancy. The work at GA will be continued under Task 9, Graphite Development.

TRITIUM DETERMINATION IN CONTROL MATERIALS

In a cooperative experiment between GA and Los Alamos Scientific Laboratory (LASL), five samples of boronated graphite irradiated in capsules BG-1 and BG-2 were analyzed at LASL by a combustion method. Earlier results from this joint effort were reported previously (Ref. 4-12). Specimen numbers and tritium content values (as reported by LASL) are given in Table 4-4. The specimens and irradiation conditions are described in Ref. 4-13.

TABLE 4-4
TRITIUM CONTENT IN BORONATED GRAPHITE SAMPLES

Specimen Number	Tritium Content (ppm H-3)
4-1-2	0.37
4-3-1	0.33
4-2-1	0.28
4-2-2	0.31
1-2-1	0.09

It was planned to utilize these tritium content data along with calculated tritium production data to determine the fraction of tritium retained in each specimen during irradiation.

An earnest attempt was made to calculate the amount of tritium produced. Effective fast cross sections were calculated using the ETR fast neutron energy spectrum (Ref. 4-14) and ENDF/B (Ref. 4-15) cross-section data for the B-10(n,2α)T and Li-7(n,nα)T reactions. These are the two direct tritium producing reactions in this case. An effective thermal cross section for the B-10(n,α)Li-7 reaction was derived by utilizing the ETR thermal neutron energy spectrum in conjunction with ENDF/B data and a self-shielding factor. The latter is necessary to account for the thermal flux depression in highly boronated material.

A calculation of the amount of tritium produced in each sample was made based on the derived effective cross sections and flux data found in Ref. 4-13. Unfortunately the thermal flux during the BG-1 and BG-2 capsule tests was not well defined as the function of the capsule tests was primarily to examine fast neutron damage in graphite. Thus, the uncertainty in the thermal flux is very large (approximately ±50%) and when viewed in conjunction with uncertainties in the tritium measurements, casts doubt on the worth of the retention data. The retention values are about 30% except for sample 1-2-1 (Peach Bottom HTGR absorber material), which gave a value of 10%. Recognizing the uncertainty in the thermal flux values,

it can still be concluded that the tritium retention in control materials is greater than the assumed value of zero, which is used in reactor calculations of tritium release from the HTGR core.

TRITIUM PERMEATION RATE THROUGH STEAM GENERATOR TUBE MATERIALS

As reported in the previous quarterly (Ref. 4-1), the tritium permeabilities through T-22 using four different tritium-helium mixtures with specific activities ranging from 3.62×10^{-5} to 6.14×10^{-3} $\mu Ci/cm^3$ were measured in the temperature range 292° to 505°C. Because the tritium source used for the preparation of these mixtures contained hydrogen, it was not possible to vary the tritium activities and the hydrogen concentrations of these mixtures independently so that the effect of these two variables on tritium permeation rate could be evaluated separately. However, the results showed that for low hydrogen concentrations (a few hundred ppm or less), the tritium permeation rate appeared to vary with $p_{HT}/\sqrt{p_{H_2}}$, where p_{HT} and p_{H_2} are the partial pressures of HT and H_2 in these mixtures, respectively. At high hydrogen concentrations (several thousand ppm), the activation energy for tritium permeation became lower and the permeation rate became much larger than that predicted on the basis of the $p_{HT}/\sqrt{p_{H_2}}$ rule.

To evaluate the effect of p_{HT} and p_{H_2} independently, a high purity and high specific activity tritium source was procured from ORNL. This source was diluted with high purity helium gas to form a tritium-helium stock mixture having a specific activity of 0.57 $\mu Ci/cm^3$. The impurity contents of this stock mixture are: O_2, 2.5 ppm; H_2, <20 ppm; N_2, 7 ppm; CO, <1 ppm; CH_4, <1 ppm; and H_2O, 4 ppm. From this stock mixture, four tritium-helium working mixtures with specific activities ranging from 3×10^{-5} to 5×10^{-3} $\mu Ci/cm^3$ were prepared. A new T-22 tubular sample having a wall thickness of 1 mm was installed in the test chamber. For each of the four tritium-helium mixtures to be tested, tritium permeation rates will be measured in the temperature range 300° to 500°C before and after the addition of increasing amounts of hydrogen into the tritium-helium gas stream passing through the test chamber. Work is now in

progress with the tritium-helium mixture with a specific activity equal to 1×10^{-4} $\mu Ci/cm^3$.

EFFECT OF HYDROLYSIS ON FUEL EXPANSION

It has been established that the reaction of fuel carbides with water vapor produces an increase in volume. This results because the product of the fuel hydrolysis reaction,

$$(U,Th)C_2 + H_2O = (U,Th)O_2 \cdot xH_2O + \text{hydrocarbons} + H_2 + C_{(s)} + CO, \quad (4\text{-}1)$$

is less dense than the original carbide, giving rise to expansion of the affected fuel.

Earlier studies on this problem utilized closed crucibles containing fuel undergoing hydrolysis and were designed to help determine particle failure fractions of carbide particles necessary to cause failure in fuel element webs. It was concluded that particle failure up to 62% (0.85 g Th/cm^3) of the fuel rod would not crack the graphite web. These experiments, however, did not allow measurement of the actual force produced when constrained fuel hydrolyzes, nor did they allow determination of the effect of hydrolysis temperature, water vapor concentration, or burnup. Accordingly, an experimental program has recently been initiated at GA to determine the expansion characteristics of hydrolyzing HTGR fuels and the concomitant stresses produced in the constraining graphite fuel elements (Ref. 4-6).

Experimental Procedure

The complete experimental apparatus described earlier (Ref. 4-6) is still under construction. For the work reported herein, a temporary rig was employed. This apparatus is shown schematically in Fig. 4-7. In this rig, a crucible containing the carbide sample is supported on the bottom

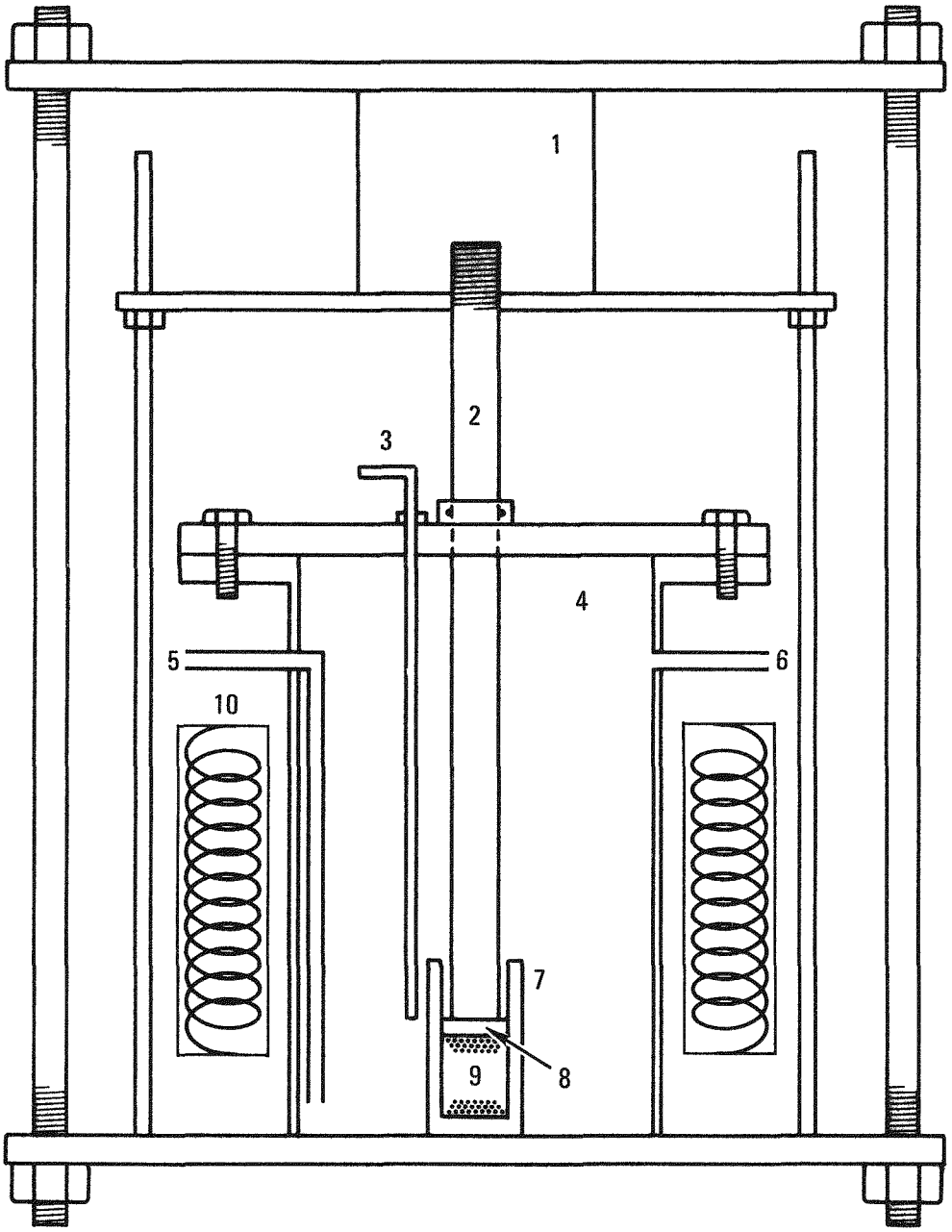

1. LOAD CELL
2. STEEL ROD
3. THERMOCOUPLE
4. STEEL PRESSURE VESSEL
5. GAS INLET
6. GAS OUTLET
7. GRAPHITE CRUCIBLE
8. GRAPHITE PLUG
9. FUEL SAMPLE
10. FURNACE

Fig. 4-7. Load cell apparatus

of the stainless steel pressure vessel. A graphite plug is inserted into the crucible and rests directly on the fuel sample. Resting on the plug is a steel rod, which penetrates the upper plate through a gas-tight, O-ring seal and is attached to a load cell. The load cell is held firmly in place by a steel plate, which is connected to the bottom plate by threaded 1/2-in. steel rods. With this arrangement the force induced in the fuel sample is transmitted directly to the load cell via the central rod.

The test crucible was machined from H-451 graphite; its dimensions are 0.625 in. i.d., 0.18 in. wall thickness, and 0.18 in. bottom thickness. All of the experiments reported herein used the same test crucible.

The concentration of water vapor in the helium carrier gas was established by bubbling the helium through a water saturator maintained at a constant 32.5° ± 0.3°C (which produced 48,000 ppmv water vapor) by a Bronwill controller-heater. The inlet lines from the saturator to the reaction vessel were heated to 90°C to prevent water vapor from condensing in the lines.

The reaction temperature was maintained by surrounding the pressure vessel with a Kanthal-wound furnace. The furnace was connected to a Barber-Coleman controller and solid-state SCR, which held the inside of the vessel to within a variance of ±2°C at 600°C. The temperature inside the vessel was measured with an Inconel sheathed, chromel-alumel thermocouple.

The effluent gas from the reaction vessel was analyzed for its hydrocarbon concentration by a Dohrman gas chromatograph with a flame ionization detector. Interfacing the chromatograph with a Carle Valve Minder and a Spectra Physics Minigrater enabled automatic analyses at operator selected time intervals from 15 to 60 min. The gaseous hydrocarbon reaction products that have been identified by gas chromatography are methane, ethane, ethylene, acetylene, propane, propylene, and n-butane. The major species

are ethane at 100°C and methane at 300°, with methane being the only significant gaseous species at 600°C and above.

It is of interest that at ≥200°C the total gaseous hydrocarbons found during complete hydrolysis constitute only about 15% of the carbon in the sample. Indeed, chemical analysis of the hydrolysis product of ThC_2, which had been completely hydrolyzed at 500°C, showed that 80% of the original carbon remained. Thus, it is surmised that part of the volume or density change in the hydrolyzed product is due to residual free carbon or solid hydrocarbons. Additional support for these findings was obtained in a temperature-programmed mass spectrographic analysis of outgassed products from a ThC_2 sample that had been completely hydrolyzed at 99°C (Run 26). It was found that above 200°C, numerous organic hydrocarbons, as complex as toluene, outgassed from the hydrolyzed product.

In order to determine the extent of reaction, the concentration of one of the major hydrocarbon products (e.g., ethane in the effluent gas) was plotted as a function of time. The total area (A_t) under this concentration-time curve was calculated using Simpson's rule. The area under the curve up to the time of interest, Q, was determined and the percent reaction at that time was calculated using the following equation:

$$\% \text{ reaction} = Q/A_t \times 100 \quad . \tag{4-2}$$

A summary of the test matrix, conditions, and results are given in Table 4-5. Most of the tests were performed with fully dense and spheroidized ThC_2 fuel kernel material mixed with reference dummy particles.

Two experiments involved the use of specially prepared fuel rods that were intended to simulate possible high failure fractions in the reactor. These rods were prepared from a mixture of ThO_2 particles and representative HTGR matrix material. Each ThO_2 particle consisted of a 500-μm kernel surrounded by a 89-μm buffer layer and a 21-μm outer LTI

layer. This particular coating was designed to fail at high temperature (2000°C) and allow conversion of the ThO_2 to the dicarbide via the reaction

$$ThO_2 + 4C = ThC_2 + 2CO \quad . \qquad (4\text{-}3)$$

The prepared fuel rods were first carbonized by heating in argon at 10°C/min up to 1200°C and holding the temperature for 1 hr. To fail the coatings and to convert the ThO_2 to dicarbide, the samples were placed in an induction furnace and heated to 2100°C for 6 hr under 30-μm pressure. The percent of failure and conversion was estimated from metallographic studies and from hydrolysis of small portions of the rods to be 95 ± 5%.

Results

The results of the runs to data are shown in Table 4-5.

Figure 4-8 shows characteristic load-time curves obtained for hydrolysis temperatures from 99° to 693°C. It is seen that the highest load was observed in the 300°C run.

Figure 4-9 is a plot of the percent of load produced as a function of the percent of hydrolysis at three different temperatures. For this particular plot, there is no temperature effect; i.e., during a time interval sufficient to hydrolyze a given amount of the fuel, the percent of the maximum load is the same at 100°, 300°, and 600°C. This is the case even though the maximum load produced varies with the temperature as does the rate of attaining this maximum load. This suggests that load can be predicted from the integrated hydrocarbon evolution which can be equated to the degree of hydrolysis. One important fact is apparent in Fig. 4-9. Initially the load increases slower than the fuel hydrolyzes. For example, when 10% of the fuel has hydrolyzed, only 3% of the load has formed. This discrepancy, which is obvious in the initial

TABLE 4-5
RATE AND LOAD DATA FOR HYDROLYSIS OF ThC_2 KERNELS CONTAINED IN GRAPHITE CRUCIBLE

Run No.	Experimental Conditions				Results			
					Load			Hydrocarbon
	Weight ThC_2 (g)	Volume (cm^3)	Loading (g/cm^3)	Temp (°C)	Maximum Load (psi)	Maximum Rate ($lb/in.^2/hr$)	Maximum Rate (%/hr)[a]	Maximum Rate (%/hr)[b]
9[c]	3.5	2.0	1.73	300[d]	963	ND[e]	ND	ND
10[c]	5.0	4.0	1.25	300[d]	1034	ND	ND	ND
14	0.25	0.97	0.26	300	112	ND	ND	ND
15	0.50	0.96	0.52	300	245	ND	ND	ND
16	0.75	0.87	0.86	300	530	ND	ND	ND
17	0.10	0.96	0.11	300	235	ND	ND	ND
18	0.75	3.08	0.24	300	122	ND	ND	ND
19	0.97	0.21	4.64	300	3099	143	4.6	5.2
20	1.00	0.22	4.64	200	2636	116	4.4	5.8
21	1.01	0.21	4.77	400	2800	162	5.8	6.9
25	1.03	0.20	5.12	600	2178	70	3.2	4.8
26	1.01	0.21	4.81	99	2356	80	3.4	3.8
27	1.00	0.22	4.42	693	1359	68	5.0	ND

[a] Percent of maximum load produced during run.

[b] Percent of total hydrocarbons produced during run.

[c] Converted fuel rod section.

[d] Temperature uncertainties are ±10°C for Runs 9 and 10 and ±2°C for the other runs.

[e] ND = not determined.

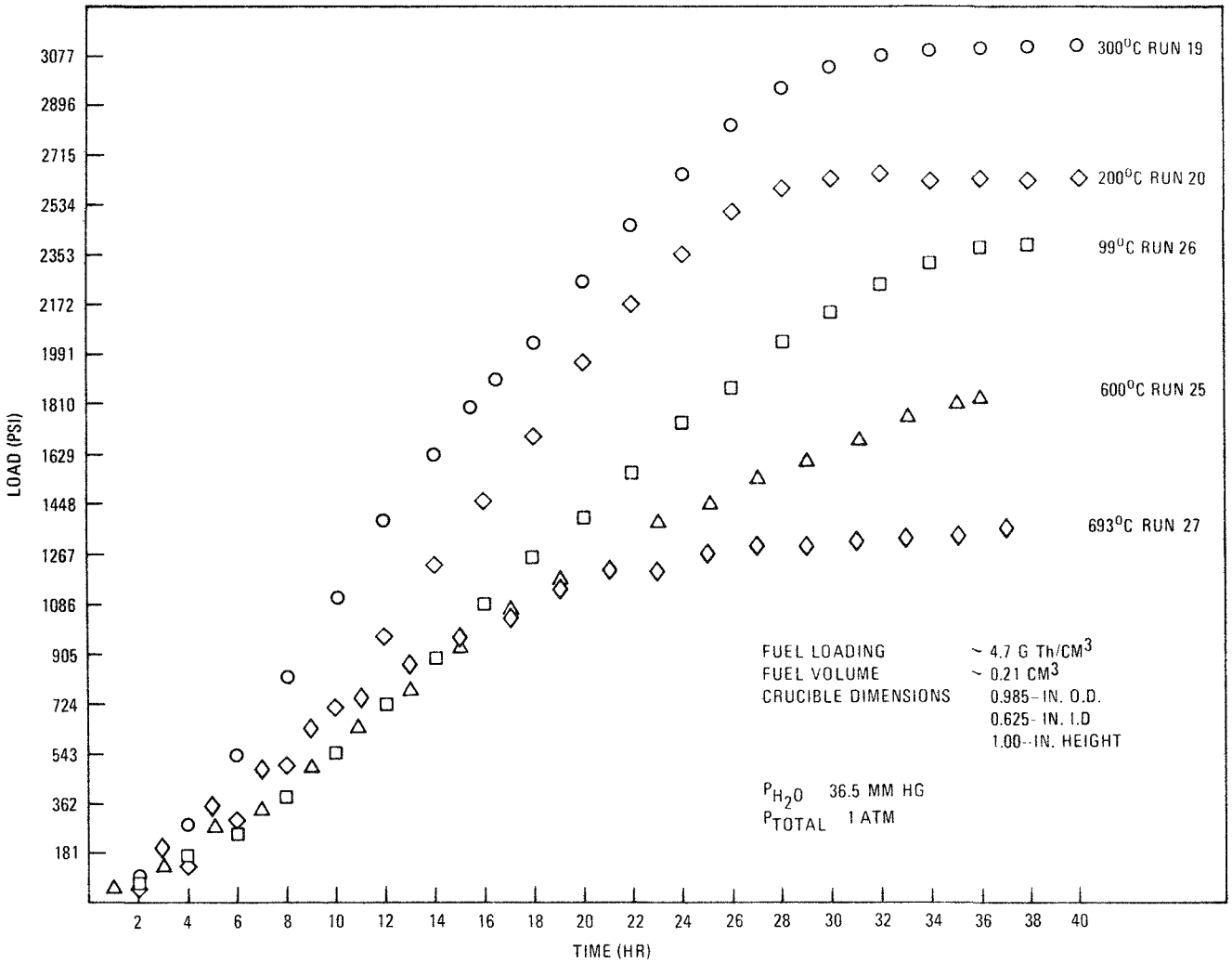

Fig. 4-8. Load development during exposure of ThC_2 to water vapor

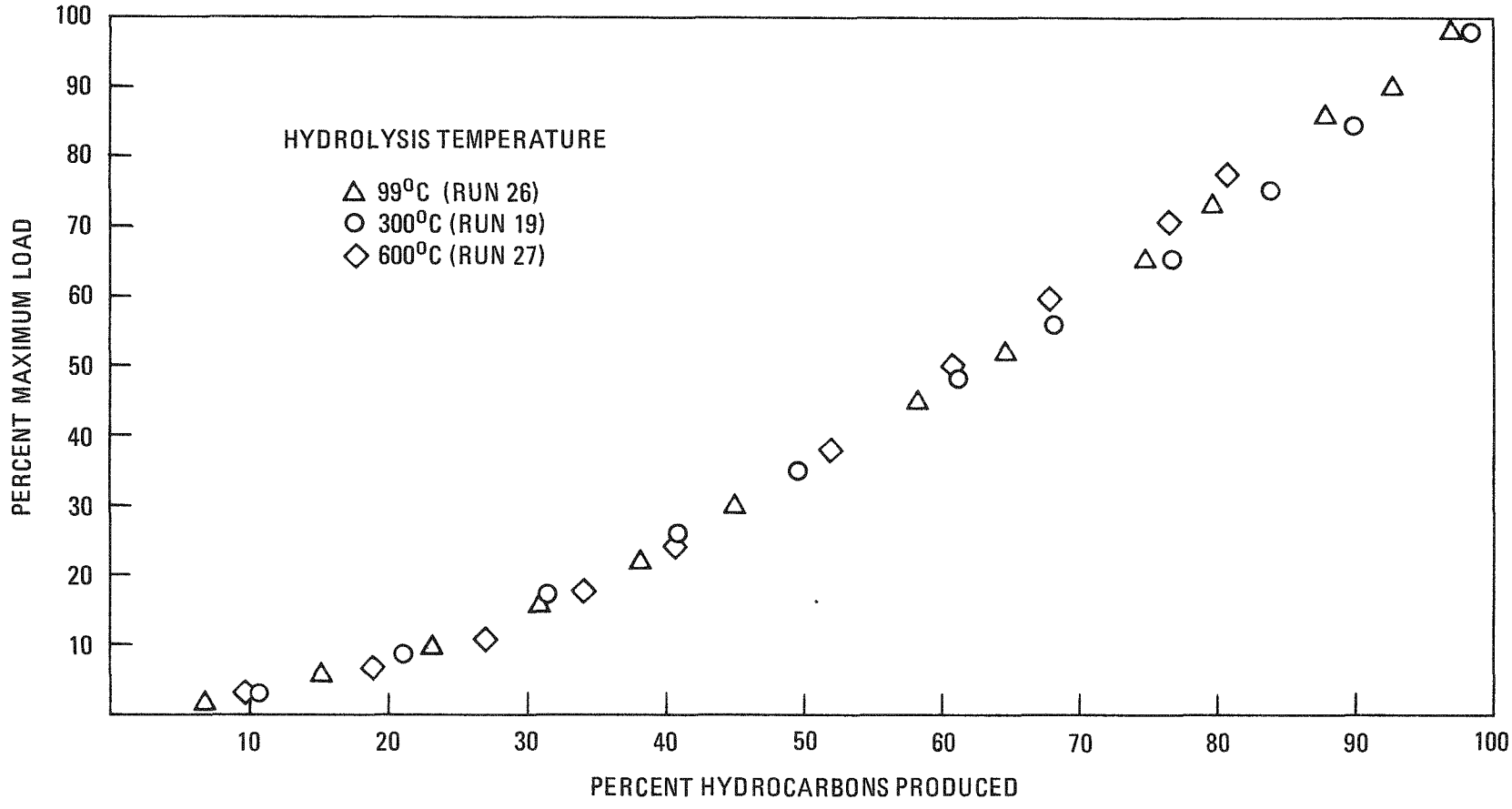

Fig. 4-9. Percent of maximum load produced as a function of the percent of fuel hydrolyzed

portion of the load-time curves, is probably due to filling the void space between the ThC_2 kernels before any load can be produced. This would cause the load to exhibit a "lag period" during which time void space is being filled.

As explained under Experimental Procedure, the extent of hydrolysis is calculated from data on the production of hydrocarbon product. Table 4-5 and the Arrhenius-type plot in Fig. 4-10 demonstrate that the rate of hydrocarbon production and the rate at which the maximum load is attained are related. Neglecting the 600° and 693°C values, the apparent activation energy, ΔH_a, based on hydrocarbon data is 0.85 kcal/mole and that based on load data is 0.81 kcal/mole. This agreement supports the conclusion that both data are measuring a single phenomenon. Furthermore, this low apparent activation energy suggests that the rate limiting process is diffusion of water vapor through the graphite crucible and into the tightly packed bed. (The ΔH_a for diffusion of water in graphite is approximately 1.7 kcal/mole. The ΔH_a for chemical reaction of water with carbide is in excess of 10 kcal/mole.)

The maximum load produced as a function of temperature when 1 g of bare ThC_2 kernels is hydrolyzed is shown in Fig. 4-11. The highest load is produced when fuel is hydrolyzed at 300°C. A uniform decrease in the load is observed above and below this temperature. At 700°C, the load produced is only 44% of the load produced at 300°C. The final load is a function of the degree of expansion of the product which, in turn, is dependent on the degree of hydration of the ThO_2 (see Eq. 4-1), the actual crystal structure of the ThO_2, sintering of the loose product (especially at higher temperatures), and the amount and nature of any free carbon or solid hydrocarbons formed. Any or all of these factors may be interacting to cause the expansion effect.

In some of the tests the initial "concentration" of the ThC_2 was varied. To do this, weighed samples of ThC_2 were dispersed in known amounts of PyC-coated ZrO_2 particles. Hydrolysis of increasing loadings

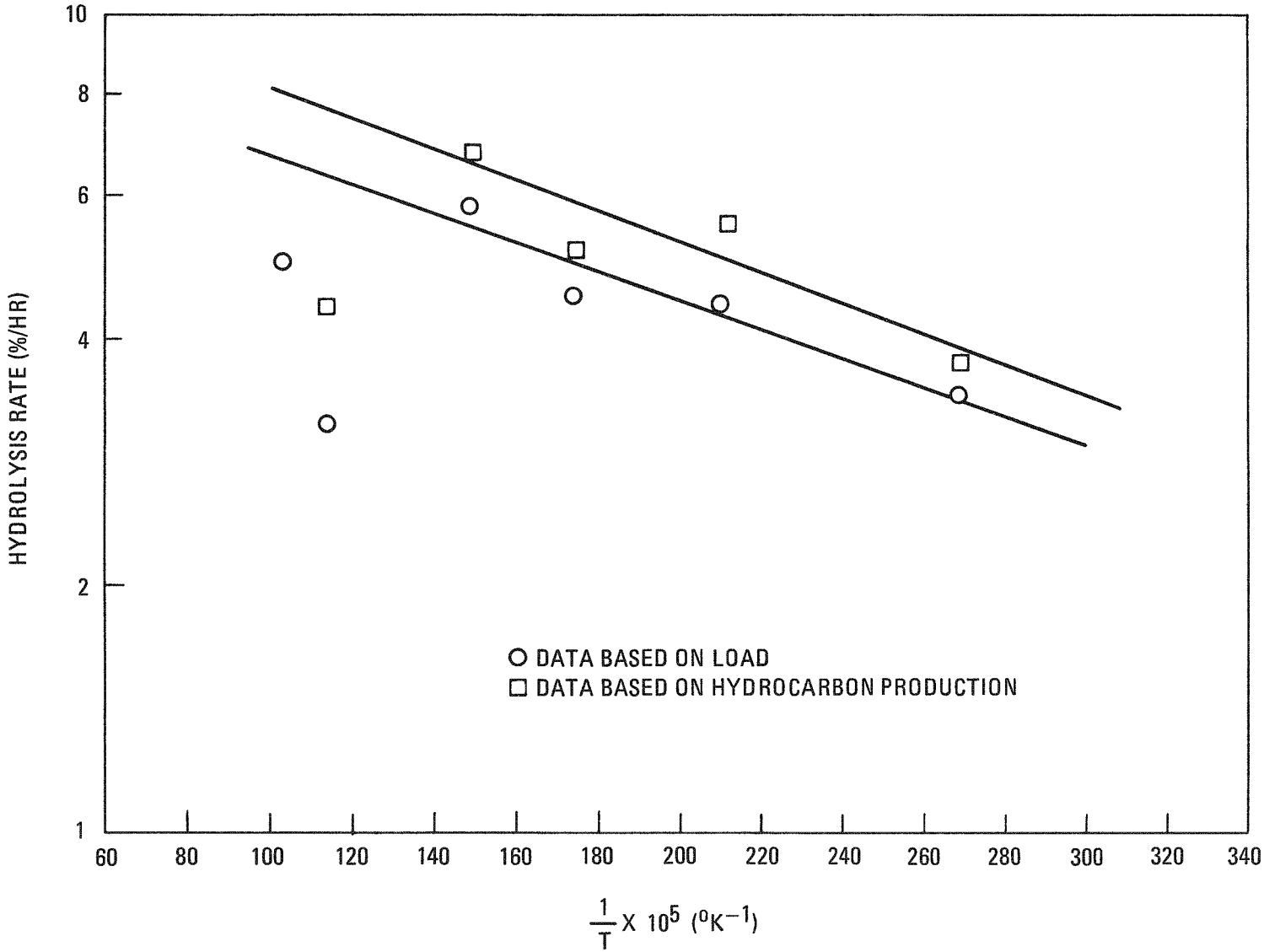

Fig. 4-10. Rate of hydrolysis of 1 g of ThC_2 enclosed in a graphite crucible as a function of 1/T

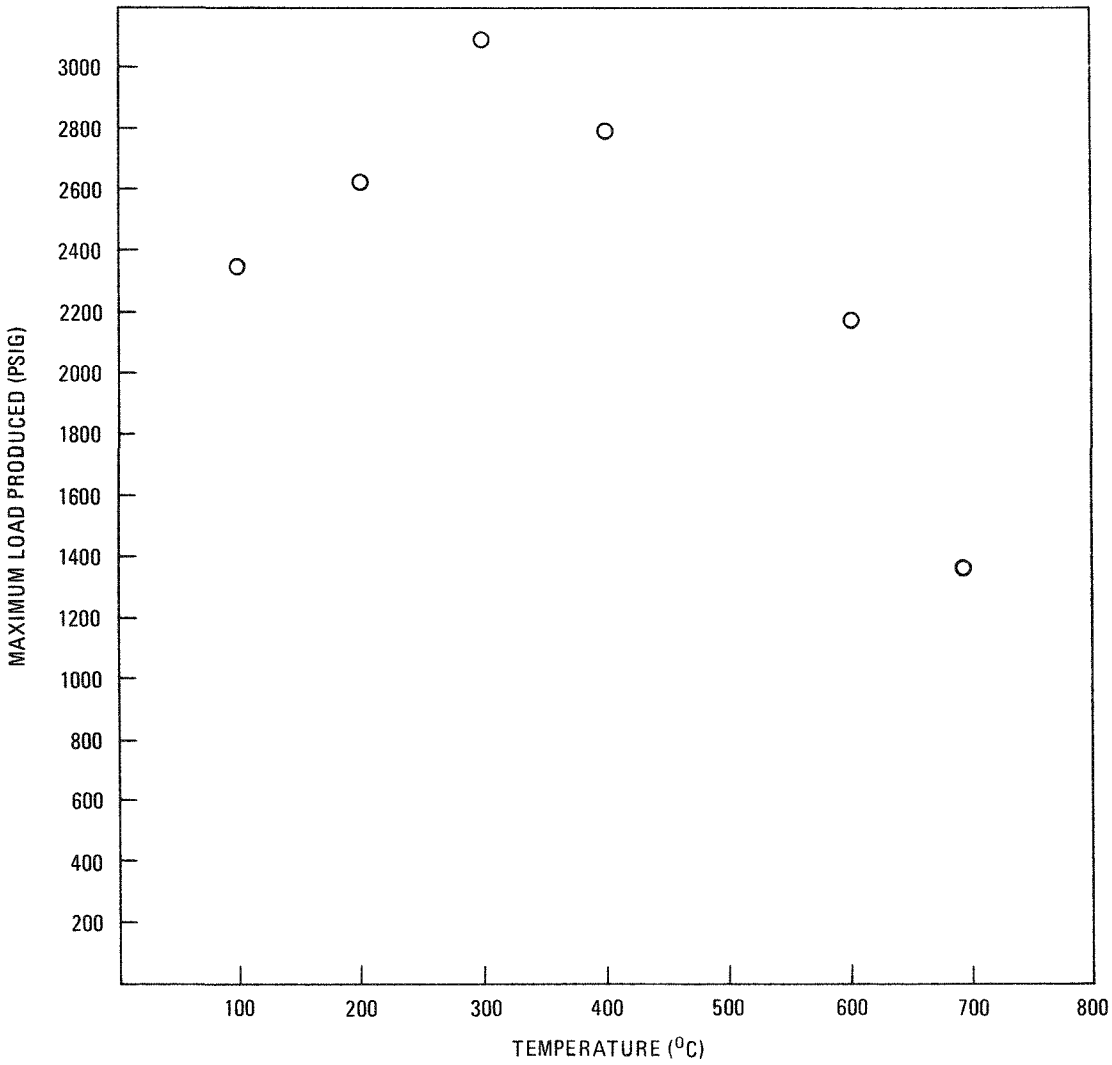

Fig. 4-11. Effect of temperature on the maximum load produced when 1 g of ThC_2 is completely hydrolyzed

at 300°C resulted in an increase in maximum load produced, as shown in Fig. 4-12. The duplicate runs with a loading of 0.25 g ThC_2/cm^3 show that for dispersed kernels, the loading (i.e., g Th/cm^3 and not the total amount of fuel) determines the force. For example, one sample contained 0.25 g ThC_2 in 0.97 cm^3 (Run 14) and produced a load of 112 psi. The other sample (Run 18) was three times as large (0.75 g ThC_2 in 3.08 cm^3) but produced only 122 psi.

Two experiments (Runs 9 and 10) using sections of LHTGR fuel rods were also completed. The rods were annealed at 2100°C to fail the coatings and to convert ThO_2 to ThC_2, as explained previously. There is a large uncertainty in the loading of the fuel rod test sections (see Fig. 4-12) because chemical analyses were not made on the actual load test samples; rather, analyses were accomplished on duplicate sections from the same rod. It is surmised that if fuel was not uniformly loaded in the rods, concentration variations could occur in discrete sections cut from the rods. The magnitude of the possible variation is shown in Fig. 4-12. In any case, by referring to Fig. 4-12, it is seen that the converted rods behaved much the same as the loose bed tests. Additional work is planned for converted fuel rods in which chemical analysis of the final product will accurately assess the fuel loading.

Other work planned for this program includes studies at higher temperatures and at varying water vapor pressures. Finally, the effect of fuel burnup will be addressed.

EFFECT OF TOTAL PRESSURE ON THE RATE OF OXIDATION OF GRAPHITE BY STEAM

In support of the HTGR Fuels and Core Development Program, the study of the effect of total pressure on the reaction rate of oxidation of H-327 graphite with steam has been completed. Since the overall reaction rate is predicted to decrease with increasing pressure, these experiments were performed to provide validation data for the predictions and to complement the existing graphite oxidation rate studies conducted at

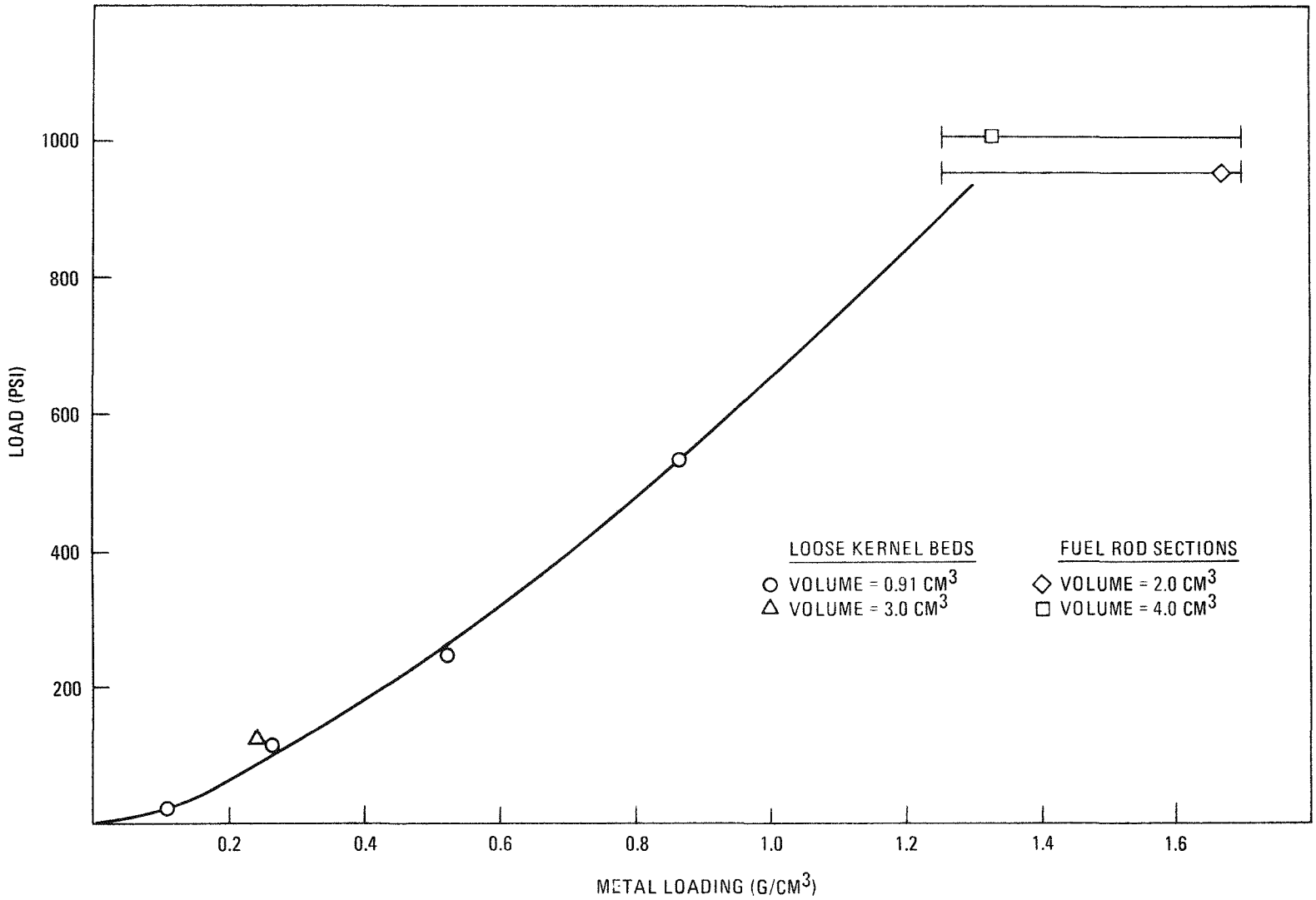

Fig. 4-12. Effect of metal loading on maximum load from ThC_2 hydrolysis

1 atm total pressure. Pressure dependence data are currently needed as input to the GOP and OXIDE-3 computer codes, which predict the consequences of a steady-state and accidental steam in-leakage on graphite integrity and coolant impurity levels.

These experiments involved the testing of cylindrical samples of H-327 graphite trepanned from fuel blocks obtained from the Graphite Development Branch at General Atomic. The tests were extended over a pressure range of 1 to 40 atm at 800° and 900°C. The data obtained are presented and compared with established theoretical predictions.

Theory

The transport and chemical reaction characteristics of porous graphites are commonly divided into three main temperature-dependent groups. At low temperatures (below ∿700°C), the rate is controlled by the chemical reactivity of the graphite and is therefore considered a mass transport independent regime; i.e., the reaction rate is pressure independent. At intermediate temperatures (∿700° to 1000°C), the rate of oxidation is limited by "in-pore" diffusion to potentially reactive sites. The overall oxidation rate in this regime has been predicted to vary as $1/P^{1/2}$. At higher temperatures, the rate of reaction is governed by bulk phase mass transport across the boundary layer to the exterior surface of the graphite body. Since the ordinary diffusion coefficient is inversely proportional to total pressure (Ref. 4-17), the mass transport, and as a consequence the rate of oxidation in this high-temperature regime, is inversely proportional to pressure.

Equations modeling water vapor transport in graphite have been developed by Hawtin (Ref. 4-18) from Crank's general solution (Ref. 4-19) of simultaneous diffusion and chemical reaction within a semi-infinite porous medium with constant surface concentration. Assuming the flux of water vapor into the porous medium is equal to the rate of reaction, the following relation is derived:

$$F = Co(D_{eff}K)^{1/2} \quad , \qquad (4\text{-}4)$$

where F = rate of water uptake, g moles/cm^2-sec

C_o = concentration of water at the boundary, g moles/cm^3 graphite

D_{eff} = diffusion coefficient of water vapor in He in graphite

K = first order volumetric reaction rate constant, sec^{-1}

Since D_{eff} is proportional to the inverse of the total He pressure, it follows that the overall rate of reaction should be proportional to $1/P^{1/2}$. This, of course, is a simplification because gas flow in graphite occurs by both ordinary diffusion (in large pores) and by Knudsen flow (in small pores). Furthermore, since Knudsen flow is a pressure insensitive transfer mechanism, it is necessary to apportion the two types of flow in the porous medium before the correct pressure dependence can be predicted.

One estimate of gaseous diffusion in porous materials such as graphite was developed by Wheeler (Ref. 4-17), who defined a probability function that predicts the distance a gaseous molecule will travel without experiencing a collision. From this concept, Wheeler developed a relationship that yields an effective diffusion coefficient as a function of the pore radius, as follows:

$$D_{eff} = 1/3\ \bar{v}\lambda(1 - e^{-2r/\lambda}) \quad , \qquad (4\text{-}5)$$

where $\bar{v}$ = mean thermal velocity

λ = mean-free path

r = radius of the pore

An expression based on kinetic theory used to approximate ordinary diffusion coefficients is given by:

$$D_{1,2} \simeq 1/3\ \bar{v}\lambda \quad , \tag{4-6}$$

where $D_{1,2}$ is the ordinary mutual gas phase diffusion coefficient. By substitution of Eq. 4-6 into Eq. 4-5, use of this approximation yields an expression from which the effect of pressure on D_{eff} can be characterized; i.e.,

$$D_{eff} = D_{1,2}\ (1 - e^{-2r/\lambda}) \quad . \tag{4-7}$$

Both $D_{1,2}$ and λ are inversely proportional to pressure. Accordingly, if $D_{1,2}$ and λ are calculated for 1 atm total pressure, their respective pressure-corrected values at other pressures can be obtained from the following expressions:

$$D^*_{1,2} = D_{1,2}/P \tag{4-8}$$

$$\lambda^* = \lambda/P \quad , \tag{4-9}$$

where $D^*_{1,2}$ and λ^* are the ordinary diffusion coefficient and mean free path at pressure P, respectively, and $D_{1,2}$ and λ are the ordinary diffusion coefficient and mean free path at 1 atm, respectively.

By redefinition of D_{eff} and combining Eqs. 4-7, 4-8, and 4-9, the effect of pressure on D_{eff} is given by:

$$D^*_{eff} = D^*_{1,2}\ (1 - e^{-2r/\lambda^*}) \tag{4-10}$$

or

$$D^{*}_{eff} = D_{1,2}/P\ (1 - e^{-2rP/\lambda}) \quad , \qquad (4\text{-}11)$$

where D^{*}_{eff} is the effective diffusion coefficient at pressure P.

Experimental

The apparatus used in performing these studies has been previously described (Ref. 4-20). The experimental investigation consisted of suspending a 1.27-cm-diameter graphite rod in the uniform heat zone of a vertical silica-lined tube furnace. Water vapor at a constant bulk phase concentration, P_{H_2O} = 22.8 mm Hg, was transported into the furnace via a carrier gas composed of either helium or a mixture of helium and hydrogen (P_{H_2} = 7.6 mm Hg). Gas flow rates were adjusted so that the linear velocity over the specimen was a constant 40 cm/sec at 900°C at all pressures for all tests. In a preliminary test series, flow rates were increased up to 10 times the reference flow without observing significant changes in reaction rate. The overall rates of oxidation were then determined by an integral or differential method. In the differential method, gas chromatographic analyses were used to monitor product gas concentrations. Instantaneous reaction rates were calculated via summation of the rate of evolution of gaseous carbon species ($CO + CO_2 + CH_4$). By the integral weight loss method, sample weight changes were measured by means of an analytical balance after suitable oxidation periods. These latter values reflect the averaged rate of weight loss over the period of exposure, which in some cases extended over several days.

Results and Discussion

All of the data obtained are given in Tables 4-6 and 4-7. The log reaction rates versus log He pressure are plotted in Figs. 4-13 and 4-14 for the 800° and 900°C runs, respectively. The straight solid lines

TABLE 4-6
RATES OF OXIDATION AT CONSTANT PARTIAL PRESSURES OF WATER VAPOR AND HYDROGEN

	P_{H_2O} = 22.8 mm Hg		P_{H_2} = 7.6 mm Hg
	Temp (°C)	Pressure (psia)	Oxidation Rate $x10^2$ (%/hr)
Series A, integral (weight loss) method	900	14.7	2.2
	900	14.7	3.3
	900	64.7	1.4
	900	64.7	2.5
	900	134.7	1.2
	900	134.7	0.85
	900	134.7	0.77
	900	134.7	0.73
	900	134.7	0.27
	900	314.7	0.53
	900	439.7	0.17
	900	439.7	0.21
Series B, differential (gas analysis) method	900	14.7	11.0
	900	37.0	5.1
	900	63.0	3.3
	900	85.0	2.0
	900	145.0	1.5
	900	305.0	1.0

TABLE 4-7
RATES OF OXIDATION AT CONSTANT PARTIAL PRESSURES OF WATER VAPOR

	P_{H_2O} = 22.6 mm Hg		
	Temp (°C)	Pressure (psia)	Oxidation Rate $x10^2$ (%/hr)
Series C, differential (gas analysis) method	900	118	11.0
	900	268	6.4
	900	400	5.3
	900	518	4.7
Series D, differential (gas analysis) method	800	14.7	7.4
	800	45	7.0
	800	97	3.3
	800	197	2.0
	800	304	1.6
	800	396	0.88
	800	503	0.81
	800	604	1.0

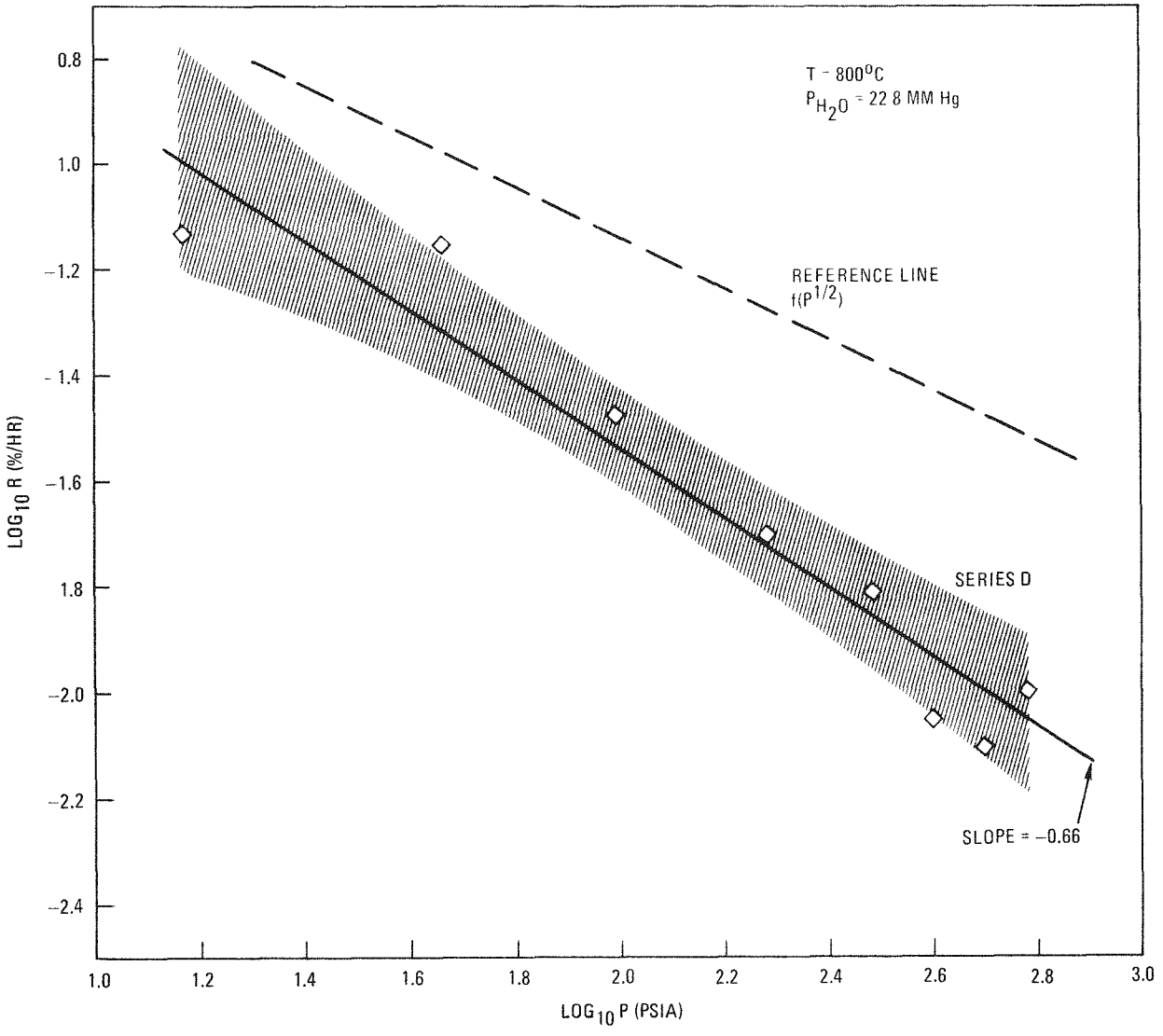

Fig. 4-13. Steam-graphite oxidation; reaction rate versus total pressure, T = 800°C

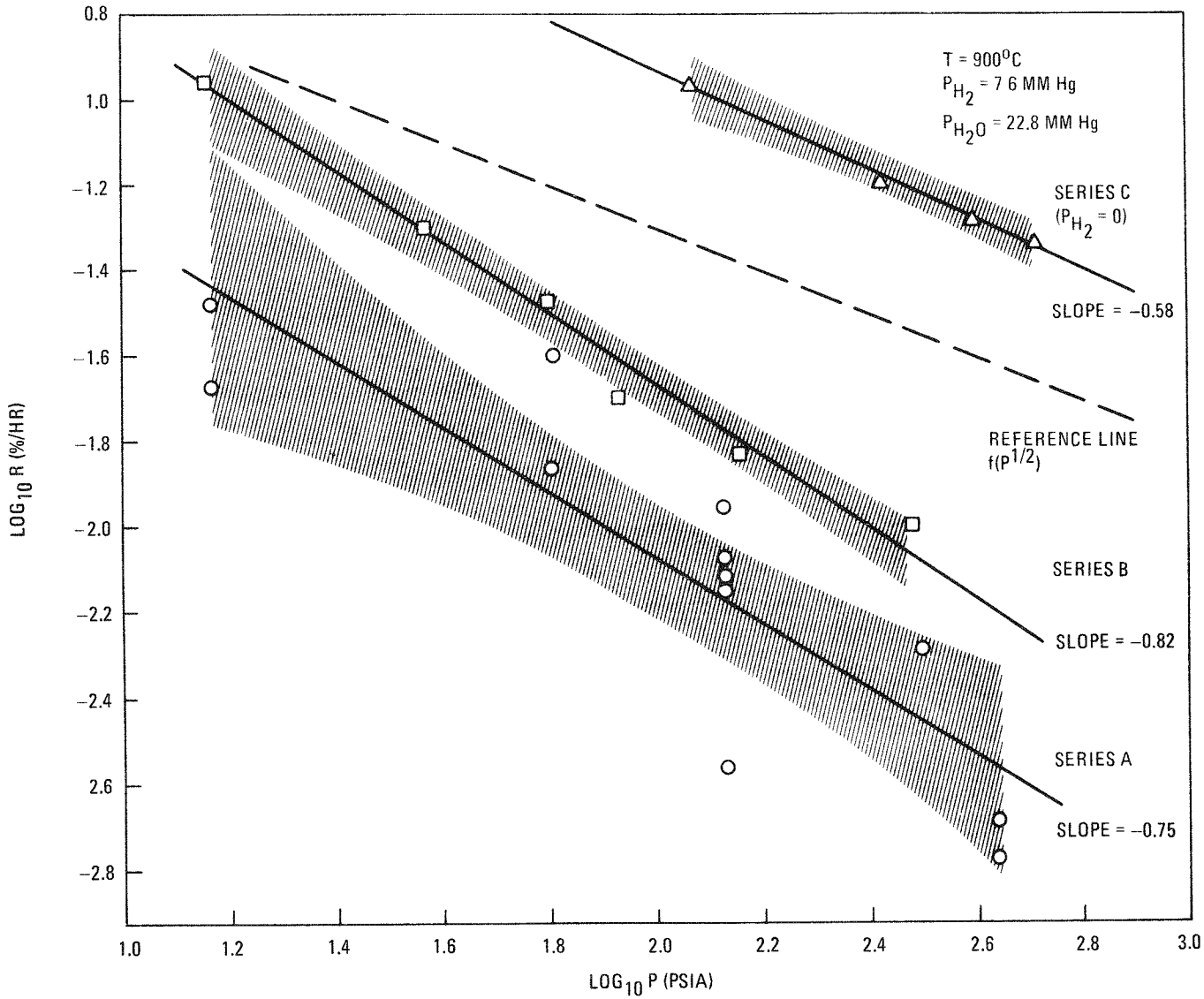

Fig. 4-14. Steam-graphite oxidation; reaction rate versus total pressure, T = 900°C

are based on least-squares analyses, while the curved lines or cross-hatched areas are the 95% confidence level bands. These curves were drawn from the results of CONFID, a computer code specifically designed for confidence level calculation.

Referring to Figs. 4-13 and 4-14 in series A and B, rates of oxidation were determined using the helium-hydrogen carrier gas mixture. Hydrogen concentrations were varied at the different pressures so that total P_{H_2} was a constant 7.6 mm Hg. Series C and D data reflect results obtained with initially hydrogen-free carrier gas. For these cases, the hydrogen pressure over the sample was low but variable, depending on the reaction rate. In Series B, C, and D the data were obtained by gas chromatographic analysis of the effluent product gas after the reaction rate had reached a steady-state level. The calculated least-squares slope for each test series is given next to each curve in Figs. 4-13 and 4-14. These calculated results indicate that a pressure dependence slightly greater than the square root dependence was operable under all the testing conditions examined.

Figure 4-15 is a plot of pore size distribution based on mercury porosimetry results obtained for H-327 graphite after being oxidized with water vapor at 900°C to 1 and 8% burnoff. It is observed that 95% of the pore radii are found to range from 5×10^{-7} to 8×10^{-4} cm. The 5% outside this range are $<5.0 \times 10^{-7}$; as such, these pores obey Knudsen flow mechanics and are accordingly independent of pressure below 40 atm.

From Eq. 4-11 an effective diffusion coefficient was estimated for various pressures by integrating over the range of pore radii. Specifically, at 1173°K and 1 atm, $\lambda_1 = 9.87 \times 10^{-5}$ and accordingly $D_{H_2O,He} = 9.05$ cm^2-sec^{-1} ($D_{H_2O,He}$ was calculated using the method given in Ref. 4-21.) Hence, at the pressures of interest, $D^*_{1,2}$ can be estimated. Table 4-8 tabulates D^*_{eff} values calculated at several pressures by Eq. 4-11, and also by the simple 1/P relation.

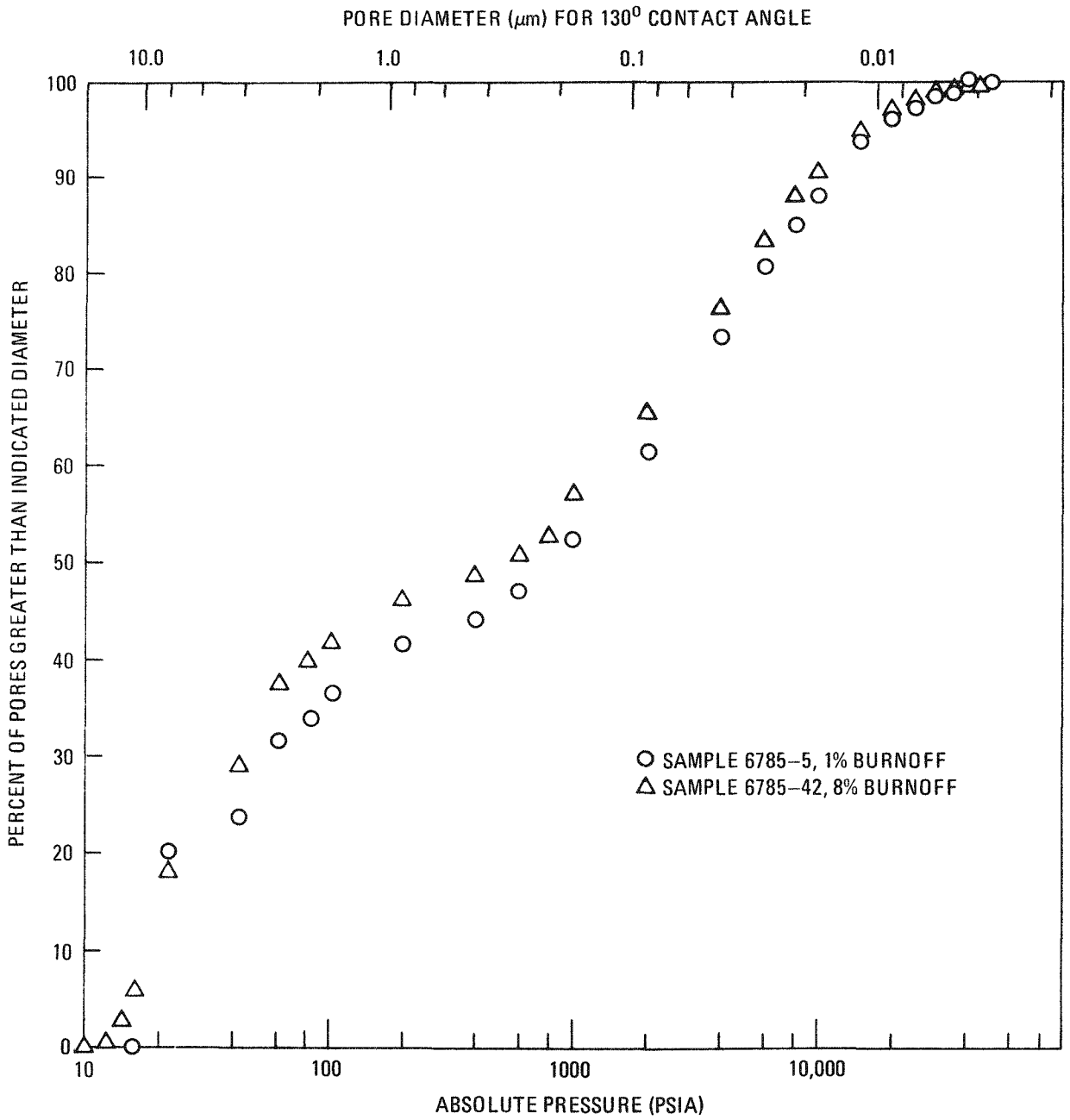

Fig. 4-15. Pore size distribution

TABLE 4-8

D^*_{eff} AND $D^*_{1,2}$ VALUES AT VARIOUS PRESSURES

	1 atm	2 atm	5 atm	10 atm	20 atm	40 atm
D^*_{eff} (Eq. 4-11)	8.50	4.39	1.79	0.90	0.45	0.25
$D^*_{1,2}$ (1/P)	9.05	4.53	1.81	0.905	0.453	0.226

It is apparent that the calculated effective diffusion coefficient for water vapor in H-327 graphite based on pore size distribution (Eq. 4-11) is virtually identical to that of ordinary gas phase diffusion; thus, a simple 1/P relationship is valid. Finally, for comparative purposes, it is convenient to normalize the experimental values obtained at high pressure to those obtained nominally at 1 atm. Accordingly, a pressure effectiveness factor, Ω, is defined which is the ratio of the observed oxidation rate at an elevated pressure to the reaction rate observed at the normal test pressure. Specifically,

$$\Omega = \frac{\text{observed reaction rate at P}}{\text{observed reaction rate at 1 atm}} = \frac{D_{eff}^{1/2} \text{ at P}}{D_{eff}^{1/2} \text{ at 1 atm}} \quad . \qquad (4\text{-}12)$$

This relationship is valid under the assumption that the intrinsic rate constant and the geometry factors are pressure independent.

The pressure effectiveness factors (Ω) for test series A, B, and D are plotted in Fig. 4-16. The dashed line represents the effect of pressure on the rate of oxidation predicted for a $1/P^{1/2}$ dependence. The solid line is derived from the mean-free path method of Wheeler (Eq. 4-11). Again, it is seen that the two theoretical lines are essentially equal. Furthermore, the bulk of the experimental data fall below the theoretical lines, indicating that on the average the present $1/P^{1/2}$ relationship would predict conservatively high graphite oxidation rates at elevated pressures.

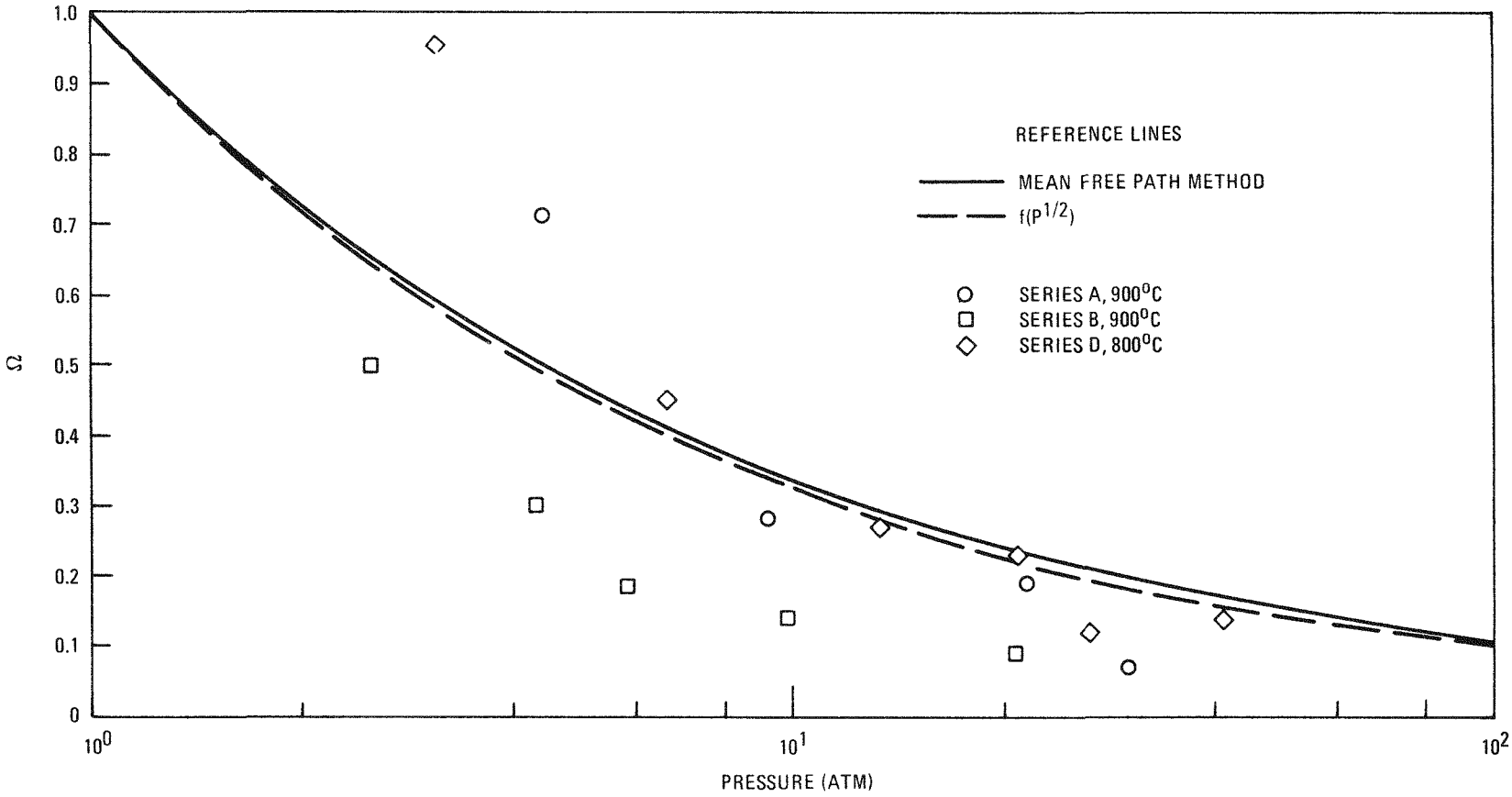

Fig. 4-16. Effectiveness factor (Ω) versus total pressure, H-327 graphite

Conclusions

The effect of total pressure on the rate of steam-graphite oxidation for H-327 has been determined for total pressures up to 40 atm in both helium and hydrogen-helium gas mixture environments. The square root of the pressure relationship within these limits appears to be an accurate (although perhaps slightly conservative) estimate.

The lower limit of an in-pore diffusion-controlled regime for H-327 graphite is less than 800°C. Both the experimental results and their respective analysis exhibit mass transport limitations at 800°C.

With the use of Eq. 4-11 and pore size distribution measurements on H-327 graphite (Fig. 4-15), it is concluded that the Knudsen flow contribution is negligible at all gas pressures of interest and that ordinary gas diffusion is predominant. This indicates that from a theoretical standpoint, the diffusion of gases in graphite should obey the 1/P dependence and the oxidation rate of these intermediate temperatures is expected to be a function of $1/P^{1/2}$.

REFERENCES

4-1. "HTGR Fuels and Core Development Program Quarterly Progress Report for the Period Ending February 28, 1975," ERDA Report GA-A13353, General Atomic Company, March 31, 1975.

4-2. "HTGR Base Program Quarterly Progress Report for the Period Ending May 31, 1974," USAEC Report GA-A13030, General Atomic Company, June 28, 1974.

4-3. Anderson, E. E., et al., "An In-Core Furnace for the High-Temperature Irradiation Testing of Reactor Fuels," Nucl. Tech. 11, 259 (1971).

4-4. Burnette, R. D., W. E. Bell, and N. L. Baldwin, "Fission Product Retention Characteristics of HTGR Fuel," paper presented at the International Conference on Nuclear Fuel Performance, British Nuclear Energy Society, London, October 15-19, 1973, Paper No. 16.

4-5. "HTGR Base Program Quarterly Progress Report for the Period Ending February 28, 1974," USAEC Report GA-A12916, General Atomic Company, March 29, 1974.

4-6. "HTGR Fuels and Core Development Program Quarterly Progress Report for the Period Ending August 31, 1974," USAEC Report GA-A13126, General Atomic Company, September 30, 1974.

4-7. "HTGR Base Program Quarterly Progress Report for the Period Ending August 31, 1970," USAEC Report GA-10288, Gulf General Atomic, September 30, 1970.

4-8. "HTGR Base Program Quarterly Progress Report for the Period Ending May 30, 1969," USAEC Report GA-9372, Gulf General Atomic, June 27, 1969.

4-9. "HTGR Base Program Quarterly Progress Report for the Period Ending February 28, 1967," USAEC Report GA-7801, General Atomic, Division of General Dynamics, April 20, 1967.

4-10. Myers, B. F., and W. E. Bell, "Strontium Transport Data For HTGR Systems," USAEC Report GA-A13168 (GA-LTR-16), General Atomic Company, December 6, 1974.

4-11. Jensen, D. D., et al., "Planning Guide for Validation of Fission Product Transport Codes," ERDA Report GA-A13386, General Atomic Company, April 15, 1975.

4-12. "HTGR Fuels and Core Development Program Quarterly Progress Report for the Period Ending November 30, 1974," USAEC Report GA-A13253, General Atomic Company, January 31, 1975.

4-13. Stansfield, O. M., "Neutron Irradiation Effects in Boronated Graphite, Hafnated Graphite, B_4C, and HfC, Summary Report on the BG-1 and BG-2 Experiments," USAEC Report GA-10648, Gulf General Atomic Company, June 13, 1971.

4-14. Malakhof, V., "ETR MICROX Calculations," General Atomic unpublished data, May 1975.

4-15. Cullen, D. E., and P. J. Hlavac "ENDF/B Cross Sections," USAEC Report BNL-17100, Battelle Northwest Laboratories, 1972.

4-16. "Public Service Company of Colorado 330-MW(e) High-Temperature Gas-Cooled Reactor Research and Development Program Quarterly Progress Report for the Period Ending December 31, 1969," USAEC Report GA-9875, Gulf General Atomic, January 30, 1970.

4-17. Wheeler, A., Adv. in Catalysis III, 264 (1951).

4-18. Hawtin, P., R. A. Huber, and D. Wilmore, "The Calculation of Graphite Corrosion and Coolant Composition in Helium Cooled HTRs," J. Brit. Nucl. Eng. Soc. 11, 71 (1972).

4-19. Crank, J., The Mathematics of Diffusion, Oxford Univ. Press, London, 1970, pp. 129-131.

4-20. "HTGR Base Program Quarterly Progress Report for the Period Ending February 28, 1973," USAEC Report GA-A12515, Gulf General Atomic Company, March 30, 1973.

4-21. Hirschfelder, J. O., C. F. Curtiss, and R. B. Bird, Molecular Theory of Gases and Liquids, John Wiley and Sons, New York, 1964, p. 539.

TASK 8 (189a 13118)

REACTOR PHYSICS

REACTOR KINETICS

In the past, HTGR transient analysis has been performed primarily with zero- or one-dimensional models. The adequacy of these modeling techniques will be evaluated in a study that will be conducted over the next 3 years if B-budget funds are made available. During this quarter, an outline of the study was prepared.

TASK 9 (189a 13119)

FUEL DEVELOPMENT AND ENGINEERING

THERMAL STABILITY OF UC_2 AND WEAK ACID RESIN (WAR) $U{\cdot}C_x{\cdot}O_y$ FUEL KERNELS

Introduction

A series of thermal gradient tests (experiment 6511) were conducted on unirradiated, LHTGR reference, TRISO coated, dense melted UC_2 and WAR $U{\cdot}C_{4.37}{\cdot}O_{0.41}$ fuel particles. The LHTGR reference UC_2 particles with 200-μm kernels were coated for irradiation in capsule tests P13Q, P13R, and P13S. TRISO coated UC_2 particles having 110-μm nominal kernel diameters were also included in the thermal gradient test series. The TRISO coated WAR $U{\cdot}C_{4.37}{\cdot}O_{0.41}$ fuel particles were fabricated by Oak Ridge National Laboratory (ORNL). This fuel particle type was irradiated in capsule tests P13P and HB-3 (Ref. 9-1). The average kernel and coating properties for the particles tested are given in Table 9-1.

Experiment 6511 is part of a continuing test sequence designed to broaden the data base used to estimate kernel migration in fissile fuel during LHTGR core operation. The kernel migration results from the unirradiated particles included in these tests will eventually be compared with kernel migration results determined from out-of-pile thermal gradient heating of irradiated particles from the same coating batches in order to establish the relationship between irradiation and kernel migration. Data available to date (Ref. 9-2) show that irradiation does not increase kernel migration rates in dense melted carbide kernels; however, there are no data on the effects of irradiation on WAR kernel migration.

TABLE 9-1
TRISO PARTICLE PARAMETERS, UNIRRADIATED THERMAL GRADIENT EXPERIMENT 6511

Sample No.	Kernel			Th/U[a]	Coating											Total Coating Thickness (μm)	Scheduled Irradiation Test Capsule
						Buffer		IPyC			SiC		OPyC				
	Type	Diameter (μm)	Density (g/cm^3)		Type	Thickness (μm)	Density (g/cm^3)	Thickness (μm)	Density (g/cm^3)	OPTAF	Thickness (μm)	Density (g/cm^3)	Thickness (μm)	Density (g/cm^3)	OPTAF		
OR1694	$U{\cdot}C_{4.37}{\cdot}O_{0.41}$	394	3.36	--	TRISO	46	1.2	20	2.01	<1.2[b]	21	3.24	39	1.91	<1.2[b]	--	P13P, HB-3
4413-21	UC_2	110	10.19	--	TRISO	44	1.22	21	1.78	--	21	3.17	19	1.91	1.00 (BAF)	105	P13L
6151-04-010	UC_2	202	10.99	0.0096	TRISO	105	0.87	33	1.88	1.23	28	3.20	36	1.82	1.14	199	P13R, P13S
6151-00-016	UC_2	200	10.99	0.0096	TRISO	97	1.18	35	1.94	1.19	31	3.20	44	1.80	1.11	200	P13Q, P13R, P13S
6151-02-020	UC_2	201	10.99	0.0096	TRISO	99	1.07	33	1.92	1.25	28	3.22	43	1.50	1.13	202	P13R, P13S

[a] Thorium added to promote sphericity of kernels during melting.

[b] Design value.

Experimental Details

Kernel migration of carbide kernels in a thermal gradient takes place by the process of carbon solution on the hot side of the kernel and rejection of carbon on the cool side of the kernel (Ref. 9-3). The result is movement of the kernel toward the hot side of a coated particle. The rate of advance of the hot side of a carbide kernel in a thermal gradient is used to calculate a kernel migration coefficient (KMC), which is defined by the expression

$$KMC = \frac{\Delta x}{\Delta t} \cdot T^2 \cdot \left(\frac{\Delta T}{\Delta x}\right)^{-1} = KD_o\, e^{-\Delta H/RT} = \beta\, e^{-\Delta H/RT} \quad , \qquad (9\text{-}1)$$

where KMC = kernel migration coefficient, $^\circ K\text{-}cm^2/sec$

$\Delta x/\Delta t$ = migration rate, cm/sec

T = temperature, $^\circ K$

$\Delta T/\Delta x$ = temperature gradient, $^\circ K/cm$

K = constant containing material property and geometry constants

D_o = pre-exponential constant, cm^2/sec

ΔH = apparent activation energy for carbon diffusion in the kernel, cal/mole

R = gas constant, $cal/^\circ K\text{-}mole$

β = pre-exponential constant, $^\circ K\text{-}cm^2/sec$

Kernel migration coefficients were calculated from the data obtained from experiment 6511, and the variation in KMC with temperature was defined using Eq. 9-1.

The experimental arrangements and procedures used for thermal gradient testing have been described previously (Refs. 9-2, 9-4). Kernel migration was induced by heating particles under a thermal gradient in the temperature range 1328° to 1820°C. The method of determining the kernel migration distance was described in Ref. 9-5.

UC_2 Kernel Migration Results

With the exception of the WAR fuel particles, the fuel tested in experiment 6511 is the same as the fuel tested in an earlier experiment (6440). There is good agreement between the results of these two tests and, for purposes of the following discussion, the KMC results for dense melted UC_2 fuel kernels have been combined.

The test conditions and range of kernel migration distances observed in experiment 6440 are given in Ref. 9-5. Similar descriptive data from experiment 6511 are given in Table 9-2.

The variation in $\log_{10}$ KMC with 1/T for dense melted UC_2 particles having 110- and 200-μm nominal kernel diameters is shown in Figs. 9-1a* and 9-1b, respectively, which show a least-squares curve fit of the data with a 90% confidence limit. The fitted values of β and ΔH and the 90% confidence interval for ΔH (see Eq. 9-1) obtained from the data are given in Table 9-3. Comparison of Figs. 9-1a and 9-1b shows the measured values for KMC to be independent of kernel size. The activation energy reported for the 200-μm nominal kernel diameter particles from experiments 6511 and 6440 is in good agreement with the value of 90.2 kcal/mole reported for carbon self diffusion in α-UC_2 (Ref. 9-6). The values for KMC measured during these tests are compared with KMC values used in LHTGR core design calculations in Fig. 9-2. The data in Fig. 9-2 were obtained in experiments 6440 and 6511 from particles having 200-μm nominal kernel diameters; the least-squares curve fit and the 90% confidence limits shown for KMC are for the data used to establish the UC_2 KMC curve used in LHTGR core design (Refs. 9-2, 9-7). The comparison shows that the design curve gives a higher KMC value relative to the data from the present studies in the temperature range ∿1350° to 1500°C.

$U{\cdot}C_{4.37}{\cdot}O_{0.41}$ (WAR) Kernel Migration Results

The behavior of the dense melted UC_2 kernels in a thermal gradient was consistent with past experience (Ref. 9-2) and theoretical predictions

*Figures appear at the end of Section 9.

TABLE 9-2
EXPERIMENTAL CONDITIONS AND RANGE OF KERNEL MIGRATION DISTANCES FOR TRISO COATED, DENSE MELTED UC_2 PARTICLES, EXPERIMENT 6511

Kernel Diameter (μm)	Temperature (°C)	Temperature Gradient (°C/cm)	Time (hr)	No. of Particles	Kernel Migration Range (μm)
110	1605	8486	21	8	4 to 14
	1475	7559	191	8	7 to 18
200	1820	4700	4	12	9 to 43
	1766	5520	2	12	6 to 18
	1605	5426	21	7	11 to 18
	1475	4316	191	7	13 to 26
	1358	3080	699	13	4 to 12
	1328	4190	387	13	1 to 9

TABLE 9-3
KMC EQUATION PARAMETERS
$KMC = \beta \exp(-\Delta H/RT)$ [a]

Particle Type	Present Study		Design Curve	
	β $\left(\frac{cm^2-°K}{sec}\right)$	ΔH [b] $\left(\frac{kcal}{mole}\right)$	β $\left(\frac{cm^2-°K}{sec}\right)$	ΔH [b] $\left(\frac{kcal}{mole}\right)$
UC_2 dense melted (110 μm)	1.47×10^4	81.6 ± 6.5	--	--
UC_2 dense melted (200 μm)	25.29×10^4	89.2 ± 3.0	0.62×10^4	74.4 ± 2.4
$U{\cdot}C_{4.37}{\cdot}O_{0.41}$ WAR	0.08×10^4	73.9 ± 18.6	--	--

[a] Data fitted in the temperature range ∿1320° to 1820°C.

[b] All confidence limits given for the 90% confidence level.

(Ref. 9-3). The fuel particles containing WAR kernels were tested to determine if the behavior of unirradiated WAR kernels in a thermal gradient is similar to the behavior of dense melted UC_2 kernels. The unirradiated WAR kernels differ from the dense melted UC_2 kernels in the following manner: (1) the WAR kernels contain a large amount of excess carbon and some oxygen in comparison to a small amount of excess carbon in dense melted UC_2, and (2) the WAR kernels have a density of 3 to 4 g/cm^3 in comparison to the 95% theoretical density (11.1 g/cm^3) of the dense melted UC_2 kernels. It is not clear whether kernel composition will affect kernel migration. Past experience suggests that the low-density porous WAR kernels will migrate much more slowly than the dense melted UC_2 kernels.

The WAR particles tested were from coating batch OR1694. The kernels were fabricated and coated at ORNL and are described chemically as $U{\cdot}C_{4.37}{\cdot}O_{0.41}$.

The migration behavior of the WAR kernels was erratic. The hot side of the kernel did not advance (as in dense melted UC_2) in most cases. The percentage of particles exhibiting advance of the hot side of the kernel surface toward the hot side of the particles is given as a function of temperature in Table 9-4. Values of $\log_{10}$ KMC are plotted versus 1/T in Fig. 9-3 along with the least-squares curve fit and the 90% confidence interval for the data when migration was observed. The values for β and ΔH for these data are given in Table 9-3. The KMC given for the WAR kernels is 5 to 6 times lower than for dense melted UC_2 over the range of test temperatures.

Many of the kernel migration values measured for the WAR $U{\cdot}C_{4.37}{\cdot}O_{0.41}$ particles were zero or negative and therefore do not appear in Fig. 9-3. In order to describe the behavior of the WAR kernels during heating under a thermal gradient, the change in the kernel diameter was calculated as follows:

$$\Delta KD\ (\%) = \frac{KD\ (t=t_1) - KD\ (t=0)}{KD\ (t=0)} \times 100 \quad ,$$

TABLE 9-4
KERNEL MIGRATION OF WAR $U{\cdot}C_{4.37}{\cdot}O_{0.41}$ PARTICLES

Average Test Temperature (°C)	Time At Temperature (hr)	Percentage of Particles Showing Kernel Migration From Start of Test[a]
1725	2	7
1783	4	0
1800	7	20
1573	21	27
1475	53	20
1440	127	0
1495	191	0
1348	387	20
1437	699	0

[a]Number of particles per each temperature = 15.

where KD = kernel diameter, μm

t = time, hr

The kernel diameter was measured both parallel and perpendicular to the thermal gradient. The results of these measurements are shown in Figs. 9-4a through 9-4d for the nominal test temperatures of 1800° and 1300°C. The kernel diameter measured along the direction of the thermal gradient generally decreased initially and then remained relatively constant (<5%) in the tests conducted at ∿1800°C. A smaller change in the direction of the thermal gradient (<∿2%) was observed for the lower temperature tests (∿1300°C). Changes in kernel diameter measured perpendicular to the direction of the temperature gradient are similar to those measured parallel to the thermal gradient. This decrease in diameter is probably due to kernel sintering.

Radiographs of representative particles after heat treatment at ∿1700° to 1800°C are shown in Figs. 9-5 and 9-6. Initially, a heavy metal corona appeared on the hot side of the kernel, as seen in Figs. 9-5a and 9-6a. After a longer time at temperature, the corona sometimes disappeared, and a heavy metal dispersion was observed in the buffer region on the cold side of the particle. At ∿1800°C this dispersion could be seen after ∿6 hr, while at ∿1350°C some dispersion was visible after ∿1086 hr. The appearance of the heavy metal dispersion in the buffer on the cold side of the WAR particles is similar to the dispersion of uranium observed in dense melted UC_2 fuel particles in the IPyC coating after extended time at temperature. Measurement of the distance between the outer SiC surface on the hot side of the particle to the cold side of the kernel in the direction of the thermal gradient indicated little change as a function of time at temperature. However, the distance between the outer SiC surface on the hot side of the particle to the hot side of the kernel in the direction of the thermal gradient usually increased as a function of time at temperature. It would appear that the kernel was preferentially shrinking or densifying on the hot side, causing the surface of the kernel on the hot side of the particle to move toward the cold side of the particle.

The behavior of the WAR $U{\cdot}C_{4.37}{\cdot}O_{0.41}$ fuel particles under the influence of a thermal gradient is characterized by the absence of significant kernel migration in comparison to the dense melted UC_2 fuel particles. The observed corona on the hot side of the WAR kernel after heat treatment is probably due to the movement of the hot side of the kernel toward the cool side of the particle, leaving a residual heavy metal deposit. There is also the possibility that a gap forms at the kernel-buffer interface on the hot side of the particles during kernel shrinkage. This gap could prevent kernel migration by removing the carbon source for kernel migration.

After completion of the thermal gradient tests at ∿1800° and 1450°C, the particles contained in the crucibles were prepared metallographically. Typical photomicrographs of the WAR $U{\cdot}C_{4.37}{\cdot}O_{0.41}$ fuel particles are shown in Fig. 9-7 for two nominal test temperatures. The redeposited graphite layer usually observed on the cool side of dense melted UC_2 kernels after kernel migration is not seen in the WAR particles. The kernel structure of WAR particles before thermal gradient heat treatment appears uniform. The preferential pullout of material from the hot side of kernels of metallographically prepared WAR particles after thermal gradient heat treatment may indicate a change in structure or composition across the WAR kernel.

Conclusions

The following observations have been made regarding kernel migration of unirradiated, TRISO coated, dense melted UC_2 and WAR $U{\cdot}C_{4.37}{\cdot}O_{0.41}$ fuel particles:

1. The KMC data from the LHTGR reference TRISO coated dense melted UC_2 fuel particles tested are slightly less than the current core design curve below ∿1500°C.

2. The measured KMC values for TRISO coated, dense melted UC_2 fuel particles with 110- and 200-μm nominal kernel diameters are independent of kernel size.

3. The TRISO coated WAR $U{\cdot}C_{4.37}{\cdot}O_{0.41}$ fuel particles exhibited little or no conventional kernel migration. The design curve now used in HTGR core design kernel migration calculations for dense melted UC_2 fuel particles has KMC values 5 to 6 times higher than KMC values calculated from $U{\cdot}C_{4.37}{\cdot}O_{0.41}$ particles that showed kernel migration. The kernel diameter parallel to the thermal gradient was found to decrease up to 5% for the WAR fuel particles. The surface of the kernel on the hot side of the particles moved toward the cold side of the WAR particles, leaving initially a heavy metal corona at the original buffer-kernel interface. After a longer time at temperature, a heavy metal dispersion was often observed in the buffer layer on the cold side of the particle. Metallographic examination of the particles after heat treatment at ∿1800° and ∿1450°C did not reveal a redeposited graphite layer on the cold side of the kernel as observed in dense melted UC_2 fuel particles.

THERMAL STABILITY OF IRRADIATED ThO_2 FUEL KERNELS

Introduction

Various forms of coated oxide particles have been tested for use as fissile or fertile fuel in HTGR systems. BISO coated ThO_2 particles have been chosen as the reference fertile fuel for the LHTGR. An increasing amount of irradiation data is demonstrating the reliability of the BISO ThO_2 fuel under irradiation conditions that simulate both steady-state and transient reactor operation (Refs. 9-5, 9-8). There are, however, only limited data describing the performance of ThO_2 kernels under the influence of a thermal gradient. Unirradiated Th and U carbide kernels migrate toward the hot side of a particle when under the influence of a thermal gradient. Out-of-pile heating tests can therefore be conducted on unirradiated coated carbide fuels and the results can be used as a data base for comparison with the performance of irradiated carbide kernels in a thermal gradient (Ref. 9-2). Irradiated oxide kernels also migrate toward the hot

side of a particle in a thermal gradient; however unirradiated oxide kernels do not, in general, migrate when subjected to thermal gradients. Definition of migration of oxide kernels must therefore rely on data obtained during irradiation testing or out-of-pile testing of irradiated oxide fuel particles.

A limited quantity of data describing in-pile kernel migration of irradiated ThO_2 fuel kernels has been obtained by ORNL (Refs. 9-9, 9-10). The data reported here are from out-of-pile experiments conducted at GA to define kernel migration rates of irradiated ThO_2 fuel kernels. Data from three out-of-pile experiments are included. The first experiment was started in July 1974 (experiment 6532) and included 348 hr of heating at ∿1550°C under a thermal gradient of 588°C/cm. The second test (experiment 6617) was initiated in November 1974. Particles were heated in the temperature range 1500° to 1550°C for a total of 589 hr under thermal gradients ranging from 400° to 700°C/cm. The third test (experiment 6613) is currently in process. Particles are being heated at ∿1300°C under thermal gradients of 200° to 700°C/cm. The data reported for experiment 6613 were recorded after 1399 hr at temperature. In addition to examining the effects of temperature on ThO_2 kernel migration, these tests are designed to study the effects of kernel burnup on migration. The PyC coated ThO_2 particles used were irradiated to burnups ranging from ∿0.5 to 13.7%.

Experimental Description

Materials

The purpose of this series of tests was to obtain out-of-pile test data on kernel migration of irradiated, BISO coated ThO_2 kernels. Particles from five irradiation samples were tested. The kernel and coating properties and irradiation conditions for each sample are summarized in Table 9-5. For comparison, similar data are included for LHTGR BISO fertile fuel. As shown in Table 9-5, the range of kernel burnups and fast neutron exposures experienced by the samples used in these tests span and exceed the range of irradiation conditions expected for LHTGR fertile fuel.

TABLE 9-5
PARTICLE PROPERTIES FOR LHTGR BISO ThO_2 FERTILE FUEL AND IRRADIATED BISO ThO_2 FERTILE FUELS USED IN OUT-OF-PILE THERMAL GRADIENT HEATING TESTS

Particle Identification	Reference LHTGR	4413-75T	4252-02-015-5	4252-02-015-6	4252-02-015-7	5466-149
Kernel						
Type	ThO_2	ThO_2	ThO_2	ThO_2	ThO_2	ThO_2
Diameter, μm	500	576	505	508	509	481
Density, g/cm^3	≥9.5	(a)	9.95	9.95	9.95	9.89
Buffer						
Thickness, μm	85	69	85	84	88	63
Density, g/cm^3	1.05	(a)	1.08	1.08	1.08	1.11
Outer PyC						
Thickness, μm	75	85	76	75	68	76
Density, g/cm^3	1.85	1.89	1.84	1.84	1.84	2.02
OPTAF	≤1.20	1.02 (BAF)	1.07	1.07	1.07	(a)
Irradiation conditions						
Capsule		P13L	HT-12	HT-13	HT-14	FTE-14
Fast neutron fluence, n/cm^2 (b)	≤8 x 10^{21}	6.4 x 10^{21}	3.1 x 10^{21} (c)	6.9 x 10^{21} (c)	11.0 x 10^{21} (c)	<1 x 10^{21}
Kernel burnup, % FIMA	≤7.5	4.7	1.5 (d)	6.8 (d)	13.7 (d)	<1 (e)
Temperature, °C	1100 (f)	1325	1100-1300 (e)	1100-1300 (e)	1100-1300 (e)	1250
Out-of-pile heating experiment No.		6532	6613,6617	6613,6617	6613,6617	6613,6617

(a) Not available.

(b) $(E \geq 0.18\ MeV)_{HTGR}$ unless otherwise noted.

(c) $(E \geq 0.18\ MeV)_{HFIR}$.

(d) See Ref. 9-5.

(e) Estimated.

(f) Time average fuel temperature (Ref. 9-11).

Experimental Conditions

The irradiated ThO_2 particle samples used in the out-of-pile tests are listed in Table 9-5. As shown, experiment 6532 contained particles from one irradiated particle sample, while experiments 6613 and 6617 each contained particles from four irradiated particle samples. The test conditions are given by experiment and irradiated particle batch number in Table 9-6. The sample from experiment 6532 and three of the four samples from experiment 6617 are no longer being heated. Sample 5466-149 from experiment 6617 and all four samples from experiment 6613 are still under test and will be heated until approximately 10 μm of kernel migration has occurred.

Thermal Gradient Heating Configuration

The purpose of these tests was to heat irradiated ThO_2 fuel particles in a thermal gradient and to observe the resulting kernel migration. A thermal gradient was imposed across the irradiated particles during out-of-pile heating by placing them in a graphite crucible between a hot electrode and a cold furnace wall. The crucible (Fig. 9-8) consisted of a slab of nuclear-grade graphite with a lengthwise slot 14 to 20 mils wide cut through the slab. Seven holes were drilled perpendicular to the slot and the face of the slab approximately halfway through the slab. The holes were slightly larger than individual coated particles. The crucibles were loaded with three to seven irradiated particles. The particles were held in this configuration by a matrix consisting of 25 wt % natural-flake graphite flour and 75% binder. The binder was 5 wt % maelic acid, 45 wt % furfuryl alcohol, and 50 wt % methyl alcohol. Loading was accomplished by filling the slot and holes with matrix, pushing individual particles into their respective holes, and smoothing the matrix over the top of the particles. The matrix was then cured by heating to 100°C in a period of ∿30 min, holding for 1 hr, and cooling to room temperature and fired by heating to 1200°C in a period of ∿1 hr, holding at 1200°C overnight, heating to 1600°C in a period of ∿1 hr, holding at 1600°C for 1 hr, and cooling to room temperature in a period of 2 hr.

TABLE 9-6
THERMAL GRADIENT HEATING CONDITIONS FOR IRRADIATED ThO_2 FUEL PARTICLES

Experiment No.	No. of Particle Batches per Experiment	Particle Batch No.	Total Heating Time (hr)	Time Average Temperature (°C)	Average Thermal Gradient (°C/cm)	Range of Migration Distances Observed (μm)
6532	1	4413-75T[a]	348	1548	588	22-33
6617	4	4252-02-015-7[b]	589	1473	727	7-14
		4252-02-015-6[a]	589	1521	405	17-29
		4252-02-015-5[a]	589	1559	705	8-45
		5466-149[a]	589	1510	699	3-7
6613	4	4252-02-015-7[b]	1399	1358	755	3-4
		4252-02-015-6[a]	1399	1302	189	3-5
		4252-02-015-5[a]	1399	1318	440	1-2
		5466-149[a]	1399	1325	360	0

[a] Seven particles per sample.

[b] Three particles per sample.

During thermal gradient heating, the crucibles are held very near to a graphite heating element by a hollow graphite ring (Ref. 9-2). Temperatures are measured periodically using micro-optical pyrometers to sight on the optical pyrometer sight holes (see Fig. 9-8). Test temperatures and temperature gradients are estimated by assuming that (1) the temperature varies linearly with position in the graphite crucibles and in the slots, (2) the gradients across the slot and particles are equal, and (3) the particle operating temperature equals the average temperature across the particle diameter at each particle location. The methods used to determine particle temperatures and temperature gradients are shown schematically in Fig. 9-8.

Measurement of Kernel Migration Distance

Kernel migration distances were determined from examination of contact microradiographs taken periodically during the heating tests. Historically, the kernel migration distance, which is defined as the advance of the kernel hot surface, has been measured by recording the change in distance between the kernel hot surface and a coating layer on the hot side of a fuel particle (Ref. 9-2). The tests reported here contained only BISO coated ThO_2 kernels and it was impossible to see the surface of the outer pyrocarbon (OPyC) layer in most cases. Kernel migration distances were therefore measured by determining the change in distance (parallel to the thermal gradient) between the cold kernel face or the cold side of any rejected layer and the hot kernel face as a function of time. This is expressed by

$$X = d'_{\parallel} - d_{\parallel} \quad , \tag{9-2}$$

where X = kernel migration distance

$d'_{\parallel}$ = distance from the kernel cool side or the cool side of any rejected layer and the kernel hot side at time t

$d_{\parallel}$ = kernel diameter parallel to the thermal gradient at time t = 0

This technique, which is illustrated schematically in Fig. 9-9, was recently tested by comparing kernel migration measurements made on unirradiated TRISO

UC_2 particles using the two techniques described above. Agreement between the two methods was excellent.

To further characterize fuel kernel behavior, the change in kernel diameter perpendicular to the thermal gradient ($\Delta d_\perp$) was also monitored as a function of time.

Measurement of Fission Product Release

During thermal gradient testing, gaseous Kr-85 and metallic Cs and Ce inventories of the irradiated particle samples are monitored. Release of Kr-85 is detected by periodically purging the heating furnace atmosphere through a liquid nitrogen cold trap and gamma counting to detect trapped Kr-85. The fractional release of Kr is determined from the ratio of the trapped Kr to the theoretically calculated Kr-85 inventory in any given sample. Release of Cs and Ce is monitored by periodically gamma counting the thermal stability crucibles that contain irradiated coated particles. To detect release, the Cs or Ce must have escaped both the coated particles and the graphite crucibles. Past experience suggests that Ce will not escape from the crucibles; consequently, little or no Ce release is detected. Cesium does, however, escape from the crucibles and Cs losses are detected. One problem with the Cs measurements is that the Cs inventory of the sample is measured rather than the quantity of escaped Cs. This makes it impossible to detect small losses of Cs that result from diffusion of Cs through the OPyC layer. The uncertainty in the measurements is 5 to 10%. The measured release must therefore exceed 5 to 10% to be considered real.

The fission product release measurements are done primarily to indicate total failure of the PyC coating on these BISO particles. The particles in these thermal gradient tests are held in place with a carbonaceous matrix that is cured and high fired prior to thermal gradient heating. The matrix adheres to both the particles and the graphite heating crucibles. During testing, the matrix shrinks somewhat (cracks in the matrix are observed on occasion). The combination of matrix shrinkage and matrix

particle bonding can cause premature failure of the PyC layer on BISO particles, which results in fission product release. Because of this failure mechanism, particle failure observed in thermal gradient tests can not be related to fuel performance. The fact that some known failed fuel is present, however, allows exploration of the effect of fuel failure and the resulting release of fission products on ThO_2 kernel migration. For this reason, fission product release measurements are made.

Metallography and Microprobe Analyses

Hot cell metallography and microprobe examinations were performed on particles from batch 4413-75T after completion of experiment 6532. Metallography and selected microprobe analyses are planned for the other test samples upon completion of experiments 6613 and 6617.

Definition of Kernel Migration Coefficient

When placed in a thermal gradient, carbon coated ThC_2, $(Th/U)C_2$, and UC_2 kernels migrate toward the high-temperature side of a coated particle (Ref. 9-2). As shown in Ref. 9-3, kernel migration of carbide kernels obeys kinetics described by solid-state diffusion of C from the hot to cool side of a kernel. When solid-state diffusion controls kernel migration, the migration rate, temperature, and temperature gradient are related by Eq. 9-1. Given (1) KMC as a function of temperature and (2) the thermal history (T, dT/dx,t) of a group of PyC coated carbide particles, the kernel migration distance can be predicted for any reactor operating condition.

The kernel migration behavior of oxide kernels is more complex. Unirradiated kernels do not, in general, migrate in a thermal gradient. It is also not clear whether migration is controlled by a solid-state or gas-phase diffusion process. Lindemer and DeNordwall (Ref. 9-9) have compared in-pile oxide migration behavior with predictions made assuming solid-state and various gas-phase diffusion models for kernel migration. Their observations suggest that oxide kernel migration kinetics are best

described by a solid-state diffusion process. Based on this recommendation and observations discussed below, the solid-state diffusion model for kernel migration (Eq. 9-1) was used to analyse the ThO_2 kernel migration results presented here.

Experimental Results

Fission Product Release

Release of Kr-85 and Cs-137 measured as a function of time at 1548°C from irradiated ThO_2 (batch 4413-75T) in experiment 6532 is shown in Fig. 9-10. The Kr-85 measurements were made at approximately 12-hr intervals. As shown, three Cs measurements were made. The release of Kr-85 that was detected implies particle failure. Fission gas samples taken after firing of the crucible containing seven irradiated ThO_2 particles suggested failure of one particle. This was confirmed radiographically. Failure of a second particle after 73 hr was detected by fission gas sampling and confirmed by radiographic examination. The kernels in these first two failed particles began to expand and take on a low density appearance almost immediately. This is illustrated in Fig. 9-11, which shows 0- and 348-hr radiographs of the two particles. Later microprobe analyses showed that the kernels had converted from ThO_2 to ThC_2. These particles were not used for kernel migration analyses. Continued gas sampling indicated failure of two more particles; however, there was no radiographic evidence to indicate conversion of additional ThO_2 kernels to ThC_2. Comparison of the Cs and Kr release data suggests immediate release of the Cs inventory in the particles that failed. This behavior is expected for ThO_2 kernels at temperatures of 1548°C.

Analysis of fission products released during experiments 6613 and 6617 is more complex since each test contained particles from four unique irradiation samples. Experiment 6617 was terminated after 589 hr at ∿1500°C. Particles from irradiation samples 5466-149, 4252-02-015-5, and 4252-02-015-6 showed less than 10% Cs release at the end of the test. Release of

Cs from particles from irradiation sample 4252-02-015-7 increased from 65% after 28 hr at temperature to 71% after 589 hr. Only three particles from 4252-02-015-7 were heated. The Cs release data therefore imply failure of at least two of the three particles. Gaseous release measurements showed release of approximately 50% of the fission gas inventory in experiment 6617 after 28 hr. No additional Kr-85 release was detected. The total Kr release is 105% of the estimated Kr-85 inventory in the particles from 4252-02-015-7. Based on the Kr and Cs measurements, it is clear that at least two and possibly all three particles from 4252-02-015-7 failed in experiment 6117, and that no additional failure occurred.

Similar results were noted in experiment 6613. Fission products detected were consistent with failure of the three particles from 4252-02-015-7. As in experiment 6617, no other failures were detected. The failures occurred after approximately 100 hr at ∿1300°C.

The particles that failed in experiments 6617 and 6613 had been irradiated to 13.7% FIMA. Test 6617 ran at ∿1500°C for 560 hr after particle failure, while test 6613 ran for approximately 1300 hr at 1300°C after particle failure. There was no indication of conversion of the ThO_2 to ThC_2 in any of these failed particles.

As discussed earlier, the failures detected during thermal gradient heating are due in part to interactions between the matrix binder, used to hold the particles in thermal stability crucibles, and the particles. The failures were discussed in detail because they will be related to kernel migration observations later.

Metallography and Microprobe Analyses

To date, the only particles examined metallographically after kernel migration are those from batch 4413-75T, which were heated for 348 hr at 1548°C under a thermal gradient of 588°C/cm. For reference, typical kernel

structures observed in these particles before and after irradiation are shown in Fig. 9-12. The kernels were featureless before irradiation. After irradiation, two structures were apparent. Some kernels contained a uniform distribution of a second phase that could possibly be identified as gas bubbles (Fig. 12-c). Grain boundaries in the remaining kernels were faintly visible (Fig. 9-12b), and the individual grains were featureless. There is no indication of the fraction of particles having either structure.

Periodic x-radiographic examinations made during postirradiation thermal gradient heating of the particles from batch 4413-75T showed that the hot side of the kernels in the five intact particles in the test advanced toward the hot side of the particles. This was confirmed by the metallographic examination. The kernel structures observed are shown in Fig. 9-13. The kernel structure shown in Fig. 9-13a was observed in three particles (No. 1, 2, and 4). There is clearly a grain boundary precipitate within the kernel that is much more pronounced on the cool side of the kernel than on the hot side. This suggests that solid-state diffusion of some species down the temperature gradient across the kernel plays a roll in ThO_2 kernel migration. The precipitate was only slightly responsive to polarized light. One kernel containing the grain boundary precipitate (particle No. 4) was rolled over within the coatings during preparation of the metallographic mount. The kernel remained intact and no individual ThO_2 grains that were surrounded by the precipitate were lost indicating that (1) the precipitate is not weak and (2) the bond between the precipitate and the ThO_2 is strong. Similar grain boundary precipitates have been observed in ThO_2 kernels that migrated in-pile during irradiation of ORNL capsule tests H-1 and H-2 (Ref. 9-12, Fig. 21). This indicates that the grain boundary precipitation observed during ThO_2 kernel migration in out-of-pile tests is not an artifact of the out-of-pile testing conditions. The precipitate observed by ORNL was optically responsive under polarized light, which suggests that it is graphitic.

The kernel structure shown in Fig. 9-13b was observed in two particles (No. 3 and 5). There is a uniformly dispersed second phase that could be gas bubbles or a precipitate that deposited in gas bubbles.

Comparison of the kernel structures shown in Figs. 9-12 and 9-13 suggests that the structures observed after kernel migration were developed from the structures present after irradiation. Comparison of Figs. 9-12b and 9-13a also suggests that a large quantity of precipitation occurred during the kernel migration process.

The metallographic mount containing particles from experiment 6532 was submitted for microprobe analysis. A bright field micrograph of the cool side of the kernel of particle No. 2 (Fig. 9-13a) is shown in Fig. 9-14 along with a backscattered electron image and carbon and thorium characteristic x-ray images of a small segment of the kernel. The backscattered electron image indicates that the grain boundaries contain light elements. The characteristic x-ray images show conclusively that the grain boundaries contain carbon and are depleted in thorium. The carbon activity within the grains (Fig. 9-13c) is background. The boundaries are also depleted in uranium. No fission products were detectable within the carbon grain boundary precipitate. Comparative standard samples of Th, U, O, and C were used for more quantitative analyses. The grain boundaries on the cold side of the kernel were shown to contain 75 to 100% C. The grain boundaries on the hot side of the kernel were too narrow for quantitative analysis. The concentration of the grain interiors remained constant within the accuracy of the microprobe measurements. The grain interiors contained approximately 85% Th, 5 to 6% U, 12% O, and 0 to 4% C. Microprobe analysis of particle No. 3 (Fig. 9-13b) showed Th, U, O, and C concentrations similar to those observed on particle No. 2. There was no indication of segregation of any species to a specific location or of concentration gradients within the kernels containing the uniformly dispersed phases.

The microprobe results for Th, U, and O were predictable based on the fission process for Th. The C concentrations in the bulk of the kernels are uncertain because the particles were shadowed with C prior to microprobe analysis. Data from particle No. 2 (Fig. 9-14) do show conclusively, however, that C precipitation within the kernel takes place during ThO_2

kernel migration. This observation coupled with the apparent bond between the ThO_2 and precipitated C is consistent with the assumption of solid-state diffusion control of ThO_2 kernel migration (Eq. 9-1).

Analysis of Kernel Migration

Kernel migration measurements were made periodically from contact radiographs made during the thermal gradient heating tests. Examples of observed kernel behavior are shown in Figs. 9-15 and 9-16. Figure 9-15 shows radiographs before starting and after completion of thermal gradient heating at 1548°C of the two particles shown in Fig. 9-13 (batch 4413-75T, kernel burnup 4.7% FIMA). It is clear from these radiographs that the hot side of the kernels migrated toward the hot side of the particles. Careful examination of the cool side of the kernel of particle No. 3 after 348 hr of heating indicates a decrease in metal density or the possible presence of a rejected layer. This region was not observed during metallographic preparation since polishing was stopped before reaching the midplane in the particle. The particles from batch 4413-75T were irradiated to a kernel burnup of 4.7% FIMA.

Examples of radiographs of particles from irradiation samples 4252-02-015-5 and -6 are shown in Fig. 9-16 before and after heating for 589 hr at about 1500°C and 600°C/cm. The general characteristics are the same as those shown in Fig. 9-15. The hot side of the kernel has advanced toward the hot side of the particles. The particles from 4252-02-015-5 experienced 1.5% FIMA (Fig. 9-16a and 9-16c), while the particle from 4252-02-015-6 experienced 6.8% FIMA (Fig. 9-16b and 9-16d). The advancing kernel interface on the higher burnup kernel moved at a constant rate toward the hot side of the particle and the kernel became "egg" shaped. The advancing interface on the lower burnup kernel was more erratic and less well defined than on the high burnup kernel. This suggests that kernel migration is dependent in part on kernel burnup, which is to be expected since unirradiated oxides do not, in general, migrate. Close examination of the cool side buffer-kernel interface shown in Fig. 9-16c suggests the presence

of a rejected layer. Metallography is planned for these samples to determine if the rejected layer is present.

The changes in kernel shape indicated by the radiographs shown in Figs. 9-15 and 9-16 have been seen at ORNL during postirradiation metallographic examination of ThO_2 fuel kernels that migrated during irradiation (Ref. 9-12, Figs. 22 and 27). ORNL investigations have also demonstrated the presence of a rejected graphite layer behind migrating ThO_2 kernels. This confirms the suspicion that a rejected graphite layer is visible on the cool side of the kernel shown in Fig. 9-16c. The general agreement between metallographic and radiographic results from both in-pile and out-of-pile ThO_2 kernel migration examinations suggests that the migration observed in irradiated ThO_2 kernels during out-of-pile tests is representative of the behavior to be expected in-pile.

As described earlier, the change in kernel diameter parallel and perpendicular to the thermal gradient was measured as a function of heating time from radiographs like those shown in Figs. 9-15 and 9-16. An example of the results obtained is given in Fig. 9-17a, which shows the average change in kernel diameter measured parallel and perpendicular to the thermal gradient during heating of irradiated particles from batch 4413-75T. Figure 9-17b shows the net kernel elongation, which is defined as the difference between the changes in kernel diameter parallel and perpendicular to the thermal gradient. Assuming that the diameter change measured perpendicular to the thermal gradient represents a uniform kernel expansion, there appears to be a delay period before the kernel hot side begins advancing unilaterally.

The observations illustrated in Fig. 9-17 were also made in other samples in these tests, as discussed in more detail below. The results are primarily from tests conducted at 1500°C since the 1300°C tests are in their initial stages.

Irradiated ThO_2 kernels from batch 4413-75T (4.7% FIMA, time average irradiation temperature 1325°C) increased in diameter 8 to 9 μm perpendicular

to the thermal gradient during heating at 1548°C. At similar thermal gradient heating temperatures, kernels from 4252-02-015-5, -6, and -7 (1.5, 6.8, and 13.7% FIMA, respectively, irradiation temperature 1100° to 1300°C) did not swell. Kernels from batch 5466-149 (<1% FIMA, irradiation temperature 1000° to 1250°C) swelled 3 to 5 μm. Two possible explanations for the swelling are that it is related to fission product gas redistribution and pressure equilibration or to the kernel migration phenomenon. Swelling is clearly not dependent on kernel burnup, which implies that it is not dependent on the pressure of trapped fission gasses within the kernels. Estimates for end-of-irradiation lifetime temperature for sample 4413-75T run as high as 1700°C. The samples were irradiated under nearly isothermal conditions in an unbonded particle cell. The fact that 8 to 9 μm of swelling was observed at 1500°C in kernels from this sample suggests that fission gas redistribution does not cause the swelling. Kernels in all of these particles migrated during thermal gradient heating, implying that the swelling is not directly related to kernel migration. The only consistent observation is that all kernels from a single production batch behaved alike. More testing of irradiated ThO_2 is needed before the importance of this phenomenon can be established.

The delay before kernel migration observed in particles from irradiation sample 4413-75T (Fig. 17b) was observed in other samples heated at ∿1500°C. The range of delay times observed in the temperature range 1494° to 1559°C is given in Table 9-7. The delay time clearly decreases with increasing burnup. The data available at 1300°C are not yet adequate to define delay times as a function of temperature.

The cause of this delay time is not clear. The kernel migration that is observed appears to be caused by diffusion of carbon down a temperature gradient across irradiated ThO_2 kernels. This implies the formation of a carbon concentration gradient across a kernel due to the presence of a thermal gradient. This phenomenon is known as thermomigration. The observed delay time could equal the time required to establish a steady-state flux of carbon across the kernels. If the diffusion of carbon is the rate limiting step, the delay time can be related to (Ref. 9-13):

TABLE 9-7
DELAY TIME BEFORE OBSERVATION OF KERNEL MIGRATION DURING OUT-OF-PILE THERMAL GRADIENT HEATING OF IRRADIATED ThO_2 FUEL PARTICLES AT 1494° to 1559°C

Out-of-Pile Experiment	Sample Batch No.	Kernel Burnup (% FIMA)	Heating Conditions		Delay Time (hr)	
			Temp (°C)	Temp Gradient (°C/cm)	Average	Range
6532	4413-75T	4.7	1548	588	57	25-111
6617	5466-149	<1	1510	699	(a)	>589
	4252-02-015-5	1.5	1559	705	190	122-310
	4252-02-015-6	6.8	1521	405	11	0-30
	4252-02-015-7	13.7	1494	539	0	0

(a) Migration had not begun after 589 hr at temperature. This sample is still under test.

$$\theta = \frac{a^2}{\pi^2 D} \quad ,$$

where θ = relaxation time

a = specimen thickness in the direction of the thermal gradient

D = carbon diffusivity in ThO_2 at the mean kernel temperature

A decrease in delay time with increasing burnup implies that D for carbon in ThO_2 increases with increasing burnup. The observed delay times decrease by a factor of 17 at ~1500°C as kernel burnups increase from 1.5 to 6.8% FIMA (Table 9-7). This implies an increase in carbon diffusivity by a factor of 17. If ThO_2 kernel migration rates are controlled by solid-state carbon diffusion across the kernel, then the migration rate is proportional to carbon diffusivity and the delay times observed at 1.5 and 6.8% FIMA imply that the kernel migration rate for ThO_2 at 6.8% FIMA should be 17 times the rate for ThO_2 at 1.5% FIMA at constant temperature and temperature gradient. As shown later, migration rates are essentially independent of kernel burnup once migration begins. Assuming that ThO_2 kernel migration is controlled by solid-state carbon diffusion therefore implies that the observed delay times can not be related to the effect of kernel burnup on carbon diffusivity in ThO_2. The rate controlling step resulting in the delay time is therefore not the rate controlling step for kernel migration.

One further observation merits discussion before presenting the kernel migration data. It was shown earlier that coatings on two particles from irradiation sample 4413-75T failed after 126 to 177 hr at 1548°C and that two to three particles from 4252-02-015-7 failed after 28 hr of heating at 1473°C. Net kernel migration distances parallel to the thermal gradient are given in Table 9-8 as a function of time for the particles in these two samples. It appears that two kernels from 4413-75T stopped migrating after 177 hr at 1548°C and two of the three kernels from 4252-02-015-7 stopped migrating after 100 hr at 1473°C. The correlation between the kernel migration behavior and apparent failure suggests that kernel migration

TABLE 9-8
KERNEL ELONGATION AS A FUNCTION OF TIME AT ∿1500°C FOR PARTICLES FROM IRRADIATION SAMPLES 4413-75T AND 4252-02-015-7

Experiment No.	Sample No.	Time Increment (hr)	Net Kernel Elongation by Particle (μm)				
			1	2	3	4	5
6532	4413-75T	0-177	11	11	15	7	14
		177-348	10	12	2	8	2
6617	4252-02-015-7	0-26	7	6	5	(a)	(a)
		26-100	7	3	2	(a)	(a)
		100-590	1	0	6	(a)	(a)

(a) Only three particles from 4252-02-015-7 were included in thermal gradient test 6617.

stops in the absence of metallic and gaseous fission products or CO/CO_2 that are released when particle coatings fail, which implies that the presence of one or more of these species is needed for ThO_2 kernel migration to take place. This observation will be tested by thermal gradient heating of irradiated particles that have been laser-failed to release all gaseous species within the particle coatings.

The primary purpose of the tests was to obtain kernel migration rates as a function of kernel burnup, temperature, and temperature gradient. The values obtained will be compared with values for the ThO_2 KMC now used to estimate ThO_2 kernel migration distances in LHTGR core design (Ref. 9-7). The values currently being used were obtained from observations of in-pile ThO_2 kernel migration made at ORNL (Ref. 9-9) and are based on the assumption that solid-state diffusion in ThO_2 kernels controls the kinetics of migration.

Based on results of the microprobe examinations, the migration data obtained in this study were analysed assuming that solid-state diffusion of carbon through irradiated ThO_2 kernels controls the rate of kernel migration. Values for KMC (Eq. 9-1) were estimated assuming that the total kernel elongation parallel to the thermal gradient equals the kernel migration distance. Total heating times were also used in the calculations. Based on failure observed in particles from sample 4252-02-015-7 at 1473°C, kernel migration data obtained after 100 hr were used for KMC calculations on the fuel having a kernel burnup of 13.7% FIMA. Two or three of the particles from 4252-02-015-7 also failed early in the thermal gradient test conducted at 1300°C. Migration data obtained at the first measurement (259 hr) will therefore be used for this sample in the 1300°C test. The data used for KMC calculations are given in Table 9-9.

Values for ThO_2 KMC determined in these out-of-pile tests are compared with the out-of-pile values determined at ORNL (Ref. 9-9) in Fig. 9-18. The data obtained from out-of-pile tests conducted at $\sim$1300°C are included, but are highly questionable because of the small values (<5 μm) for observed kernel migration distance. At $\sim$1500°C, the values for KMC determined from

TABLE 9-9
DATA USED TO CALCULATE KMC VALUES FOR IRRADIATED ThO_2 FUEL KERNELS

Irradiation Sample No.	Kernel Burnup (% FIMA)	Temperature (°C)	Gradient ($\times 10^{-1}$ °C/μm)	Time (hr)	Migration (μm)
4252-02-015-7	13.7	1473	0.07270	100	14
		1473	0.07270	100	9
		1473	0.07270	100	7
4252-02-015-6	6.8	1521	0.04050	590	21
		1521	0.04050	590	24
		1521	0.04050	590	17
		1521	0.04050	590	29
		1521	0.04050	590	28
		1521	0.04050	590	21
		1521	0.04050	590	24
4252-02-015-5	1.5	1559	0.07050	590	32
		1559	0.07050	590	8
		1559	0.07050	590	45
		1559	0.07050	590	35
		1559	0.07050	590	42
		1559	0.07050	590	8
		1559	0.07050	590	10
5466-149	<1	1510	0.06990	590	7
		1510	0.06990	590	3
		1510	0.06990	590	3
		1510	0.06990	590	4
		1510	0.06990	590	6
		1510	0.06990	590	6
4413-75T	4.7	1548	0.05880	348	27
		1548	0.05880	348	33
		1548	0.05880	348	27
		1548	0.05880	348	22
		1548	0.05880	348	22
4252-02-015-5	1.5	1318	0.04400	1399	2
		1318	0.04400	1399	1
		1318	0.04400	1399	2
		1318	0.04400	1399	2
		1318	0.04400	1399	1
		1318	0.04400	1399	1
		1318	0.04400	1399	2
4252-02-015-6	6.8	1302	0.01890	1399	4
		1302	0.01890	1399	3
		1302	0.01890	1399	4
		1302	0.01890	1399	5
		1302	0.01890	1399	3
		1302	0.01890	1399	4
		1302	0.01890	1399	4
4252-02-015-7	13.7	1358	0.07550	259	3
		1358	0.07550	259	3
		1358	0.07550	259	3

out-of-pile tests range from the nominal value obtained from in-pile results at kernel burnups of less than 1% FIMA to two times the upper 95% confidence limit for in-pile results for kernel burnups in the range 1.5 to 6.8% FIMA. Values of ThO_2 KMC for a burnup of 13.7% FIMA are slightly higher relative to the in-pile data but will not be considered further since the maximum burnup expected for LHTGR fertile fuel is 7.5% FIMA. Within the scatter of the data, the KMC values do not appear to be related to ThO_2 kernel burnup for burnups in the range 1.5 to 6.8% FIMA. Comparison of the in-pile and out-of-pile results is not appropriate at this time because of the small quantity of out-of-pile data. The out-of-pile results were, however, conducted under a well defined thermal environment at constant burnup, while the burnup varied as a function of time in the in-pile tests and temperatures and temperature gradients are quite uncertain. Uncertainties for in-pile operating temperatures range from 100° to 300°C (Ref. 9-12).

Based on the results presented in Fig. 9-18 and the assumption that the in-pile data are more precise than the out-of-pile data, the upper 95% confidence limit for ThO_2 KMC determined from in-pile ThO_2 kernel migration results should be used to describe ThO_2 kernel migration for kernel burnups less than 7.5% FIMA. The resulting value for KMC as a function of temperature (°K) is approximately

$$KMC_{ThO_2} = 1.501 \exp\left(\frac{-45,959}{RT}\right) .$$

Studies designed to define kernel migration rates in irradiated ThO_2 are continuing to allow a more precise definition of the mechanisms and kinetics of migration phenomenon.

Conclusions

The following conclusions can be drawn from the data presented:

1. ThO_2 kernels irradiated to a burnup of 4.7% FIMA convert to ThC_2 after coating failure in less than 100 hr at 1548°C. No sign of

oxide to carbide conversion at 1494°C is visible in kernels irradiated to 13.7% FIMA after heating for approximately 560 hr following coating failure detected by fission gas release.

2. Irradiated ThO_2 kernels migrate up a thermal gradient during out-of-pile heating.

3. Metallographic and microprobe examination after thermal gradient heating (1548°C, 588°C/cm) of BISO ThO_2 irradiated to 4.7% FIMA showed the presence of an intergranular carbon deposit within the ThO_2 kernels. The deposit is much more pronounced on the cool side of the kernel than on the warm side. This observation is evidence that solid-state diffusion of carbon in irradiated ThO_2 plays a role in ThO_2 kernel migration.

4. Metallographic observations of in-pile ThO_2 kernel migration show that the kernel microstructures and shapes observed in the out-of-pile ThO_2 kernel migration studies also occur in-pile during ThO_2 migration. This confirms the assumption that the out-of-pile data are representative of the in-pile ThO_2 kernel migration phenomenon.

5. At ∿1500°C, ThO_2 kernel migration was only observed after a delay time that decreased with increasing kernel burnup. The delay time increased from ∿11 hr for 6.8% FIMA, to ∿190 hr for 1.5% FIMA, and to greater than 600 hr for less than 1% FIMA. If the assumption that ThO_2 kernel migration rates are controlled by carbon diffusion in ThO_2 kernels is correct, the delay times cannot be explained in terms of the effect of kernel burnup on carbon diffusivity.

6. Kernel migration appears to stop after failure of particle coatings, indicating that the presence of fission products normally released during particle failure or CO/CO_2 is needed for ThO_2 kernel migration.

7. The assumption is made that the kernel migration in ThO_2 is not dependent upon the presence of a neutron flux. Postirradiation kernel migration rates determined for ThO_2 exceed those estimated from migration observed in-pile. The in-pile results are thought to be systematically low. For this reason, the upper 95% confidence limit determined for ThO_2 KMC from in-pile observations is thought to best describe ThO_2 kernel migration.

CAPSULE P13Q

Capsule P13Q is designed to demonstrate the performance of fuel rods fabricated using candidate large HTGR (LHTGR) processes and materials. Experiment P13Q is the GA portion of GA-ORNL cooperative experiment OF-1. The capsule completed its scheduled irradiation in the E-3 position of the ORR on February 27, 1975 after receiving an estimated peak fast neutron fluence of 10.3×10^{21} n/cm^2 $(E > 0.18 \text{ MeV})_{ORR}$. The end-of-life fission gas release based on Kr-85m was 1.2×10^{-6}, which is consistent with the very low release measured throughout irradiation and indicates a low fuel failure fraction.

Disassembly of the capsule was started at the GA hot cell facility on April 24, 1975. All three graphite fuel bodies were removed from the containment vessel in good condition. Each body was submitted for fission gas release measurements prior to removal of the fuel specimens. All of the dosimeter vials were recovered from the niobium tube containers with the exception of the primary dosimeters from crucible No. 1.

The major objectives of the P13Q irradiation test and subsequent postirradiation examinations are summarized as follows:

1. Evaluate irradiation performance of fuel rods and larger diameter fuel bodies that simulate a section of a full-sized LHTGR fuel element.

2. Evaluate irradiation performance of near-reference design LHTGR UC_2 TRISO and ThO_2 BISO fuel particles.

3. Compare irradiation stability of fuel rods fired in H-451 graphite tubes (which simulate the LHTGR cure-in-place process) with fuel rods fired in packed alumina beds.

4. Evaluate irradiation stability of candidate LHTGR fuel rod matrix materials.

5. Compare the irradiation stability of fuel rods fabricated by the reference hot-injection process with fuel rods fabricated by an alternate admix-compaction process.

6. Evaluate fuel rod dimensional change as a function of irradiation conditions, matrix composition, and firing mode.

Visual examination, fission gas release measurements, and metallography will be used to evaluate the postirradiation condition of fuel specimens tested in capsule P13Q. The results of these examinations will be reported in future quarterly progress reports.

CAPSULES P13R and P13S

Introduction

Capsules P13R and P13S are the seventh and eighth in a series of irradiation tests to demonstrate the integrity of reference and alternate LHTGR fuels over a wide range of irradiation conditions.

The integrity of coated particles and fuel rods of the general type to be used in LHTGRs has been previously demonstrated in capsules P13L, P13M, P13N, and P13P to peak design conditions (Ref. 9-14). However, since these tests a number of evolutionary improvements in the reference 1100-MW(e) fuel have been introduced, e.g., graphite shimmed rods, in-block carbonization, and ThO_2 BISO fertile particles. Irradiation of samples reflecting these improvements has been completed in capsules HRB-4, -5, and -6 (Ref. 9-15).

Capsules P13R and P13S are designed to extend GA's irradiation experience with reference-type fuel by providing data over a wide range of irradiation conditions and by evaluating a broad spectrum of property and process variables (Ref. 9-16). These tests have four primary objectives:

1. Obtain irradiation data on a broad spectrum of property (and process) variables for reference LHTGR fuel.

2. Determine the temperature-fluence dependence of in-pile fission gas release and relate to coated particle integrity.

3. Determine effect of thermal cycling on fuel integrity.

4. Test alternate fuel materials.

Fuel rod samples in P13R and P13S were irradiated at design temperatures of 1075°, 1300°, and 1500°C. The unbonded particle cells in both capsules were designed to operate at 1075°C. One series of fuel rods (cell 1, P13S) was thermal cycled twenty-one times from its nominal operating temperature of 1075°C to 1500°C. This test was the first attempt to simulate temperature cycling that results from load following and/or control rod pattern changes in the LHTGR.

Capsules P13R and P13S were discharged from the GETR on October 31, 1974 and disassembly was started at the GA hot cell facility on December 5, 1974. The major objectives of the irradiation tests and subsequent postirradiation examinations were summarized in the previous quarterly report (Ref. 9-17).

Postirradiation Examination

Capsule Disassembly

The secondary containments were slit at 0° and 180° orientations and removed to expose the thermal bond spacers. All dosimeter vials, located

in grooves of the thermal bond spacers, were recovered with the exception of two secondary dosimeter vials from capsule P13S. Transverse and longitudinal cracking of the protective tantalum thermocouple sheathing was observed, as expected. All purge gas lines were intact. The thermal bond spacers, purge gas lines, and thermocouples were removed, which exposed the primary containment of each cell. Dimensional measurements made on the thermal bond spacers and the primary and secondary containments showed no measurable change in these components during irradiation.

Fuel specimens were housed in interlocking graphite crucibles inside Inconel cans, which formed the primary containment for each cell. After removal of the Inconel cans, the fuel rods were exposed by lifting off the top segment of the graphite crucibles as shown in Fig. 9-19. The fuel rods were removed by sliding them out of the graphite crucibles into a padded plastic box or by lifting them out with master-slave manipulators. All fuel rods were removed intact and irradiation-induced damage to the fuel rods was considered to be minimal.

Slight bowing of the graphite fuel rod crucibles in cell 2 of both capsules was observed. The fuel rods were wedged in the graphite crucibles and although the fuel specimens were not damaged, they were removed with considerable difficulty. Subsequent dimensional measurements revealed the fuel specimens were restrained by the graphite crucibles as a result of shrinkage of the graphite crucibles and slight expansion of the fuel rods after irradiation to the severe fast neutron fluences [11.6 to 12.5 x 10^{21} n/cm^2 $(E > 0.18\ MeV)_{HTGR}$] experienced by these cells.

Each unbonded particle cell contained a graphite crucible assembly, which consisted of twelve annular trays arranged on a threaded graphite stock as shown in Fig. 9-20. Neutron radiographs taken of the capsules after irradiation revealed that all four of the crucible assemblies were intact. However, at least one sample tray from each cell was spilled during capsule disassembly or the fuel unloading operation because the threaded graphite stock broke. The sample trays spilled were positions

3-6, 4-1, and 4-12 in capsule P13R and positions 3-11, 4-5, and 4-6 in capsule P13S. Subsequent failure analyses will not be performed on these specific samples because only a portion of the fuel particles in each sample was recovered. However, duplicate samples of each particle type were tested in companion trays and will be examined.

Dosimetry and Burnup Analyses

Dosimeter wires of V - 0.216% Co, V - 0.522% Fe, and pure Fe were employed in capsules P13R and P13S to monitor long-term thermal (2200 m/sec) and fast (E > 0.18 MeV) neutron fluences. The wires were encapsulated in quartz ampoules and positioned along the capsules at seven axial locations at 0° and 180° radial orientations. In addition to the standard dosimetry wires, six ampoules containing purified Mn-54 were employed to evaluate the Mn-54 transmutation cross section.

After removal from the capsule, each wire was cleaned and weighed. The gamma-ray spectrum of each wire was analyzed with a Ge (Li) detector and a Sigma II 4096-channel computer analyzer. Due to the high radiation levels of the Fe and V-Co dosimetry wires, it was necessary to dissolve and aliquot them prior to gamma-ray spectrometry analysis. Thermal and fast neutron fluxes and fluences were calculated for each axial position with the DOSE-1 computer program using the gamma-ray spectrometry analyses of the dosimeter wires. A third-order polynominal fit was made through the data points to obtain the axial thermal and fast neutron fluence profiles shown in Figs. 9-21 and 9-22. A cobalt cross section at E = 0.025 eV was used to calculate the thermal fluences and a burnout cross section of 11.6 ± 2.0 barns for Mn-54, which was determined from analysis of the purified Mn-54 ampoules, was used to evaluate the fast neutron fluence levels.

The average value of the fast neutron fluence profile $(E > 0.18\ MeV)_{GETR}$ determined from the 0° and 180° dosimetry orientations for each fuel specimen is given in Tables 9-10 through 9-14. The equivalent fast fluence in

TABLE 9-10
IRRADIATION PARAMETERS AND CONDITIONS OF FUEL RODS IRRADIATED IN CAPSULE P13R

Fuel Rod Description							Irradiation Parameters					Postirradiation Condition	
		Shim		Matrix				Fast Fluence (10^{21} n/cm^2)		Burnup (% FIMA)			
Cell Position	Fuel Rod Data Retrieval No. (7161-004-)	Particle Type	Loading (vol %)	Filler	Additive	Firing Conditions[a]	Design Temp (°C)	GETR	HTGR	Fissile	Fertile	Dimensional Change, $\Delta D/D_o$ (%)	Visual Appearance[b]
1A	01-5[c]	GLCC 1099	10.0	6353	SC011	Ref.	1075	8.2	7.4	70.9	3.5	-1.76	Fair
1B	02-6	GLCC 1099	35.3	6353	SC011	Ref.	1075	9.1	8.2	72.0	3.9	-1.51	Excellent
1C	03-5	GLCC 1099	36.3	6353	SC011	Ref.	1075	9.8	8.8	72.8	4.2	-1.52	Excellent
1D	04-6	GLCC 1099	20.0	6353	SC011	1500°C	1075	10.5	9.4	73.4	4.5	-0.48	Excellent
1E	05-6[c]	GLCC 1099	25.0	6353	SC011	Ref.	1075	11.1	10.0	39.5	4.8	-0.88	Excellent
2A	06-5[c]	GLCC 1099	20.0	6353	SC011	1500°C	1075	13.3	12.0	74.7	5.5	-0.32	Excellent
2B	07-5	GLCC 1099	25.0	KS-44	SC011	Ref.	1075	13.5	12.2	74.8	5.6	+0.80	Excellent
2C	08-13[d]	GLCC 1099	30.0	6353	SC011	Packed bed	1075	13.7	12.3	74.8	5.6	-0.08	Excellent
2D	09-5	Lonza	25.0	6353	SC003	Ref.	1075	13.8	12.4	74.8	5.6	+0.02	Fair
2E	10-5[c]	GLCC 1099	33.0	6353	SC011	Ref.	1075	13.9	12.5	40.5	5.5	-0.02	Excellent
5A	16-5[c]	GLCC 1099	25.0	6353	SC011	Ref.	1300	10.6	9.5	36.4	3.1	-1.28	Good
5B	17-5	GLCC 1099	30.0	6353	SC011	Ref.	1300	10.1	9.1	68.3	2.8	-1.36	Excellent
5C	18-6	GLCC 1099	20.0	6353	SC011	1500°C	1300	9.6	8.6	67.1	2.6	-1.52	Good
5D	19-7	GLCC 1099	20.0	6353	SC011	N_2 atmosphere	1300	9.2	8.3	65.8	2.4	-1.36	Good
5E	20-6[c]	GLCC 1099	10.0	6353	SC011	Ref.	1300	8.7	7.8	64.3	2.1	-1.36	Good
6A	21-5[c]	GLCC 1099	25.0	6353	SC011	Ref.	1075	6.1	5.5	53.9	1.1	-2.00	Excellent
6B	22-5	GLCC 1099	15.0	6353	SC011	Ref.	1075	5.6	5.0	51.4	1.0	-1.60	Excellent
6C	23-5[d]	GLCC 1099	30.0	6353	SC027	Ref.	1075	5.1	4.6	48.9	0.8	-1.92	Excellent
6D	24-5	Lonza	20.0	6353	SC003	Ref.	1075	4.6	4.1	46.5	0.7	-2.08	Fair
6E	25-5[c]	GLCC 1099	25.0	6353	SC011	N_2 atmosphere	1075	4.1	3.7	43.9	0.6	-1.60	Excellent

[a] Reference firing conditions are carbonization to 1800°C in an argon atmosphere in an H-451 graphite tube to simulate the LHTGR cure-in-place process. Firing conditions that vary from this process are noted.

[b] Relative condition of fuel rod based on visual appearance; e.g., excellent condition indicates rod exhibited no significant matrix spalling, matrix cracking, or particle debonding.

[c] Thermocouple fuel rods.

[d] Fuel rods were fabricated by slug-injection process.

TABLE 9-11
IRRADIATION PARAMETERS AND CONDITIONS OF FUEL RODS IRRADIATED IN CAPSULE P13S

Fuel Rod Description							Irradiation Parameters					Postirradiation Condition	
		Shim		Matrix				Fast Fluence (10^{21} n/cm^2)		Burnup (% FIMA)			
Position	Fuel Rod Data Retrieval No. (7161-004-)	Particle Type	Loading (vol %)	Filler	Additive	Firing Conditions[a]	Design Temp (°C)	GETR	HTGR	Fissile	Fertile	Dimensional Change, $\Delta D/D_o$ (%)	Visual Appearance[b]
1A	01-7[c]	GLCC 1099	10.0	6353	SC011	Ref.	1075[d]	7.9	7.1	69.8	3.2	-1.12	Fair
1B	02-5	GLCC 1099	35.3	6353	SC011	Ref.	1075[d]	8.7	7.8	70.7	3.4	-1.28	Excellent
1C	03-6	GLCC 1099	36.3	6353	SC011	Ref.	1075[d]	9.5	8.6	71.4	3.7	-1.36	Excellent
1D	04-5	GLCC 1099	20.0	6353	SC011	1500°C	1075[d]	10.2	9.2	72 0	3.9	-0.64	Excellent
1E	05-5[c]	GLCC 1099	25.0	6353	SC011	Ref.	1075[d]	10.8	9.7	38.5	4.1	-0.72	Excellent
2A	11-6[c]	GLCC 1099	20.0	6353	SC011	N_2 atmosphere	1075	12.9	11.6	73.5	4.6	-0.24	Excellent
2B	12-5	GLCC 1099	25.0	6353	SC011	Ref.	1075	13.2	11.9	73.6	4.6	+0.16	Excellent
2C	13-6	GLCC 1099	30.0	6353	SC027	Ref.	1075	13.4	12.1	73.6	4.7	+0.08	Excellent
2D	14-5	GLCC 1099	25.0	6353	SC011	Ref.	1075	13.5	12.2	73.6	4.6	+0.04	Excellent
2E	15-5[c]	GLCC 1099	33.0	6353	SC011	Ref	1075	13.6	12.2	73.6	4.6	+0.16	Good
5A	16-6[c]	GLCC 1099	25.0	6353	SC011	Ref.	1500	10.2	9.2	35.6	2.8	-1.68	Excellent
5B	17-6	GLCC 1099	30.0	6353	SC011	Ref.	1500	9.8	8.8	67.0	2.6	-1.20	Excellent
5C	18-5	GLCC 1099	20.0	6353	SC011	1500°C	1500	9.4	8.5	66.0	2.4	-1.52	Good
5D	19-5	GLCC 1099	20.0	6353	SC011	N_2 atmosphere	1500	8.9	8.0	64.7	2.2	-1.36	Fair
5E	20-5[c]	GLCC 1099	10.0	6353	SC011	Ref.	1500	8.4	7.6	63.4	2.0	-1.60	Excellent
6A	26-5[c]	GLCC 1099	25.0	6353	SC011	Ref.	1075	5.9	5.3	53.5	1.1	-2.00	Excellent
6B	27-5	GLCC 1099	15.0	6353	SC011	Ref.	1075	5.4	4.9	26.2	1.0	-1.84	Fair
6C	28-13	GLCC 1099	30.0	6353	SC011	Packed bed	1075	4.9	4.4	48.4	0.8	-2.33	Excellent
6D	29-5	GLCC 1099	20.0	KS-44	SC011	Ref.	1075	4.4	4.0	45.5	0.7	-2.16	Excellent
6E	30-5[c]	GLCC 1099	25.0	6353	SC011	1500°C	1075	3.9	3.5	42.4	0.6	-1.76	Good

[a] Reference firing conditions are carbonization to 1800°C in an argon atmosphere in an H-451 graphite tube to simulate the LHTGR cure-in-place process. Firing conditions that vary from this process are noted.

[b] Relative condition of fuel rod based on visual appearance; e.g., excellent condition indicates rod exhibited no significant matrix spalling, matrix cracking, or particle debonding.

[c] Thermocouple fuel rods.

[d] Cell 1 was thermal cycled from 1075° to 1500°C (design) twenty-one times during capsule operation.

TABLE 9-12
RESULTS OF VISUAL EXAMINATION OF UNBONDED FISSILE PARTICLE SAMPLES IRRADIATED IN CAPSULES P13R AND P13S

Capsule	Sample Description[a]						Irradiation Conditions[c]				Visual Examination					Remarks
	Data Retrieval Number	OPyC Thickness (μm)	OPyC Density[b] (g/cm^3)	OPyC Coating Rate (μm/min)	OPyC Anisotropy (BAF_o)	Total Coating Thickness (μm)	Cell-Position	Fast Fluence (10^{21} n/cm^2) (E > 0.18 MeV) GETR	Fast Fluence (10^{21} n/cm^2) (E > 0.18 MeV) HTGR	Burnup (% FIMA)	Sample Size	OPyC Coating Failure (%)	95% Confidence Interval, P (%)	Pressure Vessel Failure (%)	95% Confidence Interval, P (%)	
P13R	6151-00-010	44	1.80	1.1	1.042	200	3-1, 2, 3	13.6	12.2	73	682	32.8	$31 \leq P \leq 33$	0.7	$0.3 \leq P \leq 1.7$	
	6151-00-035	37	1.85	3.9	1.030	191	3-4, 5[d]	13.5	12.1	74	459	0	$0 \leq P \leq 0.8$	0	$0 \leq P \leq 0.8$	(e)
	6151-00-045	40	1.81	3.8	1.024	192	3-7, 8, 9	13.4	12.0	74	749	6.8	$5.1 \leq P \leq 8.1$	6.3	$4.8 \leq P \leq 7.7$	Faceted coatings
	6151-00-046	40	1.81	3.3	1.024	191	3-10	13.3	12.0	74	254	3.5	$1.9 \leq P \leq 6.6$	2.0	$0.8 \leq P \leq 4.5$	Faceted coatings
	6151-04-015	36	1.82	1.4	1.038	199	3-11, 12	13.2	11.9	73	492	0	$0 \leq P \leq 0.8$	0	$0 \leq P \leq 0.8$	
	6151-01-015	42	1.90	0.7	1.077	197	4-2, 3[d]	12.9	11.6	73	464	100	$99.2 \leq P \leq 100$	2.8	$1.6 \leq P \leq 4.7$	
	6151-00-025	33	1.88	1.4	1.052	188	4-4, 5, 6	12.6	11.3	73	819	83.0	$81 \leq P \leq 85$	0	$0 \leq P \leq 0.7$	Faceted coatings
	6151-09-015	39	1.94	3.6	1.028	195	4-7, 8, 9	12.5	11.2	73	785	0	$0 \leq P \leq 0.7$	0	$0 \leq P \leq 0.7$	
	6151-09-025	41	1.95	4.0	1.033	194	4-10, 11[d]	12.4	11.2	73	491	0	$0 \leq P \leq 0.8$	0	$0 \leq P \leq 0.8$	
P13S	6151-03-015	45	1.77	1.5	1.020	198	3-1, 2, 3	13.3	12.0	72	729	1.5	$0.8 \leq P \leq 2.7$	0.1	$0.01 \leq P \leq 0.7$	Interrupted SiC layer
	4161-01-021	32	1.82	3.4	ND[f]	173	3-4, 5, 6	13.2	11.9	73	718	3.9	$2.7 \leq P \leq 5.6$	3.3	$2.2 \leq P \leq 4.9$	Interrupted SiC layer
	6151-08-015	36	1.76	3.6	1.018	190	3-7, 8, 9	13.0	11.7	73	688	0	$0 \leq P \leq 0.6$	0	$0 \leq P \leq 0.6$	(e)
	6151-02-025	43	1.50	0.7	1.039	202	3-10, 12[d]	12.9	11.6	72	501	46.3	$42.0 \leq P \leq 50.7$	0.2	$0.04 \leq P \leq 1.1$	
	4163-00-011	72	1.77	4.1	ND	218	4-1, 2, 3	12.6	11.3	27	767	0	$0 \leq P \leq 0.5$	0	$0 \leq P \leq 0.5$	250-μm $(Th,U)O_2$, Th/U = 1:1
	6155-01-020	42	1.81	3.4	1.025	194	4-4[d]	12.4	11.2	11	163	76.7	$696.6 \leq P \leq 82.5$	1.8	$0.6 \leq P \leq 5.3$	500-μm $(Th,U)O_2$, Th/U = 8:1
	5466-37-9	31	1.79	6.0	ND	182	4-7, 8, 9	12.2	11.0	38	801	0	$0 \leq P \leq 0.7$	0	$0 \leq P \leq 0.7$	250-μm $(Th,U)O_2$, Th/U = 1:1
	6151-00-035	37	1.85	3.9	ND	161	4-10, 11, 12	12.0	10.8	72	809	0	$0 \leq P \leq 0.7$	0	$0 \leq P \leq 0.7$	(e)

[a] All fissile particle samples are TRISO UC_2 particles with a nominal kernel diameter of 200 μm, except where noted.

[b] Measured using a density gradient column.

[c] Unbonded particle cells were designed to operate at 1075°C.

[d] Companion sample was spilled during unloading.

[e] Coating parameters are within LHTGR reference design requirements.

[f] ND = not determined.

TABLE 9-13
RESULTS OF VISUAL EXAMINATION OF UNBONDED FERTILE PARTICLE SAMPLES IRRADIATED IN CAPSULE P13R

Sample Description[a]							Irradiation Conditions				Visual Examination			
Data Retrieval Number	Buffer Thickness (μm)	OPyC Thickness (μm)	OPyC Density[b] (g/cm^3)	OPyC Coating Rate (μm/min)	OPyC Anisotropy (BAF_o)	Particle Density[c] (g/cm^3)	Cell-Position	Fast Fluence (10^{21} n/cm^2) (E > 0.18 MeV) GETR	Fast Fluence (10^{21} n/cm^2) (E > 0.18 MeV) HTGR	Burnup (% FIMA)	Sample Size	OPyC Coating Failure (%)	95% Confidence Interval, P (%)	Remarks
4252-06-018	78	77	1.82	5.8	1.029	3.54	3-1, 2	13.6	12.2	5.1	840	0.1	$0.01 \leq P \leq 0.8$	
6542-01-020	81	74	1.82	2.7	1.028	3.55	3-3, 4	13.6	12.2	5.0	1004	7.8	$6.5 \leq P \leq 9.0$	
6542-01-010	79	85	1.80	10.0	1.028	3.59	3-5[d]	13.5	12.2	5.0	455	0.2	$0.04 \leq P \leq 1.2$	(e)
6542-02-020	87	72	1.91	8.5	1.036	3.59	3-7, 8	13.4	12.1	4.9	1072	0	$0 \leq P \leq 0.5$	(e)
6542-02-030	79	74	1.89	2.2	1.042	3.54	3-9, 10	13.3	12.0	4.8	1148	10.2	$10.0 \leq P \leq 10.3$	
6542-09-010	84	75	1.93	5.0	1.042	3.56	3-11, 12	13.2	11.9	4.8	998	0	$0 \leq P \leq 0.5$	(e)
6592-11-015	87	74	1.83	2.6	ND[f]	3.35	4-2[d]	12.9	11.6	4.5	492	0.4	$0.1 \leq P \leq 1.5$	No seal coat
6542-18-015	84	70	1.84	6.5	ND	3.53	4-3, 4	12.8	11.5	4.4	953	0	$0 \leq P \leq 0.6$	(e), No seal coat
6542-02-020	87	72	1.91	8.5	1.028	3.59	4-5, 6	12.7	11.4	4.4	1149	0	$0 \leq P \leq 0.5$	(e)
6542-20-035	80	83	1.84	3.6	ND	3.50	4-7, 8	12.6	11.3	4.3	1012	0.6	$0.2 \leq P \leq 1.2$	Faceted coatings
6542-20-025	76	81	1.82	3.5	1.047	3.57	4-9, 10	12.5	11.2	4.2	1040	1.0	$0.6 \leq P \leq 1.7$	Faceted coatings
6542-25-015	79	76	1.82	10.8	ND	3.57	4-11[d]	12.3	11.1	4.1	539	1.7	$0.9 \leq P \leq 3.1$	Nonround kernels

[a] All particle samples are BISO coated ThO_2 particles with a nominal kernel diameter of 500 μm.

[b] Measured using a density gradient column.

[c] Measured using an air pycnometer.

[d] Companion sample spilled during unloading.

[e] Coating parameters are within LHTGR reference design requirements.

[f] ND = not determined.

TABLE 9-14
RESULTS OF VISUAL EXAMINATION OF UNBONDED FERTILE PARTICLE SAMPLES IRRADIATED IN CAPSULE P13S

Sample Description[a]							Irradiation Conditions				Visual Examination			
Data Retrieval Number	Buffer Thickness (μm)	OPyC Thickness (μm)	OPyC Density[b] (g/cm^3)	OPyC Coating Rate (μm/min)	OPyC Anisotropy (BAF_O)	Particle Density[c] (g/cm^3)	Cell-Position	Fast Fluence (10^{21} n/cm^2) (E > 0.18 MeV) GETR	Fast Fluence (10^{21} n/cm^2) (E > 0.18 MeV) HTGR	Burnup (% FIMA)	Sample Size	OPyC Coating Failure (%)	95% Confidence Interval, P (%)	Remarks
4252-06-010	85	76	1.82	5.8	1.029	3.54	3-1, 2	13.3	12.0	4.3	872	0	$0 \leq P \leq 0.6$	(d)
6542-22-015	85	81	1.80	4.0	1.020	3.50	3-3, 4	13.2	11.9	4.3	979	1.0	$0.5 \leq P \leq 1.5$	(d), mixed gas OPyC layer
6542-22-025	81	80	1.81	7.6	1.028	3.53	3-5, 6	13.2	11.9	4.2	964	0.3	$0.1 \leq P \leq 0.9$	(d), mixed gas OPyC layer
6542-23-025	82	73	1.89	5.8		3.58	3-7, 8	13.1	11.8	4.2	992	0	$0 \leq P \leq 0.5$	(d), mixed gas OPyC layer
6542-24-015	86	83	1.94	6.6	1.032	3.55	3-9, 10	13.0	11.7	4.1	942	0	$0 \leq P \leq 0.6$	Mixed gas OPyC layer
6252-00-025	60	42	1.81	4.2	1.015	3.77	3-11[e]	12.9	11.6	4.1	528	0.4	$0.1 \leq P \leq 1.4$	TRISO coated
6542-17-010	44	122	1.86	2.8	ND[f]	3.55	4-1	12.6	11.3	3.9	458	2.6	$1.5 \leq P \leq 4.5$	
4252-02-010	83	73	1.83	4.0	1.032	3.51	4-2, 3	12.6	11.3	3.9	925	0	$0 \leq P \leq 0.6$	(d)
6542-16-010	39	55	ND	3.7	ND	4.84	4-4[e]	12.4	11.2	3.8	349	5.4	$3.5 \leq P \leq 8.3$	
6542-19-015	81	77	1.78	7.6	1.026	3.55	4-7	12.3	11.1	3.7	495	0.6	$0.2 \leq P \leq 1.8$	
6542-19-016	82	71	1.78	7.0	1.026	3.45	4-8	12.2	11.0	3.7	502	0.2	$0.04 \leq P \leq 1.1$	
6542-21-016	81	84	1.73	8.0	1.020	3.41	4-9	12.2	11.0	3.6	508	0	$0 \leq P \leq 0.8$	Mixed gas OPyC layer
6542-21-015	79	82	1.73	7.8	1.020	3.46	4-10	12.1	10.9	3.6	513	0	$0 \leq P \leq 0.7$	Mixed gas OPyC layer
6542-12-025	84	70	1.79	6.7	ND	3.58	4-11, 12	12.0	10.8	3.6	1214	0.2	$0.1 \leq P \leq 0.8$	(d), N_2 buffer carrier gas

[a] All particle samples are BISO coated ThO_2 particles with a nominal kernel diameter of 500 μm, except where noted.

[b] Measured using a density gradient column.

[c] Measured using an air pycnometer.

[d] Coating parameters are within LHTGR reference design requirements.

[e] Companion sample spilled during unloading.

[f] ND = not determined.

an HTGR environment $(E > 0.18 \text{ MeV})_{HTGR}$, which is equal to $0.90\phi_{GETR}$ for capsules P13R and P13S, is also given for each fuel specimen.

Heavy metal burnups for each fuel specimen were calculated using the FISSIN computer code and are given in Tables 9-10 through 9-14. Heavy metal burnups of individual particle samples are currently being determined by wet chemical analysis to verify to FISSIN computer code calculations.

Fuel Rod Examinations

A description of the fuel rod matrix and process variables tested in capsules P13R and P13S is given in Tables 9-10 and 9-11. Most fuel rod specimens were carbonized at 1800°C in an argon atmosphere in H-451 graphite tubes to simulate in-block curing, and 38 of the 40 fuel rods tested were fabricated using a prototype LHTGR hot-injection press. The Great Lakes Carbon Company 1099 graphite shim particle impregnated with furfuryl alcohol, which is the prime candidate for use in LHTGR fuel rods, was used in 32 of the 40 fuel rods. Preirradiation photomicrographs of fuel rods that are representative of the different fabrication and firing processes evaluated in capsules P13R and P13S are shown in Figs. 9-23 and 9-24.

After removal from the graphite crucibles, the fuel rods were examined visually using an in-cell stereomicroscope. The criteria for evaluating fuel rod integrity after irradiation are that the fuel rods remain intact and exhibit negligible cracking or particle debonding. Representative post-irradiation photomicrographs of each rod are shown in Figs. 9-25 through 9-44. The visual appearance of the fuel rods after irradiation is summarized in Tables 9-10 and 9-11.

The general irradiation performance of the fuel rod specimens was good and fuel rod integrity was demonstrated. Very little irradiation-induced damage was observed, even in fuel rods irradiated to a fast neutron fluence 56% beyond the peak LHTGR design fast neutron fluence of 8.0×10^{21} n/cm^2 $(E > 0.18 \text{ MeV})_{HTGR}$. The fuel rod fabrication or firing process

variables tested did not influence the fuel rod irradiation performance. Fuel rods containing Lonza shim particles and low shim contents (P13R-1A, -2D, -5E, -6B, and -6D and P13S-1A, -5E, and -6B) exhibited slight cracking and particle debonding. The fuel rods irradiated in P13S cell 5 at 1500°C were in relatively good condition although the rods appeared somewhat weak around the edges, especially the rods in positions 5C and 5D, which exhibited slight circumferential cracking on the ends. Fuel rods tested in P13S cell 1 were in good condition, which indicates that thermal cycling to high temperatures during operation does not adversely affect fuel rod integrity.

Dimensional measurements were made on all fuel rods to evaluate fuel rod dimensional change as a function of irradiation conditions, shim content, particle coating density, matrix type, firing temperature, and firing mode. The measurements were made with a dial gage and micrometer, as shown in Fig. 9-45, to tolerances of ±0.0005 in.

Diametral irradiation-induced dimensional changes are given in Tables 9-10 and 9-11 and are plotted in Figs. 9-46 and 9-47 as a function of fast neutron fluence. Fuel rod shrinkages reached a maximum of ∿2% after irradiation to fast neutron fluences ranging from 4.0 to 6.0 x 10^{21} n/cm^2 $(E > 0.18 \text{ MeV})_{HTGR}$. After irradiation to higher fast neutron exposures, the fuel rod shrinkages decreased and at fast neutron fluences greater than 12.0 x 10^{21} n/cm^2 $(E > 0.18 \text{ MeV})_{HTGR}$, the fuel rod dimensional changes were positive. These results are consistent with fuel rod dimensional change data reported previously (Refs. 9-14 and 9-15). The net expansion observed in the high exposure fuel rods will not result in fuel-rod/graphite-block interaction since these rods were irradiated to fast neutron exposures ∿50% beyond the peak LHTGR design fast neutron fluences.

A large degree of scatter was observed in the axial fuel rod dimensional measurements and these data are therefore not reported. This scatter was attributed to the presence of the grafoil disks placed on the ends of the fuel rods to separate them from each other during the carbonization process.

Preirradiation length measurements were made with the grafoil disks in place; however, most of the disks deteriorated during irradiation or were partially peeled off during unloading of the fuel rods.

Unbonded Particle Examinations

Ninety-six unbonded particle samples were irradiated in cells 3 and 4 at a design temperature of 1075°C to fast neutron fluences of 10.8 to 12.2 x 10^{21} n/cm^2 (E > 0.18 MeV)$_{HTGR}$. The majority of the particles tested were 200-μm TRISO coated VSM UC_2 kernels and 500-μm BISO coated ThO_2 kernels.

Each particle sample was examined visually using an in-cell stereomicroscope, and a measure of the OPyC coating integrity and pressure vessel failure was determined by counting the number of particles with defective coatings. The irradiation parameters and the results of visual examination of each particle batch are given in Tables 9-12 through 9-14.

The irradiation performance of particle batches with coating parameters that meet LHTGR reference design requirements is summarized in Table 9-15. No particle failure was observed in the fissile particles and a failure level of only 0.15% was observed in eleven batches of fertile particles. The samples were irradiated to peak fast neutron exposures ranging from 10.8 to 12.2 x 10^{21} n/cm^2 (E > 0.18 MeV)$_{HTGR}$, which is 35 to 52% beyond the peak LHTGR design fast neutron exposure of 8.0 x 10^{21} n/cm^2. These results demonstrate the conservative nature of LHTGR reference coating designs.

A large number of fissile and fertile particle samples were tested with coating designs that fall outside the current LHTGR reference design requirements to investigate the effect of variables such as coating deposition rate, density, and faceting on fuel particle irradiation performance. Previous full-exposure tests of TRISO coated fissile particles have demonstrated that OPyC coatings with densities in the range of 1.72 to 1.96 g/cm^3 perform satisfactorily (Ref. 9-14). Fissile particles tested in

TABLE 9-15
SUMMARY OF VISUAL EXAMINATION OF UNBONDED PARTICLE SAMPLES REPRESENTATIVE OF LHTGR REFERENCE COATING DESIGNS FOLLOWING IRRADIATION IN CAPSULES P13R AND P13S

Particle Type	No. Batches/ No. Particles	Fast Neutron Fluence (10^{21} n/cm^2) (E > 0.18 MeV)$_{HTGR}$	Burnup (% FIMA)	Failure (%)		
				OPyC Coating	Pressure Vessel	95% Confidence Interval (P)
UC_2 TRISO	3/1,956[a]	10.8 to 12.1	72 to 74	0	0	$0.0 \leq P \leq 0.3$
ThO_2 BISO	11/10,573[a]	10.8 to 12.2	3.6 to 5.1	0.15	0.15	$0.1 \leq P \leq 0.2$

[a] Irradiated at a design temperature of 1075°C.

capsules P13R and P13S with OPyC coating densities in the range of 1.76 to 1.94 g/cm^3 exhibited excellent stability after irradiation to fast neutron fluences up to 12.2×10^{21} n/cm^2 $(E > 0.18\ MeV)_{HTGR}$. BISO coated fertile particles also exhibited excellent irradiation performance with OPyC coating densities in the range of 1.73 to 1.94 g/cm^3.

For the fissile and fertile particle designs tested, the OPyC coating desposition rate had a greater influence on particle survival than OPyC coating density or thickness. Low coating deposition rates have been directly correlated with high PyC anisotropy (Ref. 9-18). OPyC coatings with high anisotropy have been shown to be more unstable dimensionally and hence exhibit higher failure than isotropic OPyC coatings (Refs. 9-5, 9-14, and 9-19). No OPyC coating failure was observed in TRISO fissile particles with OPyC coatings deposited at rates greater than 1.5 μm/min. As the deposition rate decreased below 1.5 μm/min, the OPyC coating failure levels increased significantly. The onset of failure shifted to a lower coating rate as the OPyC coating density decreased. BISO coated fertile particles also exhibited similar irradiation performance as a function of OPyC coating deposition rate. However, the critical coating rate where increased failure was observed was 4.0 μm/min instead of 1.5 μm/min as in the small-diameter TRISO coated fissile particles. These data are consistent with previous irradiation results which indicate that the critical coating rate for failure increases as the particle size increases (Ref. 9-14).

Fuel particles with severely faceted coatings, nonround fuel kernels, or interrupted SiC layers exhibited higher failure rates than similarly designed fuel particles that did not have these attributes. BISO coated fertile particles with OPyC coatings deposited from acetylene-propylene (mixed gas) exhibited irradiation performance comparable to similarly designed particles with OPyC coatings deposited from propylene. Deposition of OPyC coatings from mixed gas is considered necessary in order to fabricate coated particles on a scale envisioned for the LHTGR.

Summary

The postirradiation examination results obtained to date for P13R and P13S are summarized as follows:

1. Bonded fuel rods were successfully irradiated to fast neutron exposures of 12.5×10^{21} n/cm^2 (E > 0.18 MeV)$_{HTGR}$, which is 56% beyond the LHTGR peak design fast neutron fluence of 8.0×10^{21} n/cm^2.

2. Thermal cycling to high temperatures during operation did not adversely affect fuel rod integrity.

3. Postirradiation integrity of fuel rods fired at 1500°C or in a nitrogen atmosphere was comparable to that of fuel rods fired under the LHTGR reference conditions of 1800°C in an argon atmosphere. These results contribute to the qualification of a lower firing temperature.

4. The irradiation performance of particle batches with coating parameters that meet LHTGR reference design requirements was excellent. No particle failure was observed in UC_2 TRISO particles and a low failure level of 0.15% was observed in ThO_2 BISO particles after irradiation to fast neutron fluences up to 12.2×10^{21} n/cm^2 (E > 0.18 MeV)$_{HTGR}$, which is 52% beyond the LHTGR peak design fast neutron exposure.

5. For the fissile and fertile particle designs tested, the OPyC coating deposition rate or anisotropy had a greater influence on particle survival than OPyC coating density or thickness.

CAPSULE P13T

Capsule P13T is the ninth in a GA series of LHTGR fuel irradiation tests conducted under the HTGR Fuels and Core Development Program. P13T is a large-diameter capsule containing two cells in which reference

fresh and recycle fuels will be irradiated to peak HTGR temperature-fluence conditions.

Capsule P13T began irradiation in the Oak Ridge Research (ORR) reactor on May 11, 1975. No major problems occurred during insertion. The initial temperatures were close to design values. The initial fission gas release was $\leq 1 \times 10^{-6}$ R/B (Kr-85m) for the two cells. The capsule is scheduled to be removed from the reactor in July 1976.

CAPSULES P13U AND P13V

The "Irradiation Test Plan for Capsules P13U and P13V" was issued April 11, 1975 and the request for approval-in-principle was granted by RRD. The capsules are scheduled for insertion into the GETR on November 27, 1975.

Objectives

One of the major objectives of the P13U and P13V irradiation tests is to evaluate the weak acid resin (WAR) $U{\cdot}C_3{\cdot}O_{0.5}$ TRISO particle as the recycle fissile particle and as a candidate for the fresh fuel fissile particle. Results from these tests will be used in support of performance prediction models. In addition, in-pile fission gas release results will guide capsule P13W planning. These results together with early PIE results will influence fuel manufacturing specifications for capsules P13X and P13Y, which are intended to serve as the final qualification tests for the fresh fuel system used in initial LHTGR cores.

The performance of the WAR fissile particle will be evaluated at steady-state temperatures of 1100°, 1300°, and 1500°C (Fig. 9-48). These performance data will be compared with data for dense melted UC_2 fuel irradiated under similar conditions in capsules P13R and P13S. A direct comparative test of WAR and dense UC_2 particles will be conducted in cell 2 of P13U and P13V at 1100°C to peak fast fluence and burnup. Cell 2 of P13U

will contain fuel rods fabricated with VSM UC_2 fissile/ThO_2 BISO particles and the companion cell in capsule P13V will contain WAR TRISO/ThO_2 BISO fuel.

In addition to the steady-state tests, a series of thermal cycling tests will be undertaken. The thermal cycles will simulate the most severe thermal transient to be experienced in the LHTGR during normal load-following conditions. In one set of tests (cell 1 of P13U and P13V), fuel rods made with WAR TRISO/ThO_2 BISO particles will be thermal cycled periodically from their normal operating temperature of 1200° to 1400°C in P13U and to 1600°C in P13V.

Two other cells (3 and 6 of P13V) will also undergo thermal cycling to 1600°C. Cell 3 will contain fuel rods having only ThO_2 BISO particles and cell 6 will contain fuel rods having only WAR TRISO particles. Companion tests will be conducted in capsule P13U, which will oeprate at a constant temperature of 1200°C throughout the irradiation. The purpose of these tests is to determine failure profiles for fissile and fertile particles, a task that cannot be accomplished unambiguously when the two particle types are mixed in the reference fuel rod configuration. These results should complement those obtained in cell 1 as well as provide valuable support to the performance prediction models.

A second objective of the P13U and P13V tests is to use the results in support of generic fuel specifications and fuel performance models, and to provide data for comparison with the performance of UC_2 VSM TRISO fuel.

Capsules P13U and P13V will contain the first tests at 1500°C, as well as the first thermal cycling tests, of fuel rods that have been cured-in-place and have not been removed from the graphite body prior to irradiation. The objectives of these tests are to characterize fuel rod integrity, rod-block interactions, and fuel rod dimensional change as a function of the irradiation conditions and rod variables (i.e. shim type and volume loading, matrix macroporosity and microporosity, etc.).

The series of unbonded particle tests included in cell 4 of P13U and P13V will provide additional data on reference particle performance. Samples will be selected to provide input for the fuel performance models and to aid in the evaluation of coated particle specification limits.

Because of the potential effects of the thermal and neutronic environment, it is necessary to obtain thermocouple decalibration data for conditions matching those of the sample tungsten/rhenium (W/Re) thermocouples. The objective of the thermocouple cell tests is to operate W/Re thermocouples in a thermal environment that is accurately characterized by non-decalibrating chromel-alumel (C/A) thermocouples and similar to that experienced by the majority of the fuel thermocouples in these capsules. The data will be used to empirically correct for W/Re thermocouple drift during irradiation of P13U and P13V. Thermocouples will operate over the range 900° to 1500°C at high and low neutron flux positions. One thermocouple cell will be thermal cycled to provide the decalibrating data needed for this extremely important part of the test. The cells used to accomplish this task will be of simple design, which lends itself to accurate and reliable thermal analysis for prediction of temperatures above the operating range of the non-decalibrating C/A thermocouple.

Experiment Description

Capsules P13U and P13V will be 31.75 mm in diameter and will each contain five fuel rod cells and one unbonded particle cell. The capsules are nearly identical; the only difference is that P13U will contain two cells for thermocouple experiments while P13V will contain one thermocouple cell. The space occupied by cell 2 in P13V will be divided into two shorter cells in capsule P13U, one for fuel rods and one for thermocouples. Figure 9-48 shows the layout for these capsules and the temperature-fluence conditions expected for each cell.

A total of 38 fuel rods 12.5 mm in diameter by 19.0 mm long will be irradiated in P13U and P13V. Cells 1 and 5 of P13U and P13V and cell 2 of P13V will be 119 mm long and will contain H-451 graphite bodies 24 mm in

diameter and 105 mm long. Each of these five cells will house five fuel rods. Cell 2 of P13U and cell 6 of P13U and P13V will be 79 mm long and will contain graphite bodies 24 mm in diameter by 64.7 mm long, which hold three fuel rods each. The two remaining fuel rod cells (cell 3 of P13U and P13V) are the shortest and contain only two fuel rods each; in cell 3 the graphite crucible will be 44.5 mm long.

The loose particle cells in P13U and P13V (cell 4) will contain approximately 6000 particles each: 2000 or 3000 fissile particles and 3000 or 4000 fertile particles. The particles will be irradiated in disc-shaped graphite holders (24 mm in diameter by 1.8 mm thick). These holders will contain ∿250 drilled holes in which individual particles will be placed.

The majority of the fissile and fertile particle batches used in these irradiations will be within the range of fuel product specifications envisioned for the LHTGR. Emphasis will be placed on testing WAR $U{\cdot}C_3{\cdot}O_{0.5}$ TRISO particle material from 2 to 4 different batches in fuel rod and unbonded particle samples. The WAR kernel variables will be different kernel sources, nonround kernels, and large-diameter kernels. Two of the WAR TRISO batches will be designed to have a thick SiC layer to quantify the beneficial effects the increased thickness has on particle performance. Other coating variables will be misshapen WAR TRISO particles, faceted ThO_2 BISO particles, and oriented porosity in the outer pyrocarbon layer of the ThO_2 BISO particles. Some of the batches will be density and size separated for the loose particle trays. Samples of dense melted UC_2 TRISO particles will be included for comparative purposes.

In addition to the above coated particle variables, fuel rod variables will include shim volume loading and shim type. Three near-isotropic graphite shim particles will be studied: Great Lakes Carbon Company H-451, Union Carbide TS-1240, and PoCo. The H-451 and TS-1240 shim will be impregnated with a 95% furfuryl alcohol base material.

All fuel rods tested in the capsules will be cured-in-place and will not be removed from the H-451 graphite crucibles prior to irradiation.

Several duplicate fuel bodies of each type will be prepared for preirradiation characterization studies, as well as for historical samples. Fission gas release measurements will be made on each capsule body prior to accepting it for use in the irradiation test.

Fuel and graphite temperatures will be monitored using C/A and W/Re thermocouples. Fifteen of the 38 fuel rods will be fabricated with central thermocouple holes for measuring the centerline temperatures during irradiation.

Three thermocouple cells will be included in these capsules. Capsule P13U will contain two of these experiments, one near the peak neutron flux position (TC I) and one at the lowest neutron flux position (TC II). Capsule P13V will contain a companion TC II test, which will be thermal cycled peridically to determine the effect of cycling on thermocouple decalibration.

The design of each thermocouple cell will be identical and, as currently envisioned, three temperature zones will be established to determine the effect of temperature on decalibration. Each cell will have a central slug of tungsten (or other suitable material) of proper mass to heat the central thermocouples to the design temperature. In P13U the tungsten gamma heater will operate at 1500°C and will be surrounded by two concentric graphite rings spaced to give temperatures of ∿1100° and ∿900°C (see Fig. 9-48). The temperature profile will be maintained by changing the gas composition in the gaps as the gamma flux profile changes during each reactor cycle. Two W/Re thermocouples will be placed in the 1500°C section and one in each of the graphite rings. A C/A thermocouple will be placed adjacent to the W/Re thermocouples in the graphite to establish a reference control point for the temperature throughout the irradiation since these thermocouples have been shown not to undergo decalibration.

The thermocouple cell in P13V will be thermal cycled and therefore will have a slightly different temperature profile than its companion test in P13U to prevent melting of the C/A thermocouples. The temperatures will

be reduced to 1200°, 900°, and 600°C from the center outward with the C/A thermocouples located in the 900° and 600°C sections only. The peak temperature during thermal cycling will be 1600°C, and the cycle profile will essentially duplicate that of cell 1 of P13V.

RECYCLE TEST ELEMENTS RTE-2 AND RTE-4

Sample Description

RTE-2 and RTE-4 are identical recycle test elements to test reference and alternate HTGR fuels and to provide irradiated fuel for head-end reprocessing studies at ORNL. Both of these recycle test elements were part of Phase I of the Peach Bottom Core 2 irradiation. Irradiation exposures were 3.2×10^{21} n/cm^2 ($E \geq 0.18$ MeV) and 701 EFPD for RTE-2 and 2.2×10^{21} n/cm^2 ($E \geq 0.18$ MeV) and 384 EFPD for RTE-4.

The PIE of these two test elements is being done at ORNL. Two rods from each test element were sent to GA on August 22, 1975 for TRIGA activation analysis of fission gas release. Stereo-examination and metallography were also performed to substantiate the fission gas release measurements and to fully characterize the fuel performance.

The rods examined at GA and their estimated peak fast fluences and temperatures (preliminary data) are given in Table 9-16.

The particles used in these rods were a UC_2 TRISO/ThC_2 BISO blend; the particle attritubes are listed in Table 9-17. The matrix contained ∿30% natural-flake graphite and ∿70% coal tar pitch. All of these rods were manufactured at GA by the hot-injection process and then cured-in-place. The rods were not subjected to the HCl heat treatment.

TABLE 9-16
FLUENCE AND TEMPERATURE OF RODS EXAMINED AT GA

Test Element	Rod No.[a]	Peak Temp (°C)	Peak Fast Fluence ($\times 10^{21}$ n/cm^2) (E $\geq$ 0.18 MeV)
RTE-2	6-1-2	1090	1.9
RTE-2	6-1-3	1120	1.7
RTE-4	4-7-3	1240	2.1
RTE-4	4-4-3	1240	2.1

[a] Body-hole-position.

TABLE 9-17
RTE-2 AND RTE-4 FUEL PARTICLE SPECIFICATIONS

Attribute	Particle Batch	
	4000-307	4000-226
Kernel type	UC_2	ThC_2
Kernel mean diameter, μm	99	356
Coating type	TRISO	BISO
Buffer mean thickness, μm	51	58
IPyC mean thickness, μm	21	--
SiC mean thickness, μm	20	--
SiC mean density, g/cm^3	3.21	--
OPyC mean thickness, μm	32	71
OPyC mean density, g/cm^3	1.73	1.88
OPyC mean BAF	1.03	1.06

Fuel Rod Examination

Visual Examination

The four rods were examined and photographed with the Kollmorgan periscope upon unloading from the ORNL transfer containers. Stereophotographs of these rods are shown in Figs. 9-49 through 9-52. The surfaces of all the rods looked good except for spalling at the ends. Rod 4-4-3 from RTE-4 was broken into three major sections and rod 4-7-3 had a large chip broken off one end. This damage was incurred during shipment from ORNL to GA.

Fission Gas Release Measurements

Three of the rods were activated in TRIGA for fission gas release measurements. Rod 4-4-3 from RTE-4 was not included because of the rod failure. The results for these measurements are given in Table 9-18.

TABLE 9-18
FISSION GAS RELEASE MEASUREMENTS

Test Element	Rod	R/B
RTE-4	4-7-3	2.07×10^{-4}
RTE-2	6-1-3	1.46×10^{-5}
RTE-2	6-1-2	8.98×10^{-6}

In all cases the R/B was low, which indicates a low fissile failure if it is assumed that the fertile particles do not contribute to the R/B measurement because of low burnup.

Metallographic Examination

Rods 6-1-3 from RTE-2 and 4-7-3 from RTE-4 were examined metallographically. Representative photomicrographs of the cross sections and

matrix are shown in Figs. 9-53 and 9-54. The fuel particle failures are summarized in Table 9-19.

Figure 9-55 is a representative photomicrograph of the UC_2 TRISO/ThC_2 BISO particles in rod 6-1-3 from RTE-2. The 85 ThC_2 particles that were examined looked good and there were no observed failures or kernel migration. The 339 fissile UC_2 particles that were examined all showed buffer densification and debonding, and in approximately 10% of the observed particles there was IPyC debonding. There were no cases of kernel migration in the UC_2 kernels.

TRISO UC_2 OPyC failure in rod 6-1-3 was ∿5%. Half of the failures observed were similar to that shown in Fig. 9-56 and one particle showed OPyC failure that appeared to be caused by a matrix-coating interaction (Fig. 9-57). The other OPyC failures were due to attack by external contamination, which is discussed below. The OPyC coatings also had cases of extensive soot deposits in ∿20% of the particles examined; a representative case is shown in Fig. 9-58.

No pressure vessel failure of the SiC was observed. There was ∿1.5% SiC failure due to attack by external contamination in the fuel rod. Figure 9-59 shows a typical case of this attack. All the cases were in a localized region near the matrix end cap portion of the rod. The presence of this contamination occurred because these rods were not subjected to a HCl heat treatment before irradiation.

Metallic fission product concentrations were obvious in the OPyC on the cool side of ∿10% of the fissile particles. A few mild cases of SiC attack were observed; an example is shown in Fig. 9-56. This attack only dimpled the inside SiC surface and did not penetrate more than 5 μm.

Rod 4-7-3 from RTE-4 contained the same UC_2 TRISO/ThC_2 BISO blend as rod 6-1-3 from RTE-2 but was exposed to a slightly higher irradiation temperature and lower fast fluence. The appearance of the fuel in this rod

TABLE 9-19
FUEL FAILURE SUMMARY

Failure Mode	Failure[a] (%)			
	Rod 6-1-3 RTE-2		Rod 4-7-3 RTE-4	
	Fissile	Fertile	Fissile	Fertile
OPyC failure				
Matrix-coating interaction	0.3	0	0	0
Pressure vessel	2.4	0	0	0
External contamination	2.6	0	1.8	0
Production failure	0	0	0.4	0.7
SiC failure				
Pressure vessel	0	--	0	--
External contamination	1.5	--	1.8	--
Production failure	0	--	0.4	--
Fuel particles examined	339	85	231	288

[a]From metallographic examination.

was generally good, as depicted by the UC_2 TRISO/ThC_2 BISO pair in Fig. 9-60. The 288 BISO ThC_2 particles that were examined were all intact except for several cases of production failures. Figure 9-61 shows a fissile and a fertile particle that were broken during fuel rod injection. There were no cases of kernel migration in either the ThC_2 BISO particles or the UC_2 TRISO particles.

The 231 fissile UC_2 particles that were examined all showed buffer densification and debonding. Approximately 18% of the UC_2 particles showed IPyC debonding. Soot deposits in the OPyC coatings were also observed in this rod similar to those shown in Fig. 9-58 from rod 6-1-3, but there were no OPyC failures except for external contamination attack and the production failure shown in Fig. 9-61. The area of this attack was in the matrix end cap portion of the rod; a representative case is shown in Fig. 9-62. This type of attack caused SiC failure in four particles, which accounts for 1.8% of the fissile particles examined. Metallic fission products were observed in 13.7% of the particles and mild SiC attack was obvious in 1.7% of the UC_2 particles examined (Fig. 9-63).

Discussion and Results

The results of the PIE of the fuel rods from RTE-2 and RTE-4 were consistent with results reported by ORNL (Refs. 9-20, 9-21). The only new observation was the presence of the external contamination in the fuel rods from both RTE-2 and RTE-4, which caused SiC failure.

A summary of the major conclusions and observations is as follows:

1. Fission gas release and metallographic measurements showed low total particle failure in both the RTE-2 and RTE-4 fuel rods.

2. Kernel migration was not present in either the RTE-2 or RTE-4 fuel rods examined metallographically. This is consistent with the current design predictions (Ref. 9-7).

3. Limited SiC attack by metallic fission products was present in both the RTE-2 rod, which was irradiated at 1100°C for 701 EFPD, and the RTE-4 rod, which was irradiated at 1230°C for 384 EFPD. SiC attack at these temperatures has not been observed before except in capsule P13P where limited SiC attack was reported at 1320°C (Ref. 9-22). The observation of this attack at these relatively low temperatures will aid in the characterization of the kinetics of the metallic fission product attack.

4. External contamination attack of the fissile fuel particles was present in both the RTE-2 and RTE-4 fuel rods. This phenomenon is important in showing the need for the HCl heat treatment, which eliminates this problem.

FUEL TEST ELEMENT FTE-15

Introduction

Fuel test element FTE-15 began irradiation in the Peach Bottom reactor on July 6, 1972. FTE-15 was irradiated in the A03-03 position for 315.8 EFPD of Core 2 operation and then moved to core position A14-08 for 196.1 EFPD of Core 2 operation, making a total irradiation period of 511.9 EFPD. End-of-life occurred at 897.3 EFPD of Core 2 operation on October 31, 1974. The average radial power factor over the residence time of FTE-15 in Core 2 was 0.974, and energy production was 7.3×10^4 kW-days. The test element was removed from the core, gamma scanned, and stored on December 9, 1974. The Hallam cask containing FTE-15 left Peach Bottom on January 20, 1975 and arrived at GA on January 24, 1975. Following delayed neutron studies on the cask, FTE-15 was unloaded into the high-level cell on January 29, 1975. Disassembly of the element began on March 26, 1975 and was completed on April 21, 1975.

Disassembly Operations

All disassembly operations were performed according to 278-PB-9, "Postirradiation Examination for Peach Bottom Test Element FTE-15." The

helium-filled aluminum canister containing FTE-15 was removed from the Hallam cask and injected into the high-level cell without incident. The canister was girdle-cut approximately 3/16 in. deep 4 ft from the top end of the canister and the piece was removed. The element was pulled out until clear of the canister, thereby exposing the thermocouple contacts. At this point, the identity of the element was checked and photographed as shown in Fig. 9-64. A composite photograph of the total element is shown in Fig. 9-65. Thermocouple measurements were then taken and recorded. No reading could be obtained from the W/Re thermocouple, indicating an open circuit and failure of the thermocouple. Only the total loop resistance was obtained from the C/A thermocouple. This measurement compared favorably with the preirradiation measurement (Table 9-20). Leg measurements could not be obtained, possibly due to dislodging of the thermocouple from the sheathing resulting in an isolated junction.

For sectioning, the fuel element was supported horizontally by a series of V-rollers, which facilitated horizontal and rotational movement. A special extension drill was inserted through the purge gas inlet hole in the upper reflector and a hole was drilled through the porous graphite plug. The fuel bodies were then seated against the bottom connector by using a push rod through this hole and applying force. While the bodies were held down, the upper reflector was removed by plunge cutting through the sleeve at a point about 2 in. below the sleeve-reflector joint. This section was stored for later gamma scanning. The sleeve was then girdle cut $\sim$0.37 in. deep at a point $\sim$25 in. from the bottom of the element without hitting the lower reflector. The top section was pulled away from the bottom section, exposing the thermocouples. The bottom section was plunge cut 2 in. from the bottom, and the total intact thermocouples were removed and stored for neutron welding studies. During this operation the lower reflector and trap were accidentally tilted and some charcoal particles were lost. The bottom reflector and trap section was stored for later gamma scanning. Figures 9-66 and 9-67 show the top and bottom view of the cut. No fuel particles were found on either end of the cut.

TABLE 9-20
THERMOCOUPLE RESISTANCE DATA

Thermocouple Type (Accuracy ±20 ohms)	+ to Ground Circuit (ohms)			- to Ground Circuit (ohms)			Loop (ohms)			Remarks
	Pre-irrad.	Post-irrad.	Δ ohms	Pre-irrad.	Post-irrad.	Δ ohms	Pre-irrad.	Post-irrad.	Δ ohms	
Thermocouple A (ARI S/N 38246) W-3% Re/W-25% Re	3.8	--	--	9.6	--	--	13.1	--	--	No reading, open circuit
Thermocouple B (ARI S/N 22183)	29.7	--	--	13.3	--	--	42.5	42.0	-0.5	

The fuel bodes were subsequently removed from the sleeve by inserting a push rod into the upper opening, holding the sleeve, and applying a force. The sleeve was then cut and inside diameter measurements were performed according to the PIE plan. Each fuel body was carefully examined externally, and graphite integrity was assessed (Figs. 9-68 through 9-70). Following visual inspection and dimensional measurements (Tables 9-21 through 9-23), the fuel bodies were placed in a special holding fixture to facilitate the removal of center samples. A hole was drilled through the bottom sample hole plug and a push rod was inserted. The upper sample hole plug was then unscrewed and the distance from the top of the spine samples to the edge of the holes was measured. These measurements are compared with preirradiation measurements in Table 9-24. Changes are in the range expected for H-327 graphite. For this average temperature and fluence, a shrinkage of ~0.8% is expected. The spine samples were pushed out one at a time, identified, and placed in a pan. These operations were carried out over a special pan required to catch any loose fuel particles from the drilled holes. However, none were found. No problems were encountered during the removal of spine samples, although one tensile sample from body 1 was listed as 11959-19 in the as-built drawing and was actually identified as 11952-19. The activity of each sample was measured (Table 9-25). All spine samples were distributed according to the PIE plan and the flux dosimeters from the four tensile samples were removed. The spine samples are described in Table 9-25.

Upon discharge of the spine samples, holes were drilled in the bottom of the fuel bodies to enable the fuel to be pushed out using the special discharge fixture. Figure 9-71 shows the typical setup. The graphite plugs capping the fuel holes were easily removed, and the distance from the top of the fuel rods to the edge of the fuel holes was measured. These measurements, as well as fuel stack lengths, are compared with preirradiation measurements in Table 9-26.

The fuel bodies were then placed in the mechanical push device with Dillon load gauges ranging from 0 to 250 lb, and the force needed to

TABLE 9-21
FUEL BODY DATA FOR FTE-15 FUEL BODY 1 (BOTTOM)

	Preirrad. X_1	Postirrad. X_2	$\Delta X = X_2 - X_1$	$\Delta X/X_1$ (%)
Weight of loaded body, g (accuracy: ±1 g)				
Total	5405.5	5407.25	+1.75	+0.032±0.02
Sum of components	5400.376	-	-	
Length of body, in. (accuracy: ±0.001 in.)				
0°	31.105	31.0305	-0.0745	-0.24
90°	NA	31.0355	-	-
Average	31.105	31.0330	-0.0745	-0.24±0.003
Outside diameter, in. (accuracy: ±0.001 in.)				
Top				
Across holes 1 and 4	2.7400	2.7370	-0.0030	-0.11
Across holes 3 and 6	2.7395	2.7360	-0.0035	-0.13
Across holes 2 and 5	2.7400	2.7380	-0.0020	-0.07
Average	2.7398	2.7370	-0.0028	-0.10±0.04
Center				
Across holes 1 and 4	2.7398	2.7370	-0.0028	-0.10
Across holes 3 and 6	2.7395	2.7370	-0.0025	-0.09
Across holes 2 and 5	2.7400	2.7380	-0.0020	-0.07
Average	2.7398	2.7373	-0.0024	-0.09±0.04
Bottom				
Across holes 1 and 4	2.7388	2.7380	-0.0008	-0.03
Across holes 3 and 6	2.7388	2.7380	-0.0008	-0.03
Across holes 2 and 5	2.7400	2.7370	-0.0030	-0.11
Average	2.7392	2.7377	-0.0015	-0.06±0.04
Average	2.7396	2.7373	-0.0023	-0.08±0.04
Inside diameter, in. (between holes 3 and 6) (accuracy: ±0.001 in.)				
Top	0.8084	0.8068	-0.0016	-0.20
Center	0.8090	-		
Bottom	0.8090	-		
Average	0.8080	0.8068	-0.0016	-0.20±0.12
Fuel hole diameter, in. (accuracy: ±0.001 in.)				
Hole No. 1	0.6260	0.62460	-0.0014	-0.22
2	0.6256	0.62502	-0.0006	-0.10
3	0.6257	0.62290	-0.0028	-0.45
4	0.6255	0.62420	-0.0013	-0.21
5	0.6255	0.62435	-0.0012	-0.19
6	0.6258	0.62510	-0.0007	-0.11
Average	0.6257	0.62440	-0.00133	-0.21±0.16

TABLE 9-22
FUEL BODY DATA FOR FTE-15 BODY 2 (CENTER)

	Preirrad. X_1	Postirrad. X_2	$\Delta X = X_2 - X_1$	$\Delta X/X_1$ (%)
Weight of loaded body, g (accuracy: ±1 g)				
Total	5191.5	5197.25	5.75	+0.11±0.02
Sum of components	5191.552			
Length of body, in. (accuracy: ±0.001 in.)				
0°	31.105	30.9465	-0.1585	-0.51
90°	NA	30.9520	-	
Average	31.105	30.9465	-0.1585	-0.51±0.003
Outside diameter, in. (accuracy: ±0.001 in.)				
Top				
Across holes 1 and 4	2.7397	2.7380	-0.0017	-0.06
Across holes 2 and 5	2.7400	2.7380	-0.0020	-0.07
Across holes 3 and 6	2.7399	2.7370	-0.0029	-0.11
Average	2.7399	2.7377	-0.0022	-0.08±0.04
∿1/4 down				
Across holes 1 and 4	2.724	2.7215	-0.0025	-0.09
Across holes 2 and 5	2.724	2.7200	-0.0040	-0.15
Across holes 3 and 6	2.724	2.7180	-0.0060	-0.22
Average	2.724	2.7198	-0.0042	-0.15±0.04
Center				
Across holes 1 and 4	2.704	2.6960	-0.0080	-0.30
Across holes 2 and 5	2.703	2.6940	-0.0090	-0.33
Across holes 3 and 6	2.704	2.6950	-0.0090	-0.33
Average	2.703	2.6950	-0.0087	-0.32±0.04
∿3/4 down				
Across holes 1 and 4	2.7290	2.7290	0	0
Across holes 2 and 5	2.7286	2.7260	-0.0026	-0.10
Across holes 3 and 6	2.7288	2.7280	-0.0008	-0.03
Average	2.7288	2.7277	-0.0011	-0.04±0.04
Average	2.7241	2.7200	-0.0040	-0.15±0.04
Inside diameter, in. (between holes 1 and 4) (accuracy: ±0.001 in.)				
Top	0.8070	0.8058	-0.0012	-0.15
Center	0.8070	-		
Bottom	0.8065	-		
Average	0.8068	0.8058	-0.0012	-0.15±0.12
Fuel hole diameter, in. (accuracy: ±0.001 in.)				
Hole No. 1	0.625	0.6243	-0.0007	-0.11
2	0.625	0.6244	-0.0006	-0.09
3	0.625	0.6246	-0.0004	-0.06
4	0.625	0.6248	-0.0002	-0.03
5	0.625	0.6249	-0.0001	-0.02
6	0.636[a]	0.6348	-0.0012	-0.19
Average	0.627	0.6263	-0.00053	-0.08±0.16

[a] Increased during assembly - reamed to 0.636.

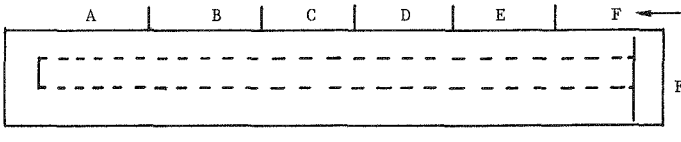

Hole							
6	0.6359	0.6359	0.636	0.6359	0.639	0.642	Average = 0.63695

TABLE 9-23
FUEL BODY DATA FOR FTE-15 BODY 3 (TOP)

	Preirrad. X_1	Postirrad. X_2	$\Delta X = X_2 - X_1$	$\Delta X/X_1$ (%)
Weight of loaded body, g (accuracy: ±1 g)				
Total	5099.7	5098.00	-1.7	-0.03±0.02
Sum of components	5090.225			
Length of body, in. (accuracy: ±0.001 in.)				
0°	31.108	30.9830	-0.125	-0.40
90°	NA	30.9825	-	-
Average	31.108	30.9830	-0.125	-0.40±0.003
Outside diameter, in. (accuracy: ±0.001 in.)				
Across holes 1 and 4	2.7389	2.7360	-0.0029	-0.11
Across holes 2 and 5	2.7390	2.73125	-0.00775	-0.28
Across holes 3 and 6	2.7390	2.7380	-0.0010	-0.04
Average	2.73897	2.7351	-0.0039	-0.14±0.04
Inside diameter, in. (between holes 1 and 4) (accuracy: ±0.001 in.)				
Top	0.806	0.8054	-0.0006	-0.07
Center	0.806	-	-	-
Bottom	0.806	-	-	-
Average	0.806	0.8054	-0.0006	-0.07±0.12
Fuel hole diameter, in. (accuracy: ±0.001 in.)				
Fuel Hole No. 1	0.62408	0.6252	+0.00112	+0.18
2	0.62406	0.6250	+0.00094	+0.15
3	0.625	0.6250	0	0
4	0.625	0.6250	0	0
5	0.631(a)	0.6361	+0.0051	+0.81
6	0.625	0.6250	0	0
Average	0.62569	0.62688	+0.00119	+0.19±0.16

(a) Increased during assembly - reamed to 0.631.

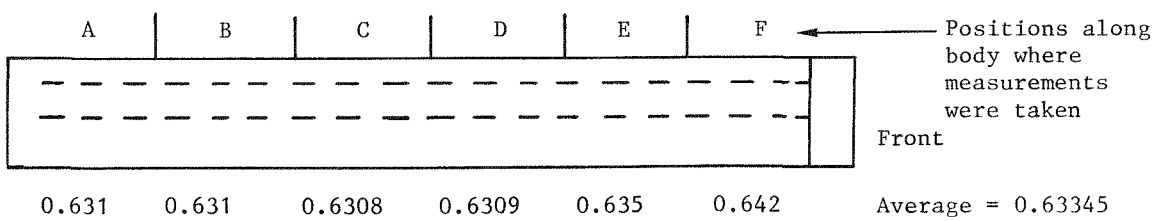

TABLE 9-24
FTE-15 DISTANCE d (TOP OF SPINE SAMPLE TO EDGE OF HOLE)
(ACCURACY: ±0.001 IN.)

Body No.	Spine Stack Length, L (in.)	Preirrad. d_1 (in.)	Postirrad. d_2 (in.)	Δd (in.)	$\Delta G^{(a)}$ (in.)	$\frac{\Delta d + \Delta G}{L}$ (%)
1	30.192	0.533	0.556	0.023	-0.0745	-0.17
2	29.670	1.055	1.143	0.088	-0.1585	-0.24
3	29.653	1.075	1.102	0.027	-0.125	-0.33

(a) ΔG = length change of graphite fuel body (from Tables 9-21 through 9-23).

TABLE 9-25
SPINE SAMPLES IN FTE-15
(ACCURACY: ±0.001 IN.)

Position	Preirrad. Length (in.)	Preirrad. Weight (g)	Mean Active Core Height[a] (in.)	Sample Type	Ident. No.	Composite Spine Length (in.) Preirrad.	Composite Spine Length (in.) Postirrad.	ΔL/L (%)	Gamma Activity Reading[b]
Bottom									
Body 1									
Δ	0.380								
1	18.849	210.3	8.654	Graphite	10				100 mr - c 50 mr - 1 ft
2	1.188	14.683	18.673	Thermal stability	TS-1-15				∞ - c 16.5r - 1 ft
3	1.250	14.623	19.892	Thermal stability	TS-2-15				∞ - c 16.5r - 1 ft
4	1.250	14.580	21.142	Thermal stability	TS-3-15	30.192	30.154	-0.13±0.003	∞ - c 19.5r - 1 ft
5	6.500	72.35	25.017	Tensile sample	11959-19				5.5 mr - c 500 mr - 1 ft
6	1.155	12.91	28.844	Graphite	8				75 mr - c 25 mr - 1 ft
d[c]	0.533								
Σ	31.105								
Body 2									
Δ	0.380								
1	7.787	87.49	34.228	Graphite	2				50 mr - c 0 - 1 ft
2	1.250	14.650	38.747	Thermal stability	TS-4				∞ - c 20r - 1 ft
3	0.500	5.583	39.622	Pyrocarbon	11953-20				100 mr - c 0 - 1 ft
4	6.50	72.275	43.122	Tensile sample.	11953-22				50 mr - c 0 - 1 ft
5	1.250	14.660	46.997	Thermal stability	TS-5				∞ - c 19.5r - 1 ft
6	0.500	5.529	47.872	Pyrocarbon	11953-19	29.670	29.335	-1.13±0.003	50 mr - c 0 - 1 ft
7	1.500	17.066	48.872	Creep sample	11953-23-4C				200 mr - c 50 mr - 1 ft
8	1.250	14.588	50.247	Thermal stability	TS-6				∞ - c 20r - 1 ft
9	1.500	17.761	51.622	Creep sample	11953-24-9C				100 mr - c 0 - 1 ft
10	1.438	18.478	53.091	Creep sample	11953-25-14C				100 mr -c 0 - 1 ft
11	0.562	5.519	54.091	Pyrocarbon	11953-21				50 mr - c 0 - 1 ft
12	5.633	64.68	57.188	Graphite	4				100 mr - c 0 - 1 ft
d[c]	1.055								
Σ	31.105								
Body 3									
Δ	0.380								
1	4.103	45.77	63.492	Graphite	7				75 mr - c 10 mr - 1 ft
2	0.500	5.578	65.793	Pyrocarbon	11954-20				100 mr - c 0 - 1 ft
3	1.500	18.478	66.793	Creep sample	11954-19-(1K)				50 mr - c 0 - 1 ft
4	1.250	13.988	68.168	Thermal stability	TS-7	29.653	29.427	-0.76±0.003	∞ - c 15r - 1 ft
5	1.250	14.691	69.418	Thermal stability	TS-8				∞ - c 15r - 1 ft
6	1.250	14.608	70.668	Thermal stability	TS-9				∞ - c 15r - 1 ft
7	19.800	224.50	81.193	Graphite	12				100 mr - c 50 mr - 1 ft
d[c]	1.075								
Σ	31.108								
Top									

[a]Active core height starts at 26.00 in. from Ref. 0. Experimental fuel height: specified 26.15 in. and measured 26.215 in. from Ref. 0. Body 1, bottom line, is 1.15 in. under active core height.

[b]Indicates reading distance; c = contact.

[c]Plenum d from Table 9-24.

TABLE 9-26
FTE-15 FUEL STACK LENGTH
(ACCURACY: ±0.001 IN.)

Hole No.	Stack Length, L/(in.) Preirrad.	Stack Length, L/(in.) Postirrad.	ΔL (in.)	ΔL/L (%)	Plenum P[a] (in.) Preirrad.	Plenum P[a] (in.) Postirrad.	ΔP (in.)	$\frac{-\Delta P + \Delta G^{(b)}}{L}$ (%)
Body 1								
1	27.350	26.888	-0.462	-1.689	2.397	2.735	+0.338	-1.508
2	27.358	26.654	-0.704	-2.573	2.375	2.799	+0.424	-1.822
3	27.230	26.680	-0.550	-2.018	2.500	2.793	+0.293	-1.350
4	27.234	26.679	-0.555	-2.037	2.498	2.841	+0.343	-1.535
5	27.261	26.626	-0.635	-2.328	2.488	2.802	+0.314	-1.425
6	27.308	26.629	-0.679	-2.485	2.439	2.774	+0.335	-1.500
Average	27.290	26.693	-0.597	-2.188±0.004	2.449	2.791	+0.341	-1.523±0.004
Body 2								
1	27.355	26.725	-0.630	-2.303	2.463	2.938	+0.475	-2.316
2	27.438	27.230	-0.208	-0.758	2.380	2.568	+0.188	-1.263
3	27.309	26.781	-0.528	-1.933	2.507	2.900	+0.393	-2.019
4	27.468	27.001	-0.467	-1.700	2.347	2.643	+0.296	-1.655
5	27.444	26.771	-0.673	-2.452	2.375	2.592	+0.217	-1.368
6	27.509	27.320	-0.189	-0.687	2.308	2.712	+0.404	-2.045
Average	27.420	26.971	-0.449	-1.637±0.004	2.397	2.726	+0.329	-1.777±0.004
Body 3								
1	27.395	26.814	-0.581	-2.121	2.406	2.621	+0.215	-1.241
2	27.454	27.179	-0.275	-1.002	2.350	2.159	-0.191	+0.240
3	27.321	26.776	-0.545	-1.995	2.483	2.678	+0.195	-1.171
4	27.463	26.936	-0.527	-1.918	2.337	2.561	+0.224	-1.271
5	27.463	26.991	-0.472	-1.719	2.341	2.557	+0.216	-1.242
6	27.491	27.177	-0.314	-1.142	2.305	2.481	+0.176	-1.095
Average	27.431	26.979	-0.452	-1.649±0.004	2.370	2.510	+0.140	-0.963±0.004

[a]Plenum P ≡ distance from top of fuel rod to edge of hole.

[b]ΔG ≡ length change in graphite fuel body (see Tables 9-21 through 9-23).

sustain movement was recorded (Table 9-27). It was noted that in body 2, holes 2, 4, and 5, no compact pushers were found. The fuel rods were pushed onto the trough and visually examined, the stack length was measured (Table 9-25), and distribution of rods was made according to the PIE plan. A large percentage of rods in holes 4 and 5 of body 2 were cracked [(Th, U)O_2 TRISO/ThC_2 BISO and UO_2 TRISO/ThC_2 BISO, respectively]. A summary of the fuel rod particle loadings and the general condition of the rods after removal is presented in Table 9-28. Stereo-examination of several of the cracked rods revealed failed fertile particles. It was postulated that as a result of out-of-specification particle coating batches, hydrolysis occurred in the failed particles and cuased swelling and cracking of the rods. Composite photographs of stacks 4 and 5 (Figs. 9-72 and 9-73, respectively), show 6 out of 11 and 10 out of 11 fuel rods broken or cracked.

The bodies were then sectioned in accordance with 9-74 and photographed (Figs. 9-75 through 9-79). Slices 1-2, 2-3, and 3-2 will be used for autoradiography. Slice 2-2 will be used for a radial Cs profile. Measurements were made of the fuel hole inside diameters for sections 1-3, 2-4, and 3-3 to complete the requirements of Tables 9-21 through 9-23. Sections 1-1, 2-1, and 3-1 will be used for residual stress examinations. All sections were numbered and stored for possible reconstruction for gamma scanning exercises.

Fuel rods 2-2-7, 2-3-7, 2-3-8, 3-2-4, and 3-3-4 and advanced fuel rod samples from FTE-4 (1A2 and 1A4) were gamma scanned using the in-cell gamma scanning equipment and then shipped to ORNL for tentative gamma scanning, burnup, and C-14 analysis. The visual examination of these rods is summarized in Table 9-29. Fission gas release measurements and metallography are planned for adjacent rods in order to determine particle failure.

Fuel Element Sleeve Examination

Photographs of the entire length of the element were taken prior to examination of the element exterior with short-focus binoculars and the

TABLE 9-27
FUEL ROD REMOVAL SUMMARY

Body No.	Hole No.	Force (lb)		Remarks
		Initial	Sustaining	
1	1	34	41	Depth of drilled hole increased after removal of stack 1
	2	34	≈0	
	3	34	≈0	
	4	10.5	≈0	
	5	34	≈0	
	6	22	≈0	
2	1	30	20	
	2	40	30	
	3	30	10	
	4	24	≈0	
	5	54	11	
	6	24	<24	
3	1	32	20	
	2	22	≈0	
	3	11	≈0	
	4	20	10	
	5	60	40	
	6	5	≈0	

TABLE 9-28
SUMMARY OF FUEL ROD VISUAL AND METROLOGY EXAMINATIONS

Body No.	Fuel Rod Shrinkage		Stack	Rod Type	Number Broken[a]
	Minimum	Maximum			
1	-1.0	-3.5	1	(150 μm) UC_2 TRISO/(450 μm)ThC_2 BISO	0
			2		0
			3		0
			4		0
			5		0
			6	(150 μm) UC_2 TRISO/(450 μm)ThC_2 BISO	0
2	+0.4 Swelling	-2.6	1	(200 μm) UC_2 TRISO/(400 μm)ThC_2 BISO	0
			2	(200 μm) UC_2 RRISO/(400 μm)ThC_2 TRISO	2
			3	(200 μm) UO_2 TRISO/(400 μm)ThO_2 BISO	1
			4	(250 μm) $(Th,U)O_2$ TRISO/(450 μm)ThC_2 BISO	6
			5	(150 μm) UO_2 TRISO/(450 μm)ThC_2 BISO	10
			6	(200 μm) UO_2 TRISO/(400 μm)ThO_2 TRISO	0
3	+0.2 Swelling	-2.7	1	(200 μm) UC_2 TRISO/(400 μm)ThC_2 BISO	0
			2	(200 μm) UC_2 TRISO/(400 μm)ThC_2 TRISO	0
			3	(200 μm) UO_2 TRISO/(400 μm)ThO_2 BISO	1
			4	(250 μm) $(Th,U)O_2$ TRISO/(450 μm)ThC_2 BISO	1
			5	(150 μm) UO_2 TRISO/(450 μm)ThC_2 BISO	2
			6	(200 μm) UO_2 TRISO/(400 μm)ThC_2 TRISO	1

[a] Each stack contains 11 rods.

TABLE 9-29
SUMMARY OF VISUAL RESULTS OF FTE-15 RODS SENT TO ORNL[a]

ROD	PARTICLE	COMMENT
3-2-4	UC_2 TRISO/ThC_2 TRISO	Rod cracked in several places. Thirteen particles broken on the surface
3-3-4	UO_2 TRISO/ThO_2 BISO	Six particles broken due to unloading striation on side. Rest of rod looked good.
2-2-7	UC_2 TRISO/ThC_2 TRISO	Eleven particles broken on surface. Numberous cracks through the rod.
2-3-7	UO_2 TRISO/ThO_2 BISO	Fifteen broken particles in unloading striation. Rest of rod looked good.
2-3-8	UO_2 TRISO/ThO_2 BISO	One broken particle on surface. Rod looked good.

[a]Fission gas release measurements and metallography planned at adjacent rods.

in-cell Kollmorgan periscope (see Fig. 9-65). No cracks or abnormalities were found. The overall length of the element and sleeve diameters at various intervals were measured and recorded (Table 9-30). The overall length was determined with a steel rule and confirmed by transversing the length with a saw head whose horizontal movement can be determined within ±1/32 in.

Sleeve outside diameters were determined with calibrated snap-on dial indicator gauges; inside diameters were measured in the hot cell hood after removal of the fuel bodies. The accuracy of the postirradiation diameter measurements was ±0.001 in. For the preirradiation dimensions, only manufactured tolerances, which are two and five times greater, are available.

Fuel Body Examination

After removal from the graphite sleeve, each fuel body was placed on a granite surface plate and examined. Little bowing was observed (<0.034 over 31 in.), except in body 3. However, due to the stepped diameters and the difficulty in making the measurements, further bowing might not have been detected. Each body was photographed and visually inspected at high magnification (Figs. 9-68 through 9-70). No cracks or abnormalities were found. Tables 9-21 through 9-23 present data on the fuel bodies, including dimensional changes in the longitudinal and transverse directions of the fuel bodies. The average values are given in Table 9-31.

All changes were so small they were insignificant. The expected shrinkage in H-327 graphite at temperatures and fluences experienced by FTE-15 are ∿0.8% axially and ∿0.4% radially.

The radial gap can be determined by comparison of the as-measured dimensions of the sleeve and graphite body (Tables 9-21 through 9-23 and Table 9-30). The results are given in Table 9-32.

TABLE 9-30
FTE-15 SLEEVE MEASUREMENTS

	Preirrad. Measurement[a] (in.)	Postirrad. Measurement (in.)	ΔD/D (%)
Overall length of element (including thermocouple sheath) (accuracy: 1/32 in.)	145.655	144.500	0.793 ±0.02
Outer diameter (accuracy: ±0.001 in.)			
At joint to bottom connector	3.485 ±0.005[b]	3.481	-0.11
24 in. above joint		3.484	-0.03
48 in. above joint		3.486	+0.03
72 in. above joint		3.480	-0.14
96 in. above joint		3.482	-0.09
At joint to upper reflector		3.485	0
Average		3.483	-0.06 ±0.14
Inner diameter (accuracy: ±0.001 in.)			
At cut near upper reflector - average I.D.	2.752[c] ±0.002	2.7489	-0.11
At cut near bottom reflector		2.7448	-0.26
At approximate midpoint - average I.D.		2.7449	-0.26
Average		2.7462	-0.21 ±0.07

[a] The sleeves were Quality Assurance examined at the source of supply and found to meet requirements. There is no record of the actual dimensions.

[b] Sleeve O.D. per drawing is 3.485 ±0.005 in.

[c] Sleeve I.D. per drawing is 2.752 ±0.002 in.

TABLE 9-31
AVERAGE DIMENSIONAL CHANGES
(%)

	Length (±0.003)(a)	O.D. (±0.04)(a)	I.D. (±0.12)(a)	Fuel Hole (±0.16)(a)
Top, body 3	-0.40	-0.14	-0.07	+0.19
Center, body 2	-0.51	-0.15	-0.15	-0.08
Bottom, body 1	-0.24	-0.08	-0.20	-0.21

(a)Systematic error.

TABLE 9-32
CALCULATED RADIAL GAPS

	Radial Gap (10^{-3} in.)	
	BOL	EOL
Top, body 3		
∿0.768 in. from top	7	7
Center, body 2		
Top	6	4(a)
∿10 in. from top	14	13(a)
∿Center	24	25(a)
∿24 in. from top	12	9(a)
Bottom, body 1		
Bottom	6	4

(a)Radial gaps are based on only one measurement taken at the center body position on the sleevs

Figure 9-79 shows the outside diameters of the element and the positions at which the gaps were determined. The systematic error in the calculations was ±4 mils; therefore, the gaps remained nearly constant within the error limits.

Figure 9-74 shows the manner in which each of the fuel bodies was sectioned for the purposes of measuring fuel hole diameters and providing samples for autoradiography, radial Cs profiles, and residual stress

examination. Each slice was photographed (Figs. 9-75 through 9-78) and found to contain no internal cracks or abnormalities. Methods for determination of residual stresses are still under development and no results are currently available.

REFERENCES

9-1. Sims, J. R., Jr., "Preirradiation Description of Fuel Materials Branch Samples Contained In Capsules HB-1, HB-3, and HB-5," ERDA Report GA-A13310, General Atomic Company, February 1, 1975.

9-2. Stansfield, O. M., C. B. Scott, and J. Chin, "Kernel Migration in Coated Carbide Fuel Particles," Nucl. Tech. 25, 517 (1975).

9-3. Gulden, T. D., "Carbon Thermal Diffusion in the UC_2-Carbon System," J. Am. Ceram. Soc. 55, 14 (1972).

9-4. Scott, C. B., and O. M. Stansfield, "Stability of Irradiated Coated-Particle Fuels in a Thermal Gradient," Gulf General Atomic Report Gulf-GA-A12081, September 1972.

9-5. "HTGR Fuels and Core Development Program Quarterly Progress Report for the Period Ending August 30, 1974," USAEC Report GA-A13126, General Atomic Company, September 30, 1974.

9-6. Wallace, T. C., et al., "Carbon Diffusion in the Carbides of Uranium," USAEC Report LA-DC-8840, Los Alamos Scientific Laboratory, 1968.

9-7. Smith, C. L., "Fuel Particle Behavior Under Normal and Transient Conditions," USAEC Report GA-A12971 (GA-LTR-15), General Atomic Company, October 1, 1974.

9-8. "HTGR Base Program Quarterly Progress Report for the Period Ending November 30, 1972," USAEC Report Gulf-GA-A12422, Gulf General Atomic Company, January 25, 1973.

9-9. Lindemer, T. B., and H. J. DeNordwall, "An Analysis of Chemical Failure of Coated UO_2 and Other Oxide Fuels in the High-Temperature Gas-Cooled Reactor," USAEC Report ORNL-4926, Oak Ridge National Laboratory, January 1974.

9-10. Lindemer, T. B., and R. A. Olstad, "HTGR Fuel Kernel Migration Data for the Th-U-C-O System as of April 1, 1974," USAEC Report ORNL-TM-4493, Oak Ridge National Laboratory, June 1974.

9-11. Shenoy, A. S., and D. W. McEachern, "HTGR Core Thermal Design Methods and Analysis," General Atomic Company Report GA-A12985 (GA-LTR-17), December 31, 1974.

9-12. Olstad, R. A., et al., "An Irradiation Test of Candidate HTGR Recycle Fuels in the H-1 and H-2 Capsules," USAEC Report ORNL-TM-4397, Oak Ridge National Laboratory, July 1974.

9-13. Shaw, J. G., and W. A. Oates, "Thermomigration of Carbon in Metals," Met. Trans. 2, 2127 (1971).

9-14. Harmon, D. P., and C. B. Scott, "Development and Irradiation Performance of LHTGR Fuel," USAEC Report GA-A13173, General Atomic Company, to be published.

9-15. Scott, C. B., "Postirradiation Examination of Capsules HRB-4, HRB-5, and HRB-6," USAEC Report GA-A13267, General Atomic Company, to be published.

9-16. Young, C. A., and D. P. Harmon, "Preirradiation Report: Fuel Materials for P13R and P13S Irradiation Capsules," USAEC Report GA-A13026, General Atomic Company, November 1974.

9-17. "HTGR Fuels and Core Development Program Quarterly Progress Report for the Period Ending February 28, 1975," ERDA Report GA-A13353, General Atomic Company, March 31, 1975.

9-18. Stevens, D. W., "Optical Anisotropy and Preferred Orientation in Nearly Isotropic Pyrocarbons," General Atomic Report GA-A13307, January 22, 1975.

9-19. Scott, C. B., and D. P. Harmon, "Postirradiation Examination of Capsule F-30," General Atomic Report GA-A13208, April 1, 1975.

9-20. "Monthly Progress Report for the Gas-Cooled Reactor Programs at Oak Ridge National Laboratory," USAEC Report GCR:74-14, Oak Ridge National Laboratory, May 1974, pp. 46-48.

9-21. "Monthly Progress Report for the Gas-Cooled Reactor Programs at Oak Ridge National Laboratory," USAEC Report GCR:74-32, Oak Ridge National Laboratory, October 1974, pp. 77-80.

9-22. "HTGR Base Program Quarterly Progress Report for the Period Ending May 31, 1973," USAEC Report GA-A12599, General Atomic Company, June 29, 1973.

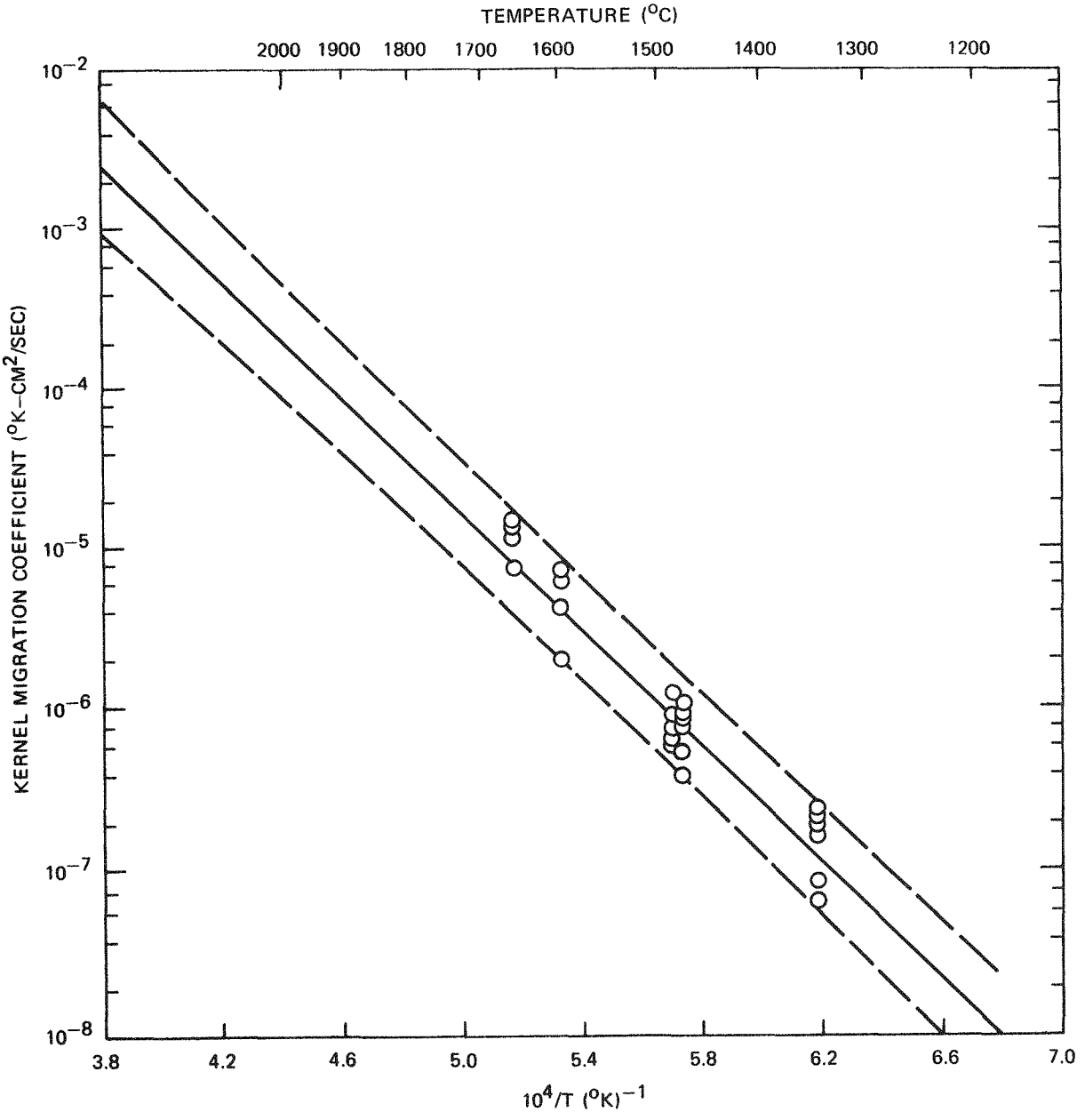

Fig. 9-1. Kernel migration coefficient versus 1/T, TRISO coated dense melted UC_2 fuel particles (experiments 6511 and 6440): (a) 110-μm nominal kernel diameter

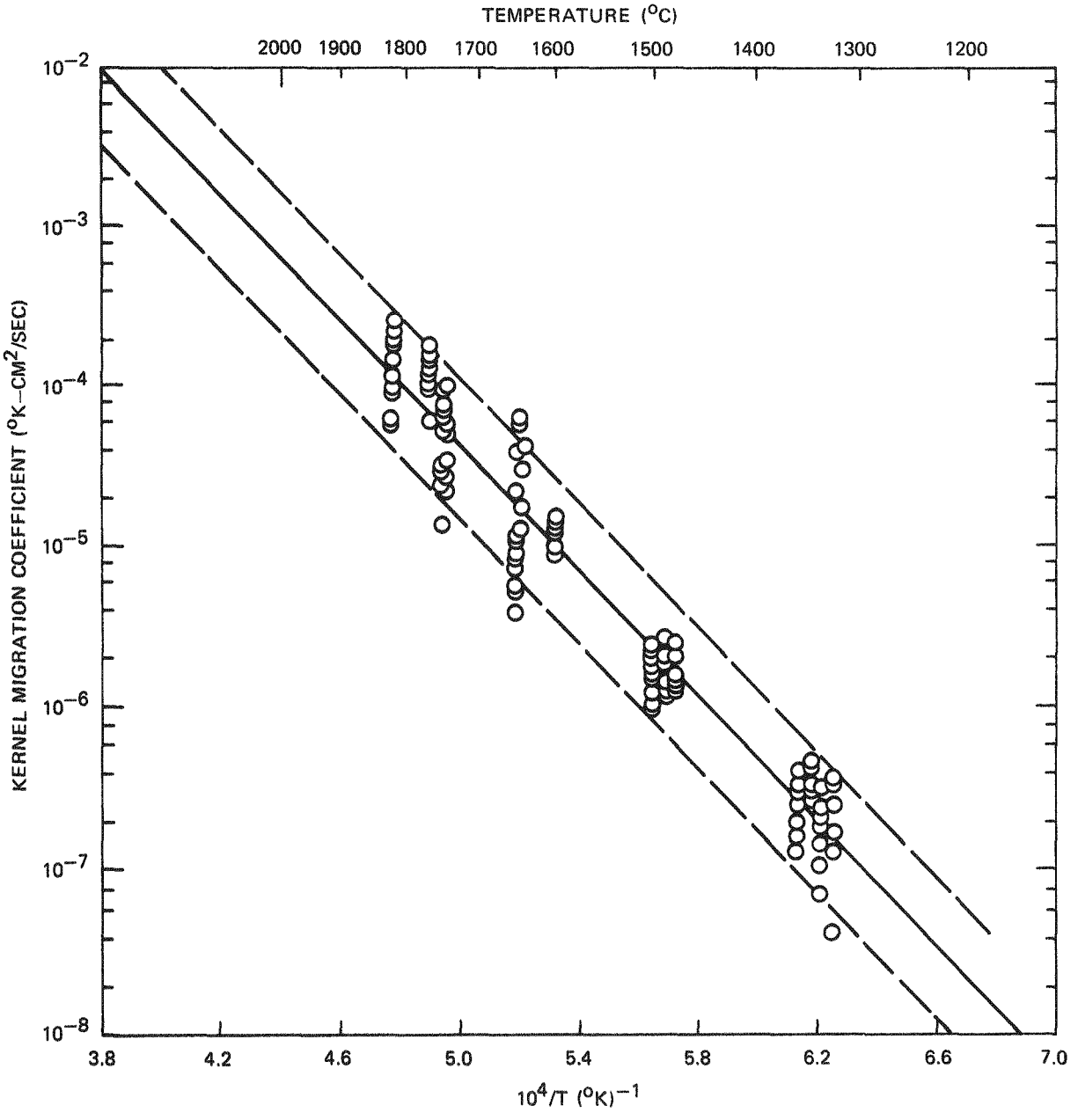

Fig. 9-1. Kernel migration coefficient versus 1/T, TRISO coated dense melted UC_2 fuel particles (experiments 6511 and 6440): (b) 200-μm nominal kernel diameter)

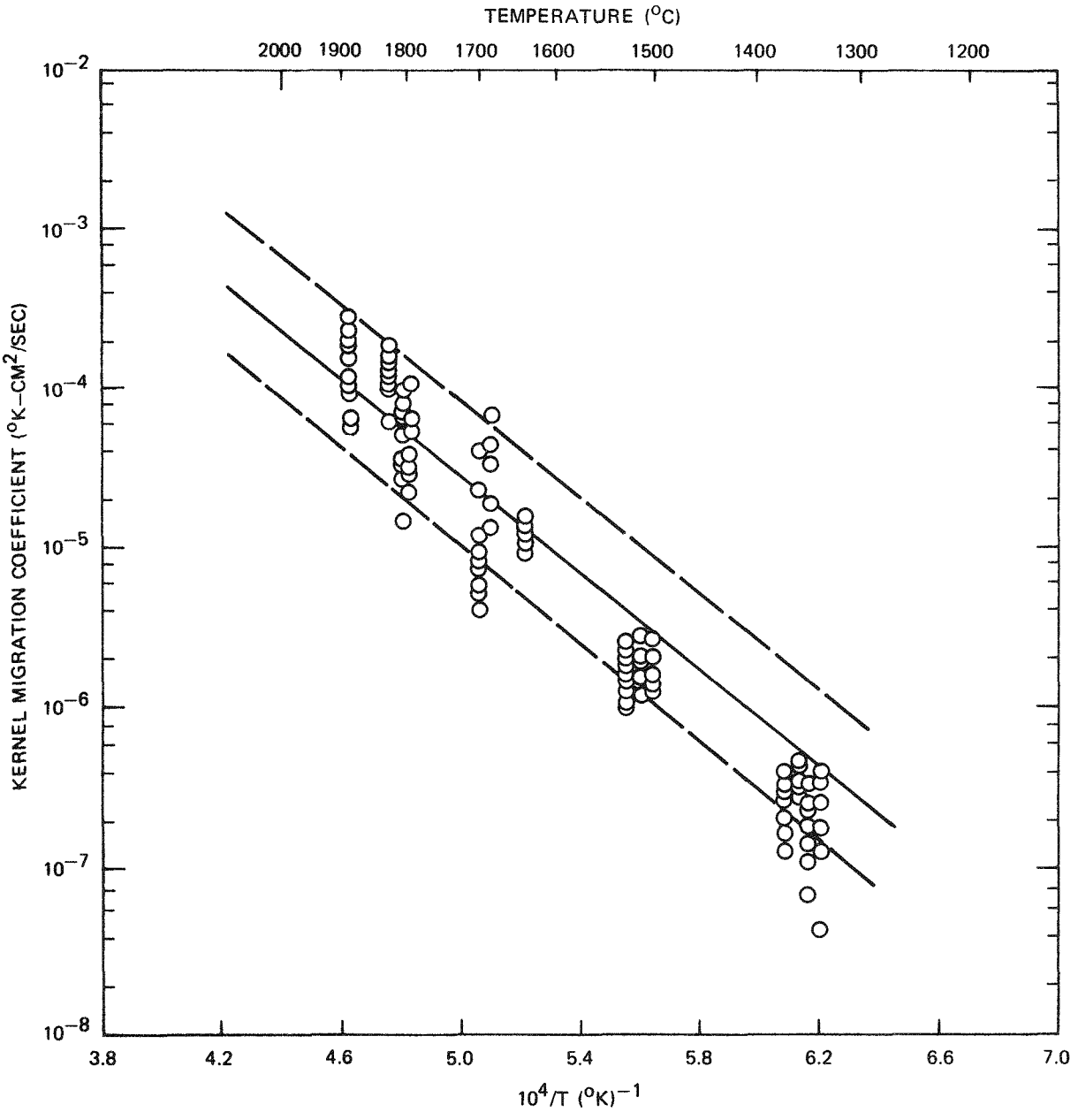

Fig. 9-2. Comparison of data from experiments 6511 and 6440 with least-squares curve fit and 90% confidence limits for KMC used in LHTGR core design studies; TRISO dense melted UC_2 particles, 200-μm kernels

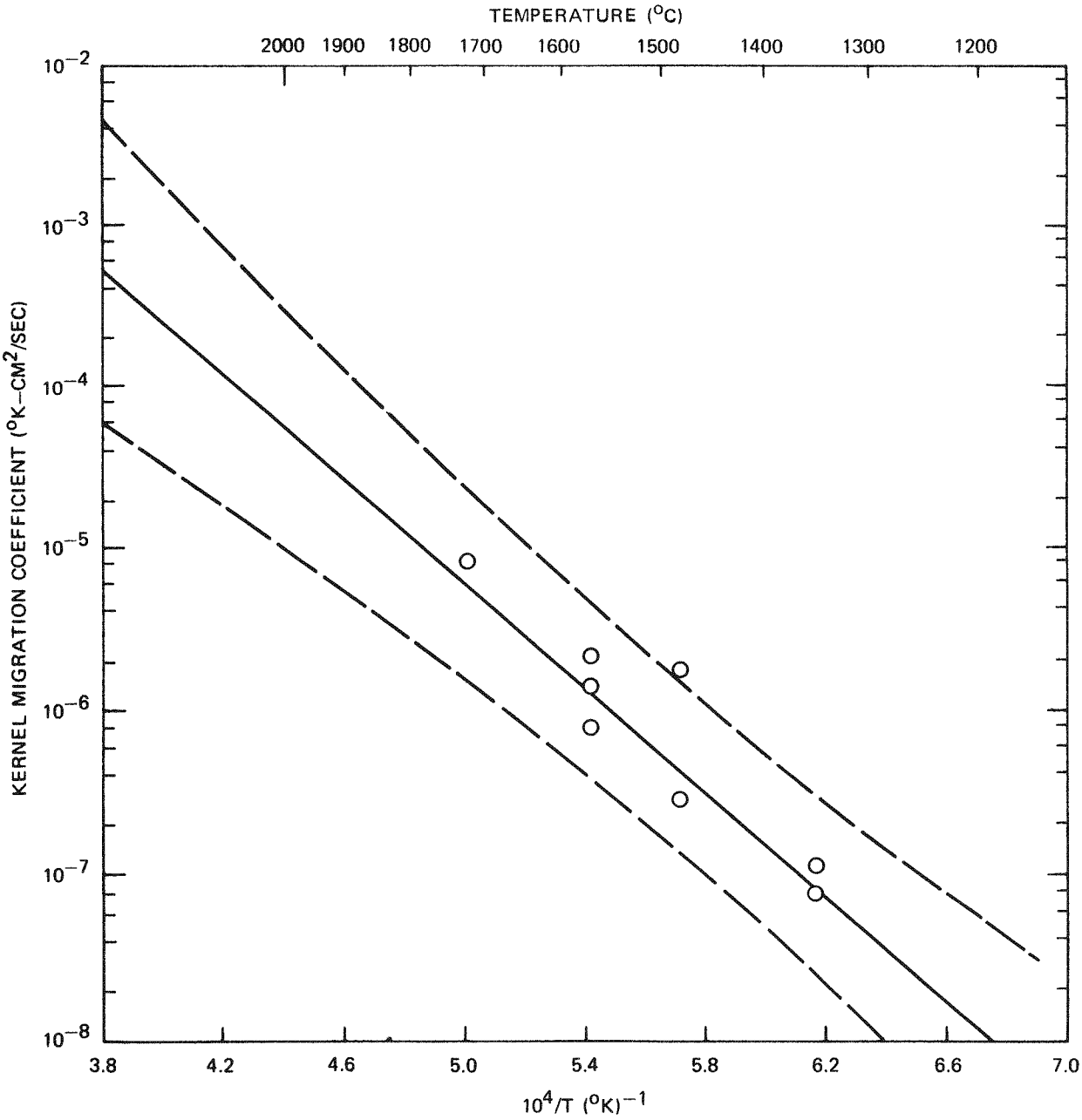

Fig. 9-3. Kernel migration coefficient for $U{\cdot}C_{4.37} \cdot O_{0.41}$ TRISO WAR particles with a least-squares curve fit of the data and a 90% confidence interval

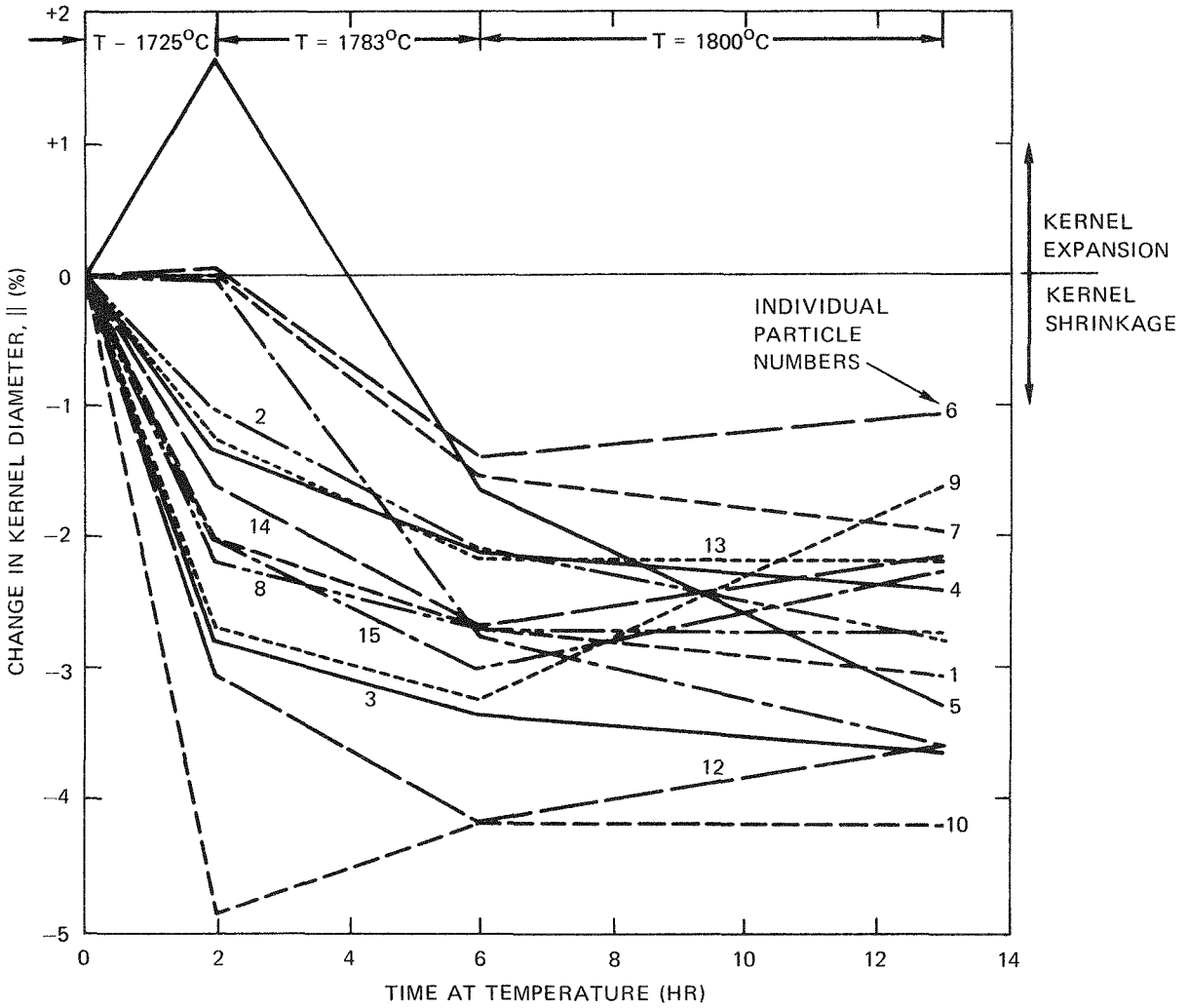

Fig. 9-4. Change in WAR $U{\cdot}C_{4.37}{\cdot}O_{0.41}$ kernel diameter versus time: (a) 1700° to 1800°C, parallel to thermal gradient

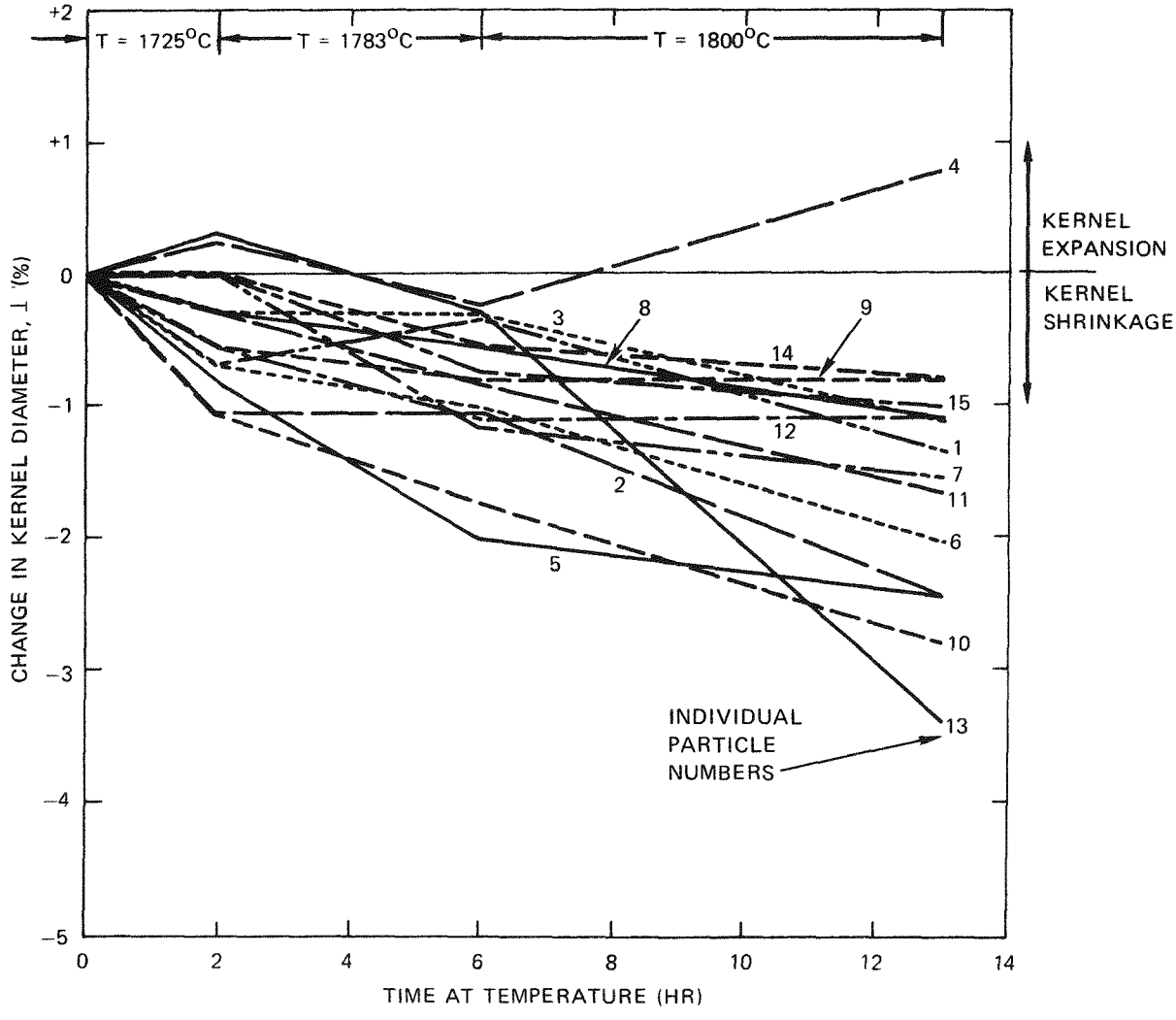

Fig. 9-4. Change in WAR $U{\cdot}C_{4.37}{\cdot}O_{0.41}$ kernel diameter versus time: (b) 1700° to 1800°C, perpendicular to thermal gradient

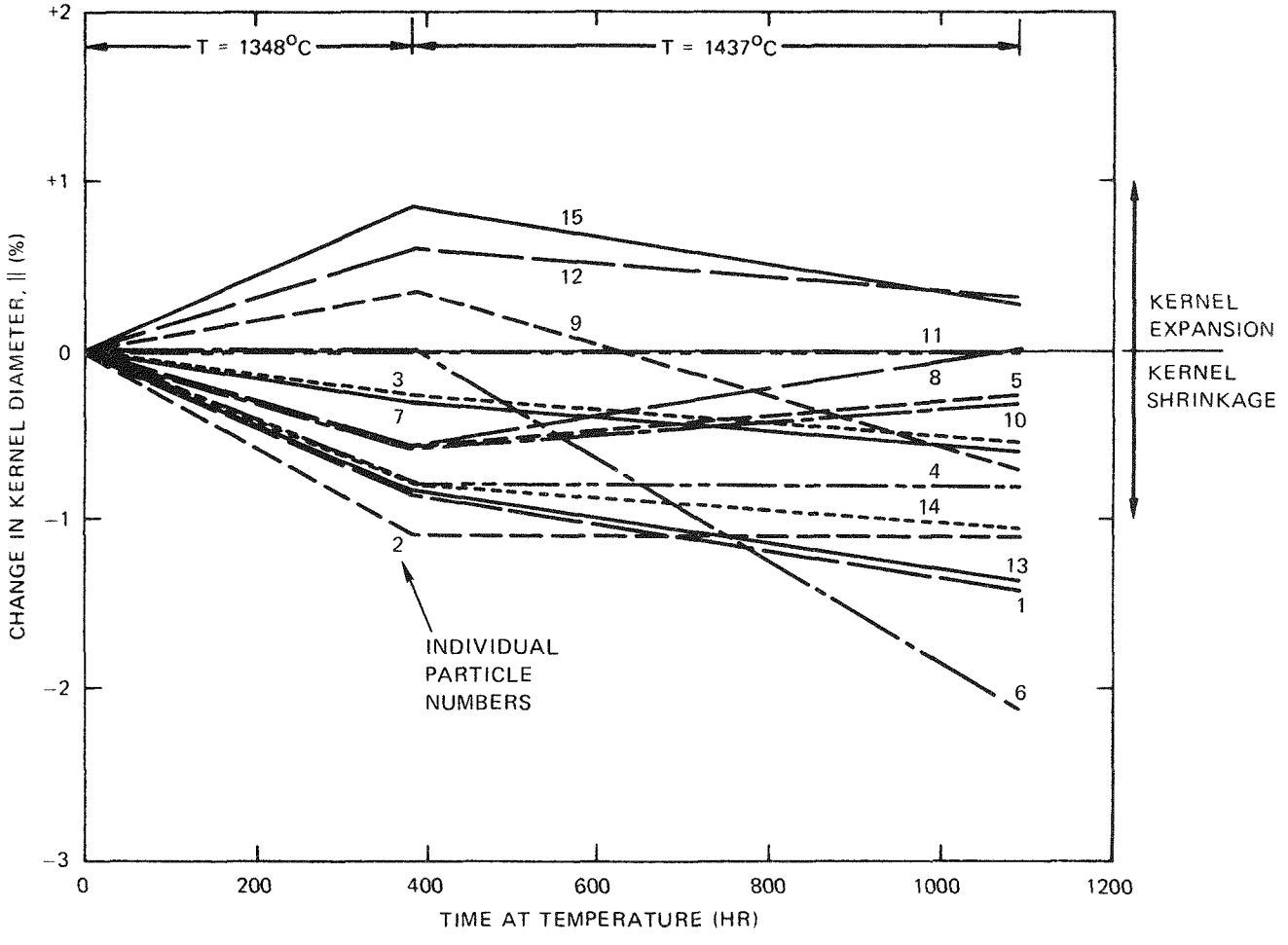

Fig. 9-4. Change in WAR $U{\cdot}C_{4.37}{\cdot}O_{0.41}$ kernel diameter versus time: (c) 1350° to 1450°C, parallel to thermal gradient

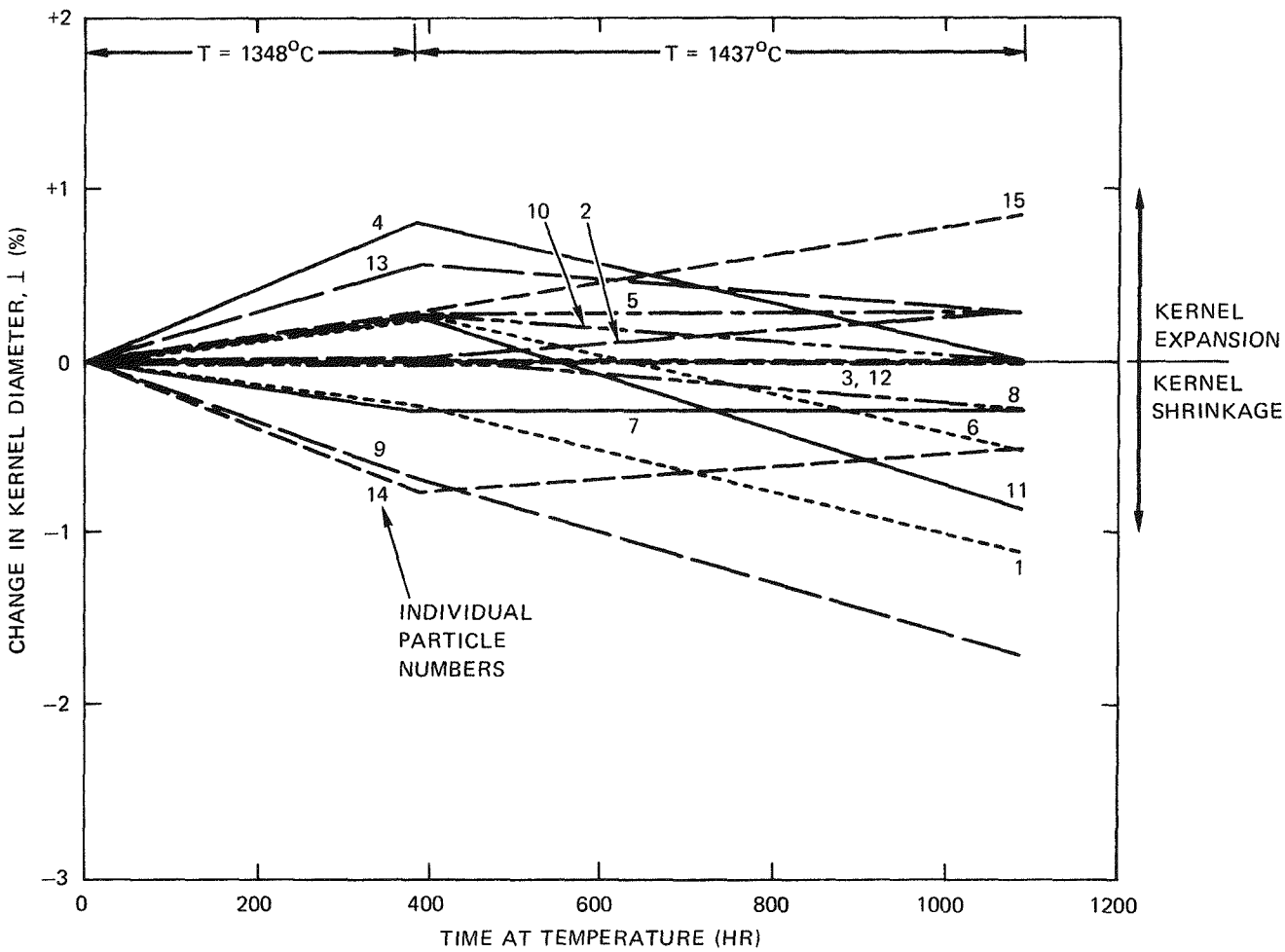

Fig. 9-4. Change in WAR $U{\cdot}C_{4.37} \cdot O_{0.41}$ kernel diameter versus time: (d) 1350° to 1450°C, perpendicular to thermal gradient

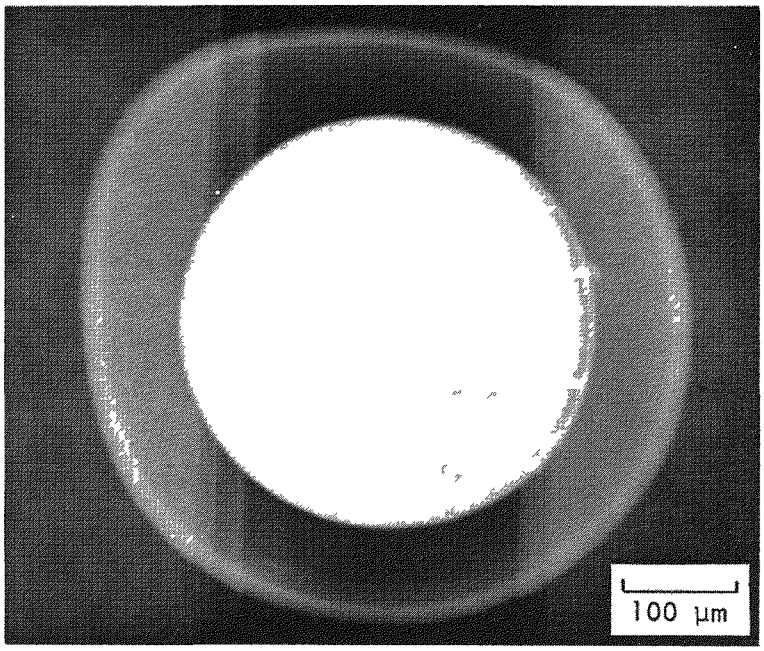

HOT SIDE

LA182

T ≃ 1725°C, $\Delta T/\Delta X$ ≃ 6141°C/cm, time (total) = 2 hr

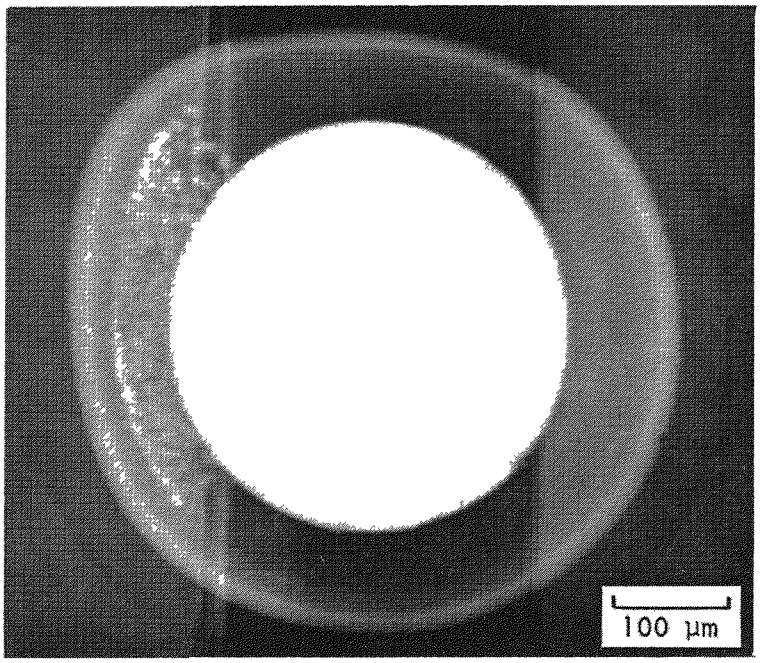

HOT SIDE

LA287

T ≃ 1769°C, $\Delta T/\Delta X$ ≃ 6198°C/cm, time (total) = 13 hr

Fig. 9-5. X-ray radiograph of $U \cdot C_{4.37} \cdot O_{0.41}$ WAR particle No. 12 (OR1694, crucible No. 6) after heat treatment in a thermal gradient

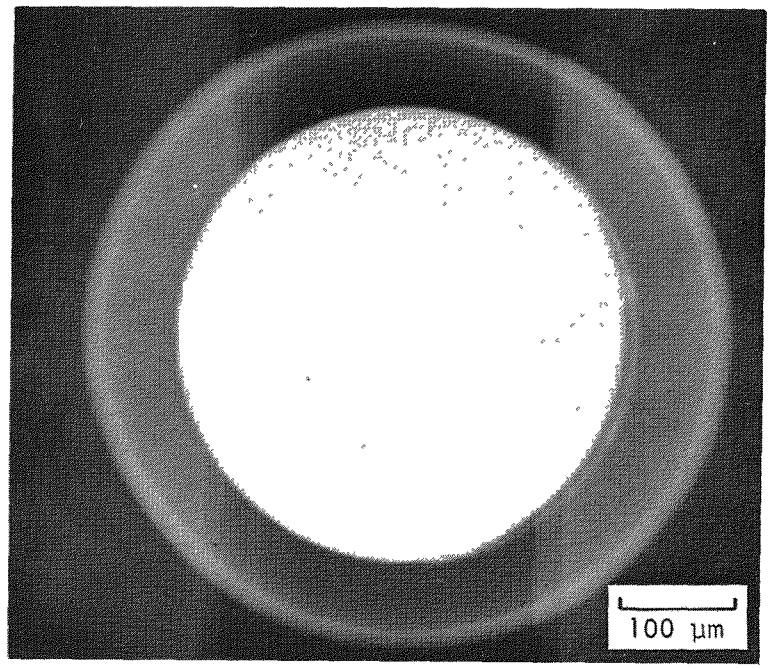

HOT SIDE

LA182

T ≃ 1725°C, $\Delta T/\Delta X$ ≃ 6141°C/cm, time (total) = 2 hr

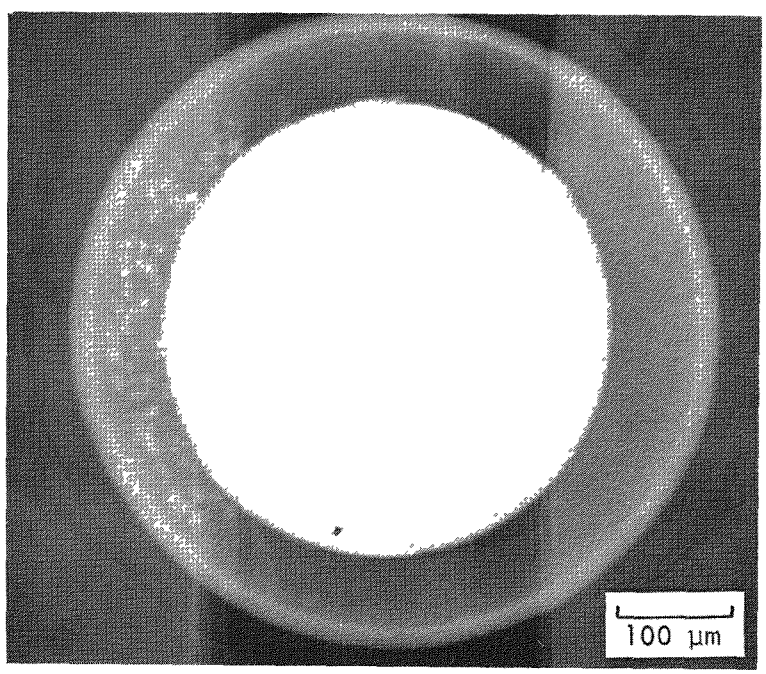

HOT SIDE

LA287

T ≃ 1769°C, $\Delta T/\Delta X$ ≃ 6198°C/cm, time (total) = 13 hr

Fig. 9-6. X-ray radiograph of $U{\cdot}C_{4.37}{\cdot}O_{0.41}$ WAR particle No. 15 (OR1694, crucible No. 6) after heat treatment in a thermal gradient

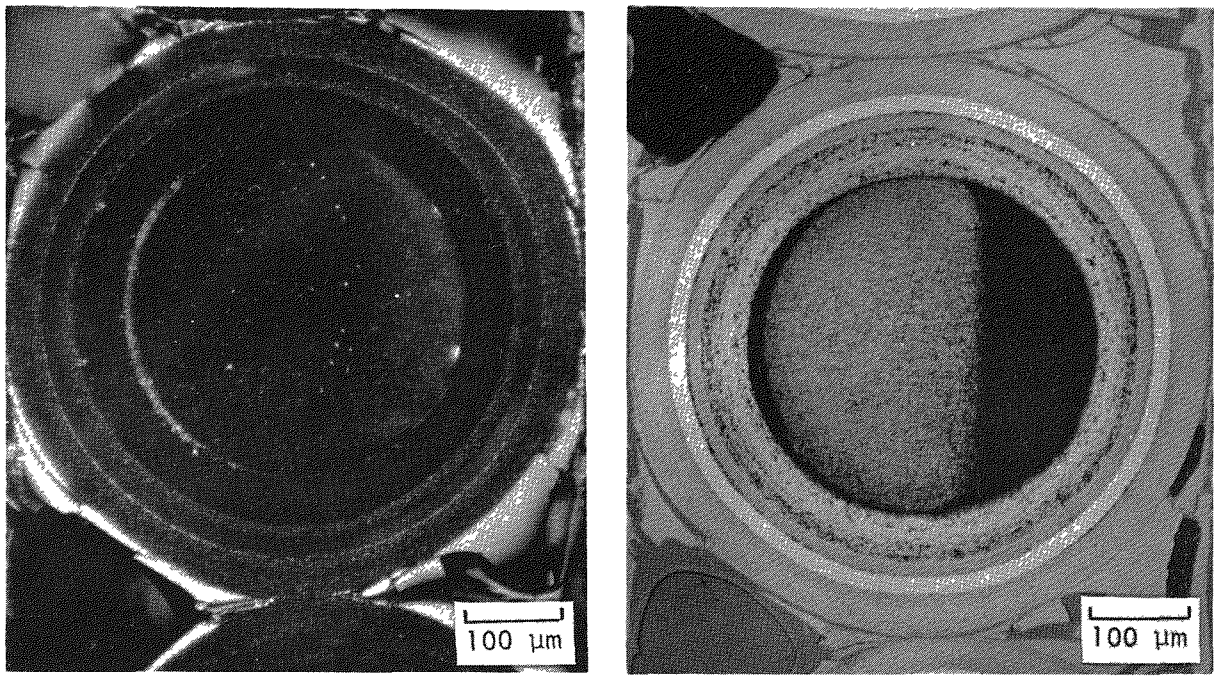

(a) (b)

T ≃ 1769°C, $\Delta T/\Delta X$ ≃ 6198°C/cm, time = 13 hr

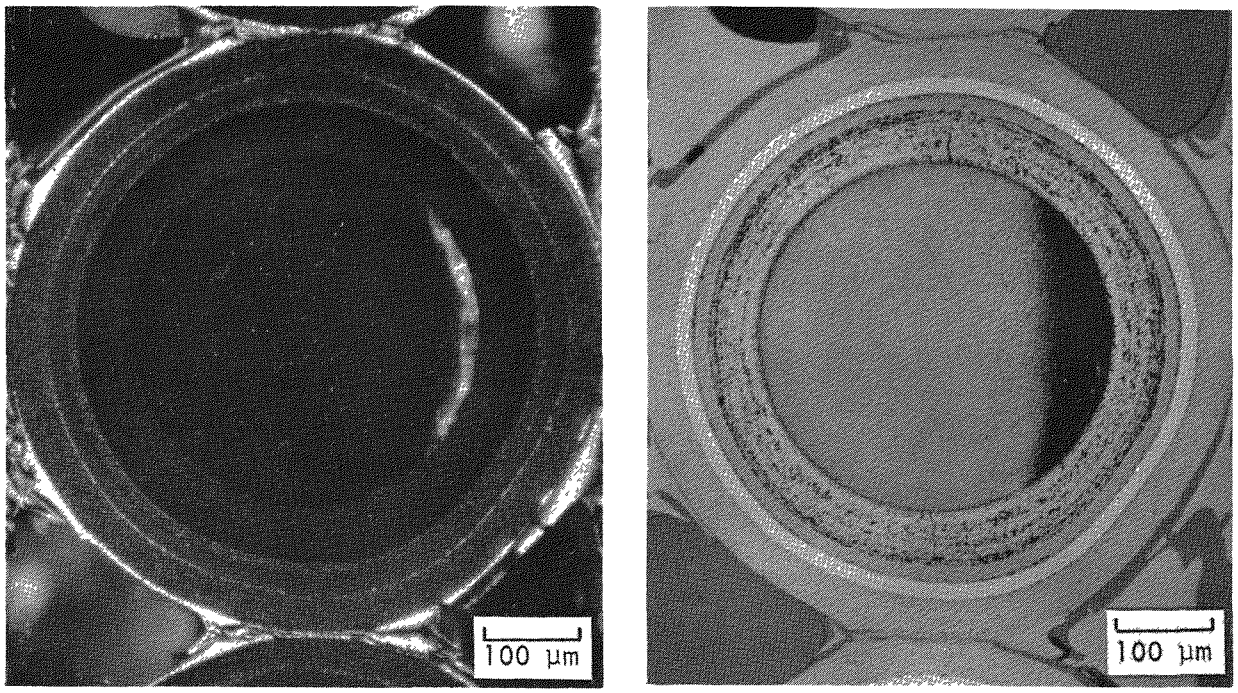

(c) (d)

T ≃ 1470°C, $\Delta T/\Delta X$ ≃ 5097°C/cm, time = 371 hr

Fig. 9-7. Photomicrographs of WAR $U{\cdot}C_{4.37}{\cdot}O_{0.41}$ fuel particles after thermal gradient tests: (a) and (c) polarized light, (b) and (d) bright field

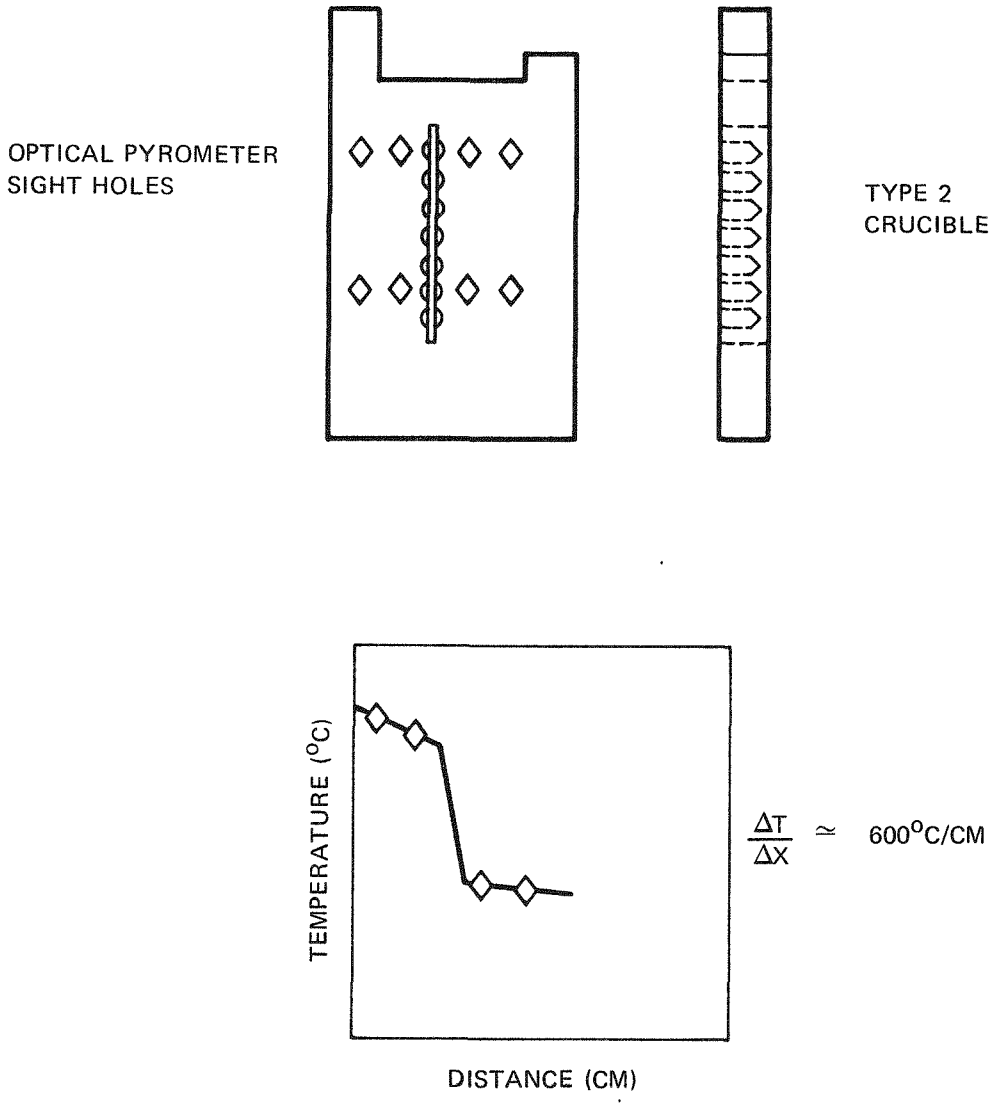

Fig. 9-8. Schematic representation of crucible configuration used in thermal gradient heating of irradiated ThO_2 fuel particles

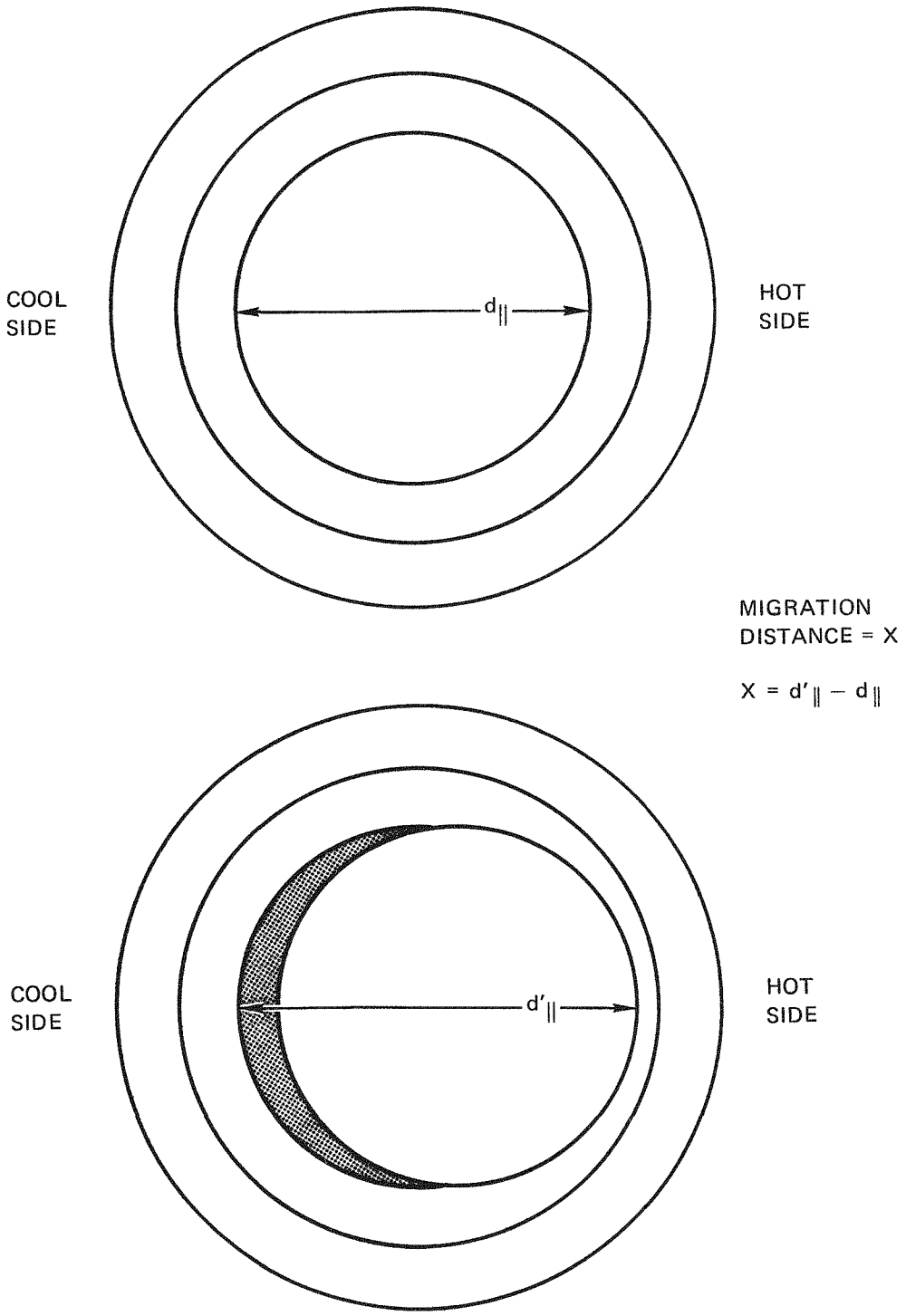

Fig. 9-9. Schematic illustration of the method used to determine the kernel migration distance (X) of irradiated BISO coated ThO_2 kernels from contact microradiographs

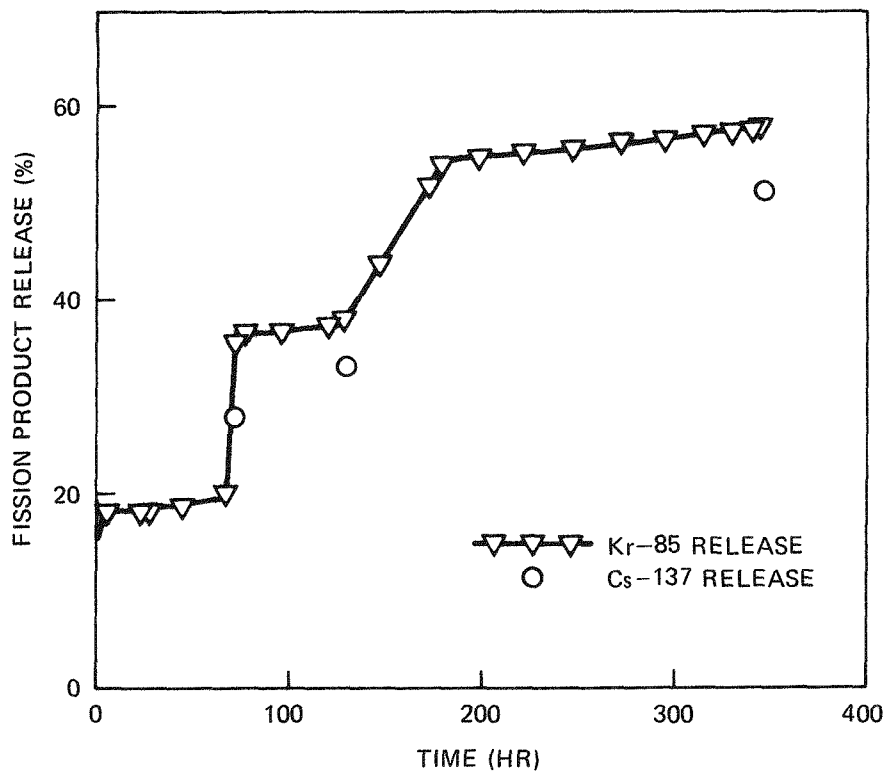

Fig. 9-10. Release of Kr-85m and Cs-137 from irradiated ThO_2 particles measured as a function of time at 1548°C in thermal gradient experiment 6532

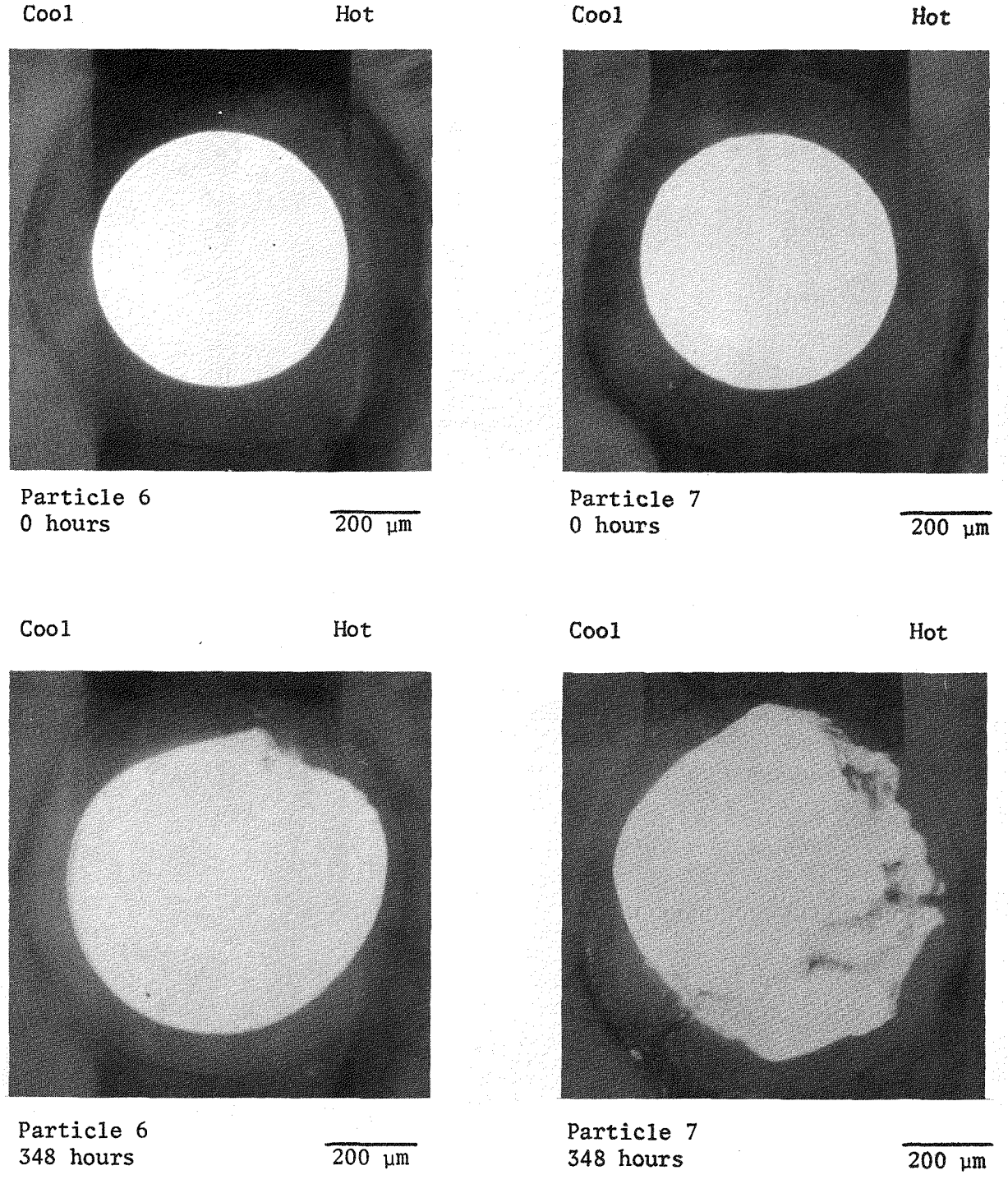

Fig. 9-11. Zero- and 348-hr radiographs of irradiated BISO ThO_2 particles failing after less than 73 hr of heating at ∿1550°C under a thermal gradient of 588°C/cm. The particles are from batch 4413-75T and were irradiated at 1325°C to a fast neutron exposure of 6.4 x 10^{21} n/cm^2 (E ≥ 0.18 MeV)$_{HTGR}$ and kernel burnup of 4.7% FIMA in capsule P13L.

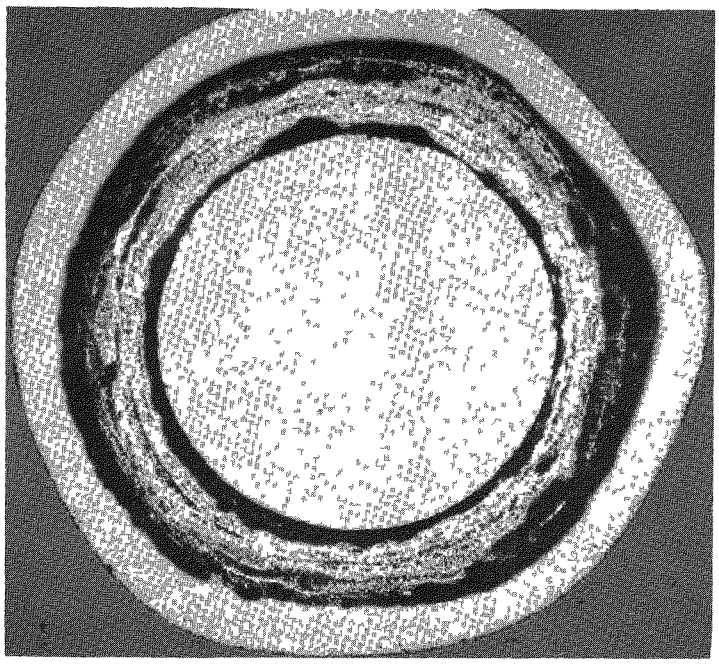

M29317-10

100 μm

(a)

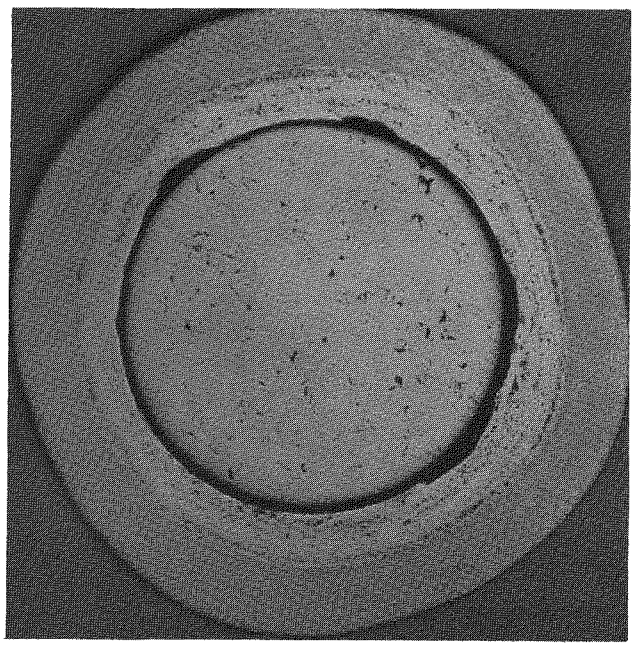

M386-337

100 μm

(b)

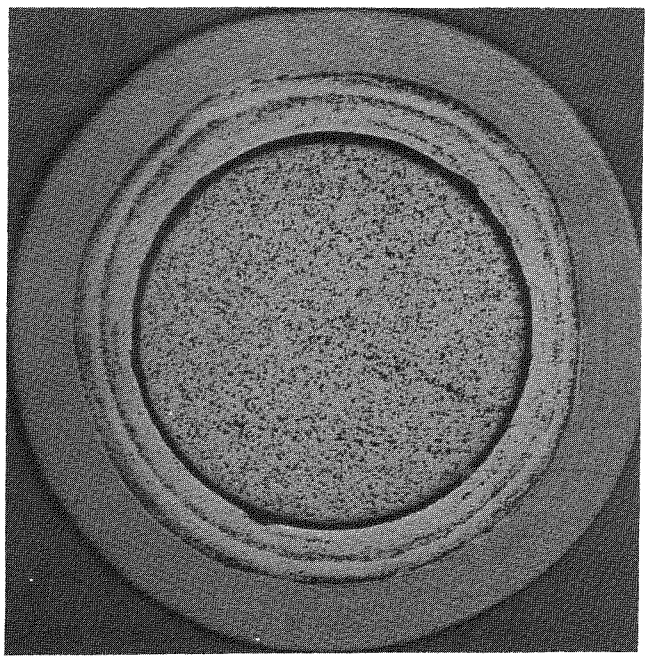

M386-342

100 μm

(c)

Fig. 9-12. Photomicrographs of BISO ThO_2 particles from batch 4413-75T: (a) preirradiation, (b,c) after irradiation at 1325°C to a fast neutron exposure of 6.4 x 10^{21} n/cm^2 $(E \geq 0.18 \text{ MeV})_{HTGR}$ and kernel burnup of 4.7% FIMA

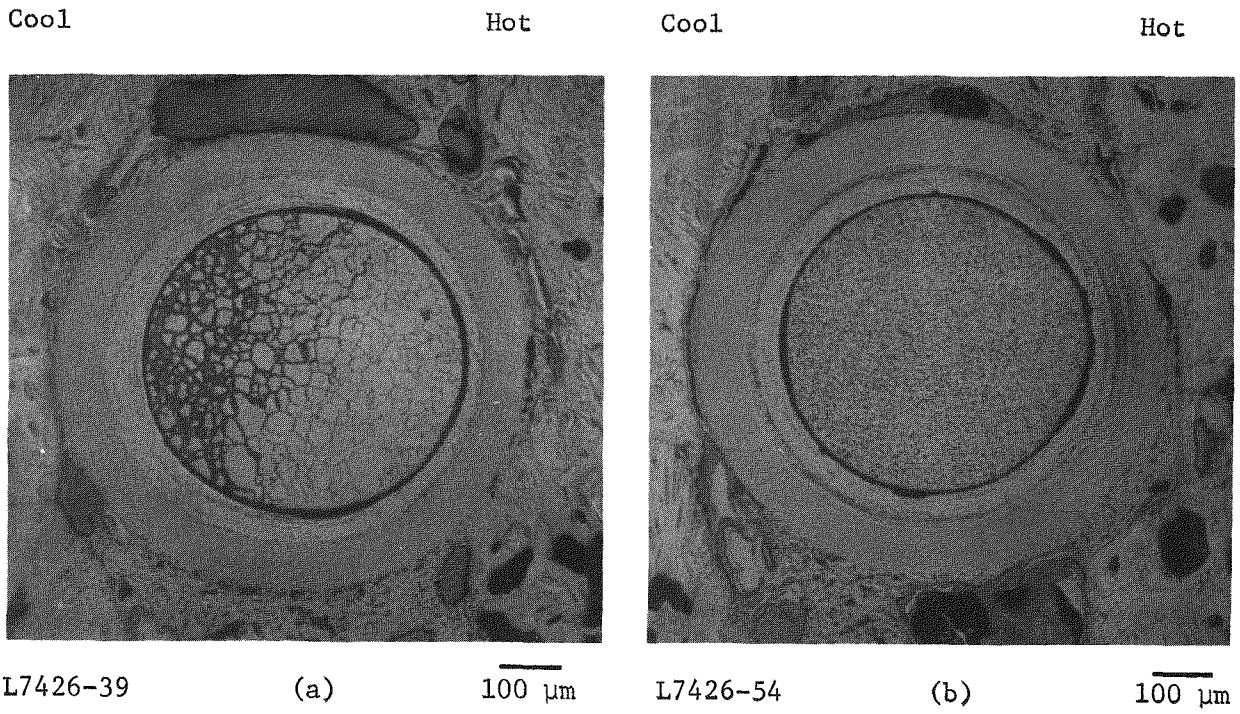

Fig. 9-13. Photomicrographs of irradiated BISO ThO_2 particles from batch 4413-75T after heating for 348 hr at 1548°C under a thermal gradient of 588°C/cm: (a) particle No. 2 and (b) particle No. 3

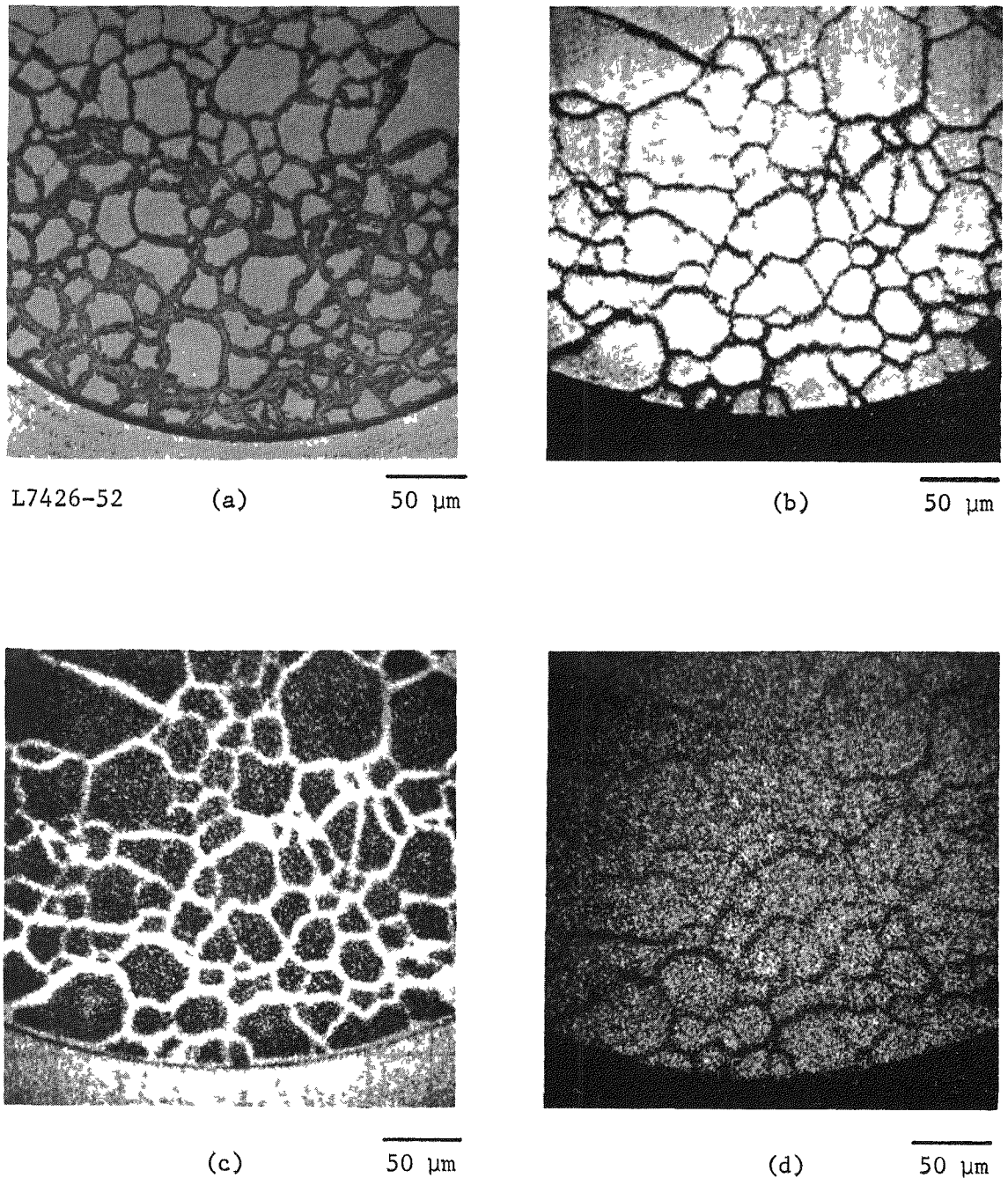

Fig. 9-14. X-ray traces across the cool side kernel-buffer interface of irradiated BISO ThO_2 particle No. 2 after 348 hr at 1548°C under a thermal gradient of 588°C/cm. The particles are from batch 4413-75T: (a) bright field, (b) back scattered electron, (c) carbon, and (d) Th.

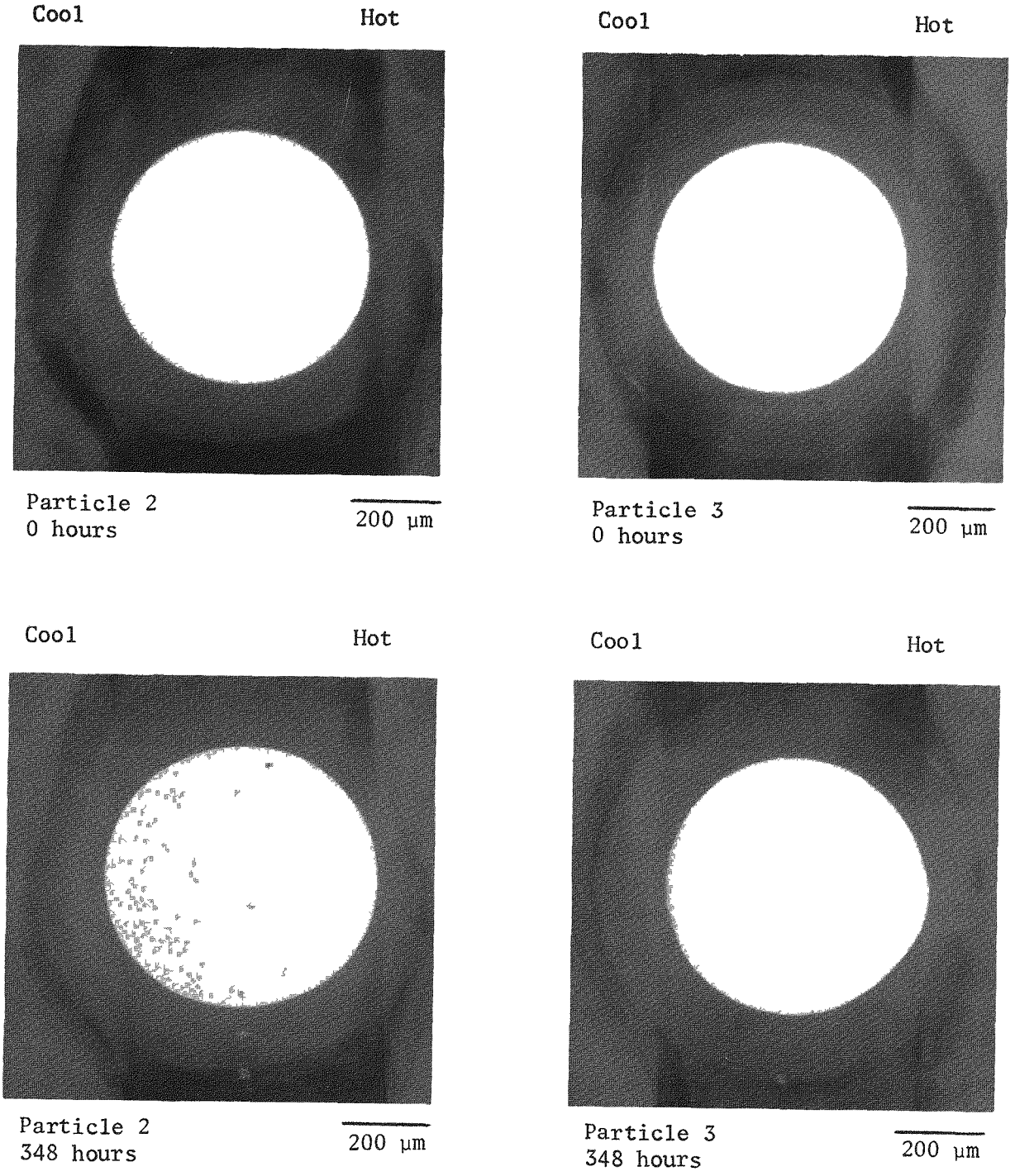

Fig. 9-15. Radiographs showing irradiated BISO ThO_2 particles 2 and 3 after 0 and 348 hours of heating at 1548°C under a thermal gradient of 588°C/cm. Particles are from batch 4413-75T and were irradiated at 1325°C to a fast neutron exposure of 6.4×10^{21} n/cm^2 $(E \geq 0.18 \text{ MeV})_{HTGR}$ and 4.7% FIMA in capsule P13L.

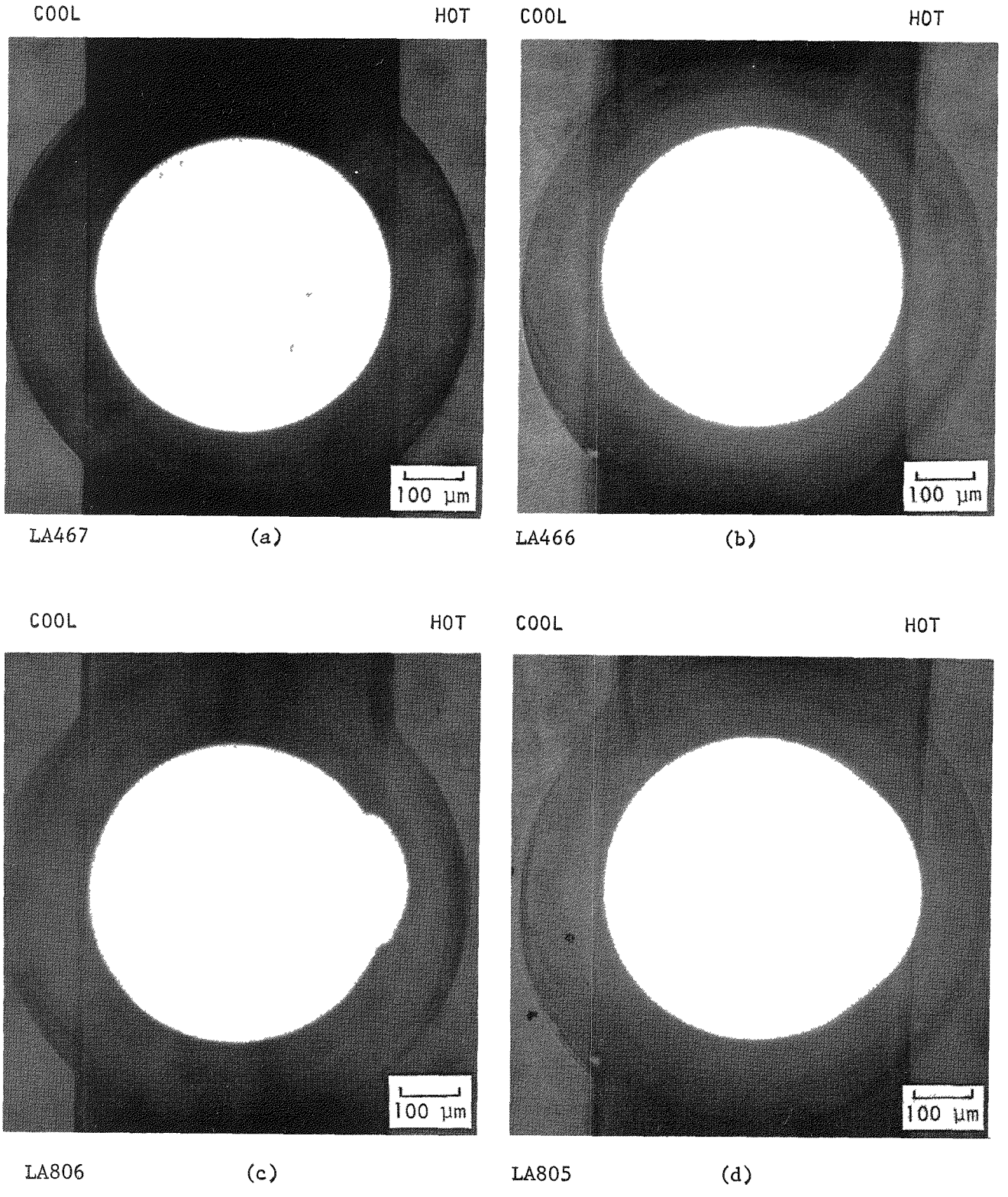

Fig. 9-16. Radiographs of BISO ThO_2 fertile particles (1) irradiated to 1.5% FIMA (a) and then heated for 589 hr at 1559°C under a thermal gradient of 705°C/cm (c), and (2) irradiated to 6.8% FIMA (b) and then heated for 589 hr at 1521°C under a thermal gradient of 405°C/cm (d)

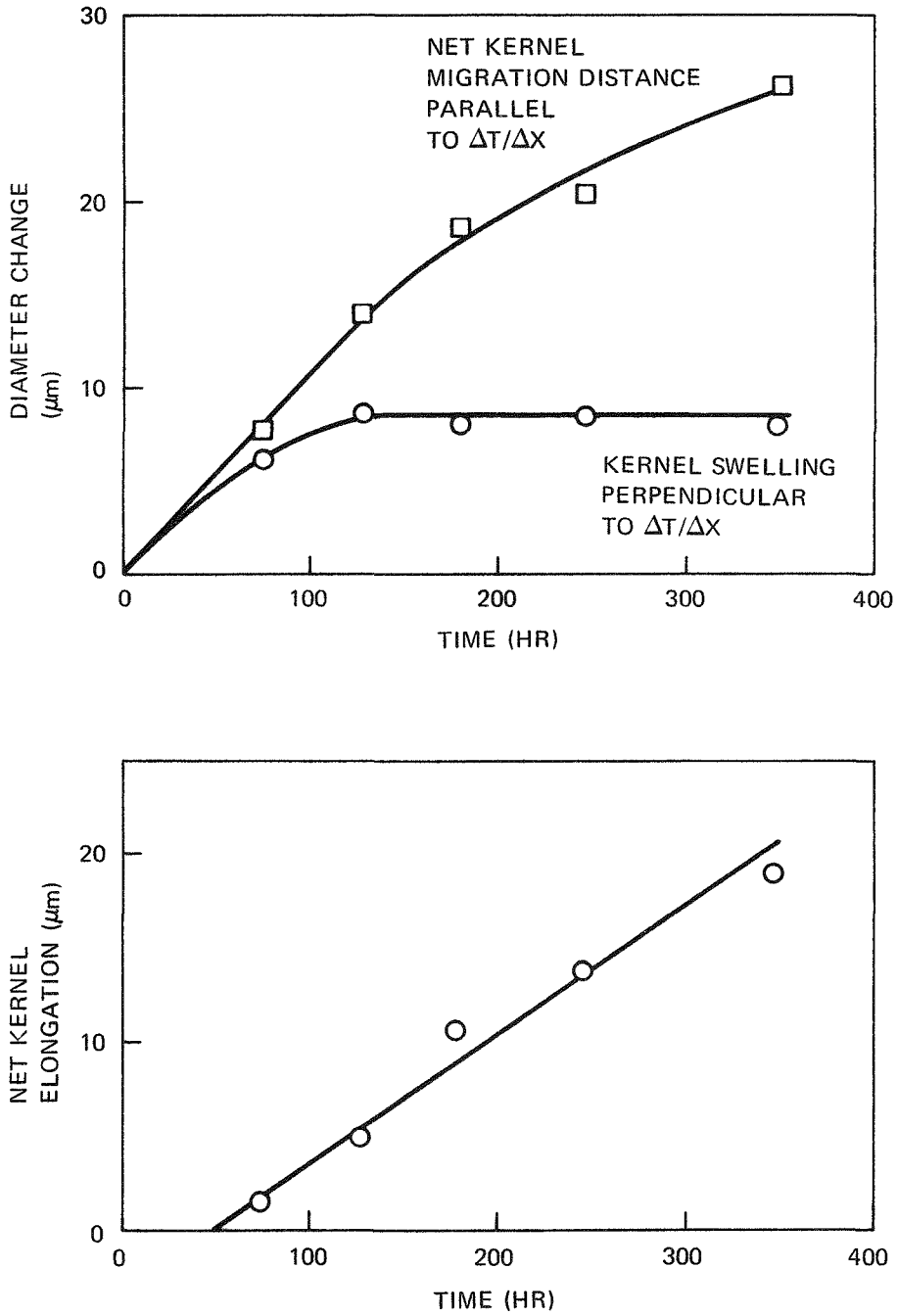

Fig. 9-17. Average ThO_2 kernel diameter change versus time (top) measured parallel and perpendicular to a thermal gradient during heating at 1548°C and 588°C/cm and net kernel elongation versus time (bottom). Particles were irradiated at an average temperature of 1325°C to a fast neutron exposure of 6.6 x 10^{21} n/cm^2 $(E \geq 0.18\ MeV)_{HTGR}$ and kernel burnup of 4.7% FIMA in capsule P13L.

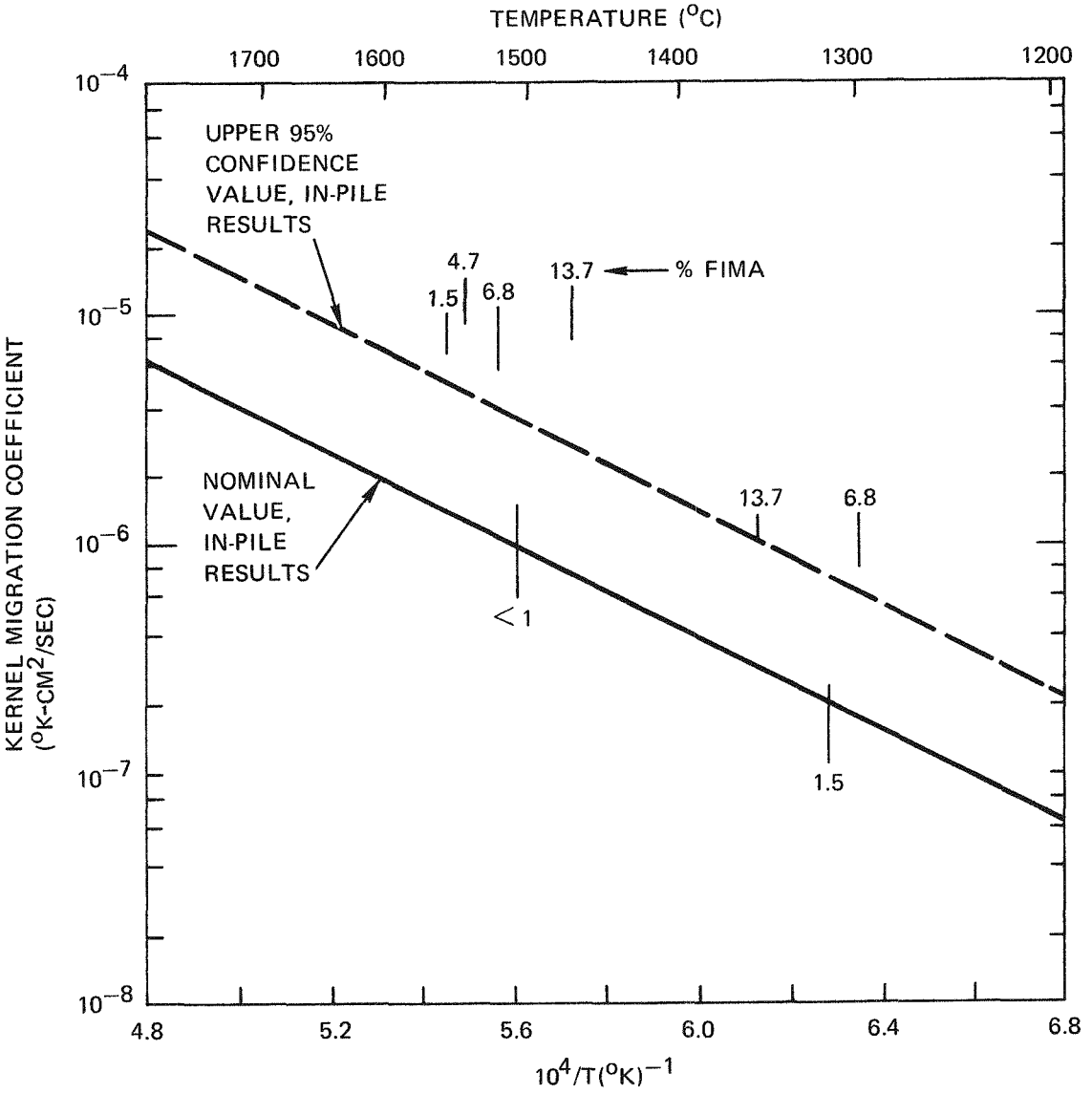

Fig. 9-18. Comparison of nominal and upper 95% confidence limits for ThO_2 KMC versus 1/T from ORNL in-pile data (Ref. 9-4) and KMC values determined from out-of-pile thermal gradient heating of irradiated ThO_2 particles at GA

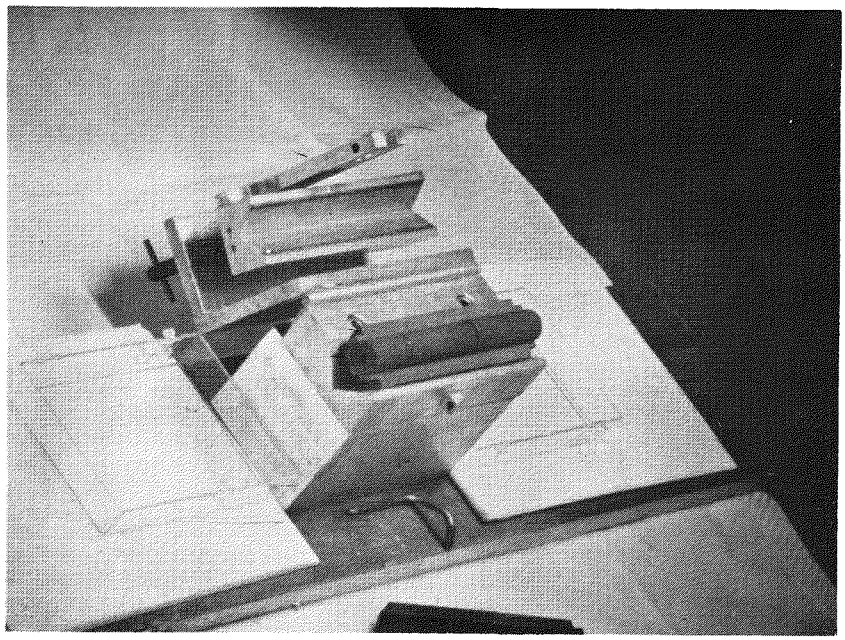

K7440-80b

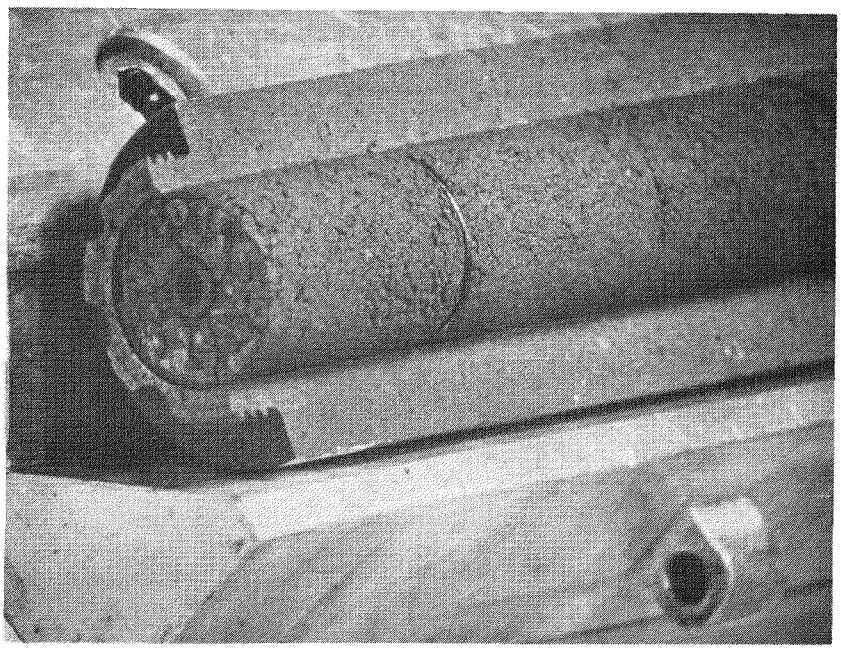

K7440-81

Fig. 9-19. Photomicrographs showing P13S cell No. 2 fuel rods during removal from split graphite crucible

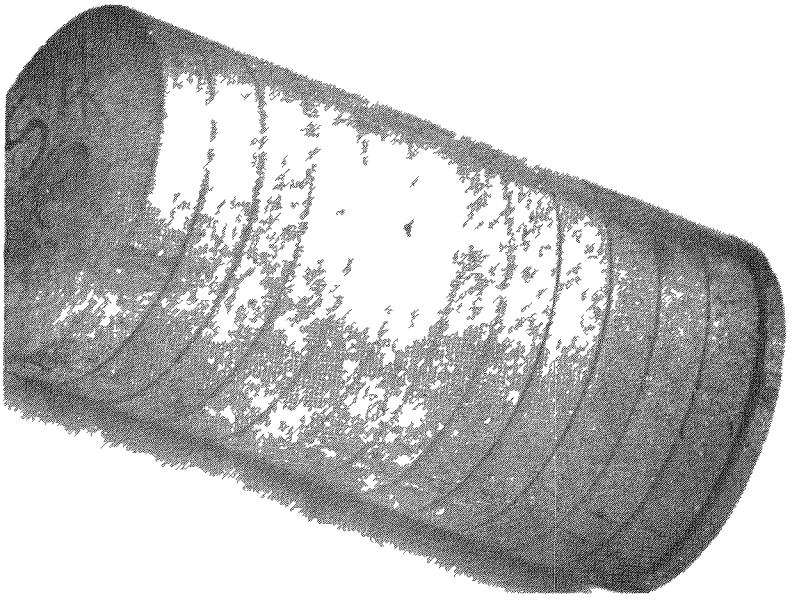

K7425-95 (a)

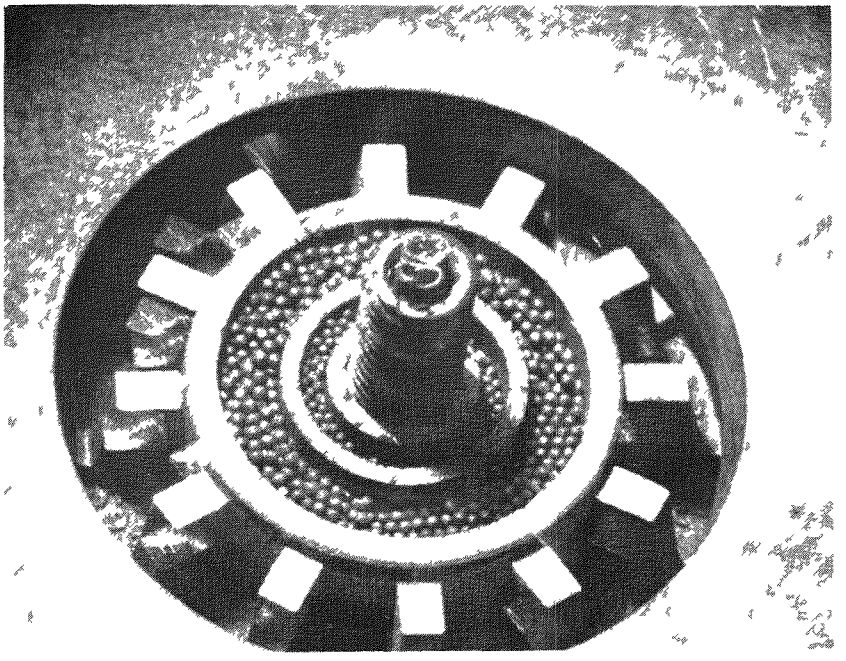

K7425-102 (b)

Fig. 9-20. Representative photomicrographs showing: (a) unbonded particle crucible assembly after removal from primary containment, and (b) unloading of unbonded particle samples from crucible

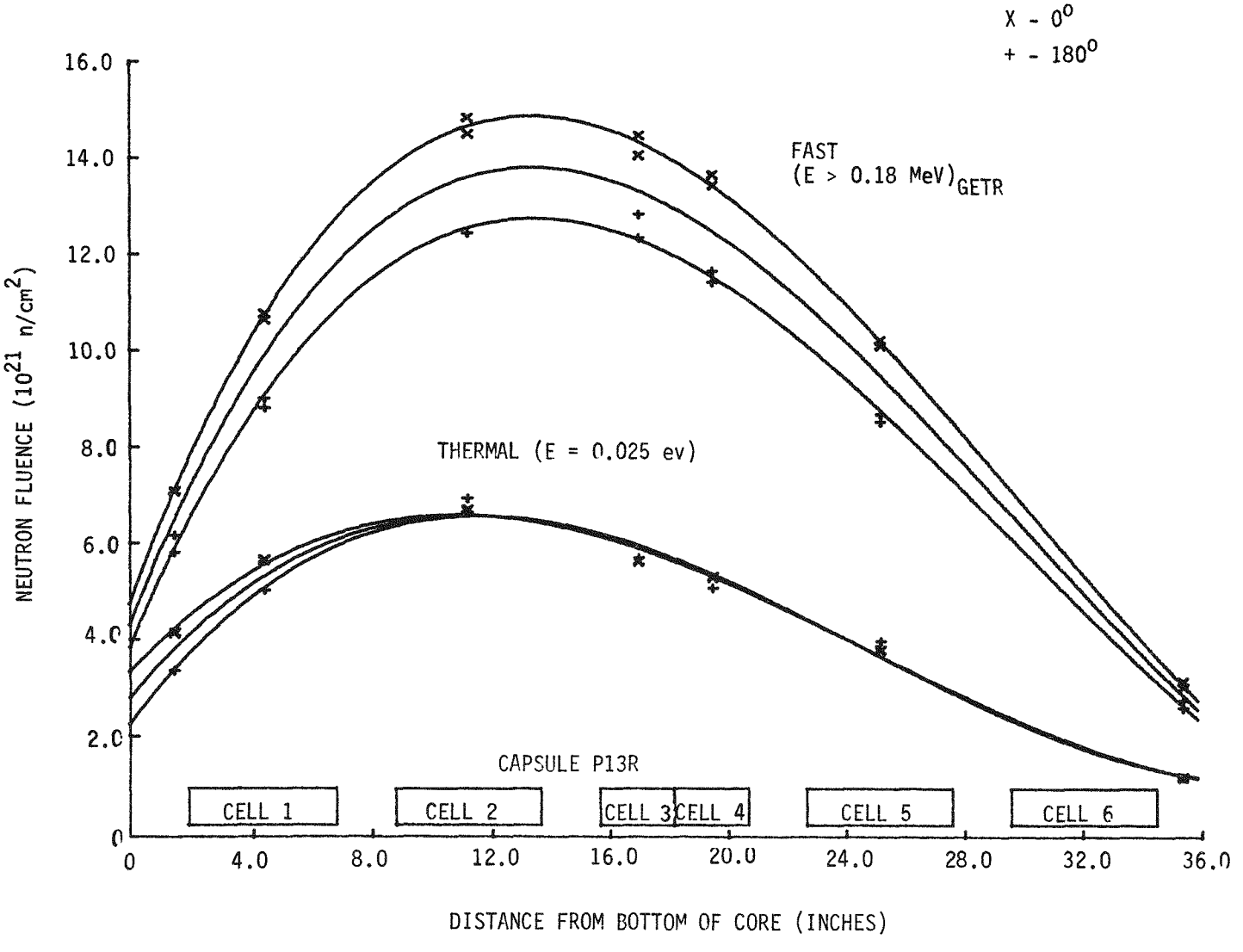

Fig. 9-21. Capsule P13R GETR fast and thermal neutron fluence profiles

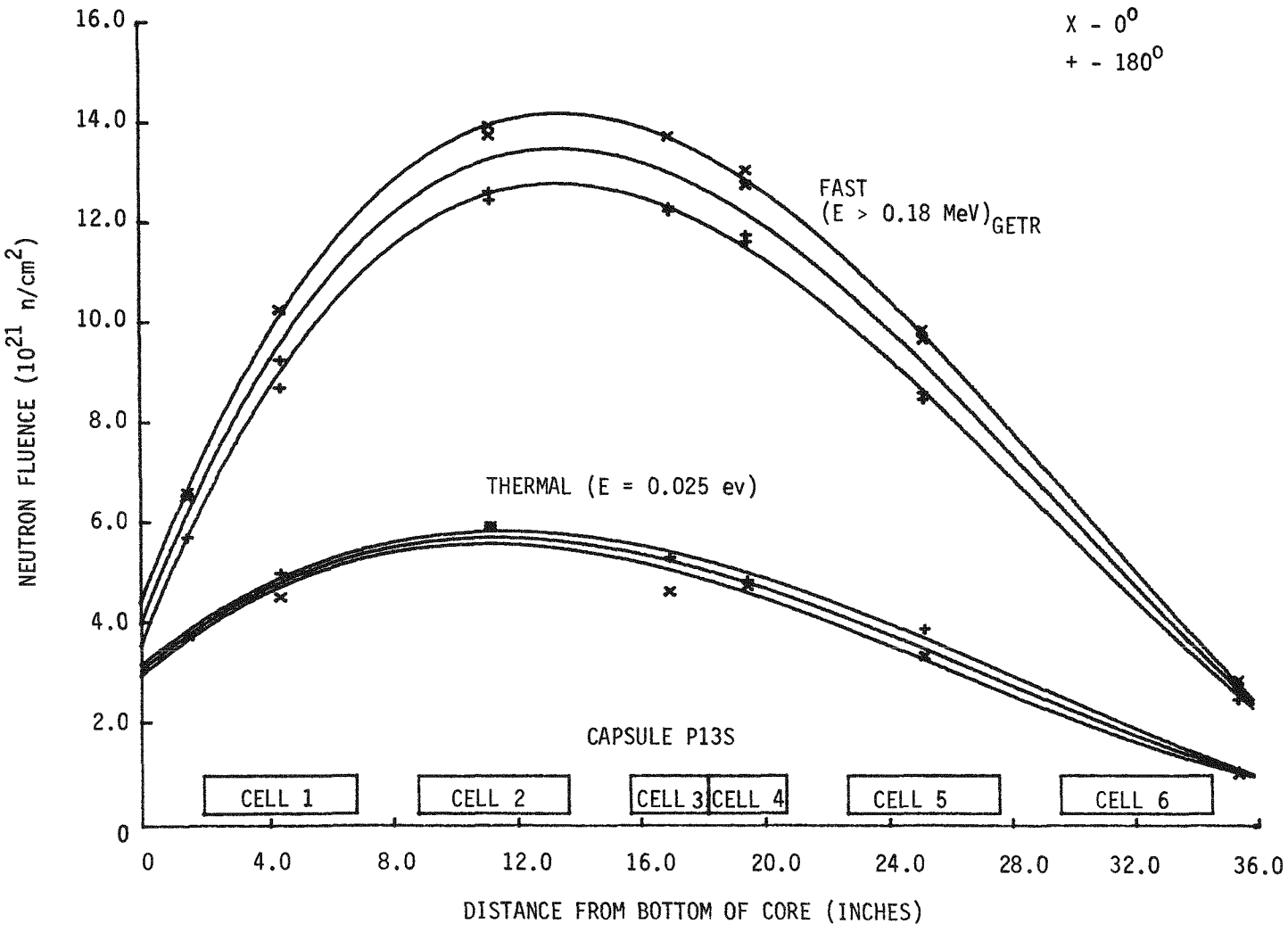

Fig. 9-22. Capsule P13S GETR fast and thermal neutron fluence profiles

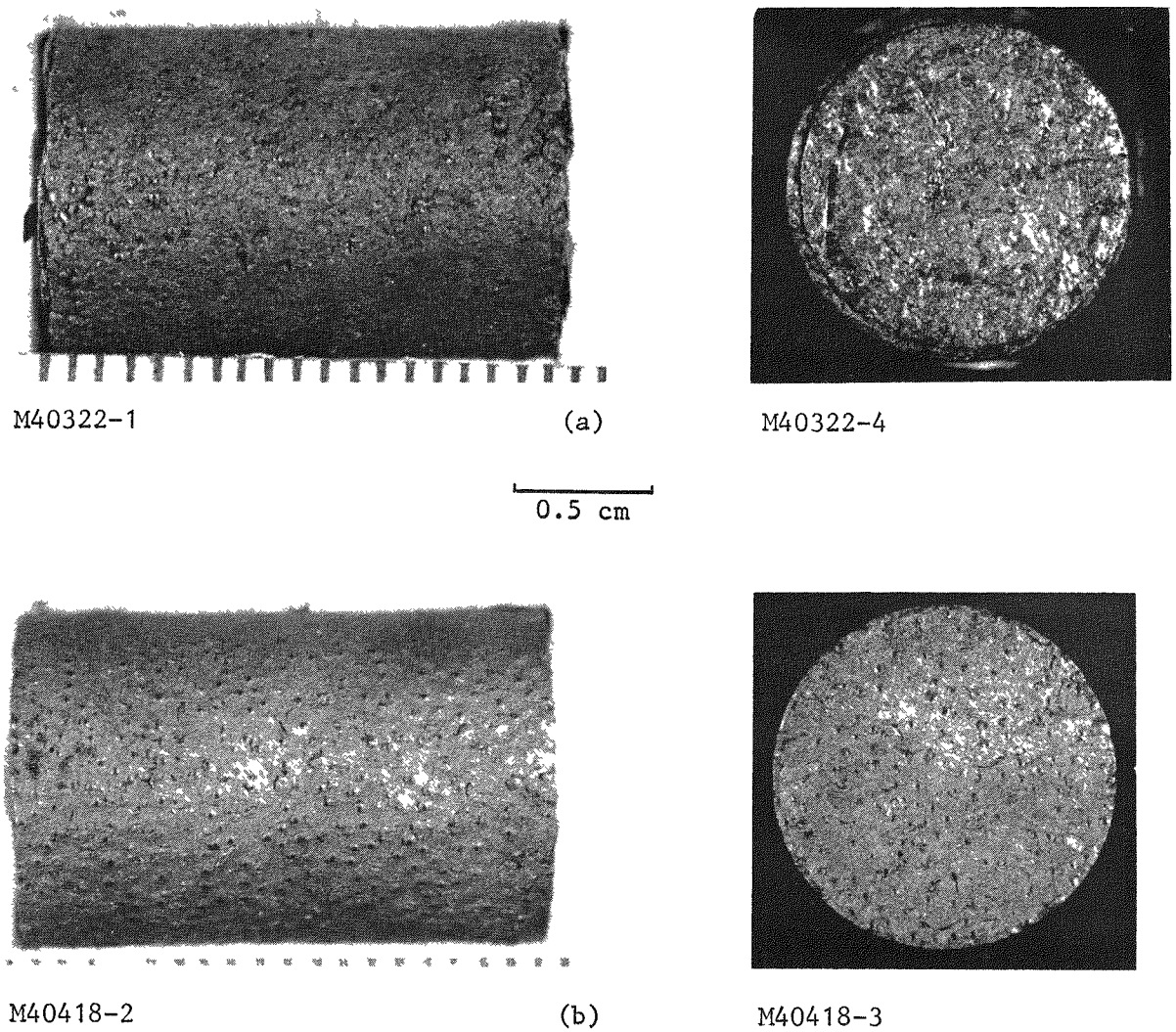

Fig. 9-23. Representative preirradiation photomicrographs of fuel rods tested in capsules P13R and P13S: (a) fired at 1800°C in argon which is the reference heat treatment for LHTGR fuel production, and (b) slug-injected fuel rod fired in packed bed of alumina

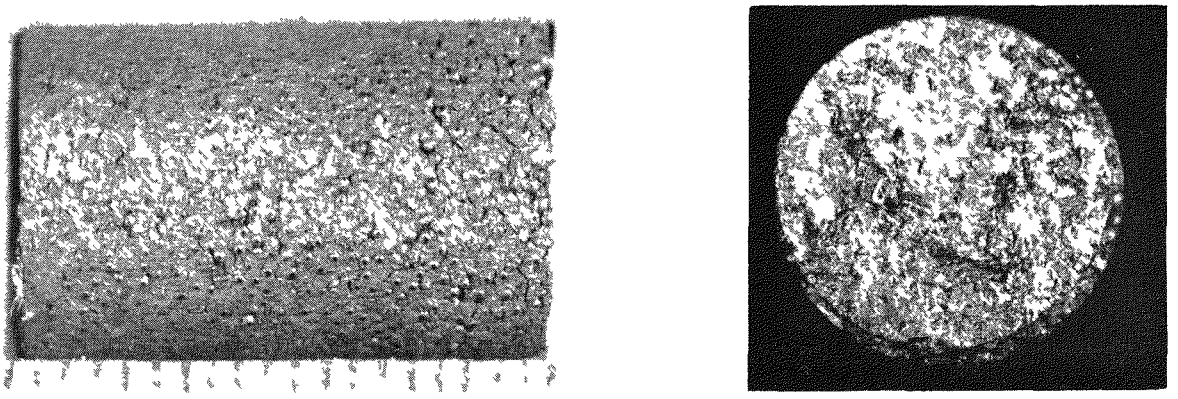

Fig. 9-24. Representative preirradiation photomicrographs of fuel rods tested in capsules P13R and P13S: (a) fired at 1500°C and (b) fired in a N_2 atmosphere. The grafoil disks placed on the ends of each rod to prevent sticking during firing in H-451 graphite tubes remained on the rods.

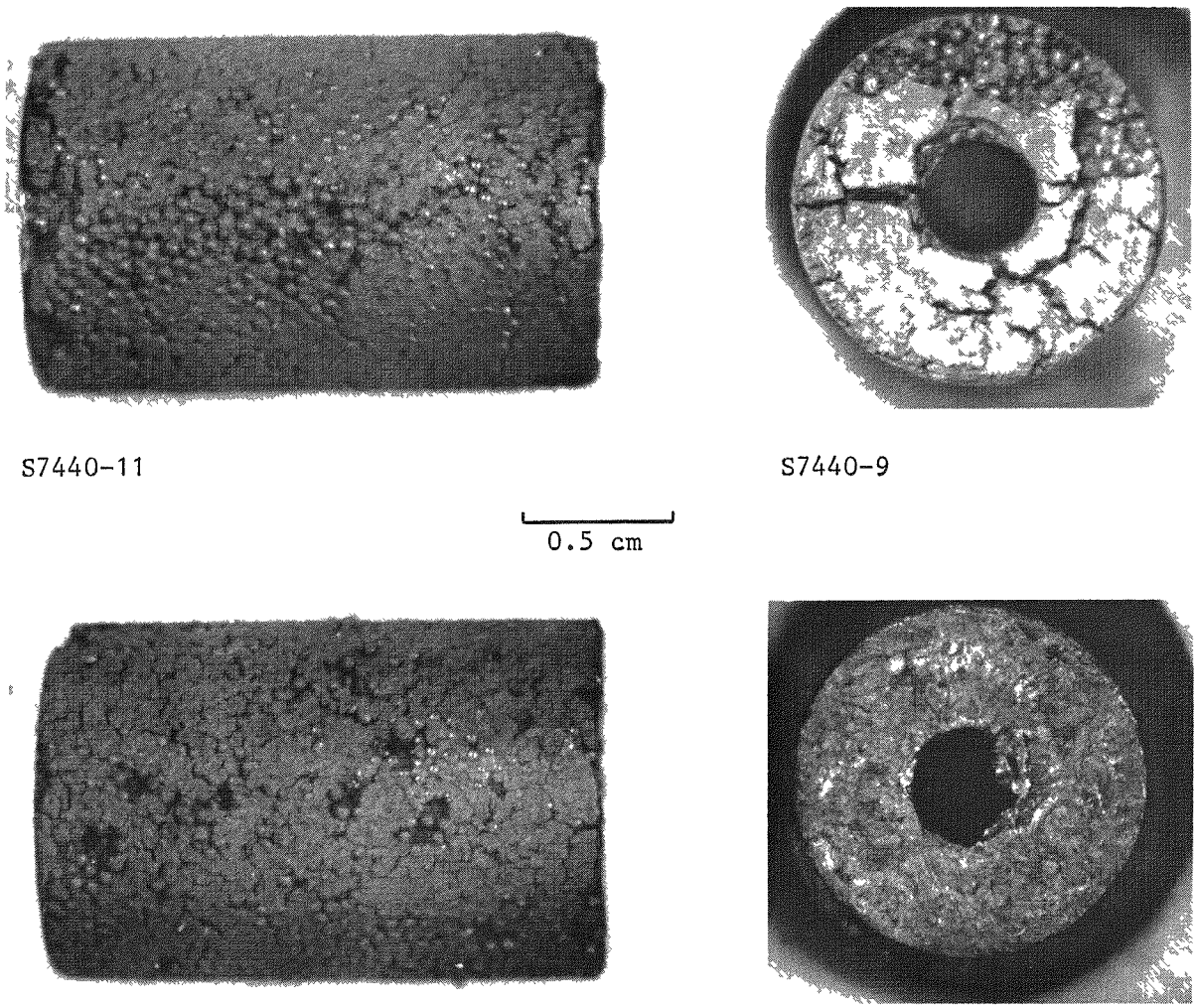

Fig. 9-25. Photomicrographs of fuel rod 7161-004-01-5 (top) after irradiation in capsule P13R (position 1A) to a fast neutron fluence of 7.4 x 10^{21} n/cm^2 (E > 0.18 MeV)$_{HTGR}$ at 1075°C (design) and of fuel rod 7161-004-01-7 (bottom) after irradiation in capsule P13S (position 1A) to a fast neutron fluence of 7.1 x 10^{21} n/cm^2 (E > 0.18 MeV)$_{HTGR}$. Cell No. 1 of capsule P13S was thermal cycled from 1075° to 1500°C (design) twenty-one times during irradiation.

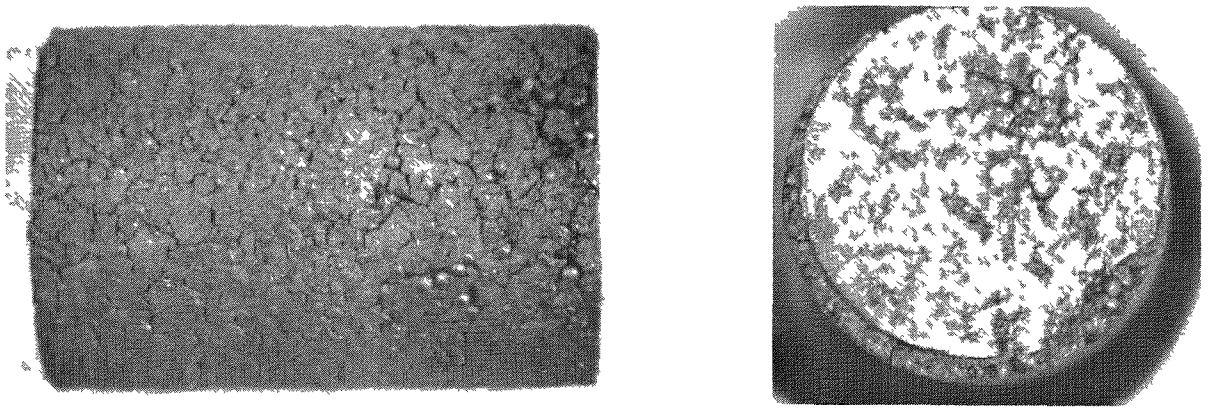

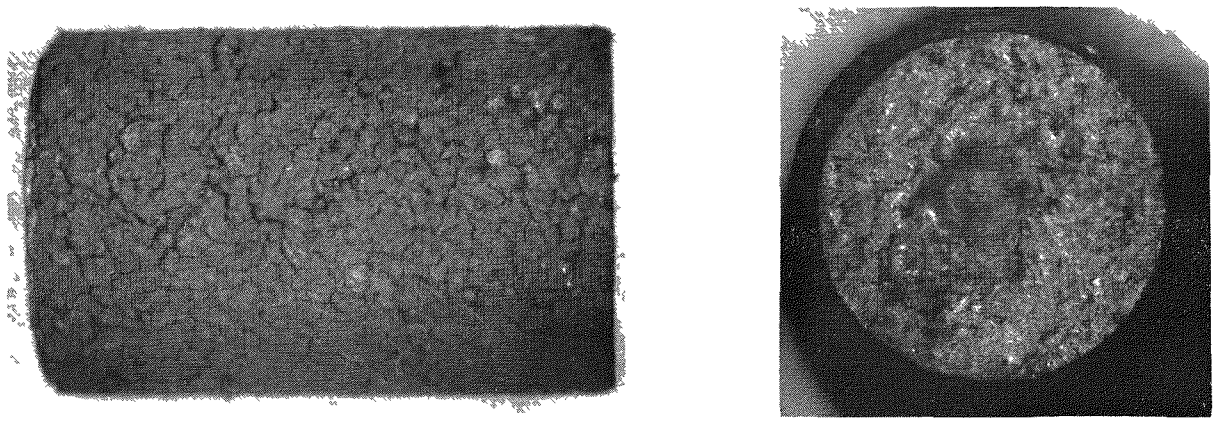

Fig. 9-26. Photomicrographs of fuel rod 7161-004-02-6 (top) after irradiation in capsule P13R (position 1B) to a fast neutron fluence of 8.2×10^{21} n/cm^2 (E > 0.18 MeV)$_{HTGR}$ at 1075°C (design) and of fuel rod 7161-004-02-5 (bottom) after irradiation in capsule P13S (position 1B) to a fast neutron fluence of 7.8×10^{21} n/cm^2 (E > 0.18 MeV)$_{HTGR}$. Cell No. 1 of capsule P13S was thermal cycled from 1075° to 1500°C (design) twenty-one times during irradiation.

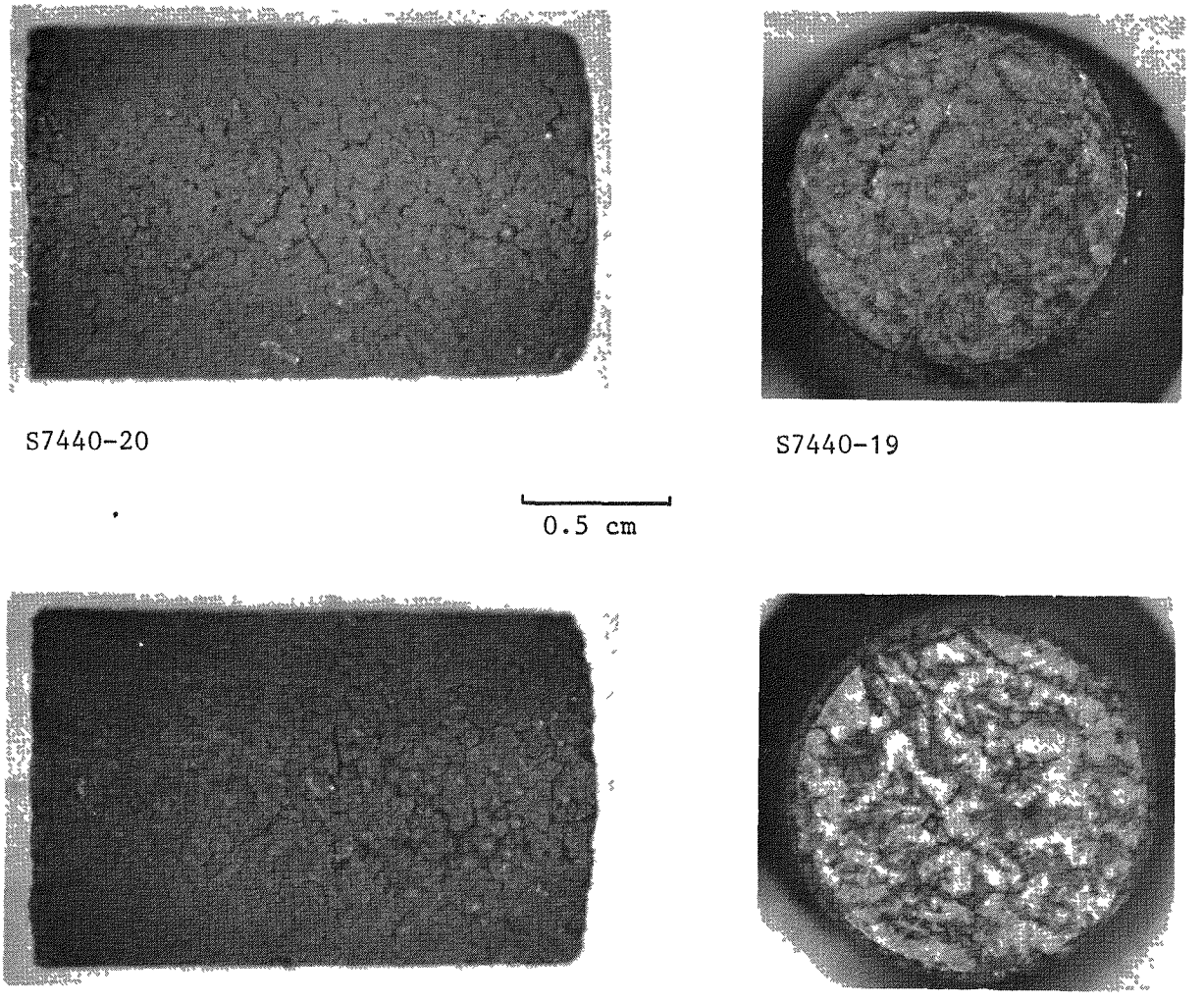

Fig. 9-27. Photomicrographs of fuel rod 7161-004-03-5 (top) after irradiation in capsule P13R (position 1C) to a fast neutron fluence of 8.8×10^{21} n/cm^2 (E > 0.18 MeV)$_{HTGR}$ at 1075°C (design) and of fuel rod 7161-004-03-6 (bottom) after irradiation in capsule P13S (position 1C) to a fast neutron fluence of 8.6×10^{21} n/cm^2 (E > 0.18 MeV)$_{HTGR}$. Cell No. 1 of capsule P13S was thermal cycled from 1075° to 1500°C (design) twenty-one times during irradiation.

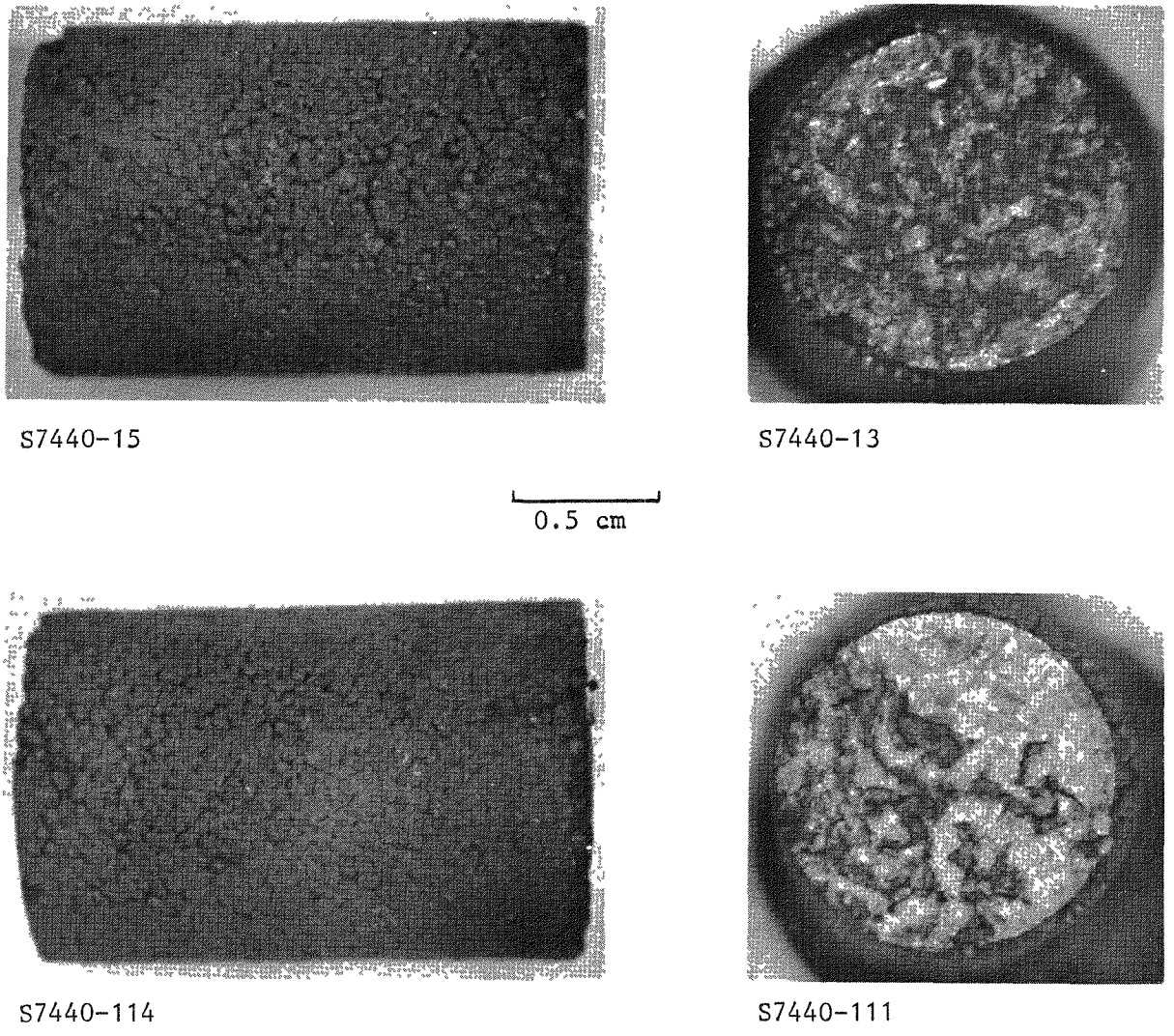

Fig. 9-28. Photomicrographs of fuel rod 7161-004-04-6 (top) after irradiation in capsule P13R (position 1D) to a fast neutron fluence of 9.4×10^{21} n/cm^2 (E > 0.18 MeV)$_{HTGR}$ at 1075°C (design) and of fuel rod 7161-004-04-5 (bottom) after irradiation in capsule P13S (position 1D) to a fast neutron fluence of 9.2×10^{21} n/cm^2 (E > 0.18 MeV)$_{HTGR}$. Cell No. 1 of capsule P13S was thermal cycled from 1075° to 1500°C (design) twenty-one times during irradiation.

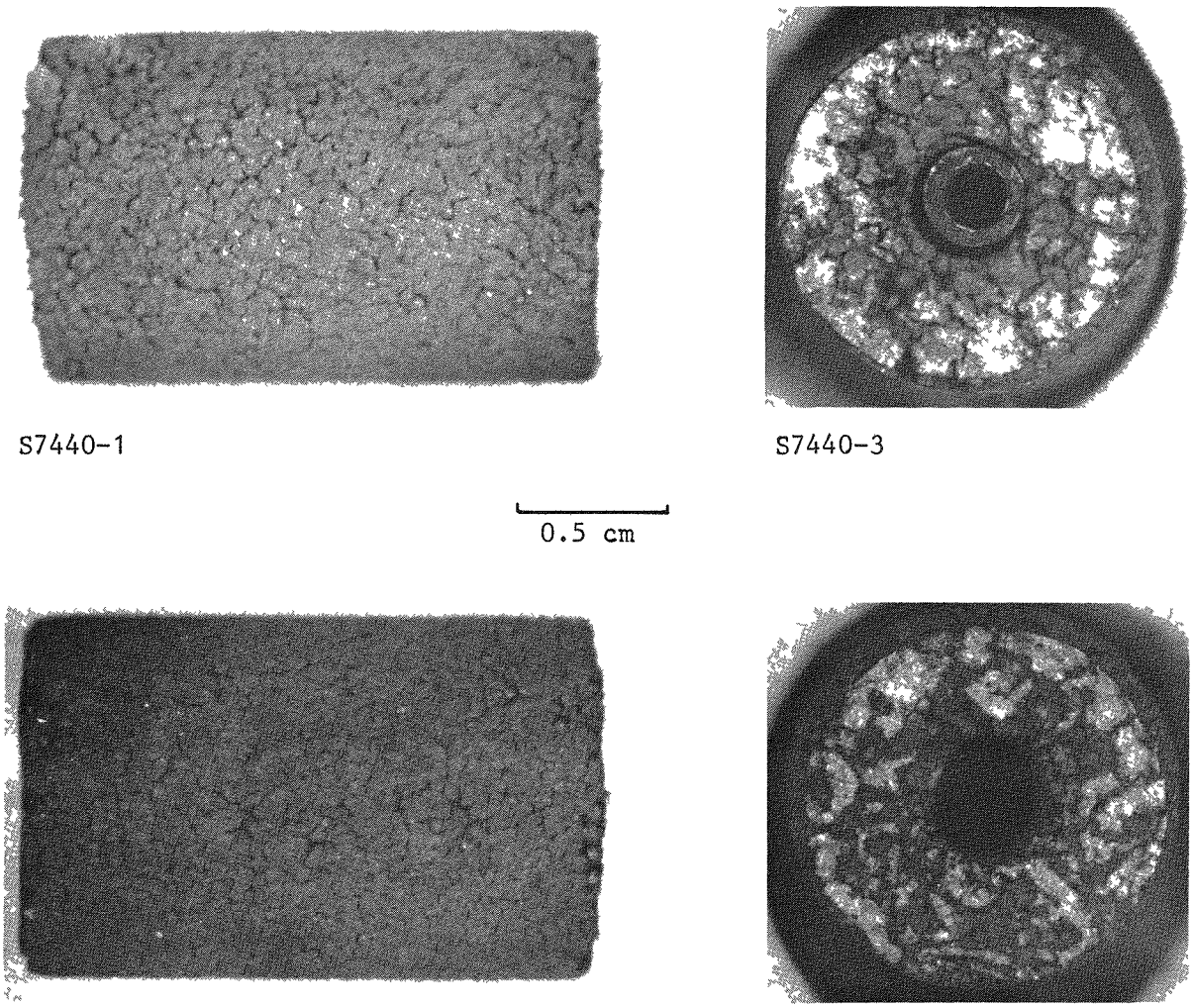

Fig. 9-29. Photomicrographs of fuel rod 7161-004-05-6 (top) after irradiation in capsule P13R (position 1E) to a fast neutron fluence of 10.0 x 10^{21} n/cm^2 (E > 0.18 MeV)$_{HTGR}$ at 1075°C (design) and of fuel rod 7161-004-05-5 (bottom) after irradiation in capsule P13S (position 1E) to a fast neutron fluence of 9.7 x 10^{21} n/cm^2 (E > 0.18 MeV)$_{HTGR}$. Cell No. 1 of capsule P13S was thermal cycled from 1075° to 1500°C (design) twenty-one times during irradiation.

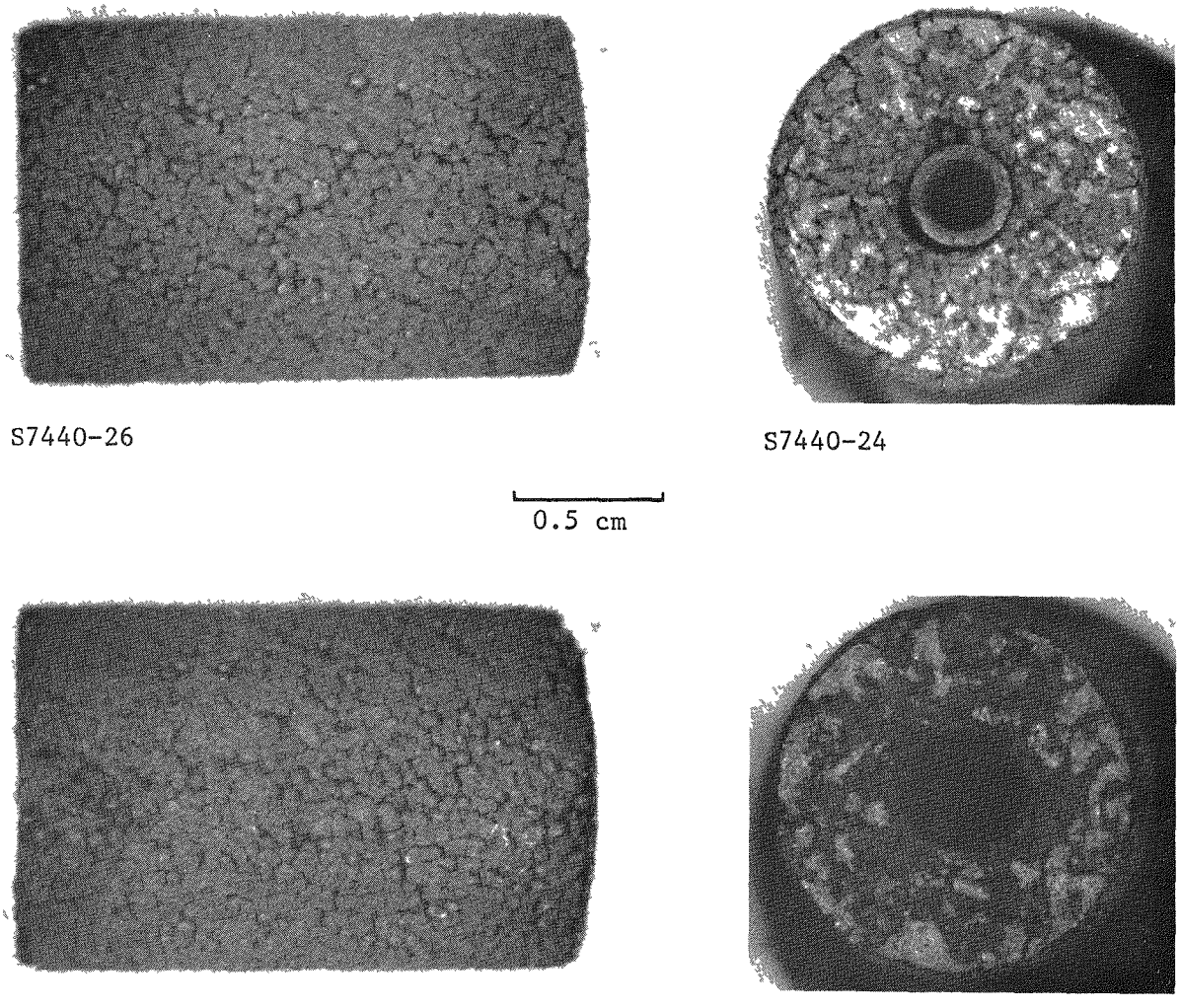

Fig. 9-30. Photomicrographs of fuel rod 7161-004-06-5 (top) after irradiation in capsule P13R (position 2A) to a fast neutron fluence of 12.0×10^{21} n/cm^2 (E > 0.18 MeV)$_{HTGR}$ at 1075°C (design) and of fuel rod 7161-004-11-6 (bottom) after irradiation in capsule P13S (position 2A) to a fast neutron fluence of 11.6×10^{21} n/cm^2 (E > 0.18 MeV)$_{HTGR}$ at 1075°C (design).

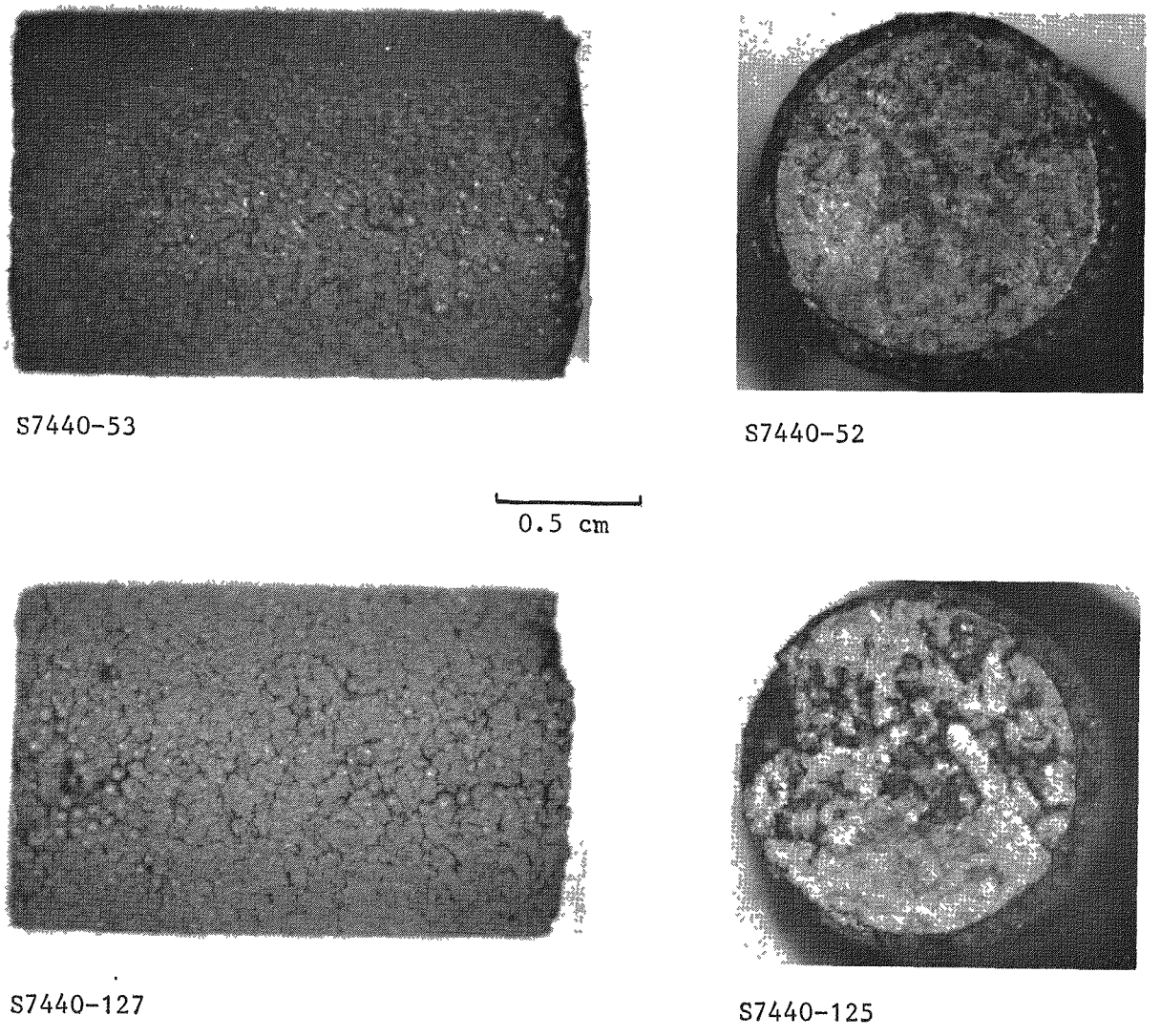

Fig. 9-31. Photomicrographs of fuel rod 7161-004-07-5 (top) after irradiation in capsule P13R (position 2B) to a fast neutron fluence of 12.2 x 10^{21} n/cm^2 (E > 0.18 MeV)$_{HTGR}$ at 1075°C (design) and of fuel rod 7161-004-12-5 (bottom) after irradiation in capsule P13S (position 2B) to a fast neutron fluence of 11.9 x 10^{21} n/cm^2 (E > 0.18 MeV)$_{HTGR}$ at 1075°C (design).

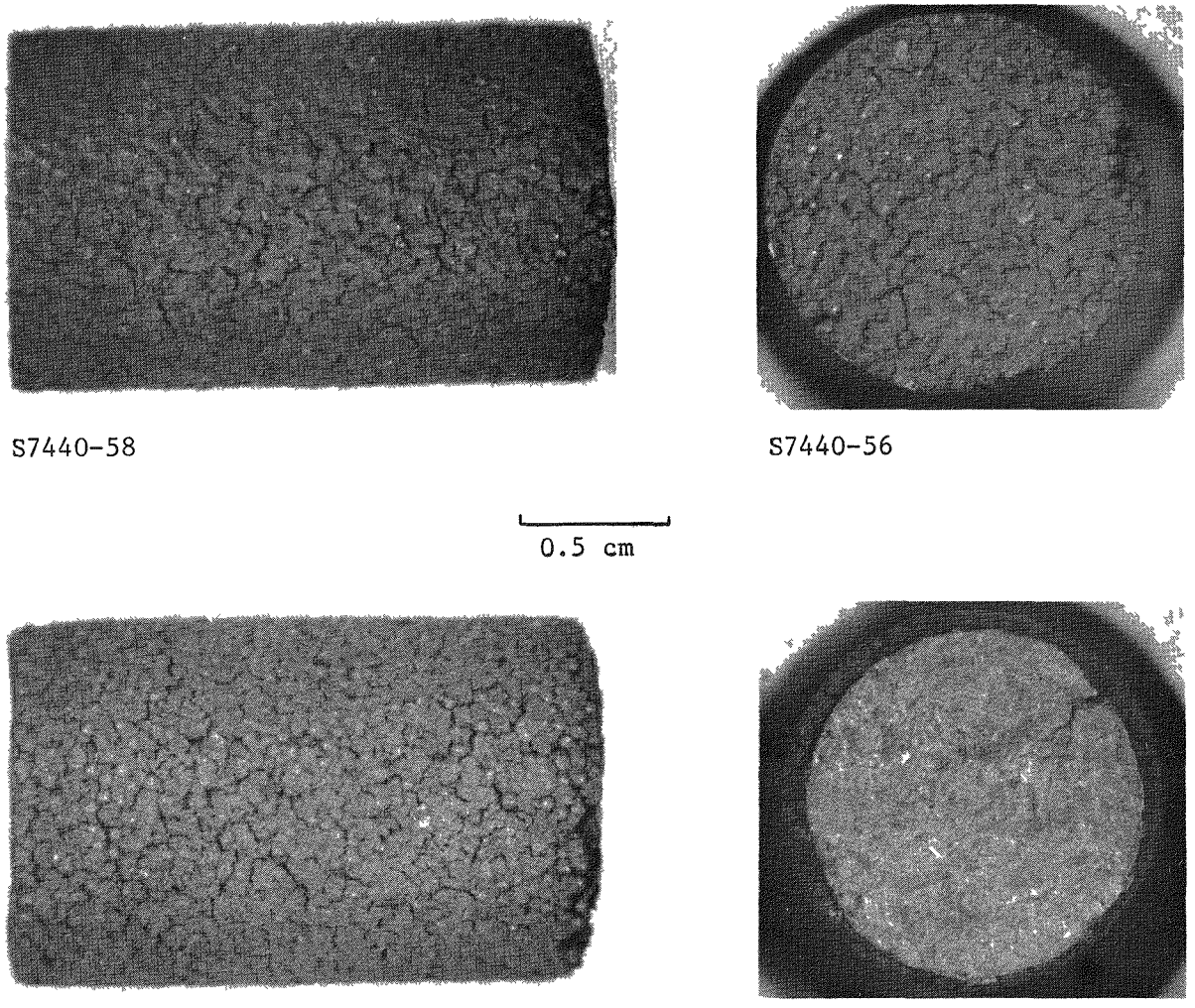

Fig. 9-32. Photomicrographs of fuel rod 7161-004-08-013 (top) after irradiation in capsule P13R (position 2C) to a fast neutron fluence of 12.3×10^{21} n/cm^2 (E > 0.18 MeV)$_{HTGR}$ at 1075°C (design) and of fuel rod 7161-004-13-6 (bottom) after irradiation in capsule P13S (position 2C) to a fast neutron fluence of 12.1×10^{21} n/cm^2 (E > 0.18 MeV)$_{HTGR}$ at 1075°C (design)

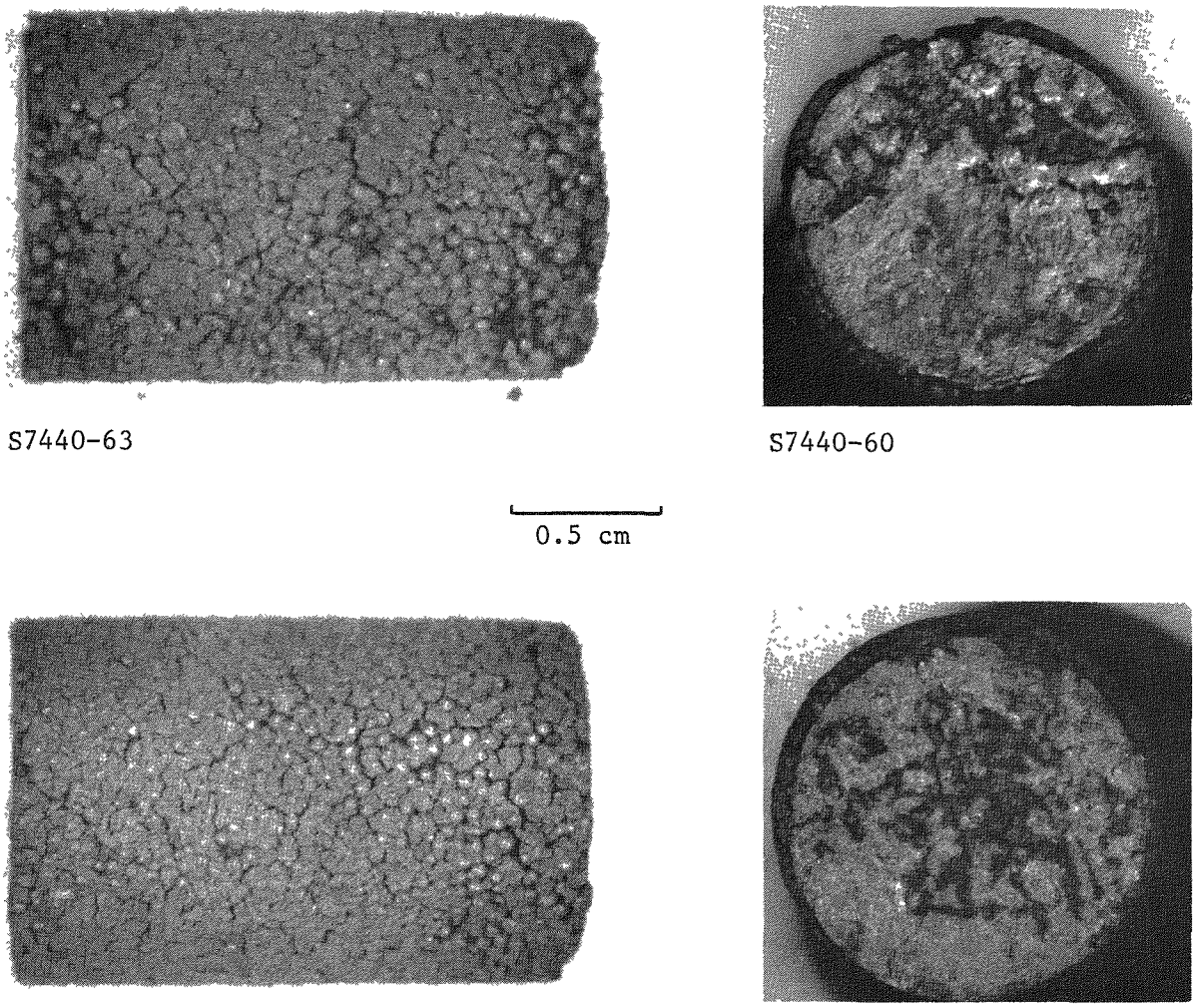

Fig. 9-33. Photomicrographs of fuel rod 7161-004-09-5 (top) after irradiation in capsule P13R (position 2D) to a fast neutron fluence of 12.4 x 10^{21} n/cm^2 (E > 0.18 MeV)$_{HTGR}$ at 1075°C (design) and of fuel rod 7161-004-14-5 (bottom) after irradiation in capsule P13S (position 2D) to a fast neutron fluence of 12.2 x 10^{21} n/cm^2 (E > 0.18 MeV)$_{HTGR}$ at 1075°C (design).

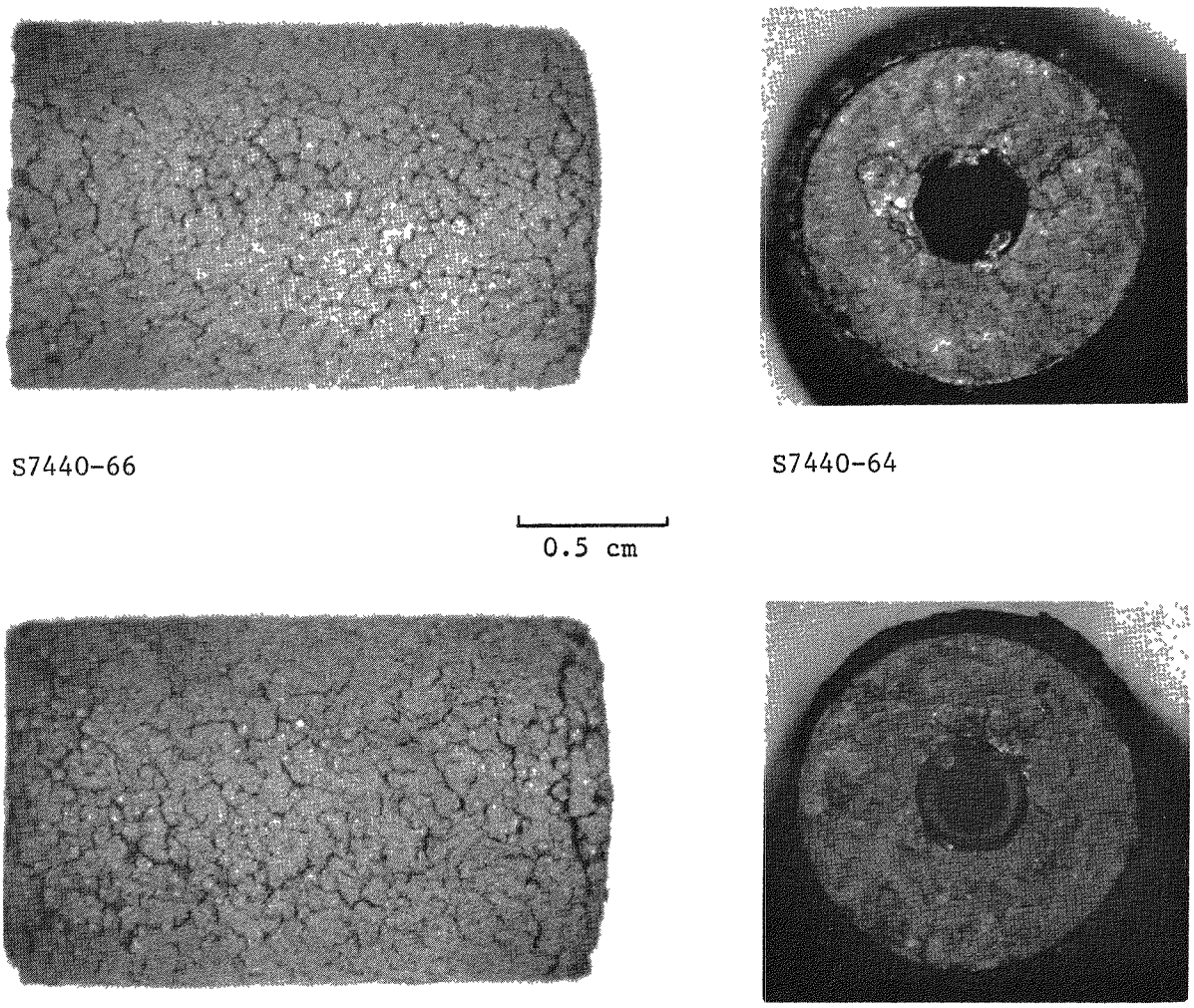

Fig. 9-34. Photomicrographs of fuel rod 7161-004-10-5 (top) after irradiation in capsule P13R (position 2E) to a fast neutron fluence of 12.5 x 10^{21} n/cm^2 (E > 0.18 MeV)$_{HTGR}$ at 1075°C (design) and of fuel rod 7161-004-15-5 (bottom) after irradiation in capsule P13S$_2$ (position 2E) to a fast neutron fluence of 12.2 x 10^{21} n/cm^2 (E > 0.18 MeV)$_{HTGR}$ at 1075°C (design).

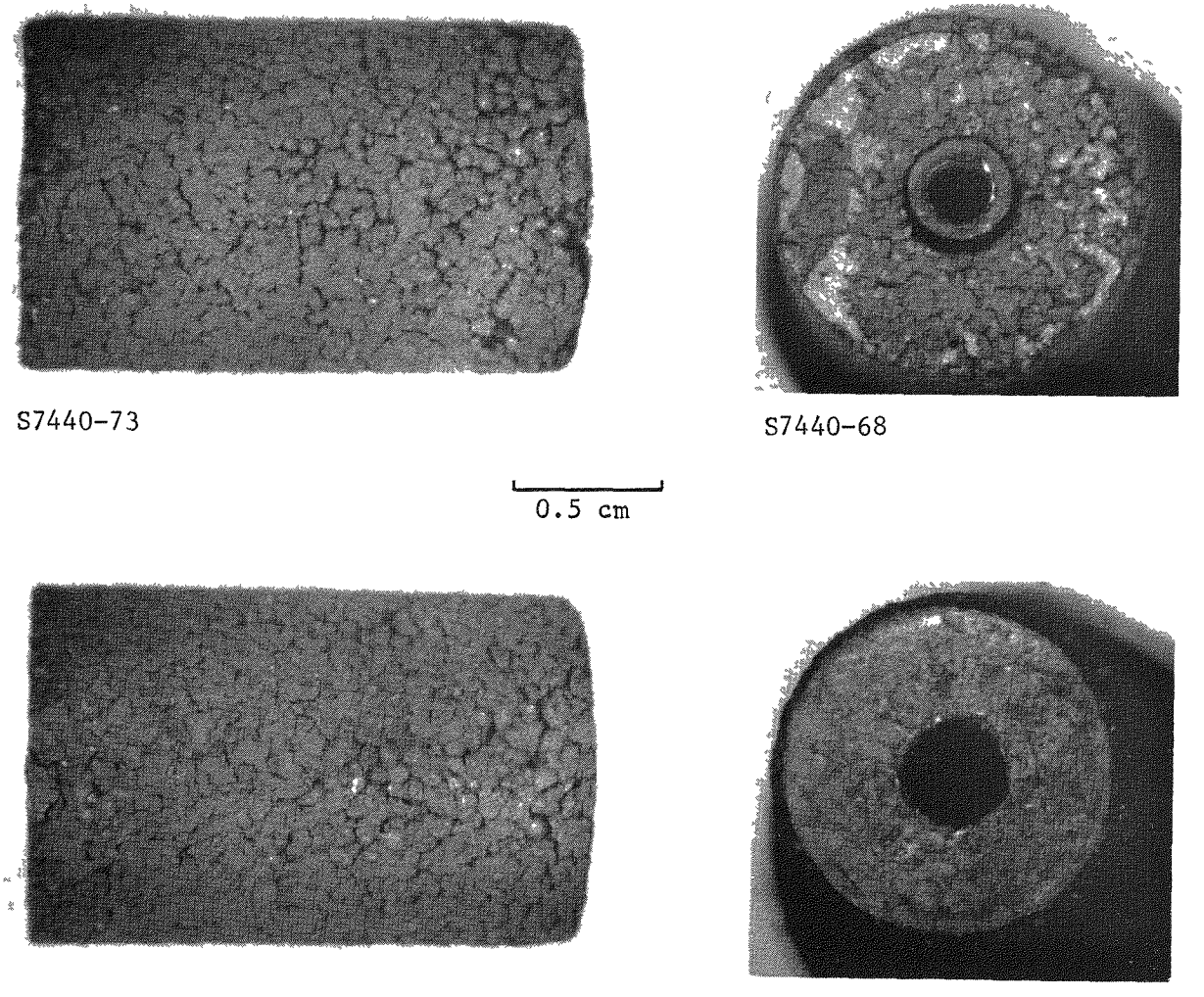

Fig. 9-35. Photomicrographs of fuel rod 7161-004-16-5 (top) after irradiation in capsule P13R (position 5A) to a fast neutron fluence of 9.5×10^{21} n/cm^2 (E > 0.18 MeV)$_{HTGR}$ at 1300°C (design) and of fuel rod 7161-004-16-6 (bottom) after irradiation in capsule P13S (position 5A) to a fast neutron fluence of 9.2×10^{21} n/cm^2 (E > 0.18 MeV)$_{HTGR}$ at 1500°C (design).

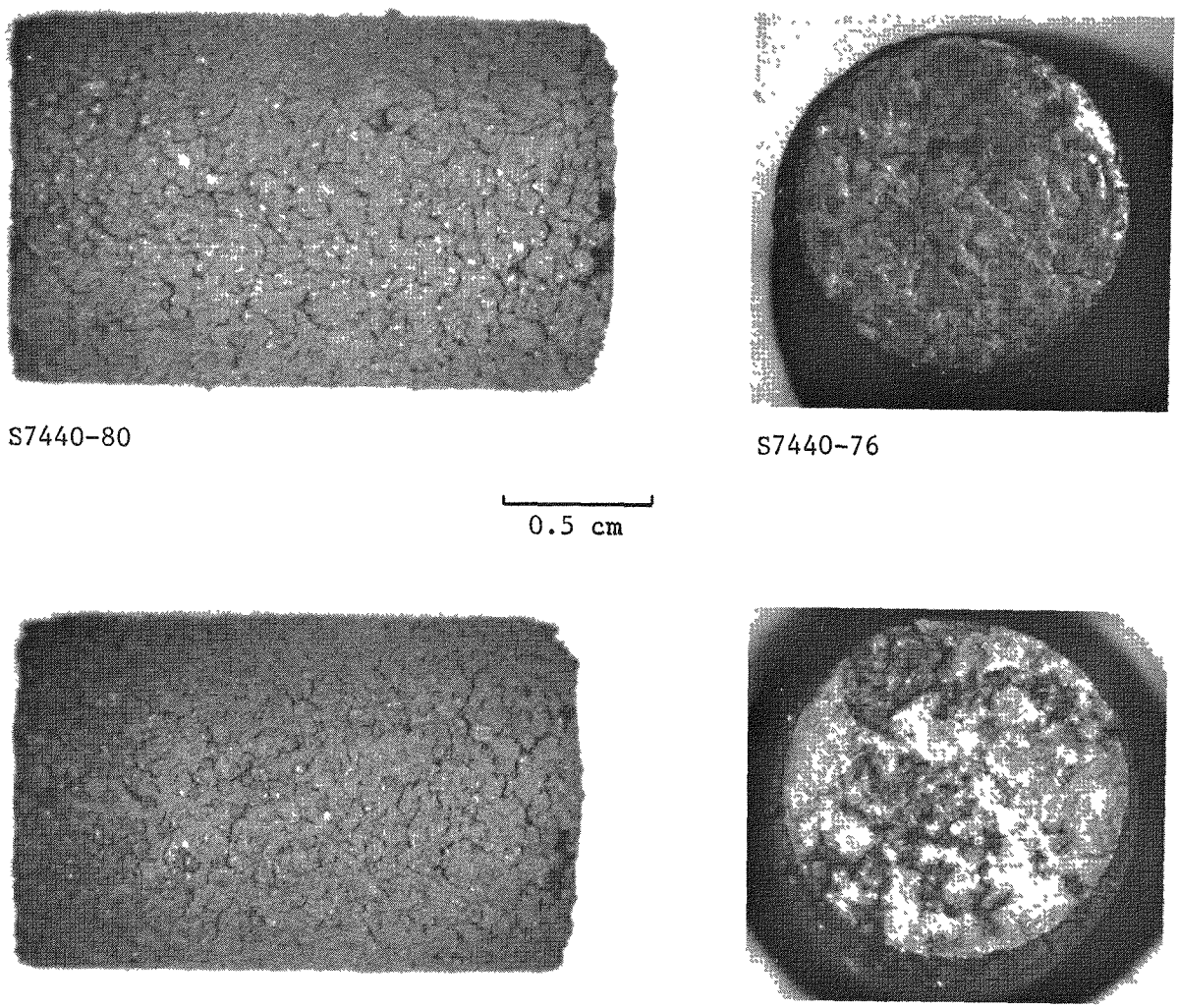

Fig. 9-36. Photomicrographs of fuel rod 7161-004-17-5 (top) after irradiation in capsule P13R (position 5B) to a fast neutron fluence of 9.1×10^{21} n/cm^2 (E > 0.18 MeV)$_{HTGR}$ at 1300°C (design) and of fuel rod 7161-004-17-6 (bottom) after irradiation in capsule P13S$_2$ (position 5B) to a fast neutron fluence of 8.8×10^{21} n/cm^2 (E > 0.18 MeV)$_{HTGR}$ at 1500°C (design).

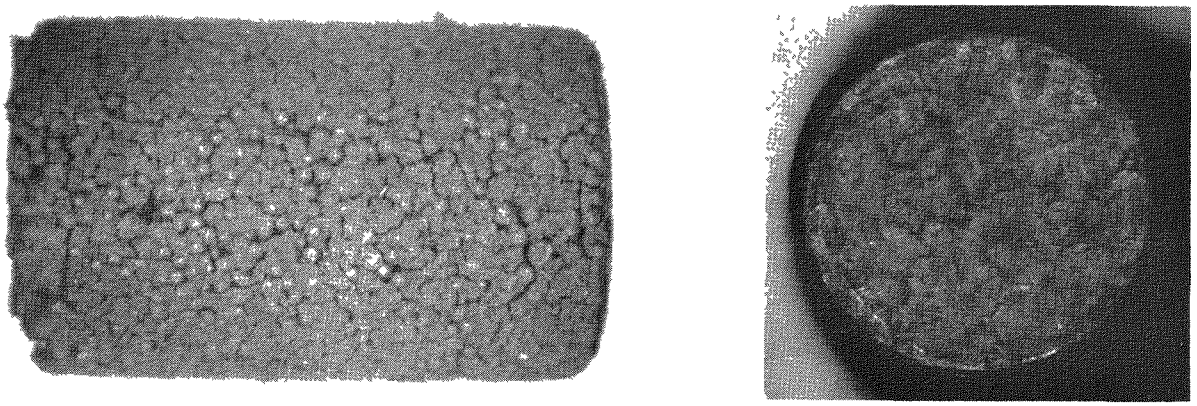

S7440-84 S7440-83

0.5 cm

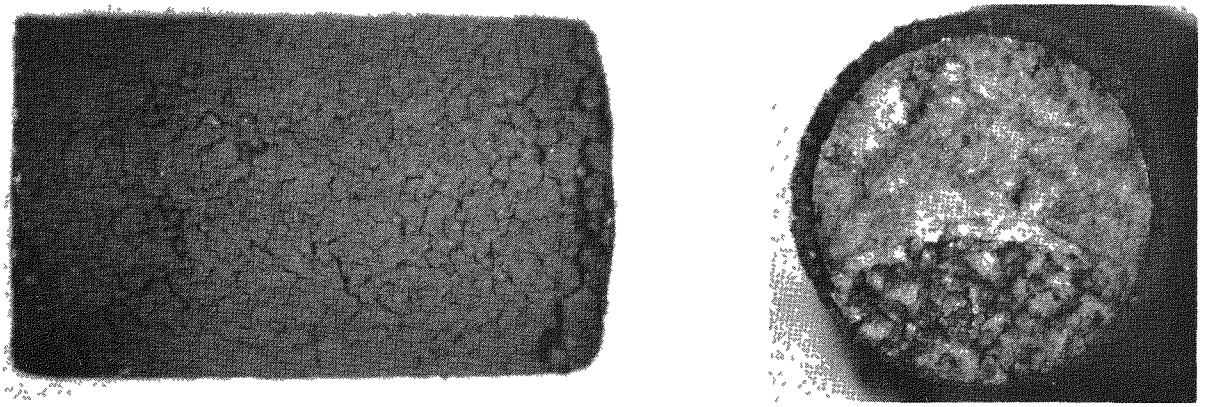

S7440-153 S7440-152

Fig. 9-37. Photomicrographs of fuel rod 7161-004-18-6 (top) after irradiation in capsule P13R (position 5C) to a fast neutron fluence of 8.6×10^{21} n/cm^2 (E > 0.18 MeV)$_{HTGR}$ at 1300°C (design) and of fuel rod 7161-004-18-5 (bottom) after irradiation in capsule P13S (position 5C) to a fast neutron fluence of 8.5×10^{21} n/cm^2 (E > 0.18 MeV)$_{HTGR}$ at 1500°C (design).

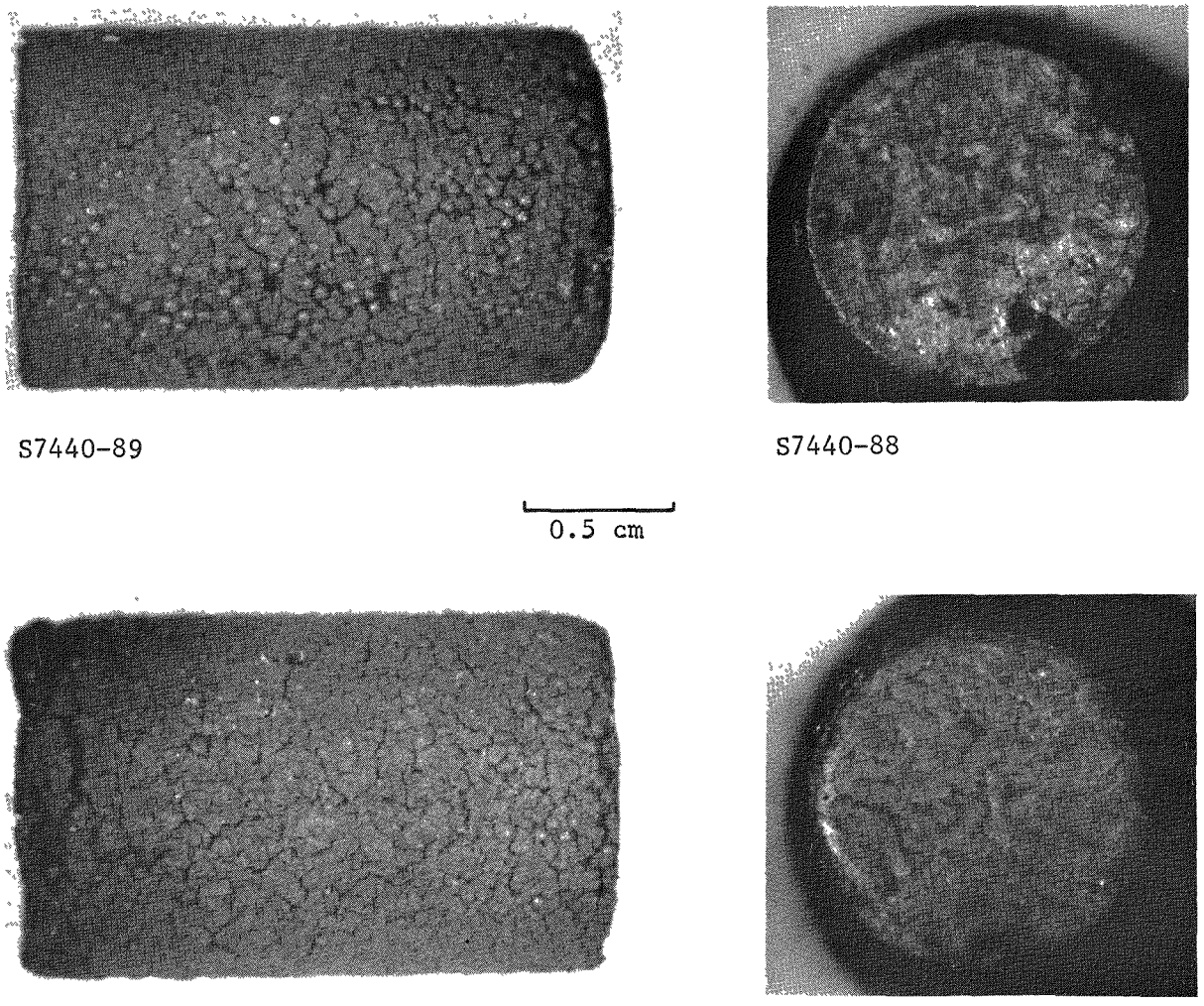

Fig. 9-38. Photomicrographs of fuel rod 7161-004-19-7 (top) after irradiation in capsule P13R (position 5D) to a fast neutron fluence of 6.3×10^{21} n/cm^2 (E > 0.18 MeV)$_{HTGR}$ at 1300°C (design) and of fuel rod 7161-004-19-5 (bottom) after irradiation in capsule P13S (position 5D) to a fast neutron fluence of 8.0×10^{21} n/cm^2 (E > 0.18 MeV)$_{HTGR}$ at 1500°C (design).

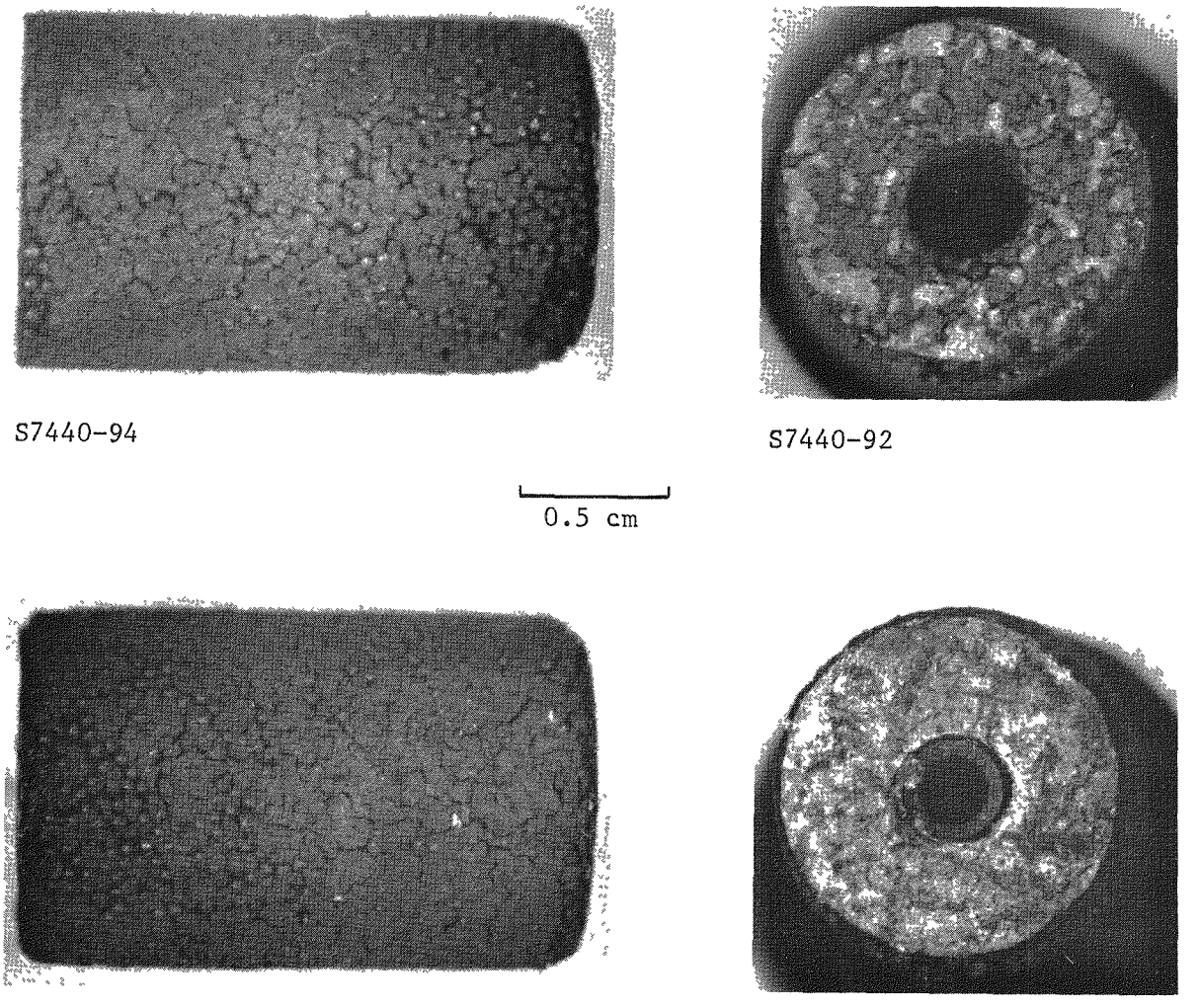

Fig. 9-39. Photomicrographs of fuel rod 7161-004-20-6 (top) after irradiation in capsule P13R (position 5E) to a fast neutron fluence of 7.8×10^{21} n/cm^2 (E > 0.18 MeV)$_{HTGR}$ at 1300°C (design) and of fuel rod 7161-004-20-5 (bottom) after irradiation in capsule P13S (position 5E) to a fast neutron fluence of 7.6×10^{21} n/cm^2 (E > 0.18 MeV)$_{HTGR}$ at 1500°C (design).

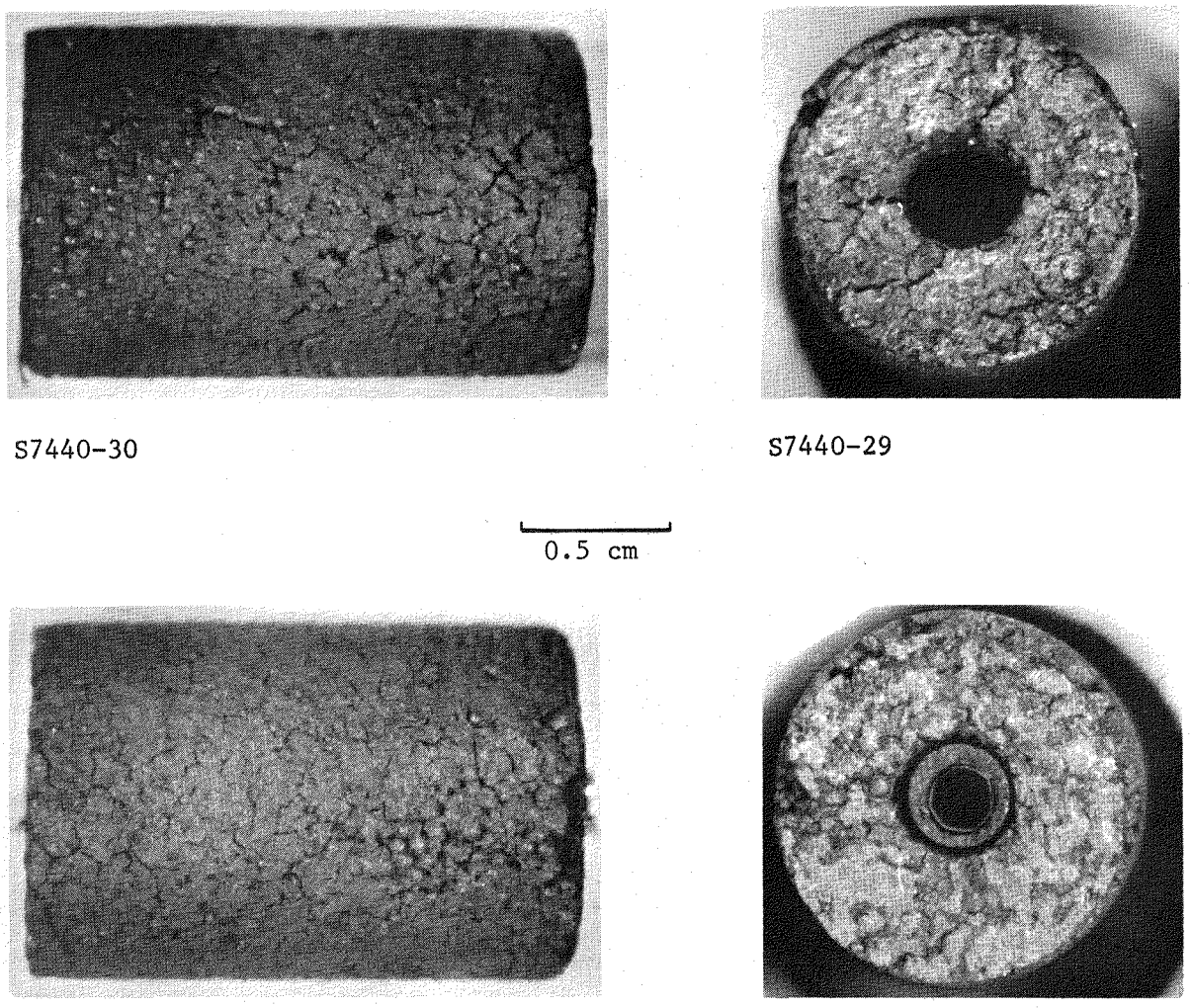

Fig. 9-40. Photomicrographs of fuel rod 7161-004-21-5 (top) after irradiation in capsule P13R (position 6A) to a fast neutron fluence of 5.5×10^{21} n/cm^2 (E > 0.18 MeV)$_{HTGR}$ at 1075°C (design) and of fuel rod 7161-004-26-5 (bottom) after irradiation in capsule P13S (position 6A) to a fast neutron fluence of 5.3×10^{21} n/cm^2 (E > 0.18 MeV)$_{HTGR}$ at 1075°C (design).

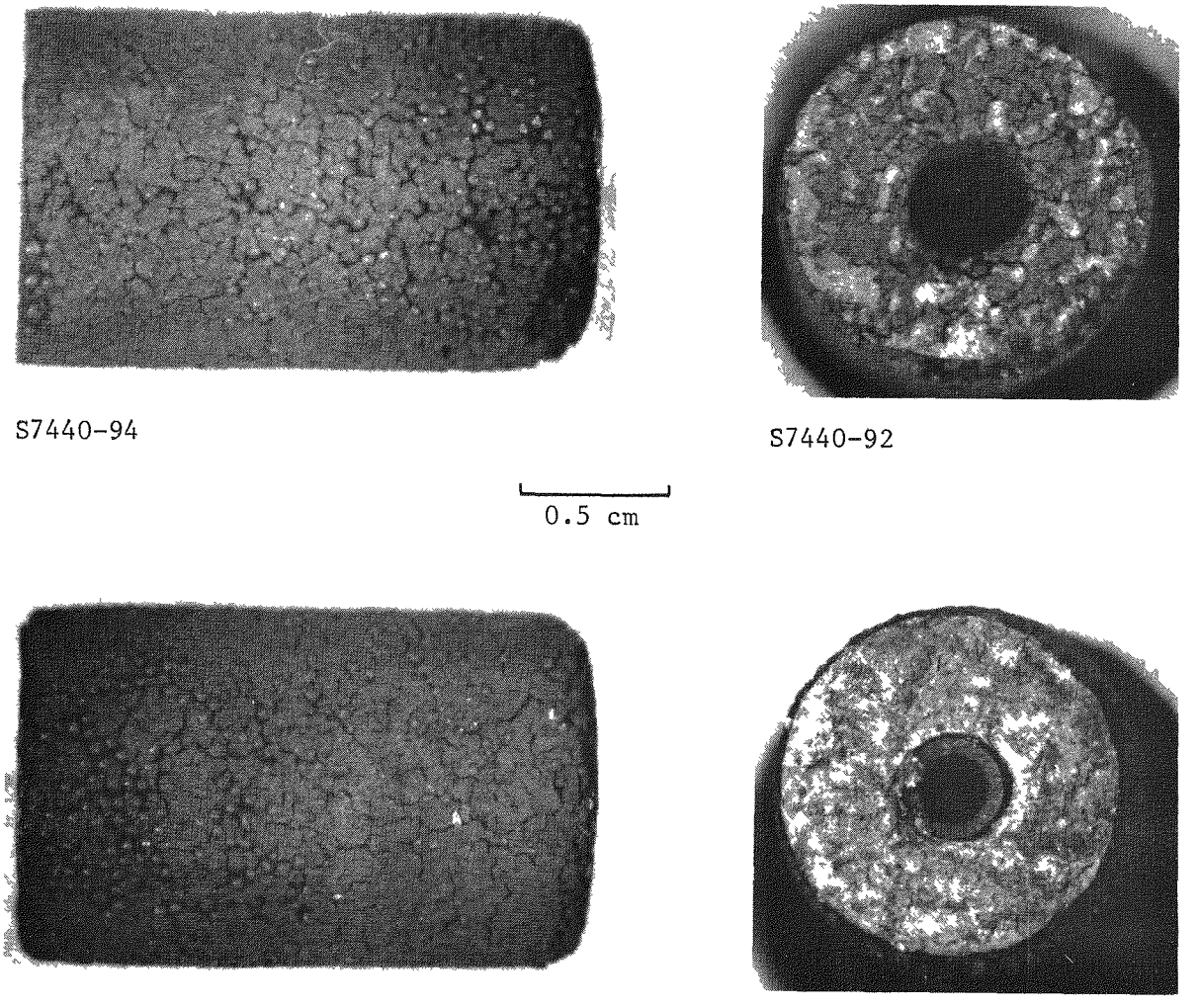

Fig. 9-39. Photomicrographs of fuel rod 7161-004-20-6 (top) after irradiation in capsule P13R (position 5E) to a fast neutron fluence of 7.8×10^{21} n/cm^2 (E > 0.18 MeV)$_{HTGR}$ at 1300°C (design) and of fuel rod 7161-004-20-5 (bottom) after irradiation in capsule P13S (position 5E) to a fast neutron fluence of 7.6×10^{21} n/cm^2 (E > 0.18 MeV)$_{HTGR}$ at 1500°C (design).

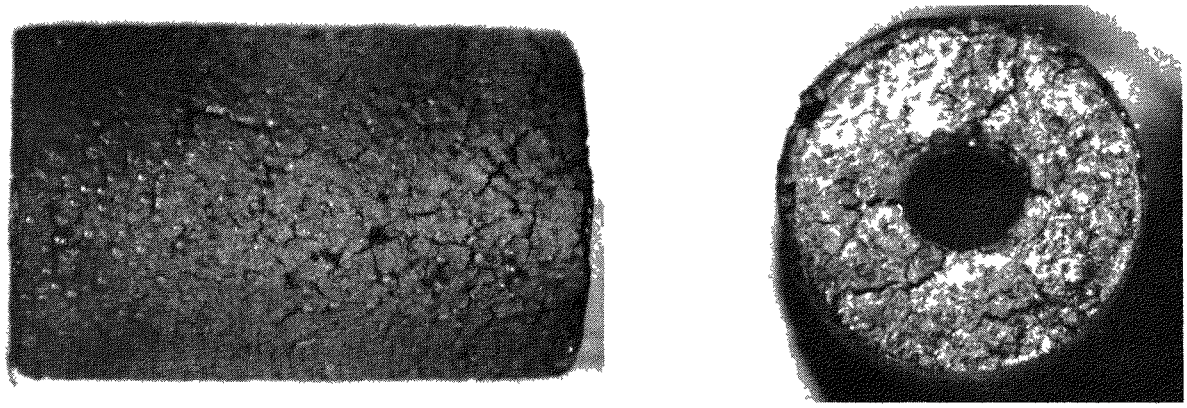

S7440-30 S7440-29

0.5 cm

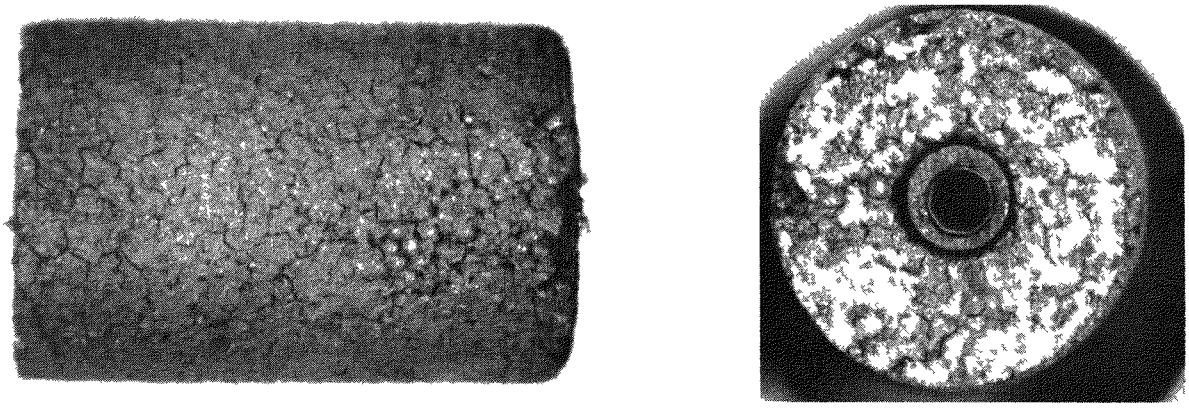

S7440-169 S7440-166

Fig. 9-40. Photomicrographs of fuel rod 7161-004-21-5 (top) after irradiation in capsule P13R (position 6A) to a fast neutron fluence of 5.5×10^{21} n/cm^2 (E > 0.18 MeV)$_{HTGR}$ at 1075°C (design) and of fuel rod 7161-004-26-5 (bottom) after irradiation in capsule P13S (position 6A) to a fast neutron fluence of 5.3×10^{21} n/cm^2 (E > 0.18 MeV)$_{HTGR}$ at 1075°C (design).

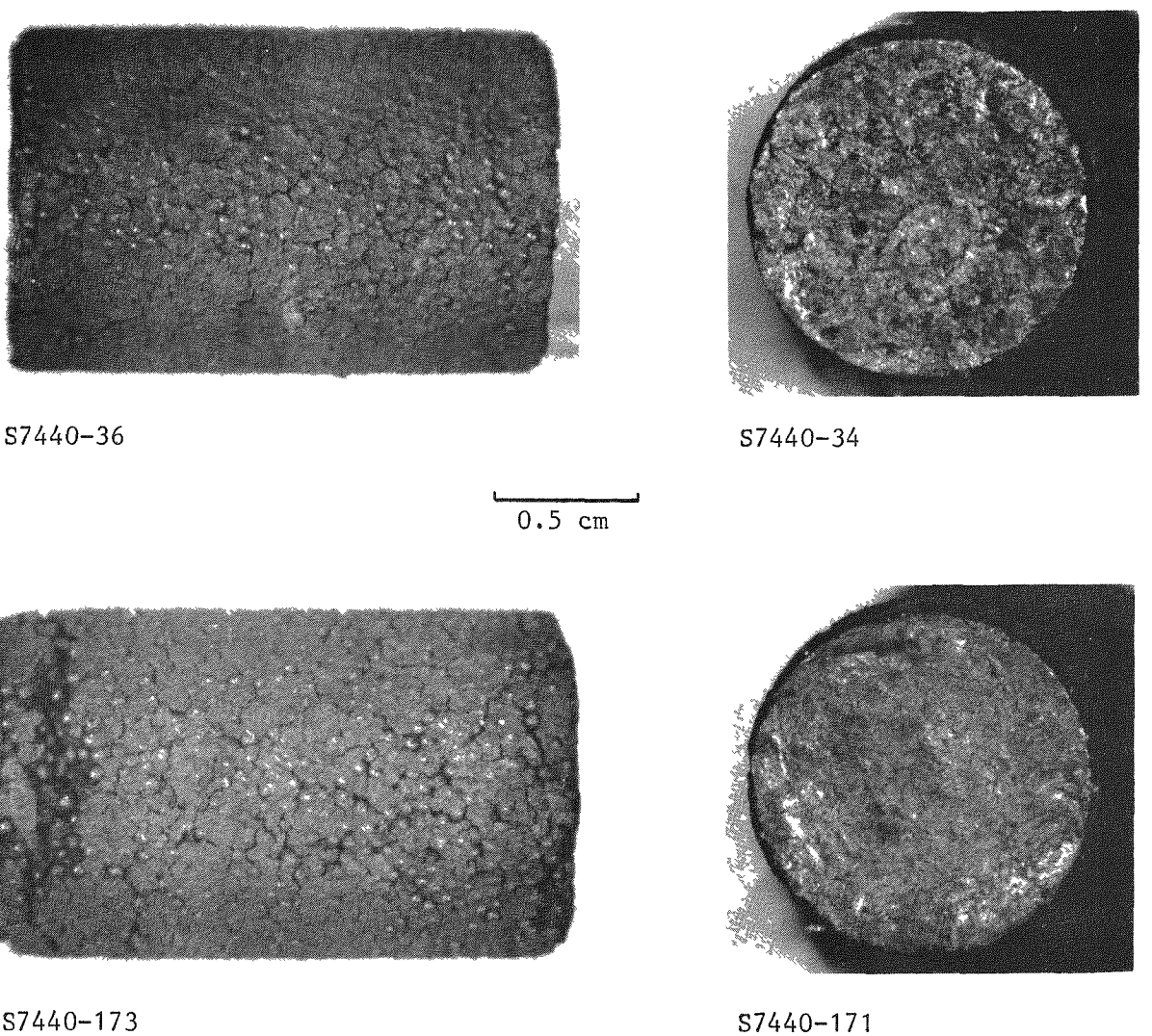

Fig. 9-41. Photomicrographs of fuel rod 7161-004-22-5 (top) after irradiation in capsule P13R (position 6B) to a fast neutron fluence of 5.0×10^{21} n/cm^2 (E > 0.18 MeV)$_{HTGR}$ at 1075°C (design) and of fuel rod 7161-004-27-5 (bottom) after irradiation in capsule P13S (position 6B) to a fast neutron fluence of 4.9×10^{21} n/cm^2 (E > 0.18 MeV)$_{HTGR}$ at 1075°C (design).

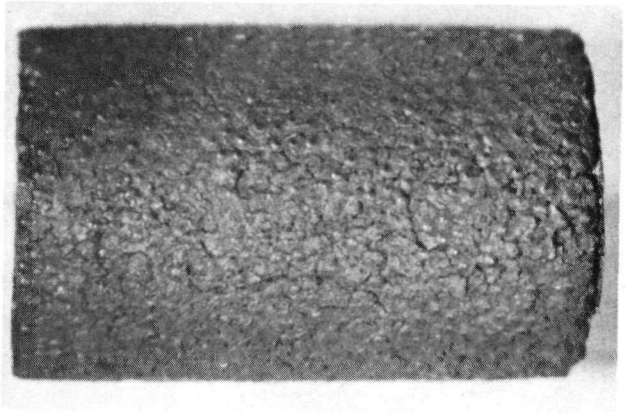

S7440-40

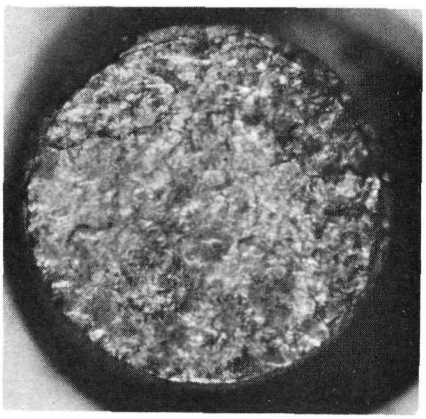

S7440-38

0.5 cm

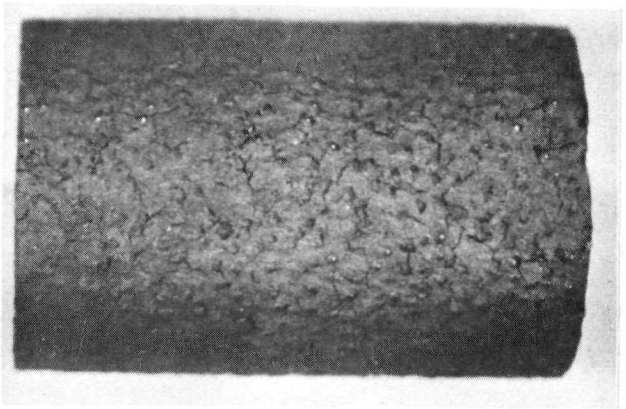

S7440-176

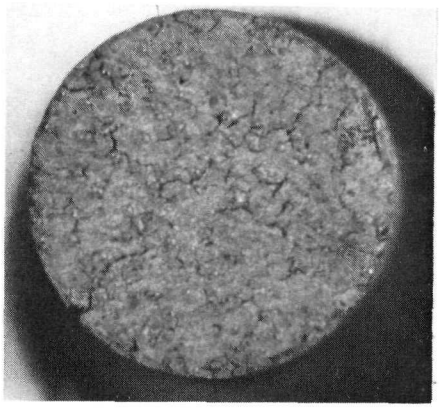

S7440-174

Fig. 9-42. Photomicrographs of fuel rod 7161-004-23-5 (top) after irradiation in capsule P13R (position 6C) to a fast neutron fluence of 4.6×10^{21} n/cm^2 (E > 0.18 MeV)$_{HTGR}$ at 1075°C (design) and of fuel rod 7161-004-28-13 (bottom) after irradiation in capsule P13S (position 6C) to a fast neutron fluence of 4.4×10^{21} (E > 0.18 MeV)$_{HTGR}$ at 1075°C (design).

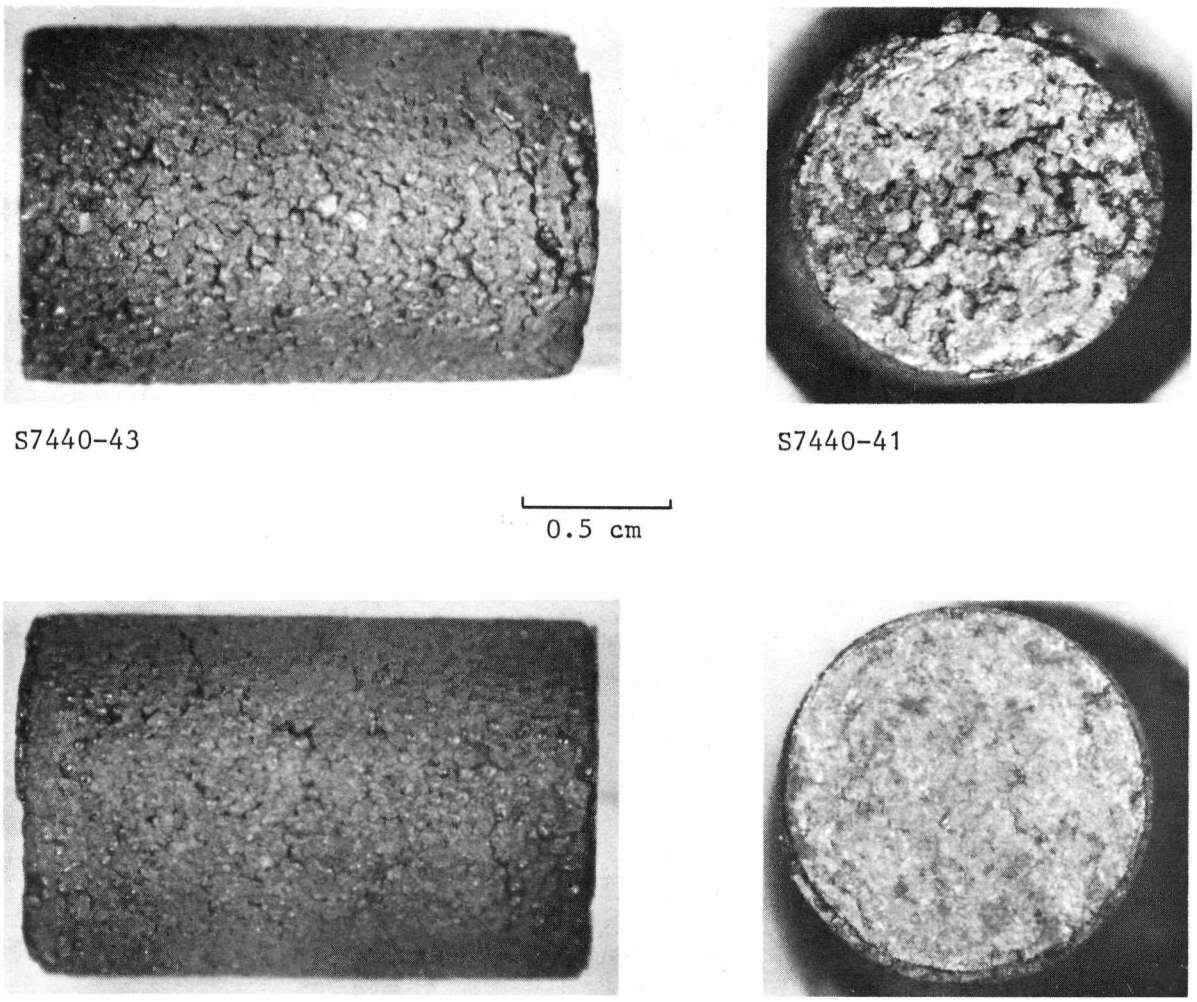

Fig. 9-43. Photomicrographs of fuel rod 7161-004-24-5 (top) after irradiation in capsule P13R (position 6D) to a fast neutron fluence of 4.1 x 10^{21} n/cm^2 (E > 0.18 MeV)$_{HTGR}$ at 1075°C (design) and of fuel rod 7161-004-29-5 (bottom) after irradiation in capsule P13S (position 6D) to a fast neutron fluence of 4.0 x 10^{21} n/cm^2 (E > 0.18 MeV)$_{HTGR}$ at 1075°C (design).

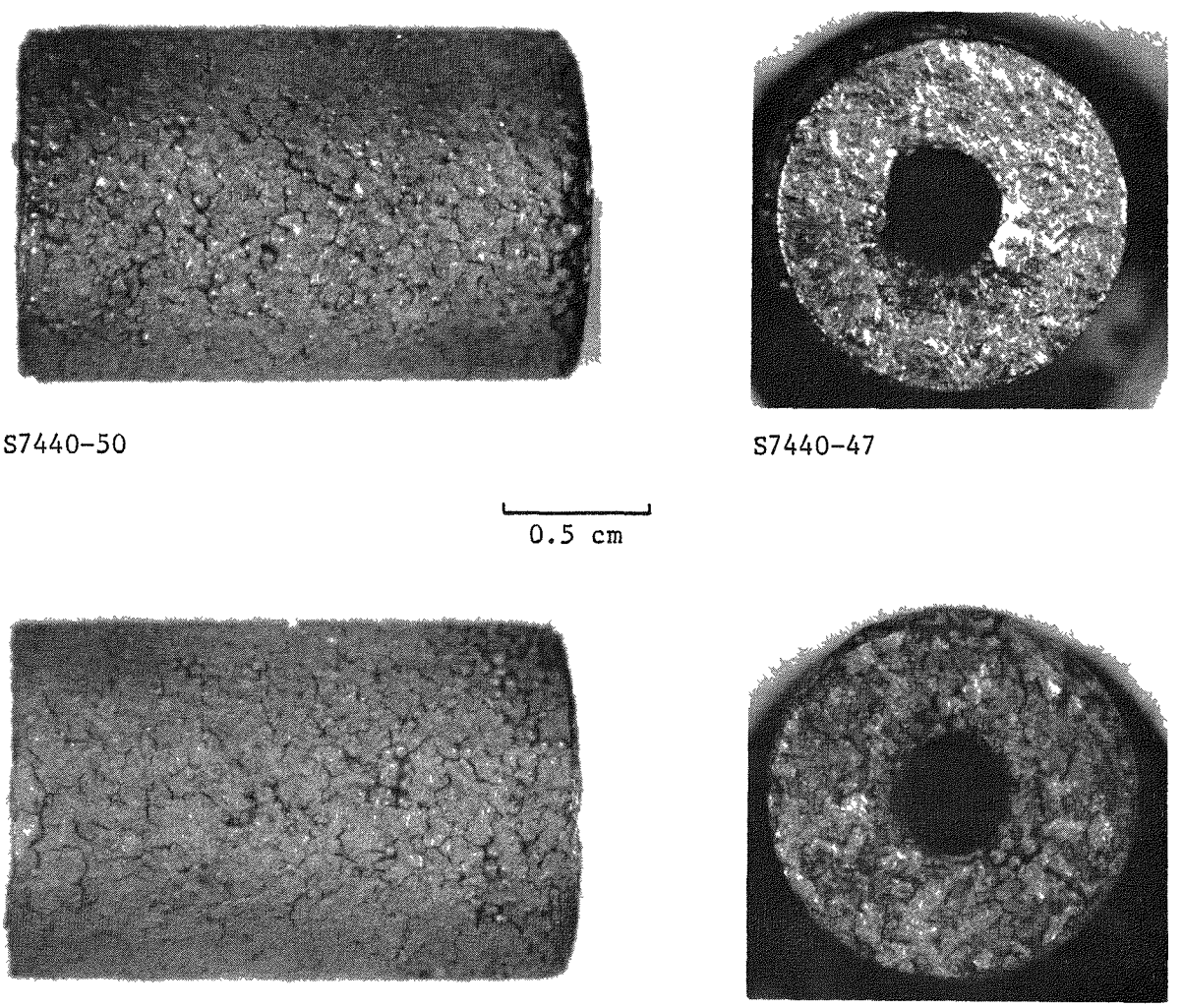

Fig. 9-44. Photomicrographs of fuel rod 7161-004-25-5 (top) after irradiation in capsule P13R (position 6E) to a fast neutron fluence of 3.7×10^{21} n/cm^2 (E > 0.18 MeV)$_{HTGR}$ at 1075°C (design) and of fuel rod 7161-004-30-5 (bottom) after irradiation in capsule P13S (position 6E) to a fast neutron fluence of 3.5×10^{21} n/cm^2 (E > 0.18 MeV)$_{HTGR}$ at 1075°C (design).

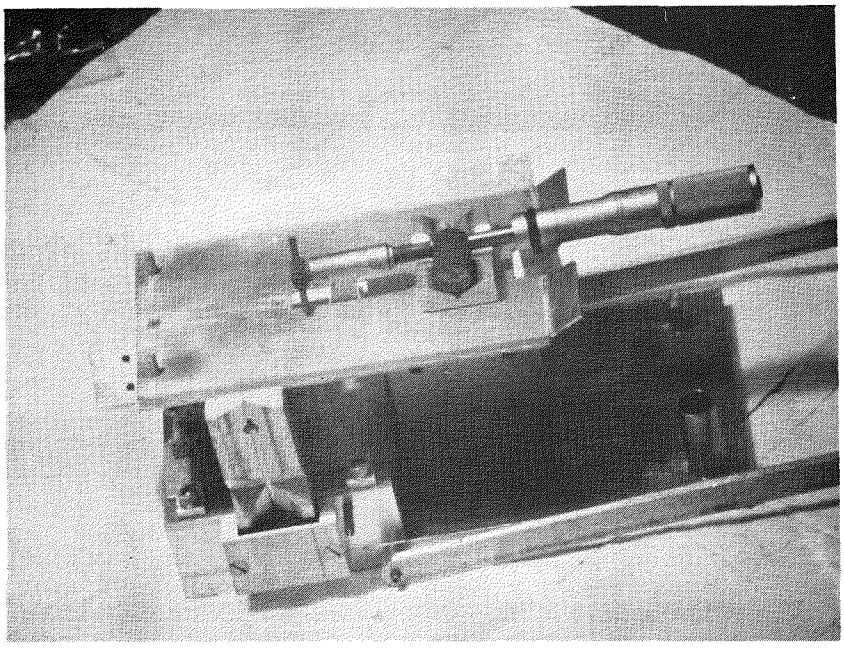

K7440-31 (a)

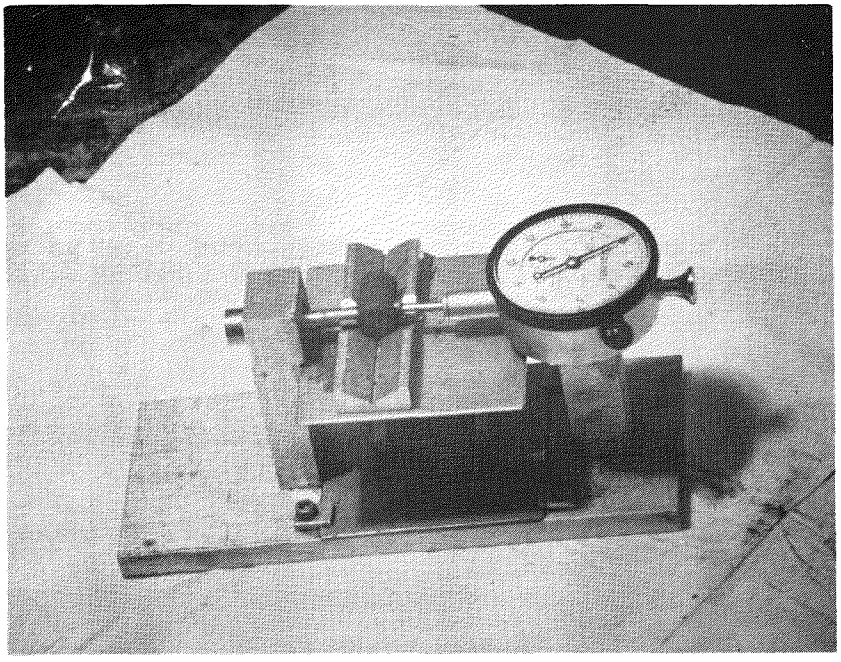

K7440-32 (b)

Fig. 9-45. Photomicrographs showing fuel rod dimensional measurements being made using: (a) micrometer and (b) dial gage

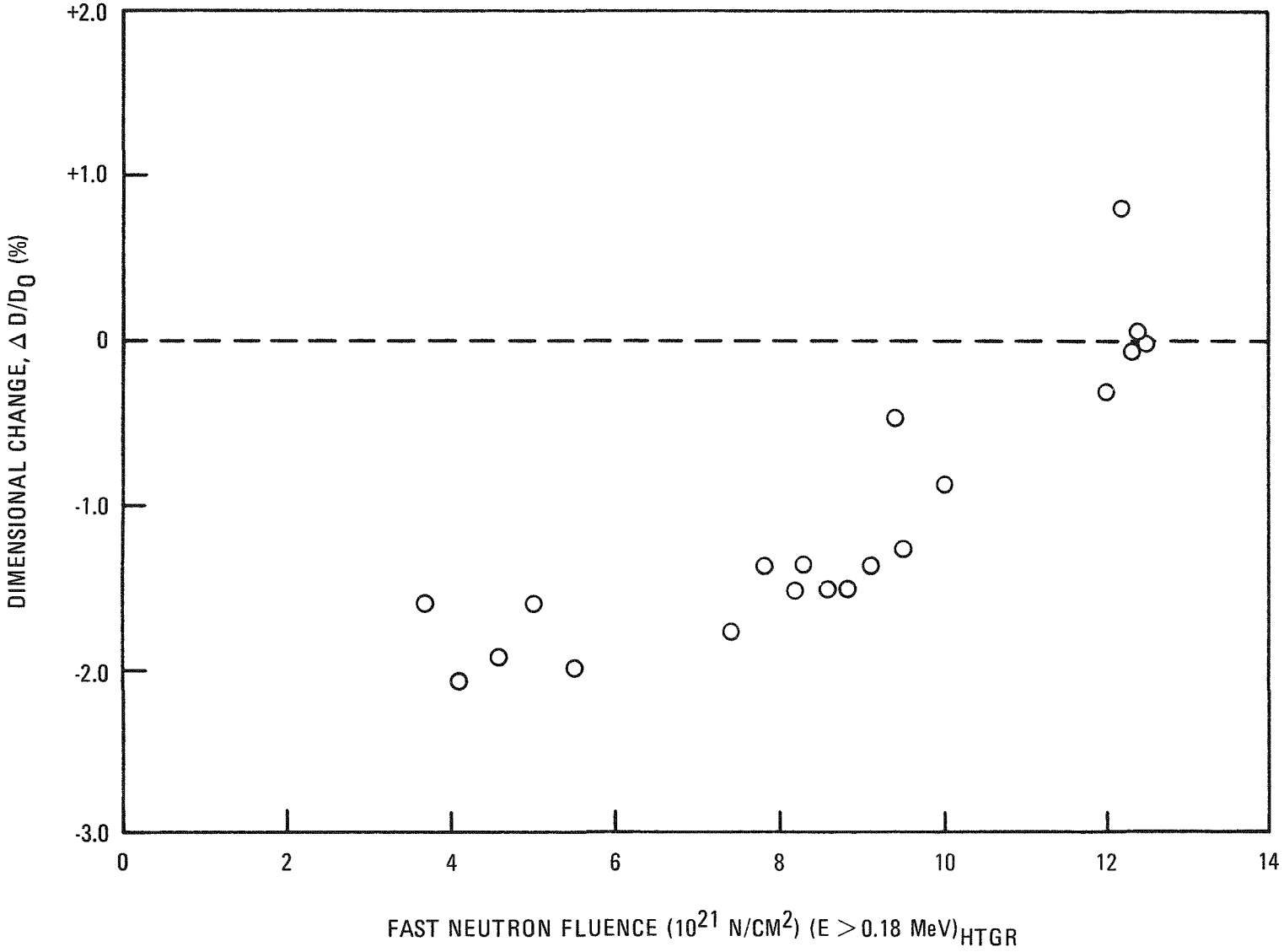

Fig. 9-46. Measured diametral dimensional change of fuel rods irradiated in capsule P13R

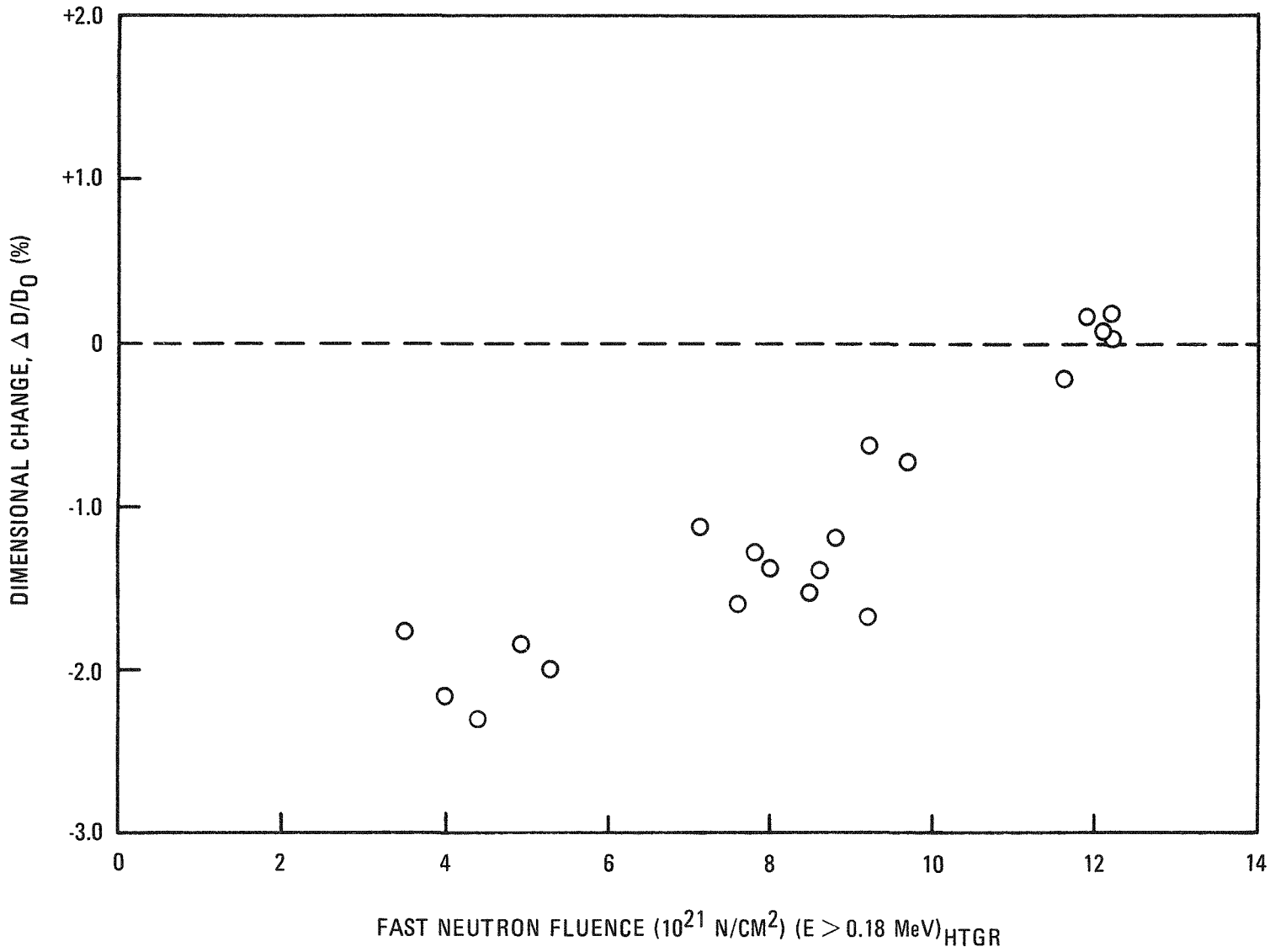

Fig. 9-47. Measured diametral dimensional change of fuel rods irradiated in capsule P13S

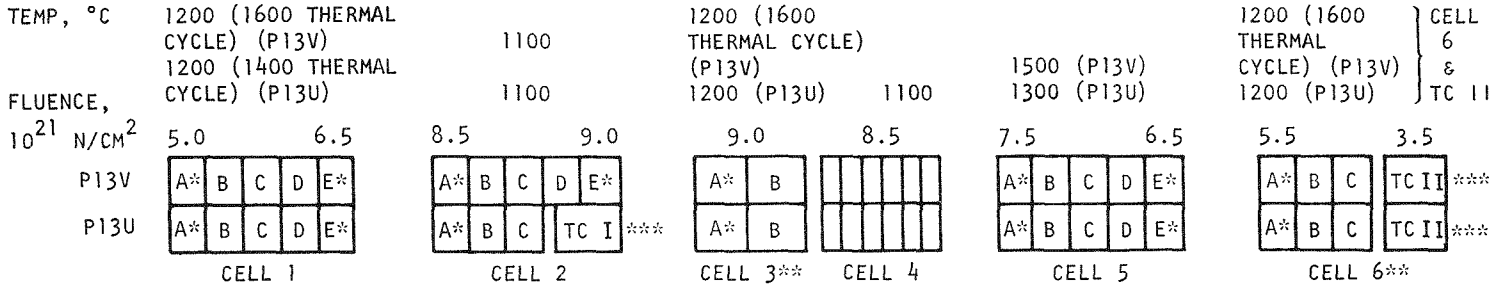

38 FUEL RODS, 12.5 mm IN DIAMETER BY 19.0 mm LONG (CELLS 1, 2, 3, 5, AND 6)

8 TO 10 FISSILE PARTICLE SAMPLES AND 8 TO 10 FERTILE PARTICLE SAMPLES (UNBONDED PARTICLE CELL 4)

*THERMOCOUPLE RODS

**CELL 3: ThO_2 BISO PARTICLES ONLY (IN FUEL RODS)

CELL 6: WAR TRISO PARTICLES ONLY (IN FUEL RODS)

***THERMOCOUPLE CELLS

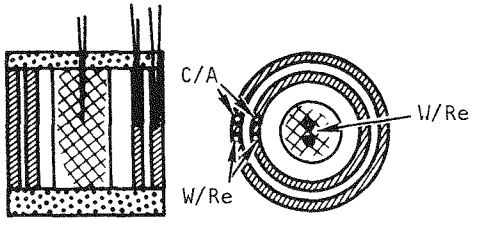

Fig. 9-48. Schematic layout showing temperature-fluence conditions for capsules P13U and P13V

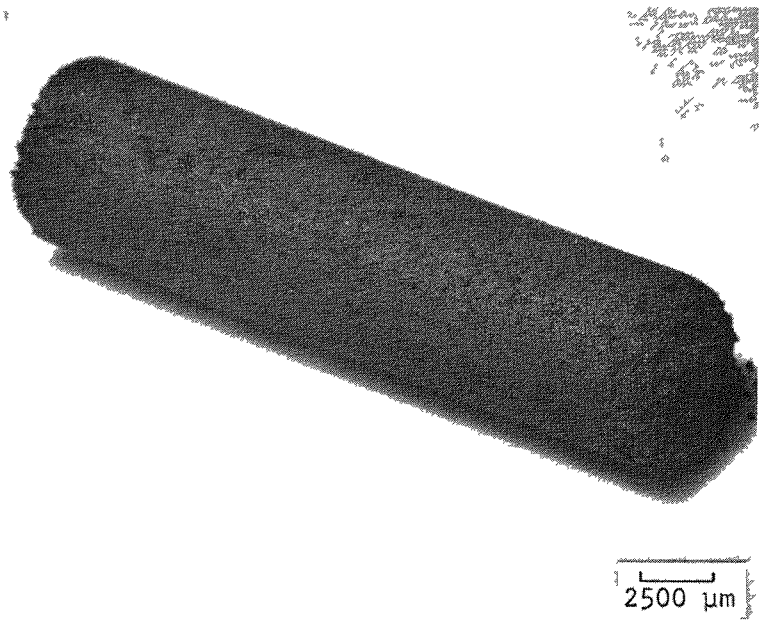

K7430-1

Fig. 9-49. Visual examination of RTE-2 fuel rod 6-1-2

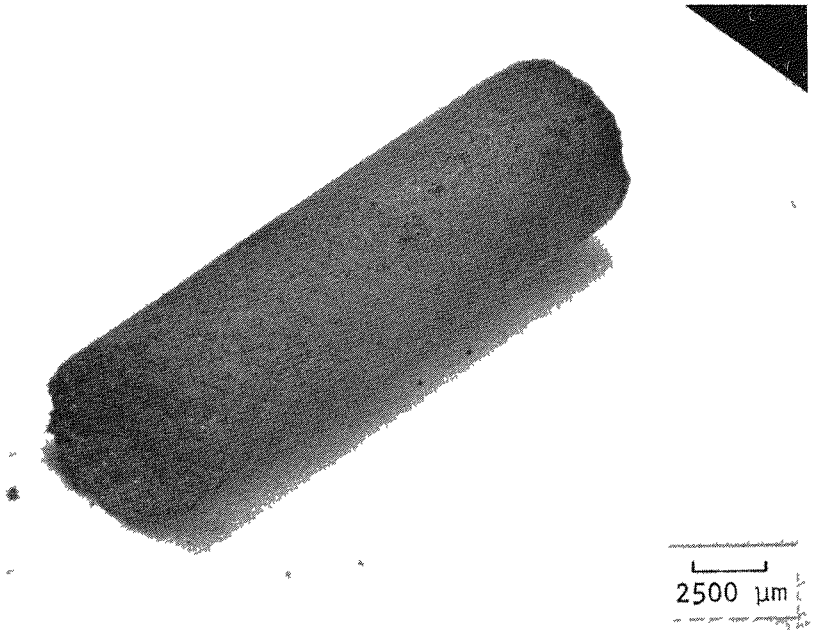

K7430-2

Fig. 9-50. Visual examination of RTE-2 fuel rod 6-1-3

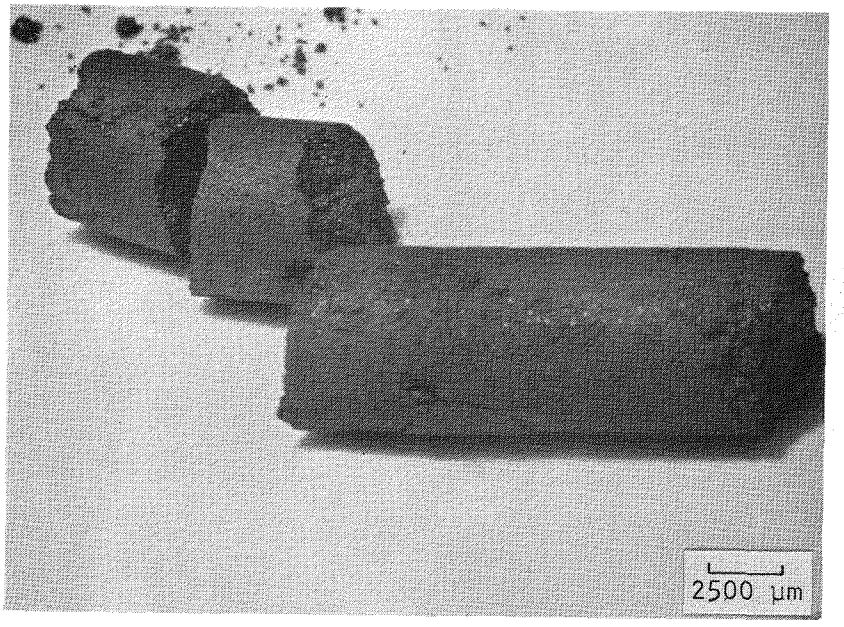

K7430-3

Fig. 9-51. Visual examination of RTE-4 fuel rod 4-4-3

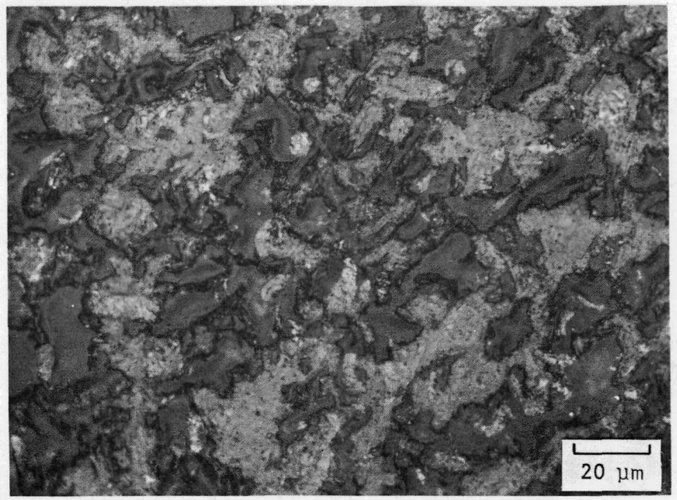

L7430-28 (a)

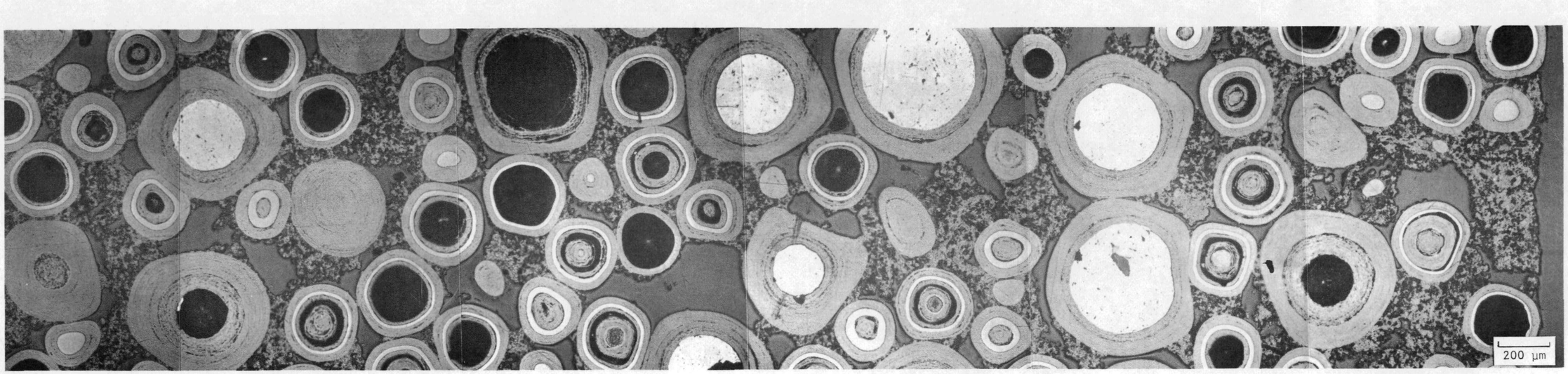

L7430 (4-9) (b)

Fig. 9-53. Photomicrographs of RTE-4 fuel rod 4-7-3 (UC_2 TRISO/ThC_2 blend). Irradiation conditions: 2.1 x 10^{21} n/cm^2 (E > 0.18 MeV) at 1240°C. (a) Typical graphite matrix and (b) composite radial cross section.

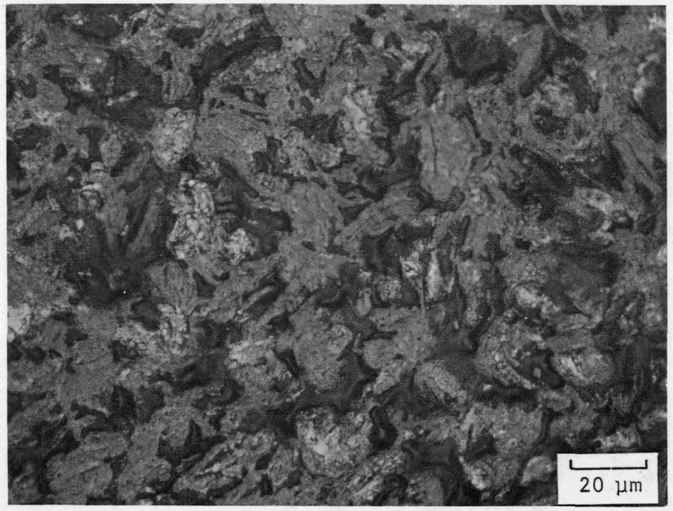

L7430-64 (a)

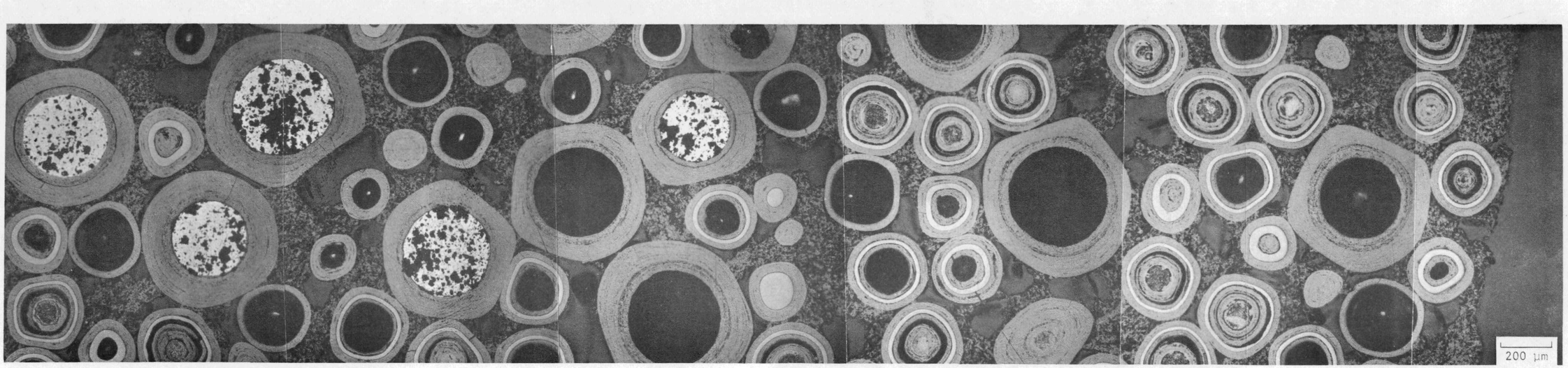

L7430 (47A-52) (b)

Fig. 9-54. Photomicrographs of RTE-2 fuel rod 6-1-3 (UC_2 TRISO/ThC_2 blend). Irradiation conditions: 1.4×10^{21} n/cm^2 (E > 0.18 MeV) at 1120°C. (a) Typical graphite matrix and (b) composite radial cross section.

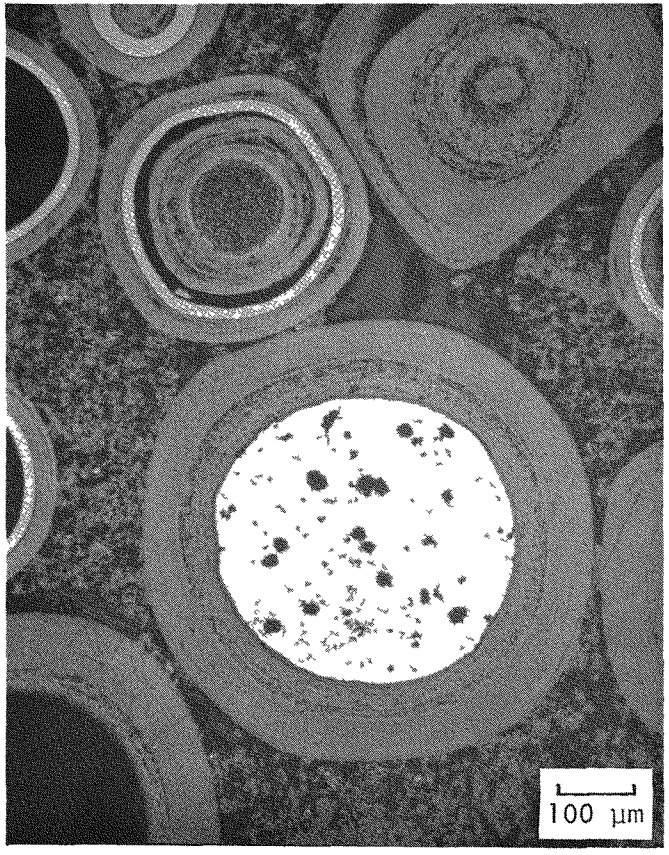

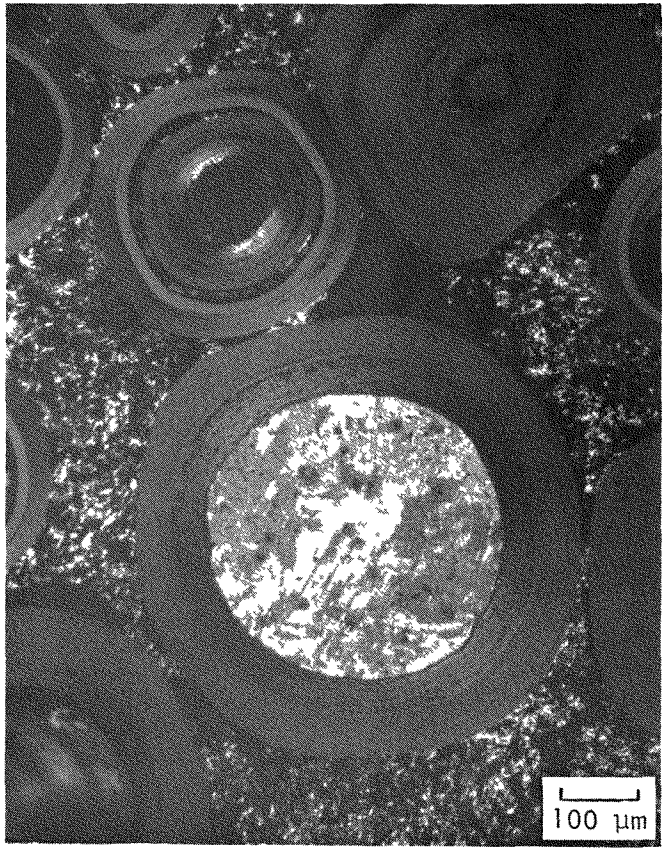

L7430-34 (a) L7430-35 (b)

Fig. 9-55. Representative fuel particles from RTE-2 fuel rod 6-1-3. Irradiation conditions: 1.4×10^{21} n/cm^2 (E > 0.18 MeV) at 1120°C. (a) UC_2 TRISO/ThC_2 BISO particles and (b) dark field of same particles.

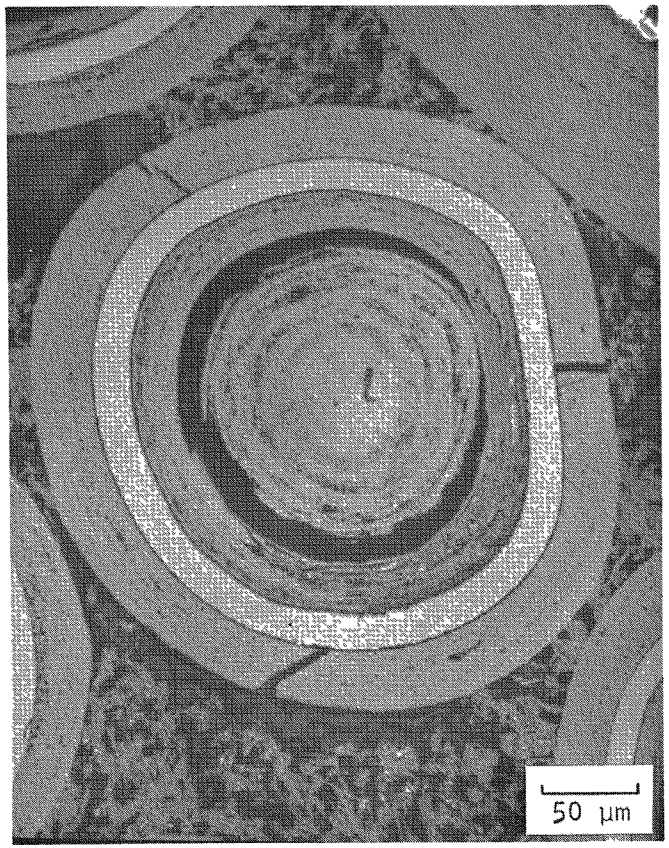

L7430-44 (a)

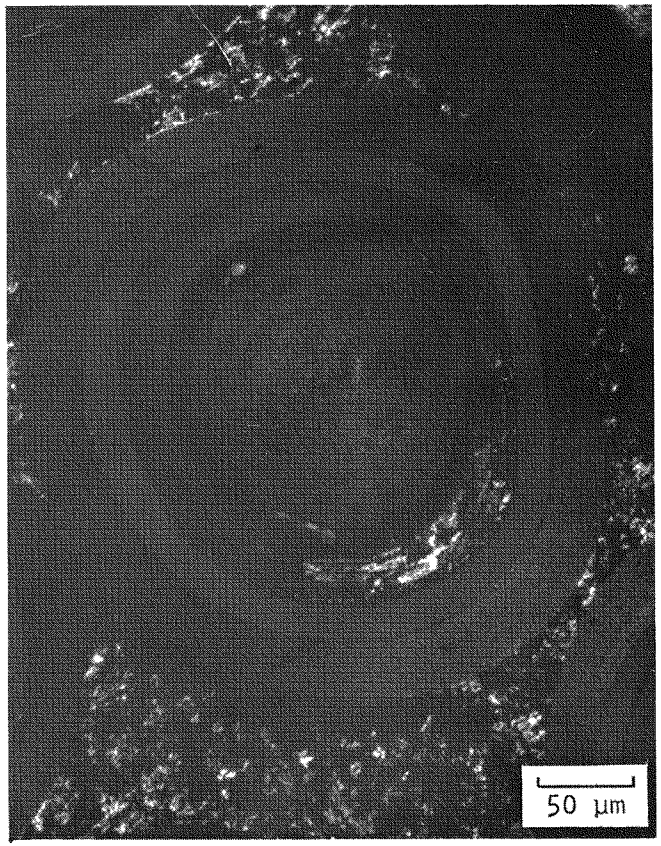

L7430-45 (b)

Fig. 9-56. UC_2 TRISO particle from RTE-2 fuel rod 6-1-3 showing OPyC failure and metallic fission product attack of the SiC: (a) bright field showing metallic fission product attack, and (b) dark field showing metallic fission product concentration

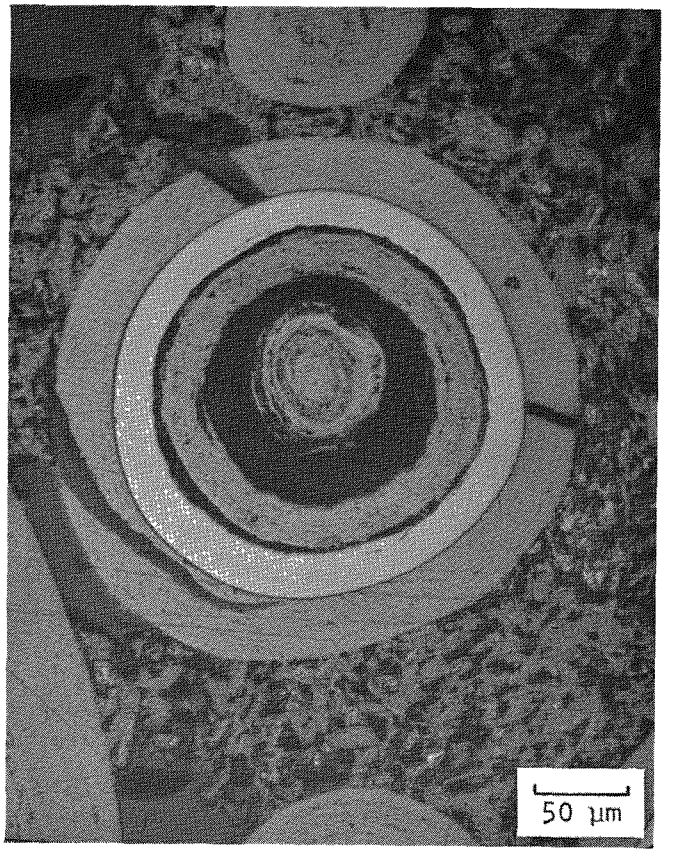

L7430-46

Fig. 9-57. UC_2 TRISO particle from RTE-2 fuel rod 6-1-3. Failure of OPyC is due to matrix-coating interaction.

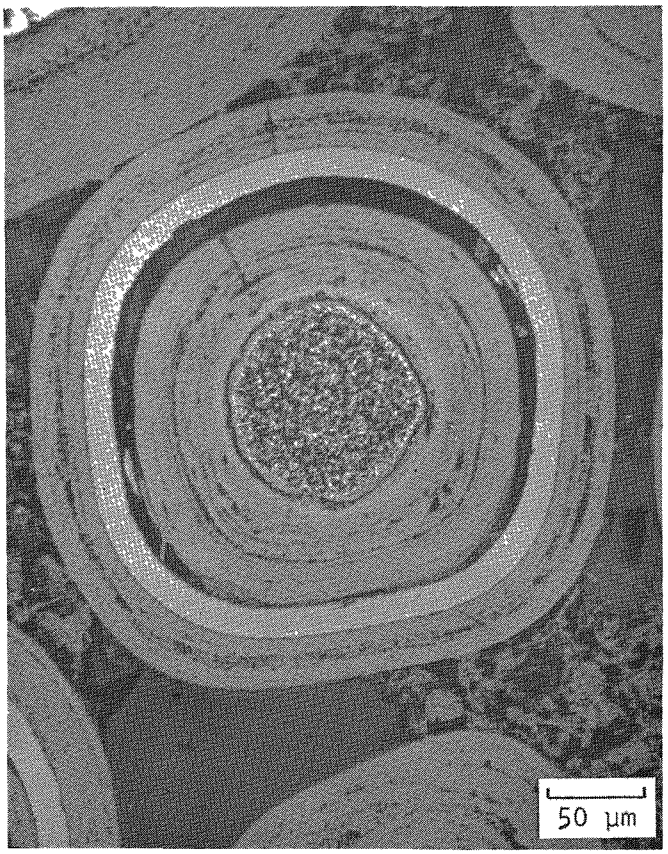

L7430-43

Fig. 9-58. UC_2 TRISO particle from RTE-2 fuel rod 6-1-3. Laminations in OPyC are due to soot deposits.

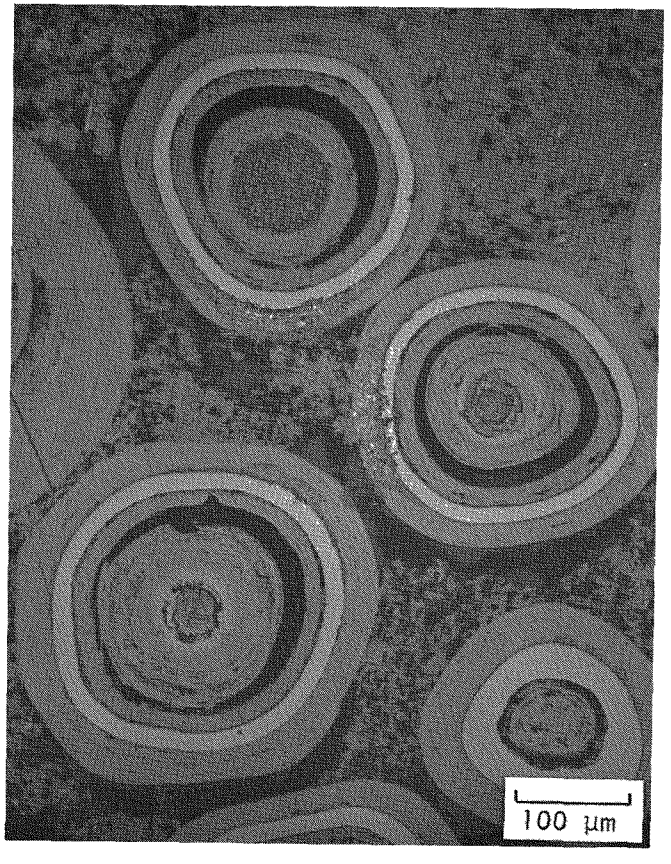

L7430-39 (a)

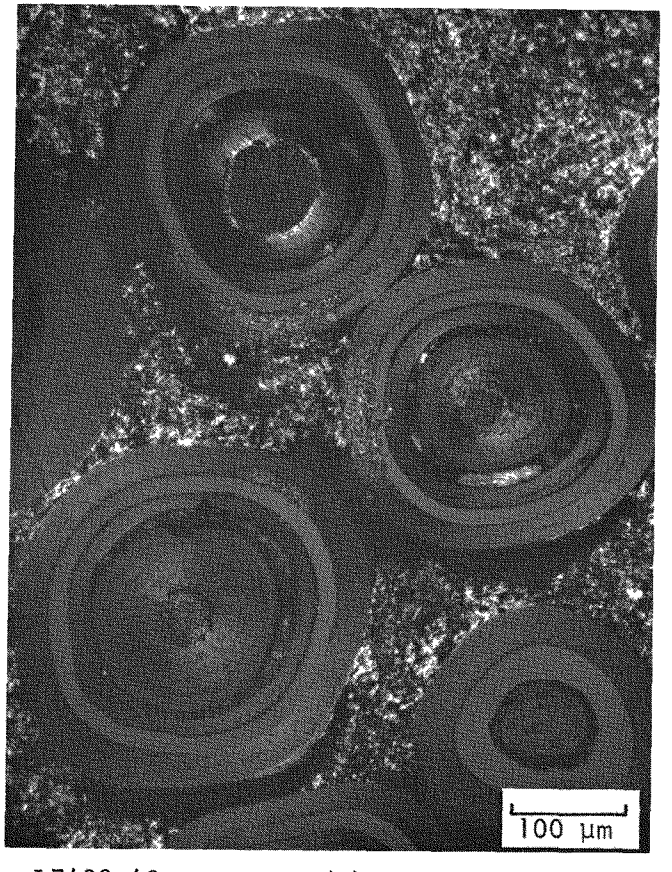

L7430-40 (b)

Fig. 9-59. Area of external fuel particle attack in RTE-2 fuel rod 6-1-3 because of contamination: (a) light field and (b) dark field

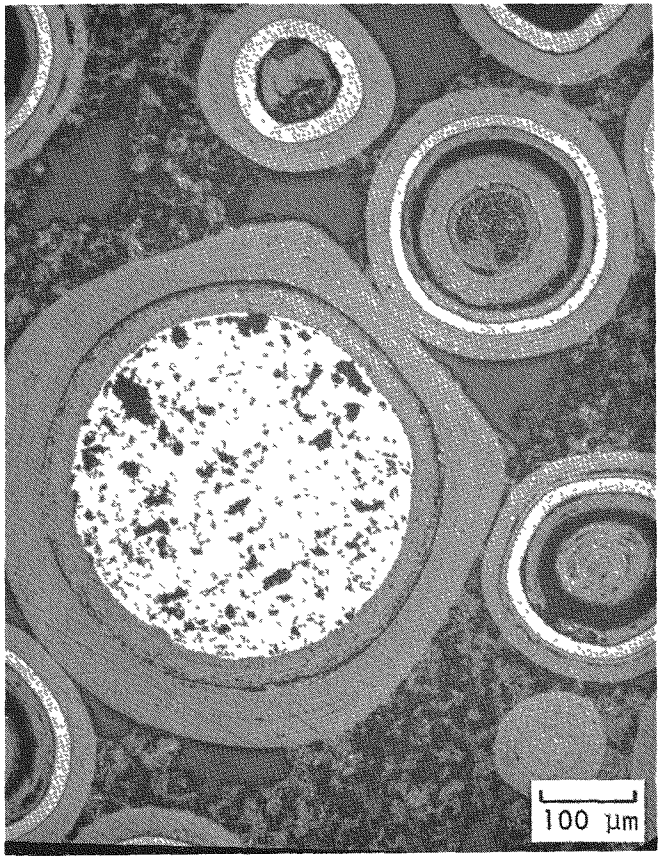

L7430-25 (a)

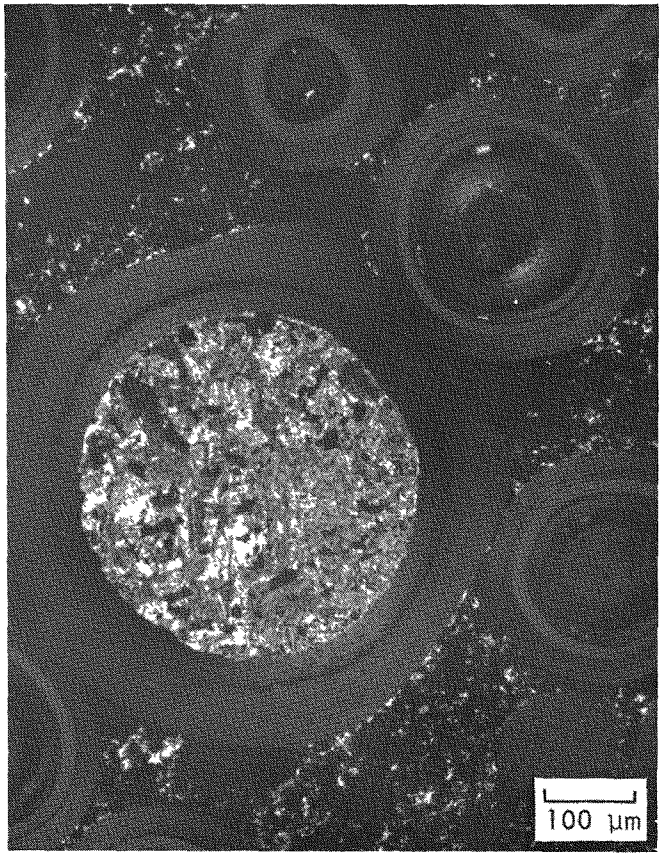

L7430-24 (b)

Fig. 9-60. Typical fuel particles from RTE-4 fuel rod 4-7-3: (a) UC_2 TRISO/ThC_2 BISO pair with ThC_2 kernel beginning to hydrolyze, and (b) dark field of same pair

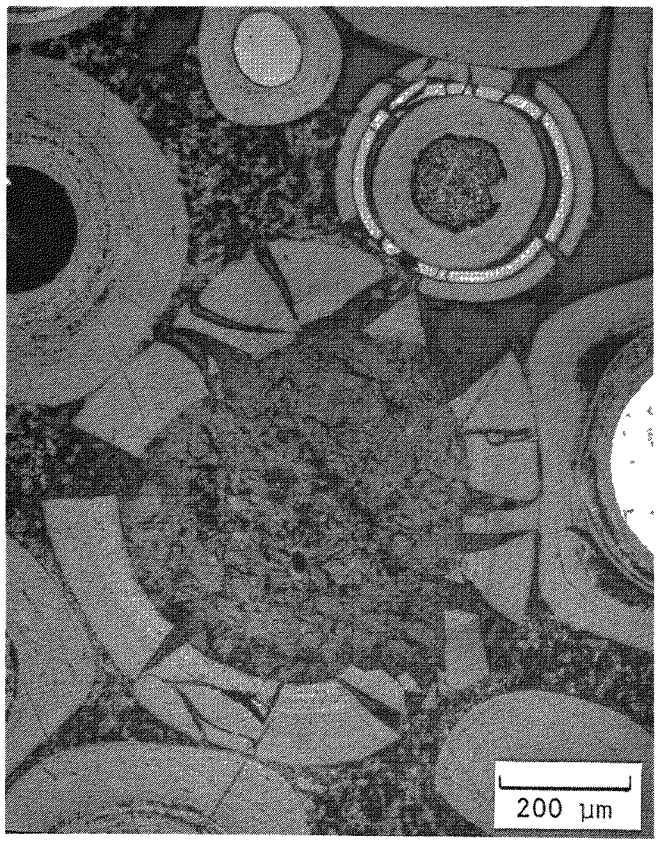

L7430-3

Fig. 9-61. Production failure of UC_2 TRISO/ThC_2 BISO pair in RTE-4 fuel rod 4-2-3. Failure was due to constraint of particles during fuel rod injection.

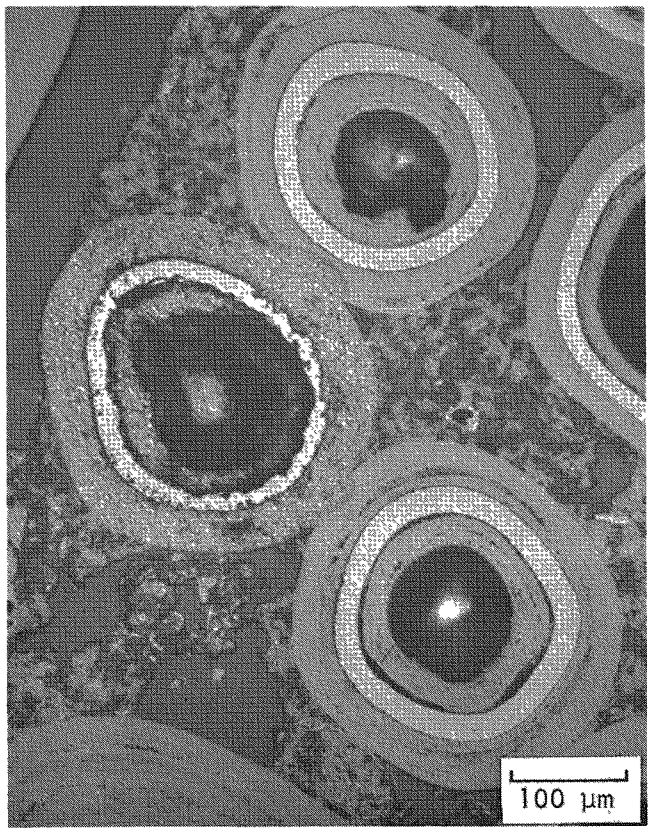

L7430-18 (a)

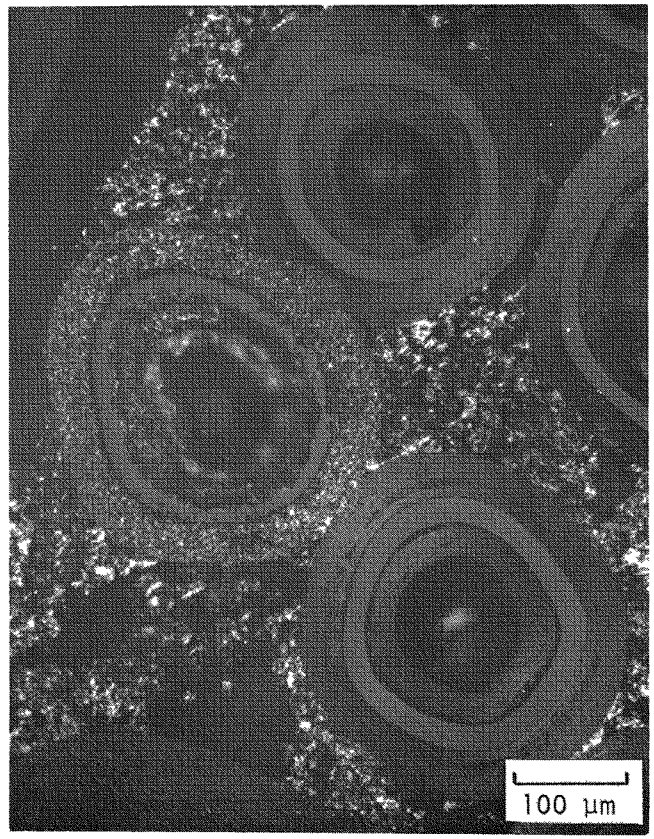

L7430-19 (b)

Fig. 9-62. Area of external fuel particle attack in RTE-4 fuel rod 4-7-3 because of contamination: (a)bright field and (b) dark field

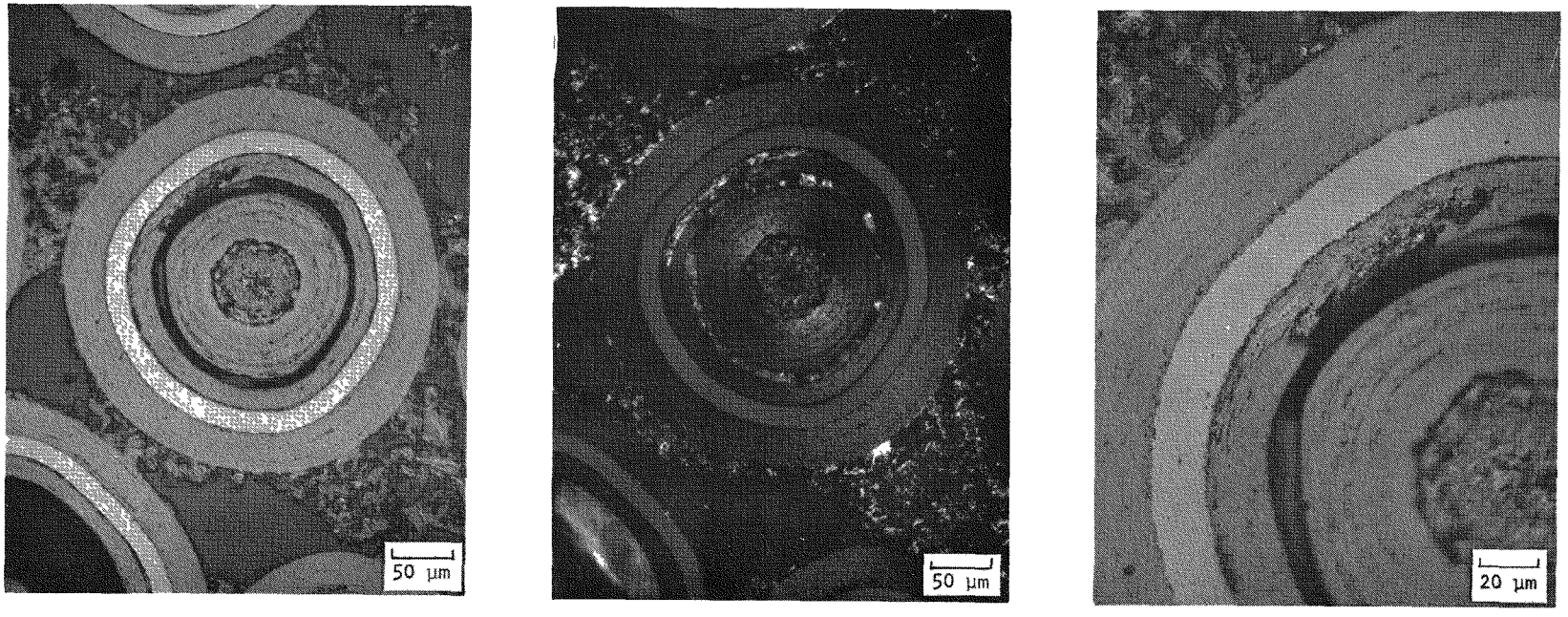

L7430-15 (a) L7430-16 (b) L7430-17 (c)

Fig. 9-63. TRISO UC_2 particle in RTE-4 fuel rod 4-7-3 showing SiC attack by metallic fission products: (a) light field, (b) dark field showing metallic fission product concentration, and (c) high magnification of attack

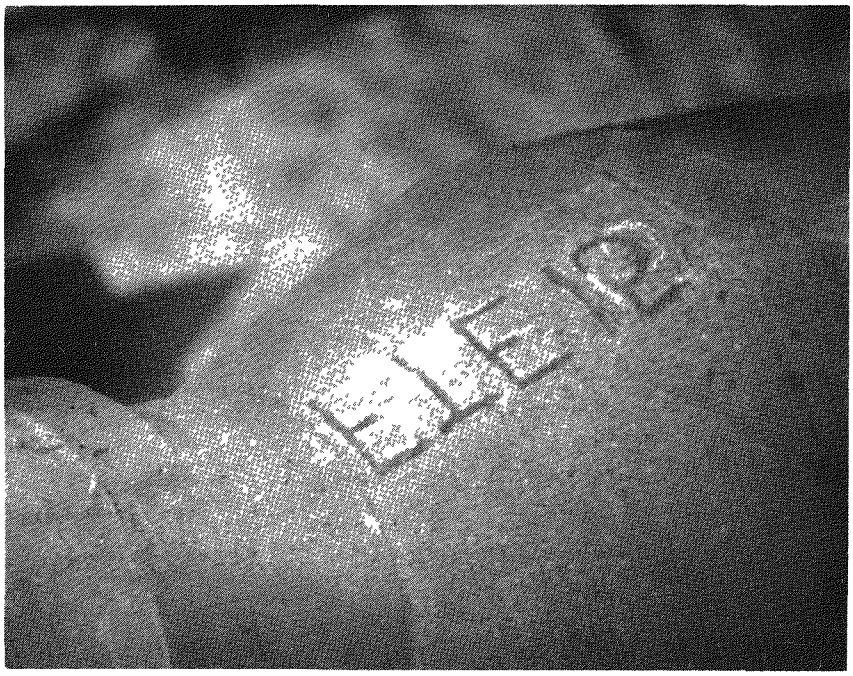

Fig. 9-64. Fuel test element identification, FTE-15 (mirror image)

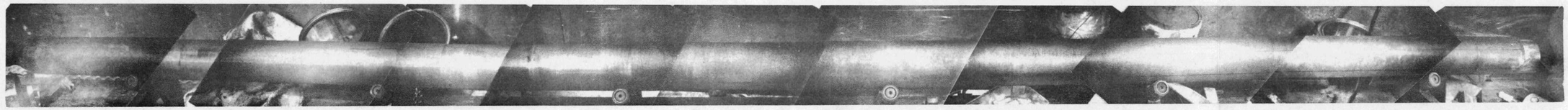

Fig. 9-65. FTE-15 composite photograph of total element (mirror image)

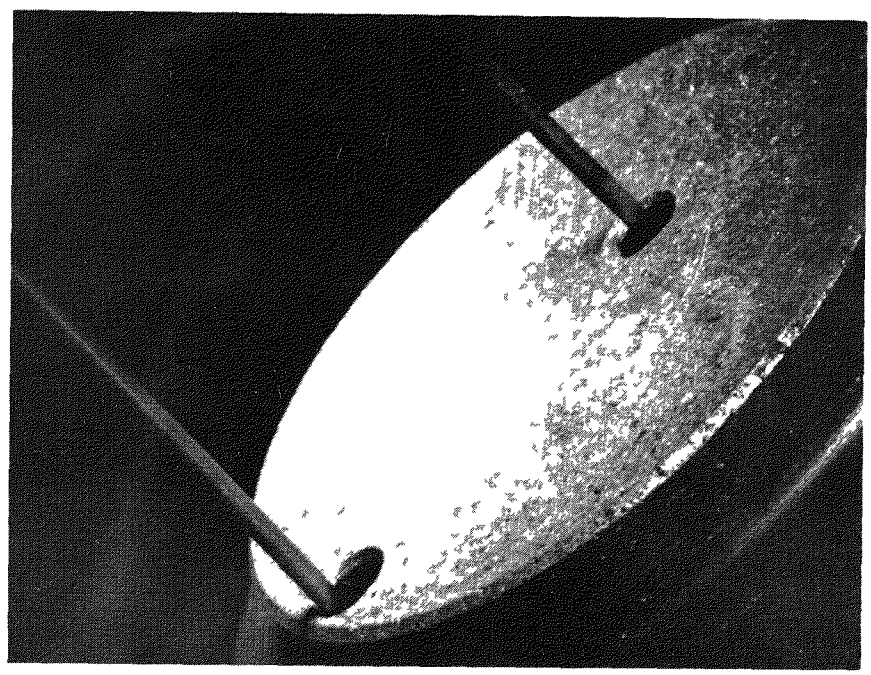

Fig. 9-66. FTE-15 thermocouple cut (lower reflector)

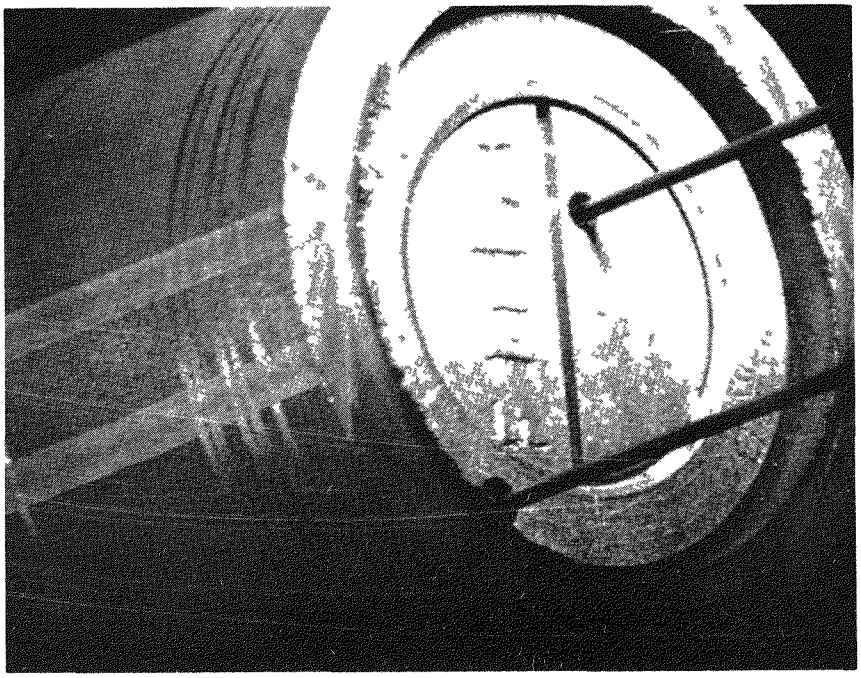

Fig. 9-67. FTE-15 thermocouple cut (bottom of body 1)

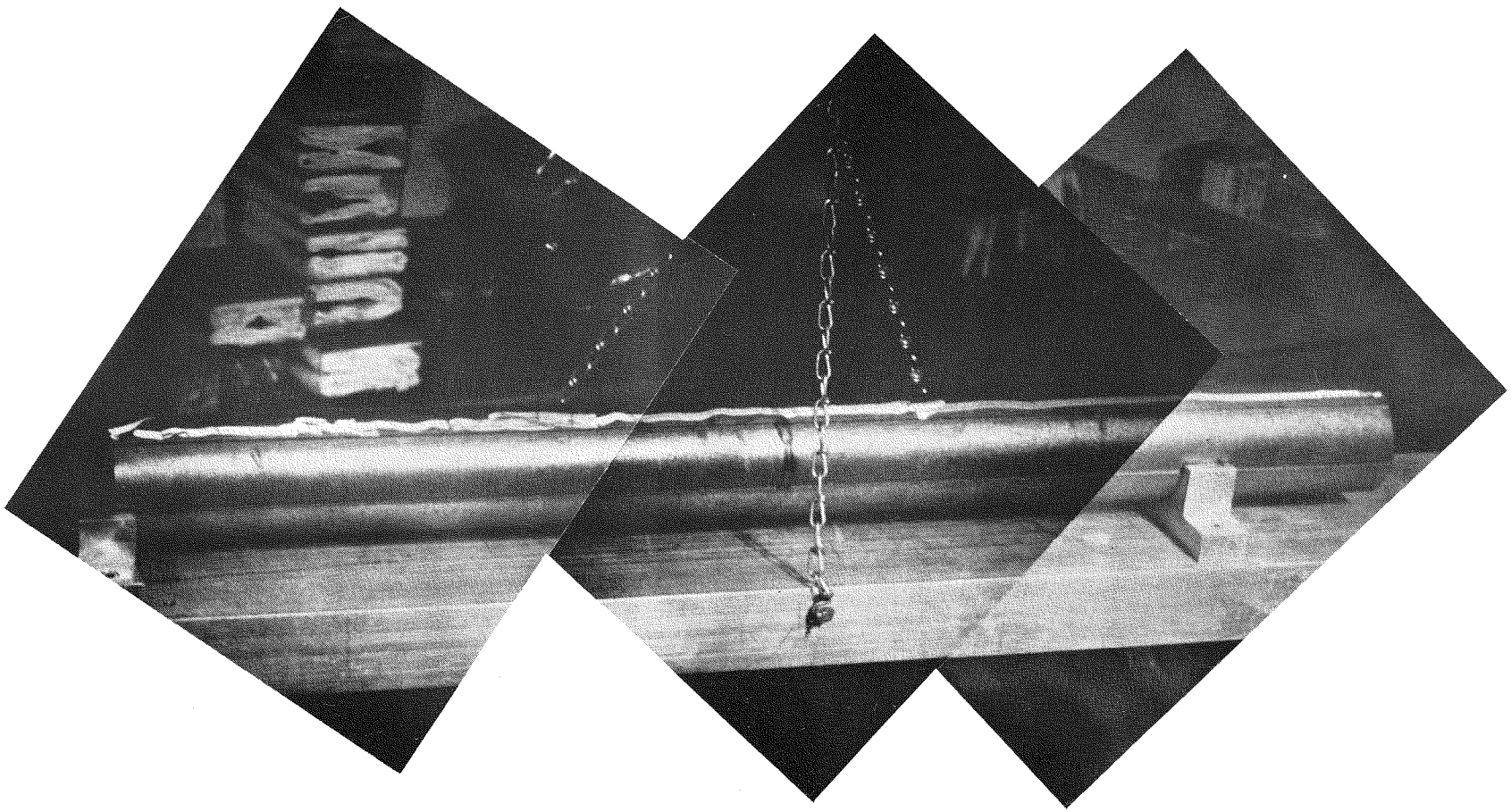

Fig. 9-68. Bottom fuel body (1) FTE-15 (mirror image)

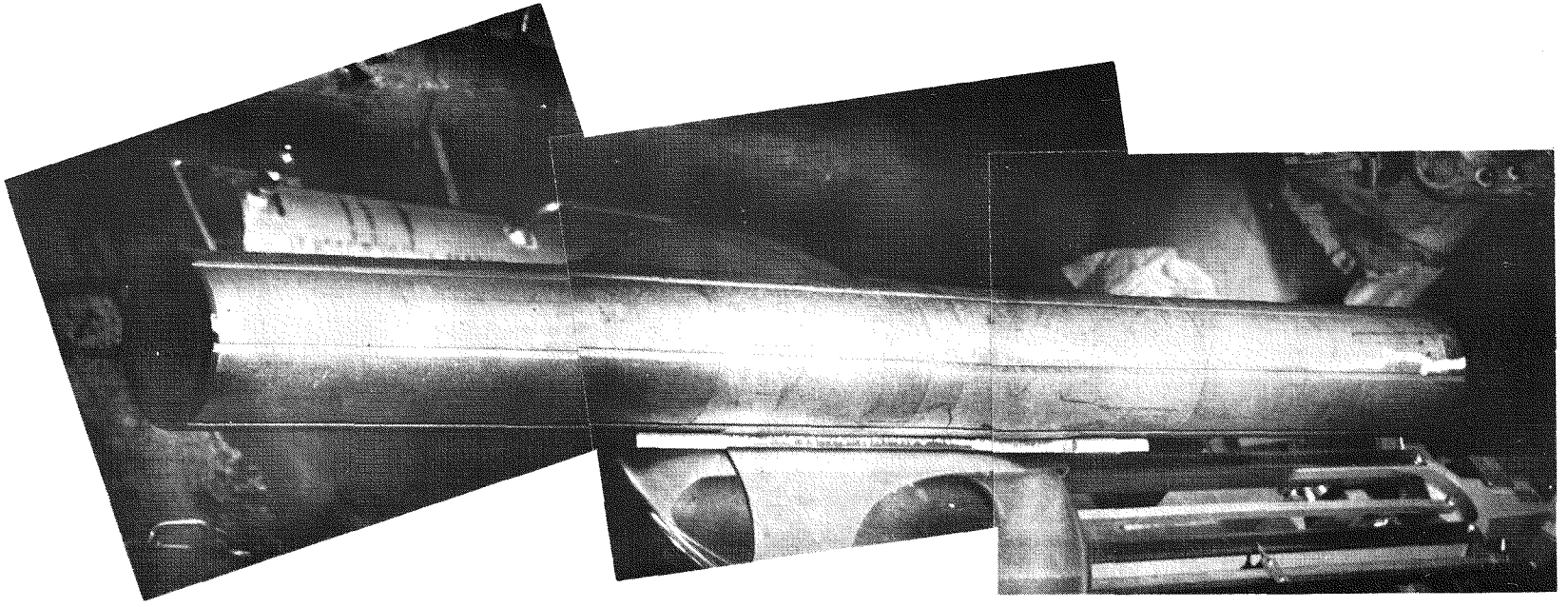

Fig. 9-69. Center fuel body (2) from FTE-15 (mirror image)

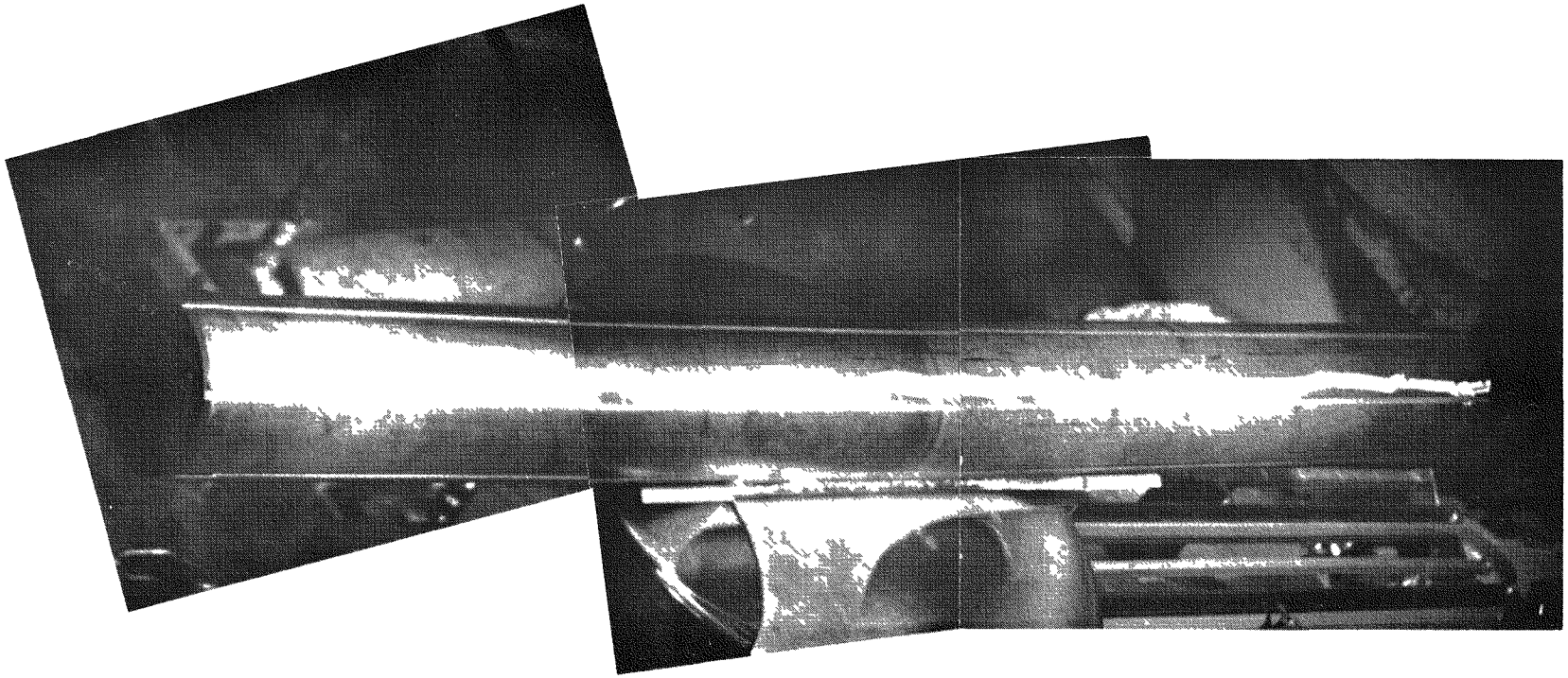

Fig. 9-70. Top fuel body (3) from FTE-15 (mirror image)

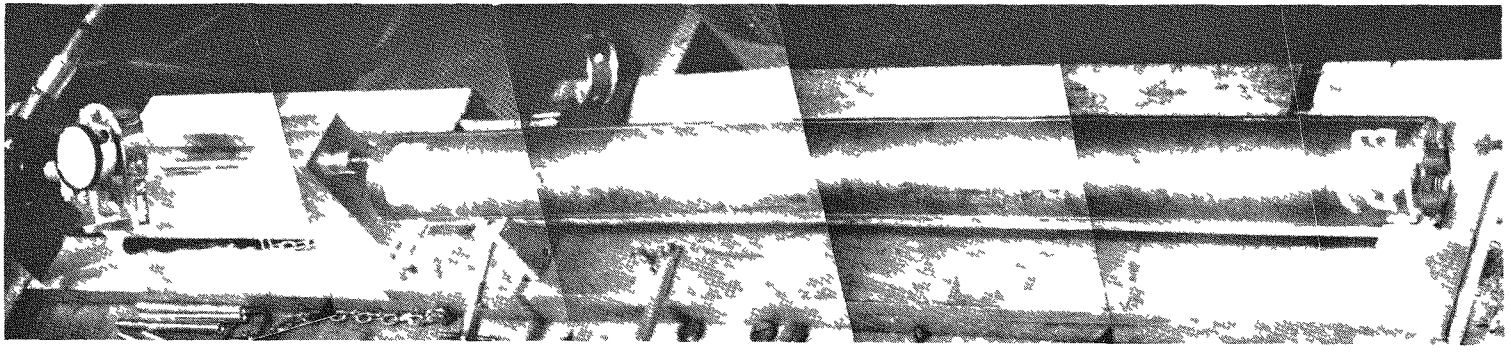

Fig. 9-71. Typical fuel body discharge setup

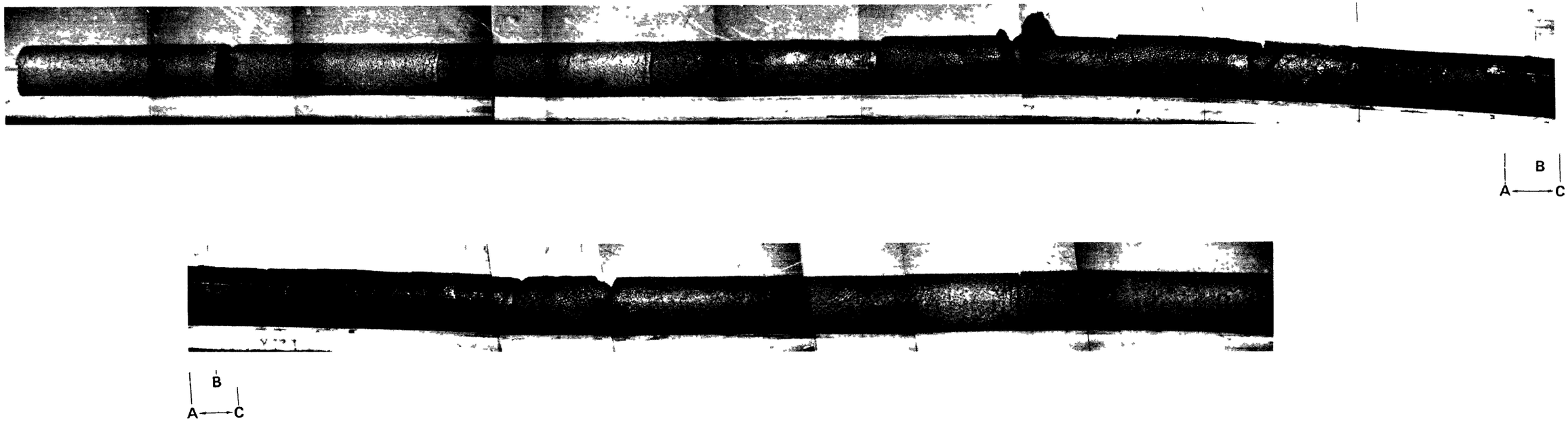

Fig. 9-72. FTE-15 composite photograph of stack 4, body 2 (center body)

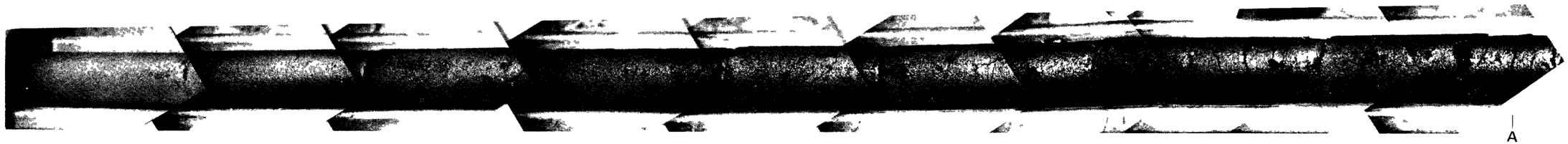

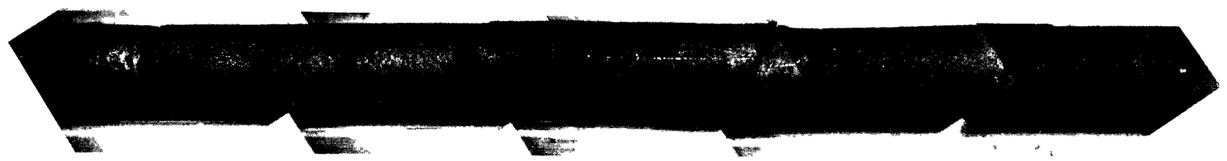

Fig. 9-73. FTE-15 composite photograph of stack 5, body 2 (center body)

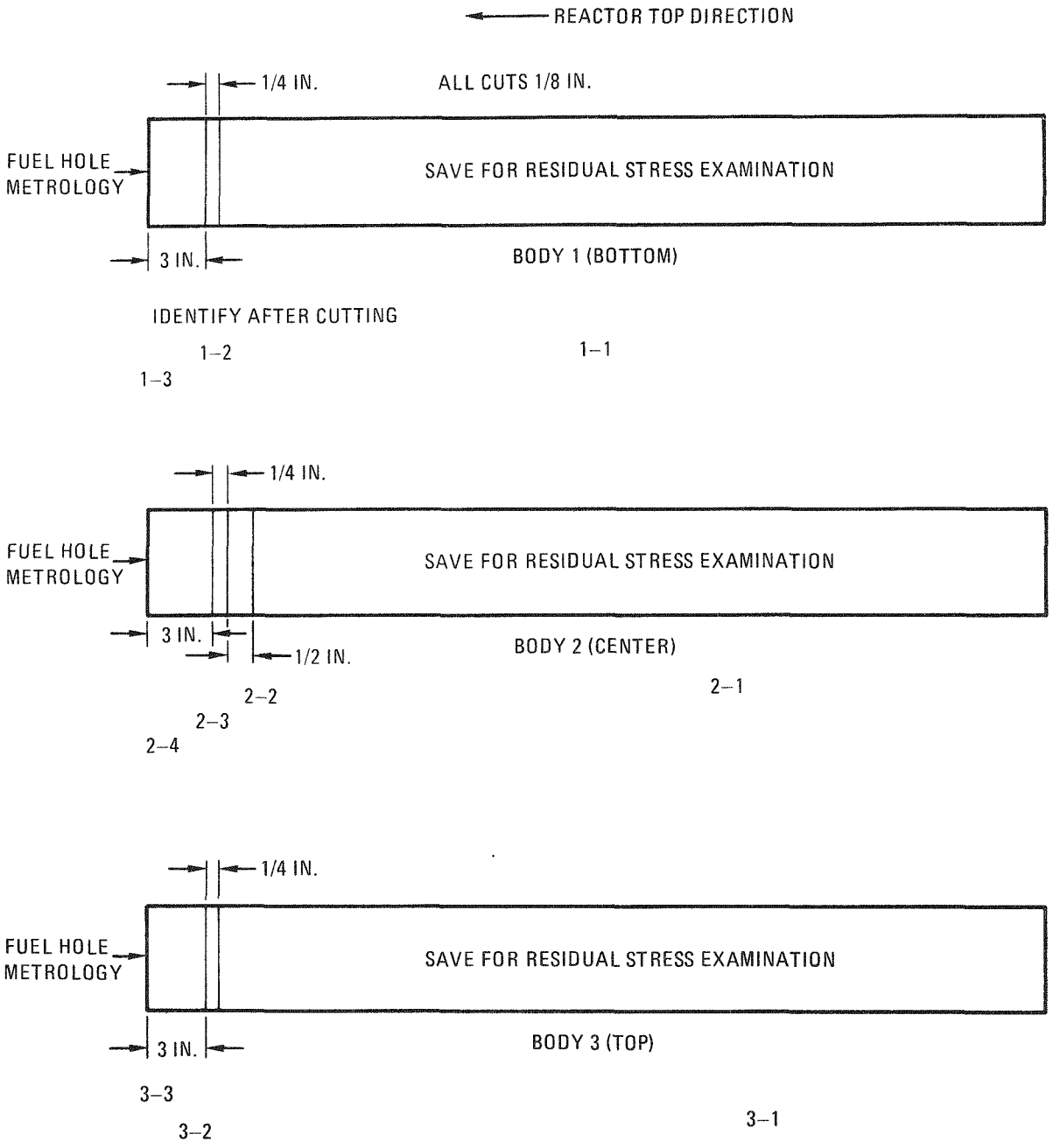

DISPOSITION:

STRIP CUTTING: 1–1, 2–1, 3–1
AUTORADIOGRAPHY: 1–2, 2–3, 3–2
RADIAL Cs PROFILE: 2–2
FUEL HOLE METROLOGY: 1–3, 2–4, 3–3

Fig. 9-74. Optional sectioning plan for FTE-15 fuel bodies

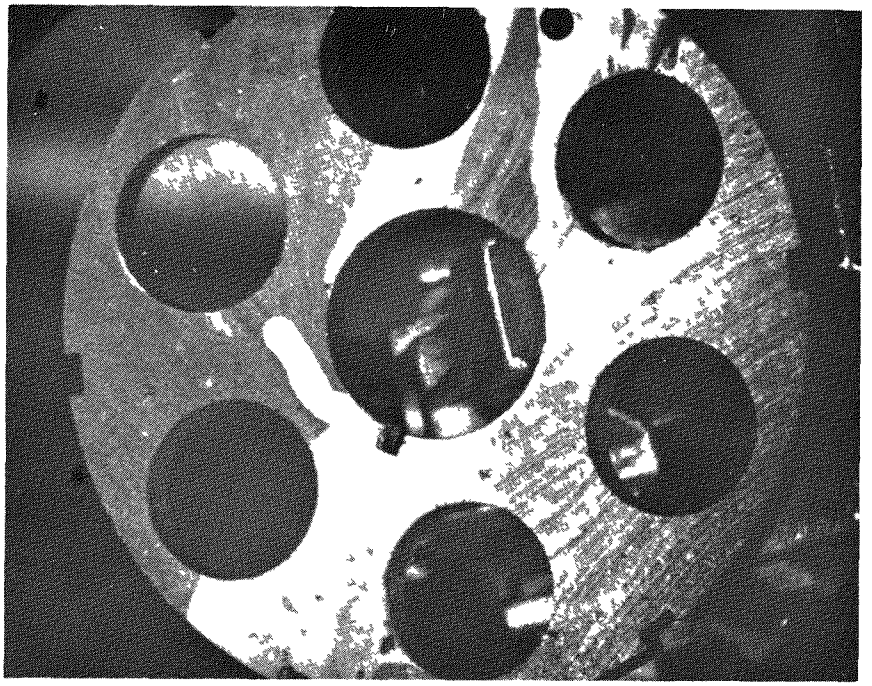

Fig. 9-75. FTE-15 slice 1-2 (top view)

(4) (5)

(3)

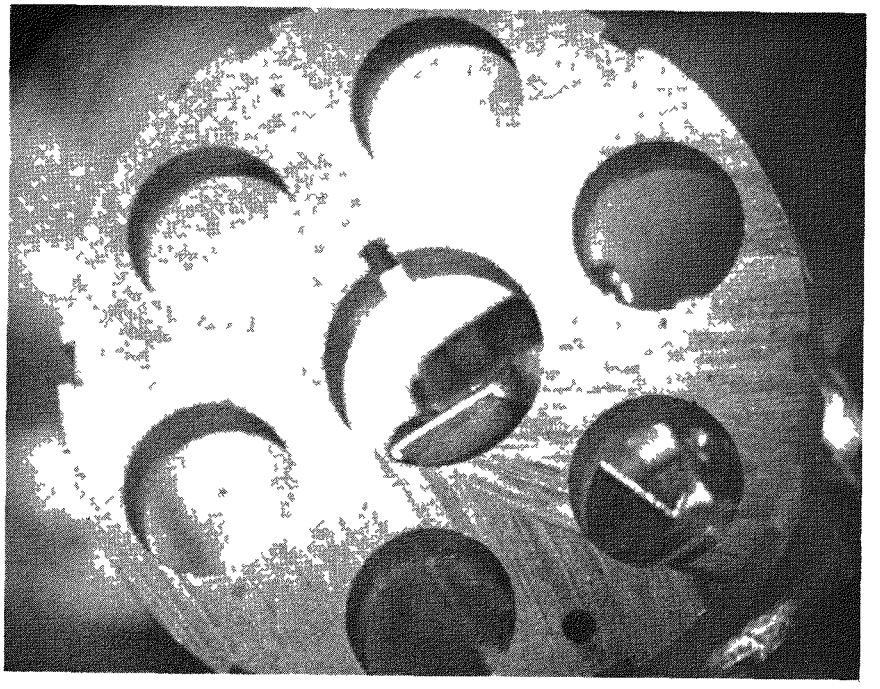

(2) (6)

(1)

Fig. 9-76. FTE-15 slice 2-2 (top view)

(6) (5)

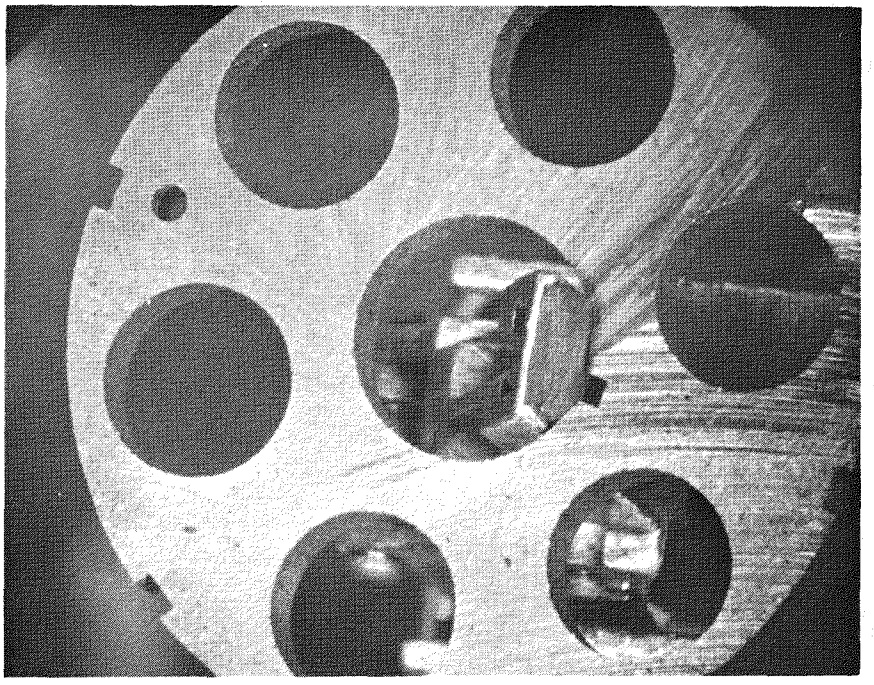

(1) (4)

(2) (3)

Fig. 9-77. FTE-15 slice 2-3 (bottom view)

(1) (2)

(6) 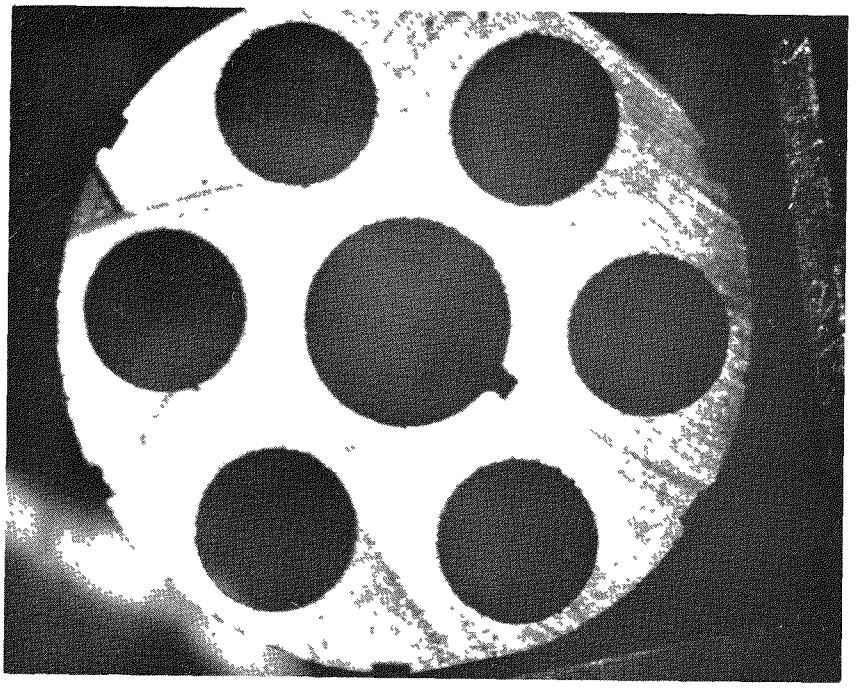 (3)

(5) (4)

Fig. 9-78. FTE-15 slice 3-2 (top view)

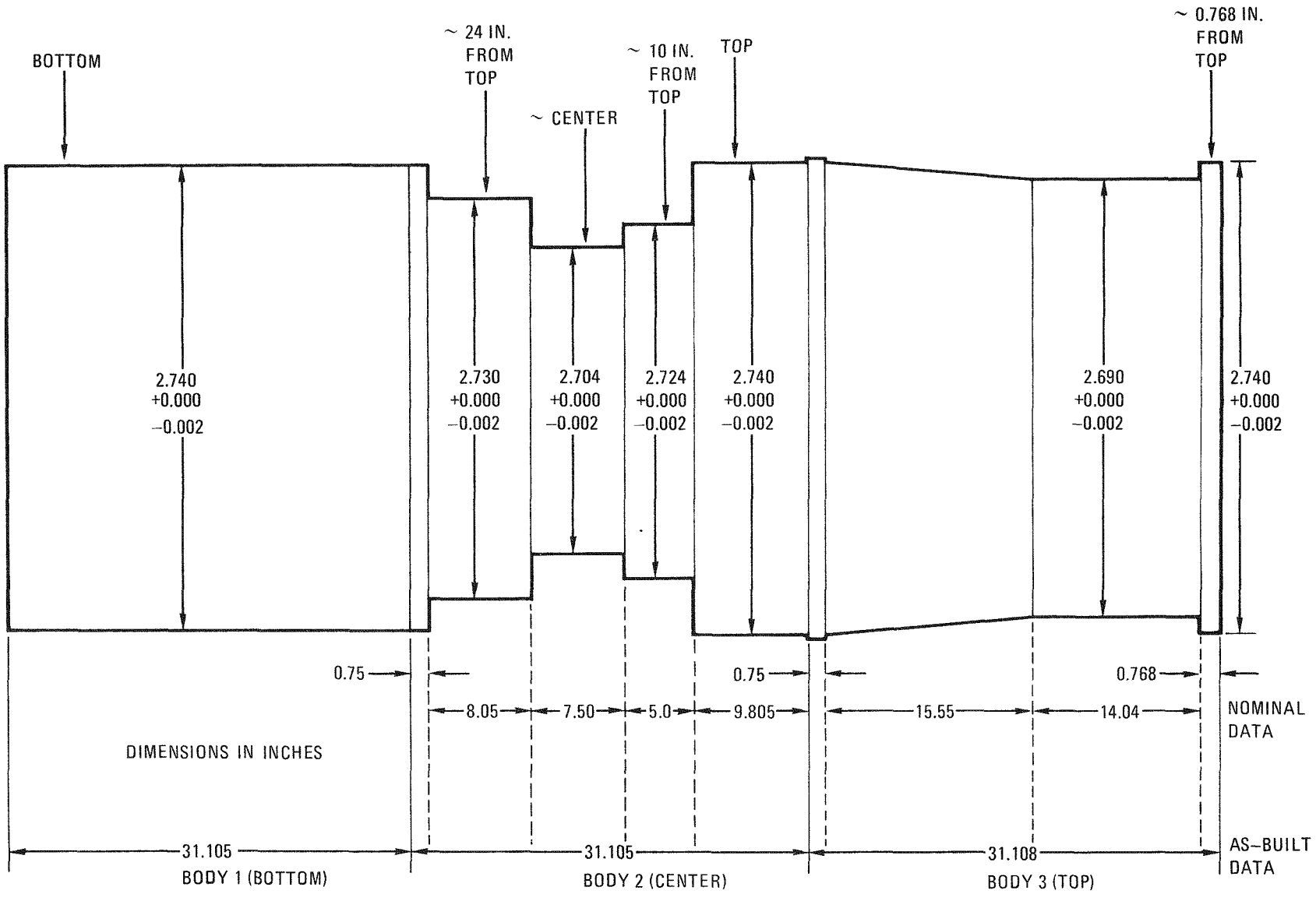

Fig. 9-79. FTE-15 fuel body outside dimensions

TASK 11 (189a 13121)

GRAPHITE DEVELOPMENT

INTRODUCTION

The objective of the Graphite Development Program is to evaluate and identify near-isotropic graphites for core blocks of HTGRs. The graphites under investigation have been supplied by major carbon and graphite producers in the United States and Europe. The major emphasis in this program is on the United States graphites, with a much smaller effort devoted to the European materials. The work on the European graphites is to provide confirmatory and comparative data with European HTGR programs where United States graphites are also being evaluated.

The disposition of the graphites supplied by the Great Lakes Carbon Company (GLCC) was given in the previous quarterly report (Ref. 11-1, Table 11-1). An update and correction of the disposition of the GLCC materials is given in Table 11-1.* Additional data on raw materials have been supplied by GLCC. Lot 266 was made from a single coke batch designated A_1. Lots 408, 424, and 426 were prepared from a blend of cokes A_3 and B_1, and lots 438 and 440 were made from a blend of cokes B_1 and C_1. Cokes A_1 and A_2 represent different commercial production runs from one refinery source. Cokes B_1 and C_1 represent cokes from the same type of crude as A_1 and A_3 but from different refineries. The objective of blending cokes A_3 and B_1 and B_1 and C_1 is to produce a graphite microstructure that is common in the H-451 grade. Great Lakes Carbon Company representatives believe it is highly improbable that a coke source from a single feedstock or refinery can be maintained over an extended period.

The characterization and irradiation experiments are designed to determine whether the above approach to manufacturing the graphite will have any effect on the properties or irradiation behavior.

*Tables appear at the end of Section 11.

GRAPHITE CHARACTERIZATION

In-depth characterization of grades TS-1240 and H-451 is continuing. Preliminary characterization of grade SO-818 (lot 1) has started. Initial characterization data (density, impurities, tensile properties, thermal expansion, and thermal conductivity) for grades H-451 and TS-1240 were reported previously (Refs. 11-2 through 11-7). Additional density and tensile property data for grades TS-1240 and H-451 are given in Tables 11-2 through 11-5. Preliminary density and tensile property data for grade SO-818 are given in Tables 11-6 and 11-7. Impurity data for H-451, TS-1240, and SO-818 are given in Table 11-8. Additional thermal expansivity data for grade H-451 are given in Table 11-9.

The tensile property data presented in Tables 11-2 through 11-7 were obtained on specimens 0.505 in. in diameter by 3.00 in. long. Each specimen was loaded to 1000 psi, unloaded to zero stress, and reloaded to fracture while recording the stress-strain curve. The elastic modulus for the second loading was taken as the chord modulus between 100 and 1000 psi. Values of ultimate strength, strain to fracture, and permanent deformation in the specimens after the first loading cycle were also obtained from the stress-strain curve.

GRAPHITE IRRADIATIONS

Capsule OG-2

Temperatures and Fluences

Temperatures in the OG-2 capsule were recorded by 24 chromel-alumel and 6 tungsten-rhenium thermocouples. Three of the tungsten-rhenium thermocouples were located in crucibles 4 and 5 where the temperature was more than 1100°C, and two were located next to chromel-alumel thermocouples in lower temperature crucibles in order to provide data on neutron-induced decalibration. All crucibles contained at least one thermocouple on the

centerline, and eight out of the ten crucibles contained at least one thermocouple near the periphery. Two of the high-temperature tungsten-rhenium thermocouples failed at the start of a reactor cycle 60% through the capsule life. All others operated to the end-of-life.

After correcting the output of the tungsten-rhenium thermocouples for decalibration, the time-averaged temperatures during the time the reactor was above 80% full power were calculated for each crucible. The mean centerline and peripheral temperature are given in Table 11-10. The temperatures are in close agreement with design values and with the values observed in capsule OG-1.

Neutron fluences were calculated from the activities of vanadium - 0.216% cobalt, vanadium - 0.52% iron (88.25% enriched in Fe-54), and titanium flux wires that were located in 28 positions in the capsule. Thermal fluences were calculated from cobalt activation, assuming a cross section of 36.8 b for the $^{59}Co(n,\gamma)^{60}Co$ reaction. Fast fluences ($E > 0.18$ MeV) were calculated from iron and titanium activation, using effective cross sections of 46.5 mb for the $^{54}Fe(n,p)^{54}Mn$ reaction and 6.85 mb for the $^{46}Ti(n,p)^{46}Sc$ reaction. Interpolated fluences at the center of each crucible are listed in Table 11-10.

Thermal Property Measurements

Thermal expansivity measurements were made on 98 graphite samples irradiated in capsule OG-2. The measurements were made in a fused silica dilatometer between room temperature and 100°C less than the irradiation temperature. The data have not yet been analyzed.

The thermal diffusivity of 87 discs irradiated at three different temperatures was measured by the heat-pulse method between room temperature and 800°C. Analysis has not been completed.

Mechanical Property Measurements

Room temperature tensile tests are being conducted on 0.25-in.-diameter by 0.9-in.-long specimens of H-451, TS-1240, and H-327 graphite irradiated in capsule OG-2. The specimens are cemented between aluminum end pieces and tested in an Instron tensile testing machine. Strains are measured with a 0.5-in. gauge length extensometer. The specimens are loaded to 1000 psi, unloaded to 100 psi, and reloaded to failure. Young's modulus is measured from the slope of the 100 to 1000 psi reloading line.

About 40% of the scheduled tests has been completed. The results are tabulated in Tables 11-11 and 11-12, together with test data on unirradiated companion specimens.

The results on H-451 graphite, combined with the data from specimens irradiated in capsule OG-1, show that during irradiation at 600°C both the strength and Young's modulus increase to a plateau. For irradiation at 900°C, the strength and modulus show a second increase beyond the plateau, with the strength increasing by 77% of the unirradiated value and the modulus increasing by 123% at 5.9×10^{21} n/cm^2. These trends are consistent with Dragon project measurements of the increase in sonic modulus of near-isotropic graphites.

Preliminary results on TS-1240 graphite indicate that both the strength and modulus increase somewhat less than in H-451 graphite irradiated under similar conditions. The scatter in the data is considerably greater for irradiated TS-1240 than for irradiated H-451 graphite.

Capsule OG-3

The loading of specimens into capsule OG-3 was completed according to the original test plan, with a few minor exceptions. The exceptions mainly concerned the omission of some radially oriented specimens of P_3JHAN and 2020 graphites irradiated in capsules OG-1 and OG-2, which entered the

expansion phase earlier than anticipated. The assembly of the capsule has progressed as far as the containment tubes. The capsule is scheduled to be shipped to ORNL on May 16, 1975 and to be ready for insertion in the ORR about June 15, 1975.

Capsule OG-4

Capsule OG-4 will be loaded with all-virgin specimens and will be inserted in the ORR as soon as practicable after the removal of capsule OG-3. The thermal design will be somewhat modified from OG-1 through -3 to provide better coverage at low temperatures.

A tentative test plan for capsule OG-4 has been drafted. The plan will concentrate on obtaining qualification-level data on Airco Speer grade SO-818 graphite and the most recent lot of GLCC H-451 graphite (lot 440). Side-by-side comparisons of the dimensional changes in several U.S. and European near-isotropic graphites will also be included.

GRAPHITE STANDARD

A revised draft of the proposed RDT standard E6-1 "Near-Isotropic Petroleum-Coke-Based Graphites for High-Temperature Gas-Cooled Reactor Core Components," was written and is being reviewed by the major carbon companies and RRD. The draft will be revised and sent to RRD for approval. The approval date has been delayed until June 30, 1975.

REFERENCES

11-1. "HTGR Fuels and Core Development Program Quarterly Progress Report for the Period Ending February 28, 1975," USAEC Report GA-A13353, March 31, 1975.

11-2. "HTGR Base Program Quarterly Progress Report for the Period Ending February 28, 1974," USAEC Report GA-A12916, General Atomic Company, March 29, 1974.

11-3. "HTGR Base Program Quarterly Progress Report for the Period Ending May 31, 1974," USAEC Report GA-A13030, General Atomic Company, June 28, 1974.

11-4. "HTGR Fuels and Core Development Program Quarterly Progress Report for the Period Ending August 30, 1974," USAEC Report GA-A13126, General Atomic Company, September 30, 1974.

11-5. Engle, G. B., R. J. Price, W. R. Johnson, and L. A. Beavan, "Development Status of Near-Isotropic Graphites for Large HTGRs," USAEC Report GA-A12944, General Atomic Company, June 1, 1974.

11-6. "HTGR Fuels and Core Development Program Quarterly Progress Report for the Period Ending November 30, 1974," USAEC Report GA-A13253, General Atomic Company, January 31, 1975.

TABLE 11-1
DISPOSITION OF H-451 GRAPHITE LOGS

Coke Lots Used	GLCC Lot No.	Approximate Number of Logs Tested by GLCC	Number of Logs Delivered to GA[a]	Approximate Date of Delivery	Disposition of Logs Under Task 11
A_1	266	3	2	Aug. 1972	Preliminary characterization completed on 2 logs. Specimens from one log irradiated in OG-1 and OG-2.
A_3+B_1	408	21	18[b]	Aug. 1973	Characterization under way on 4 logs. Specimens from one log irradiated in OG-2.
A_3+B_1	424	11	3	March 1974	No evaluation work under way.
A_3+B_1	426	127	73	March 1974	Characterization under way on 4 logs. Specimens from 3 logs will be irradiated in OG-3.
B_1+C_1	438	26	0	--	No evaluation work planned.
B_1+C_1	440	26	0	April 1975	Characterization work planned on 4 logs. Specimens from 3 logs will be irradiated in OG-4.

[a] Many of the logs delivered to GA will be used for programs other than Task 11; however, Task 11 coordinates the deliveries.

[b] Five logs delivered to ORNL for their HTGR program work.

TABLE 11-2
TENSILE PROPERTIES OF TS-1240 GRAPHITE, LOT 1
Log 6484-29, density = 1.83 g/cm^3, 0.505-in.-diameter by 3.00-in.-long samples

Specimen No.	Position and Orientation[a]	Density (g/cm^3)	Elastic Modulus on Second Loading (10^6 psi)	Permanent Set After First Loading (%)	Fracture Strain (%)	Ultimate Strength (psi)
6484-29-1A-L001	EC(∥)	1.796	1.17	0.018	0.265	2041
-L004		1.802	1.22	0.020	0.314	2527
-L005		1.804	1.22	0.014	0.288	2381
-L009		1.799	1.19	0.015	0.299	2441
-1B-L011		1.798	1.23	0.017	0.319	2565
-L014		1.794	1.27	0.021	0.325	2585
-L015		1.795	1.23	0.018	0.325	2603
-L019		1.802	1.23	0.019	0.304	2425
Mean		1.799	1.22	0.018	0.305	2446
Std. dev.		0.004	0.03	0.002	0.021	183
-1A-L025	EC(⊥)	1.801	1.13	0.025	0.350	2500
-L026		1.802	1.14	0.019	0.298	2191
-L027		1.801	1.09	0.018	0.234	1808
-L030		1.809	1.19	0.018	0.342	2596
-1B-L037		1.805	1.19	0.016	0.333	2575
-L038		1.801	1.14	0.018	0.241	1887
-L039		1.801	1.17	0.022	0.239	1875
-L042		1.809	1.20	0.017	0.239	2007
Mean		1.804	1.16	0.019	0.284	2180
Std. dev.		0.004	0.04	0.003	0.052	333
-3A-L050	MLC(∥)	1.794	1.34	0.009	0.312	2596
-L053		1.798	1.22	0.016	0.291	2390
-L054		1.798	1.27	0.014	0.324	2651
-L058		1.795	1.14	0.016	0.261	2116
-3B-L061		1.797	1.19	0.022	0.302	2338
-L064		1.792	1.22	0.017	0.259	2152
-L065		1.792	1.17	0.016	0.252	2072
-L069		1.792	1.20	0.016	0.298	2426
Mean		1.795	1.22	0.016	0.287	2343
Std. dev.		0.003	0.06	0.004	0.027	217
-3A-L075	MLC(⊥)	1.799	1.02	0.022	0.147	1235
-L076		1.795	1.02	0.020	0.160	1240
-L077		1.794	1.02	0.026	0.164	1229
-L080		1.792	1.04	0.014	0.200	1563
-3B-L087		1.792	--	--	--	894
-L088		1.792	0.94	0.017	0.145	1054
-L089		1.793	0.07	0.023	0.134	1108
-L092		1.794	1.08	0.019	0.156	1328
Mean		1.794	1.03	0.020	0.155	1206
Std. dev.		0.002	0.04	0.004	0.023	198

TABLE 11-2 (Continued)

Specimen No.	Position and Orientation[a]	Density (g/cm^3)	Elastic Modulus on Second Loading (10^6 psi)	Permanent Set After First Loading (%)	Fracture Strain (%)	Ultimate Strength (psi)
6484-29-1A-L101	EE (∥)	1.804	1.27	0.015	(b)	(b)
-L103		1.807	1.27	0.020	(b)	(b)
-L105		1.807	1.23	0.020	(b)	(b)
-L107		1.807	1.25	0.011	0.311	2440
-1B-L111		1.793	1.17	0.017	0.330	2545
-L112		1.785	1.16	0.017	0.320	2435
-L114		1.791	1.20	0.022	(b)	(b)
-L116		1.809	1.25	0.013	0.314	2655
Mean		1.800	1.22	0.017	0.319	2519
Std. dev.		0.009	0.04	0.004	0.008	104
-1A-L125	EE (⊥)	1.820	1.12	0.020	0.355	2566
-L126		1.809	1.08	0.023	0.329	2323
-L129		1.811	1.13	0.020	0.323	2327
-L130		1.806	1.12	0.029	0.339	2471
-1B-L142		1.809	1.13	0.021	0.331	2421
-L143		1.805	1.12	0.019	0.316	2383
-L146		1.813	1.16	0.024	0.254	1997
-L147		1.800	1.08	0.019	0.266	1927
Mean		1.808	1.12	0.022	0.314	2302
Std. dev.		0.006	0.03	0.003	0.035	225
-3A-L151	MLE(∥)	1.804	1.27	0.021	0.335	2743
-L153		1.803	1.34	0.016	(b)	(b)
-L155		1.807	1.32	0.079	(b)	(b)
-L157		1.805	1.23	0.018	0.354	2753
-3B-L161		1.800	1.22	0.018	0.365	2804
-L162		1.792	1.20	0.014	0.302	2467
-L164		1.797	1.27	0.020	0.336	2665
-L166		1.797	1.23	0.014	0.316	2605
Mean		1.801	1.26	0.017	0.335	2672
Std. dev.		0.005	0.05	0.003	0.023	123
-3A-L175	MLE(⊥)	1.807	1.09	0.019	0.192	1549
-L176		1.807	1.10	0.025	0.241	1758
-L179		1.802	1.09	0.022	0.251	1844
-L180		1.803	1.08	0.024	0.229	1724
-3B-L193		1.802	1.09	0.020	0.189	1543
-L194		1.799	1.09	0.024	0.170	1394
-L197		1.793	0.97	0.026	0.136	1023
-L198		1.791	(c)	(c)	0.136	998
Mean		1.800	1.07	0.023	0.201	1479
Std. dev.		0.006	0.05	0.003	0.041	322

[a] EC = end center, MLC = midlength center, EE = end edge, MLE = midlength edge.

[b] Bond failure.

[c] Sample broke during first loading cycle.

TABLE 11-3
TENSILE PROPERTIES OF H-451 GRAPHITE, LOT 426
Log 6484-33, density = 1.75 g/cm^3, 0.505-in.-diameter by 3.00-in.-long samples

Specimen No.	Position and Orientation[a]	Density (g/cm^3)	Elastic Modulus on Second Loading (10^6 psi)	Permanent Set After First Loading (%)	Fracture Strain (%)	Ultimate Strength (psi)
6484-33-1A-L001	EC(∥)	1.720	1.19	0.013	0.338	2700
-L004		1.730	1.27	0.015	0.350	2846
-L005		1.737	1.21	0.015	0.339	2802
-L009		1.728	1.23	0.016	0.354	2833
-1B-L011		1.724	1.23	0.011	0.327	2686
-L014		1.722	1.23	0.014	0.328	2661
-L015		1.716	1.20	0.015	0.329	2666
-L019		1.710	1.20	0.015	0.318	2544
-1A-L002A						2844
-L002B						2687
-L006A						2948
-L006B						2387
-L007A						2774
-L007B						2738
-1B-L012A						2770
-L012B						2619
-L016A						2623
-L016B						2645
-L017A						2088
-L017B						2647
Mean		1.723	1.22	0.014	0.337	2675
Std. dev.		0.008	0.03	0.002	0.013	185
-1A-L025	EC(⊥)	1.753	1.10	0.016	0.341	2491
-L026		1.743	1.13	0.016	0.367	2747
-L027		1.741	1.12	0.015	0.333	2449
-L030		1.753	1.16	0.012	0.364	2746
-1B-L037		1.743	1.14	0.016	0.380	2741
-L038		1.738	1.08	0.011	0.312	2310
-L039		1.730	1.19	0.018	0.325	2288
-L042		1.749	1.13	0.015	0.359	2611
-1A-L028						2130
-L029						2347
-L031						2455
-L032						2396
-L033						2220
-L034						1921
-1B-L040						2057
-L041						1408
-L043						2520
-L044						2496
-L045						1787
-L046						1946
Mean		1.744	1.13	0.015	0.348	2302
Std. dev.		0.008	0.03	0.002	0.023	347

TABLE 11-3 (Continued)

Specimen No.	Position and Orientation[a]	Density (g/cm^3)	Elastic Modulus on Second Loading (10^6 psi)	Permanent Set After First Loading (%)	Fracture Strain (%)	Ultimate Strength (psi)
6484-33-1A-L101	EE(||)	1.756	1.32	0.011	0.352	3017
-L103		1.751	1.34	0.014	0.372	3180
-L105		1.756	1.30	0.009	0.337	2906
-L107		1.755	1.34	0.013	0.339	2946
-1B-L111		1.755	1.32	0.010	0.314	2825
-L112		1.750	1.28	0.013	0.339	2917
-L114		1.752	1.32	0.009	0.221	2194
-L116		1.753	1.27	0.011	0.364	3070
-1A-L102A						2934
-L102B						2863
-L104A						3223
-L104B						3135
-L109A						2877
-L109B						2871
-L110A						2931
-L110B						3033
-1B-L119A						2717
-L119B						2740
-L120A						2856
-L120B						3157
Mean		1.753	1.31	0.011	0.330	2920
Std. dev.		0.002	0.03	0.002	0.047	221
-1A-L125	EE(⊥)	1.767	1.14	0.015	0.373	2722
-L126		1.757	1.14	0.017	0.376	2701
-L129		1.764	1.10	0.015	0.350	2577
-L130		1.759	1.13	0.014	0.358	2620
-1B-L142		1.736	1.08	0.015	0.346	2249
-L143		1.728	1.06	0.019	0.338	2380
-L146		1.756	1.12	0.015	0.352	2544
-L147		1.754	1.12	0.013	0.337	2499
-1A-L127						2736
-L128						2731
-L131						2612
-L132						2646
-L133						2595
-L134						2674
-1B-L140						2642
-L141						2559
-L144						2239
-L145						2124
-L148						2446
-L149						2386
Mean		1.753	1.11	0.015	0.354	2534
Std. dev.		0.014	0.03	0.002	0.014	177

TABLE 11-3 (Continued)

Specimen No.	Position and Orientation[a]	Density (g/cm^3)	Elastic Modulus on Second Loading (10^6 psi)	Permanent Set After First Loading (%)	Fracture Strain (%)	Ultimate Strength (psi)
6484-33-3A-L050	MLC(∥)	1.697	1.15	0.015	0.255	2093
-L053		1.700	1.17	0.016	0.280	2201
-L054		1.694	1.20	0.015	0.243	1961
-L058		1.711	1.14	0.011	0.219	1854
-3B-L061		1.712	1.17	0.013	0.210	1837
-L064		1.719	1.24	0.010	0.312	2625
-L065		1.717	1.17	0.016	0.250	2083
-L069		1.707	1.20	0.017	0.294	2389
-3A-L051A						2196
-L051B						1898
-L055A						2071
-L055B						1987
-L056A						2271
-L056B						2615
-3B-L062A						2125
-L062B						2057
-L066A						1872
-L066B						2000
-L067A						2142
-L067B						2184
Mean		1.707	1.18	0.14	0.258	2073
Std. dev.		0.010	0.03	0.02	0.035	216
-3A-L075	MLC(⊥)	1.709	1.05	0.017	0.156	1455
-L076		1.710	0.97	0.010	0.131	1179
-L077		1.712	0.97	0.010	0.222	1640
-L080		1.708	(b)	(b)	(b)	884
-3B-L087		1.698	0.96	0.018	0.229	1625
-L088		1.703	0.99	0.016	0.248	1748
-L089		1.706	0.96	0.016	0.199	1421
-L092		1.700	0.95	0.020	0.252	1699
-3A-L078						1809
-L079						1708
-L081						1389
-L082						1398
-L083						1539
-L084						1399
-L090						1429
-3B-L091						1339
-L093						1598
-L094						1648
-L095						1623
-L096						1773
Mean		1.706	0.98	0.015	0.205	1515
Std. dev.		0.005	0.03	0.004	0.046	223

TABLE 11-3 (Continued)

Specimen No.	Position and Orientation(a)	Density (g/cm^3)	Elastic Modulus on Second Loading (10^6 psi)	Permanent Set After First Loading (%)	Fracture Strain (%)	Ultimate Strength (psi)
6484-33-3A-L151	MLE(‖)	1.747	1.30	0.008	(c)	(c)
-L153		1.745	1.32	0.009	0.364	3092
-L155		1.739	1.28	0.015	0.324	2808
-L157		1.726	1.23	0.008	0.346	2888
-3B-L161		1.738	1.30	0.010	0.328	2903
-L162		1.749	1.37	0.013	0.374	3187
-L164		1.761	1.36	0.007	0.349	3167
-L166		1.755	1.30	0.011	0.387	3282
-3A-L154A						2948
-L154B						2902
-L160A						2142
-L160B						2315
-3B-L163A						3207
-L163B						3187
-L165A						3092
-L169A						3095
-L169B						2593
Mean		1.745	1.31	0.010	0.353	2966
Std. dev.		0.012	0.04	0.003	0.023	293
-3A-L175	MLE(⊥)	1.702	0.95	0.018	0.204	1449
-L176		1.710	0.97	0.015	0.195	1474
-L179		1.741	1.09	0.016	0.341	2448
-L180		1.739	1.08	0.017	0.309	2272
-3B-L193		1.729	1.09	0.013	0.282	2146
-L194		1.743	1.08	0.011	0.353	2499
-L197		1.740	1.10	0.014	0.277	2107
-L198		1.729	1.03	0.019	0.248	1823
-3A-L177						1597
-L178						1926
-L181						2351
-L182						2295
-L184						1511
-3B-L191						2435
-L192						2325
-L195						2290
-L196						2237
-L199						1960
-L200						1531
Mean		1.729	1.05	0.015	0.272	2036
Std. dev.		0.015	0.06	0.003	0.059	366

(a) EC = end center, MLC = midlength center, EE = end edge, MLE = midlength edge.

(b) Sample broke during first cycle.

(c) Bond failure.

TABLE 11-4
TENSILE PROPERTIES OF H-451 GRAPHITE, LOT 426
Log 6484-34, density = 1.73 g/cm^3, 0.505-in.-diameter by 3.00-in.-long samples

Specimen No.	Position and Orientation[a]	Density (g/cm^3)	Elastic Modulus on Second Loading (10^6 psi)	Permanent Set After First Loading (%)	Fracture Strain (%)	Ultimate Strength (psi)
6484-34-1A-L001	EC(∥)	1.701	1.19	0.014	0.268	2025
-L004		1.700	1.16	0.016	0.253	1996
-L005		1.709	1.20	0.015	0.240	2019
-L009		1.715	1.25	0.010	0.256	2368
-1B-L011		1.698	1.17	0.014	0.238	1962
-L014		1.703	1.17	0.013	0.221	1862
-L015		1.709	1.17	0.013	0.229	1911
-L019		1.711	1.16	0.006	0.256	2198
-1A-L002A						2138
-L002B						2090
-L006A						1945
-L006B						2076
-L007A						2045
-L007B						2079
-1B-L012A						1940
-L012B						1748
-L016A						2140
-L016B						2082
-L017A						2160
-L017B						2137
Mean		1.706	1.18	0.013	0.245	2046
Std. dev.		0.006	0.03	0.003	0.016	134
-1A-L025	EC(⊥)	1.731	1.12	0.010	0.327	2507
-L026		1.716	1.12	0.011	0.311	2282
-L027		1.705	1.01	0.011	0.186	1450
-L030		1.693	1.07	0.012	0.286	2094
-1B-L037		1.727	1.16	0.012	0.360	2647
-L038		1.705	1.13	0.019	0.239	1742
-L039		1.698	0.97	0.017	0.212	1515
-L042		1.721	1.13	0.016	0.357	2544
-1A-L028						1192
-L029						1216
-L031						1842
-L032						1581
-L033						1646
-L034						1629
-1B-L040						1441
-L041						1301
-L043						1970
-L044						1681
-L045						1676
-L046						1766
Mean		1.712	1.09	0.014	0.285	1786
Std. dev.		0.014	0.07	0.003	0.066	432

TABLE 11-4 (Continued)

Specimen No.	Position and Orientation[a]	Density (g/cm^3)	Elastic Modulus on Second Loading (10^6 psi)	Permanent Set After First Loading (%)	Fracture Strain (%)	Ultimate Strength (psi)
6484-34-3A-L050	MLC(∥)	1.711	1.16	0.011	0.239	2019
-L053		1.713	1.16	0.006	0.231	2032
-L054		1.716	1.19	0.011	0.245	2033
-L058		1.704	1.16	0.014	0.262	2171
-3B-L061		1.713	1.20	0.011	0.265	2158
-L064		1.716	1.23	0.014	0.265	2229
-L065		1.718	1.20	0.008	0.243	2102
-L069		1.711	1.19	0.013	0.279	2191
-3A-L051A						2033
-L053B						2028
-L054B						2120
-L055A						2071
-3B-L061B						2053
-L062A						1808
-L064B						2095
-L065B						1949
-L066A						2148
-L068A						2005
-L068B						1823
-L069B						2070
Mean		1.712	1.19	0.011	0.254	2057
Std. dev.		0.004	0.02	0.003	0.016	108
-3A-L075	MLC(⊥)	1.709	1.00	0.016	0.225	1624
-L076		1.711	1.01	0.014	0.222	1580
-L077		1.710	1.03	0.018	0.235	1675
-L080		1.707	0.87	0.025	0.162	1040
-3B-L087		1.710	1.00	0.015	0.156	1235
-L088		1.713	1.00	0.017	0.226	1566
-L089		1.711	1.01	0.020	0.219	1575
-L092		1.713	1.04	0.018	0.290	1969
-3A-L078A						1977
-L079A						1278
-L081A						1188
-L082A						940
-L084A						1373
-3B-L090A						1385
-L091A						1608
-L093A						1873
-L094A						1811
-L096A						1418
Mean		1.710	0.99	0.018	0.217	1506
Std. dev.		0.002	0.05	0.003	0.042	300

TABLE 11-4 (Continued)

Specimen No.	Position and Orientation[a]	Density (g/cm^3)	Elastic Modulus on Second Loading (10^6 psi)	Permanent Set After First Loading (%)	Fracture Strain (%)	Ultimate Strength (psi)
6484-34-1A-L101	EE(||)	1.715	1.14	0.007	0.354	2953
-L103		1.715	1.39	0.004	0.345	2924
-L105		1.724	1.27	0.010	0.369	3040
-L107		1.726	1.32	0.007	0.348	2949
-1B-L111		1.713	1.24	0.008	0.341	2861
-L112		1.716	1.25	0.007	0.312	2715
-L114		1.722	1.25	0.010	0.355	2941
-L116		1.721	1.34	0.009	0.287	2821
-1A-L102A						2090
-L102B						2088
-L104A						2543
-L104B						2495
-L108A						2996
-L108B						2884
-1B-L113A						2549
-L113B						2581
-L119A						2695
-L119B						2777
-L120A						2440
-L120B						2686
Mean		1.719	1.27	0.008	0.339	2701
Std. dev.		0.005	0.08	0.002	0.026	275
-1A-L125	EE(⊥)	1.749	1.14	0.015	0.344	2548
-L126		1.737	1.14	0.013	0.319	2429
-L129		1.705	1.06	0.012	0.290	2107
-L130		1.744	1.14	0.014	0.304	2315
-1B-L142		1.692	1.02	0.012	0.218	1638
-L143		1.733	1.08	0.016	0.389	2516
-L146		1.726	1.08	0.014	(b)	(b)
-L147		1.714	1.12	0.011	0.267	2077
-1A-L127						2534
-L128						2671
-L131						1851
-L132						1648
-L133						1613
-L134						2677
-1B-L140						1752
-L141						2244
-L144						1998
-L145						2086
-L148						1896
-L149						2021
Mean		1.725	1.10	0.013	0.304	2138
Std. dev.		0.002	0.04	0.002	0.055	355

TABLE 11-4 (Continued)

Specimen No.	Position and Orientation[a]	Density (g/cm^3)	Elastic Modulus on Second Loading (10^6 psi)	Permanent Set After First Loading (%)	Fracture Strain (%)	Ultimate Strength (psi)
6484-34-3A-L151	MLE(||)	1.740	1.30	0.011	0.358	3120
-L153		1.725	1.36	0.010	0.336	2854
-L155		1.730	1.30	0.010	0.356	2994
-L157		1.740	1.32	0.011	0.394	3282
-3B-L161		1.725	1.27	0.010	0.333	2812
-L162		1.726	1.28	0.009	0.327	2881
-L164		1.743	1.34	0.012	0.337	3000
-L166		1.733	1.32	0.011	0.371	3094
-3A-L154A						2446
-L154B						2243
-L155B						3039
-L156B						2841
-L157B						3077
-L160A						2926
-L160B						2696
-3B-L163A						2580
-L163B						2597
-L165A						2715
-L169A						2680
-L169B						2520
Mean		1.733	1.31	0.010	0.351	2817
Std. dev.		0.007	0.03	0.001	0.023	260
-3A-L175	MLE(⊥)	1.712	1.36	0.013	0.335	2430
-L176		1.723	1.10	0.013	0.345	2494
-L181A		1.702	0.99	0.014	0.261	1870
-L180		1.710	1.06	0.013	0.237	1823
-3B-L193		1.718	1.10	0.017	0.283	2154
-L194		1.708	1.19	0.014	0.199	1570
-L197		1.707	1.08	0.011	0.294	2190
-L198		1.709	1.09	0.012	0.244	1903
-3A-L178A						2499
-L182A						1287
-L183A						1436
-L184A						2145
-3B-L191A						2617
-L192A						2262
-L196A						1599
-L199A						2292
-L200A						1845
Mean		1.712	1.12	0.013	0.275	2024
Std. dev.		0.006	0.11	0.002	0.050	398

[a] EC = end center, MLC = midlength center, EE = end edge, MLE = midlength edge.

[b] Bond failure.

TABLE 11-5
TENSILE PROPERTIES OF H-451 GRAPHITE, LOT 426
Log 6484-41, density = 1.72 g/cm^3, 0.505-in.-diameter by 3.00-in.-long samples

Specimen No.	Position and Orientation[a]	Density (g/cm^3)	Elastic Modulus on Second Loading (10^6 psi)	Permanent Set After First Loading (%)	Fracture Strain (%)	Ultimate Strength (psi)
6484-41-1A-L002A	EC(||)	1.694	1.08	0.012	0.250	1994
-L002B						1663
-L003A						1643
-L005A		1.668	1.02	0.019	0.235	1758
-L005B						1842
-L006A		1.697	1.06	0.017	0.211	1699
-L006B						1528
-L008A		1.689	1.08	0.016	0.235	1795
-L008B						1742
-L009A						1717
-1B-L002A		1.685	1.00	0.021	0.247	1720
-L002B						1757
-L003A						1493
-L005A		1.681	1.08	0.020	0.249	1860
-L005B						1643
-L006A		1.686	1.10	0.019	0.246	1887
-L006B						1573
-L008A		1.681	1.07	0.018	0.229	1696
-L008B						1727
-L009A						1667
Mean		1.685	1.06	0.018	0.238	1720
Std. dev.		0.009	0.03	0.003	0.013	120
-1A-L011	EC(⊥)	1.699	1.03	0.016	0.312	2170
-L012						1638
-L013		1.664	0.98	0.024	0.256	1680
-L014						1737
-L015						1378
-L017						2042
-L018		1.667	0.98	0.024	0.295	1939
-L019						1677
-L020		1.684	0.94	0.016	0.219	1595
-L021						2055
-1B-L011		1.702	1.04	0.017	0.329	2290
-L012						2007
-L013		1.678	0.98	0.016	0.194	1428
-L014						1168
-L015						1742
-L017						2277
-L018		1.694	0.97	0.020	0.239	1680
-L019						1817
-L020		1.686	0.99	0.018	0.275	1692
-L021						1747
Mean		1.684	0.99	0.019	0.265	1788
Std. dev.		0.014	0.03	0.003	0.047	294

TABLE 11-5 (Continued)

Specimen No.	Position and Orientation[a]	Density (g/cm^3)	Elastic Modulus on Second Loading (10^6 psi)	Permanent Set After First Loading (%)	Fracture Strain (%)	Ultimate Strength (psi)
6484-41-3A-L031A	MLE(||)	1.745	1.28	0.012	0.349	2868
-L031B						2747
-L034A		1.709	1.20	0.016	0.312	2547
-L034B						2509
-L035A		1.734	1.28	0.012	0.320	2743
-L035B						2822
-L038A		1.722	1.27	0.017	0.342	2774
-L038B						2880
-L039A						2845
-L039B						2782
-3B-L031A		1.724	1.25	0.011	0.328	2746
-L031B						2794
-L034A		1.699	1.23	0.021	0.293	2270
-L034B						2017
-L035A		1.722	1.23	0.016	0.327	2696
-L035B						2852
-L038A		1.722	1.23	0.017	0.354	2876
-L038B						2789
-L039A						2687
-L039B						2864
Mean		1.722	1.25	0.015	0.328	2705
Std. dev.		0.014	0.03	0.003	0.020	220
-3A-L041	MLE(⊥)	1.735	1.10	0.016	0.328	2346
-L042						1691
-L043		1.713	1.07	0.015	0.211	1687
-L044						2304
-L045						2249
-L047						2224
-L048		1.710	1.03	0.021	0.310	2115
-L049						1950
-L050		1.708	1.05	0.023	0.308	2139
-L051						2340
-3B-L041		1.704	1.01	0.021	0.223	1644
-L042						1998
-L043		1.730	1.03	0.018	0.251	1931
-L044						2391
-L045						1858
-L047						1911
-L048		1.700	0.99	0.020	0.249	1705
-L049						1766
-L050		1.714	1.01	0.025	0.282	1965
-L051						1697
Mean		1.714	1.04	0.020	0.270	1995
Std. dev.		0.012	0.04	0.003	0.043	253

TABLE 11-5 (Continued)

Specimen No.	Position and Orientation[a]	Density (g/cm^3)	Elastic Modulus on Second Loading (10^6 psi)	Permanent Set After First Loading (%)	Fracture Strain (%)	Ultimate Strength (psi)
6484-41-1A-L031A	EE(||)	1.728	1.20	0.011	0.261	2239
-L031B						2403
-L034A		1.692	1.10	0.009	0.274	2171
-L034B						2289
-L035A		1.714	1.14	0.012	0.304	2323
-L035B						2440
-L038A		1.710	1.22	0.010	0.320	2535
-L038B						2390
-L039A						2383
-L039B						2278
-1B-L031A		1.718	1.25	0.011	0.316	2501
-L031B						2616
-L034A		1.679	1.02	0.017	0.244	1742
-L034B						2640
-L035A		1.718	1.18	0.011	0.299	2438
-L035B						2507
-L038A		1.706	1.20	0.021	0.320	2465
-L038B						2396
-L039A						2745
-L039B						2455
Mean		1.708	1.16	0.013	0.292	2398
Std. dev.		0.016	0.07	0.004	0.029	207
-1A-L041	EE(⊥)	1.732	1.05	0.015	0.334	2294
-L042			1.07	0.019	0.294	2132
-L043		1.711	1.06	0.019	0.267	2091
-L044						2046
-L045						1995
-L047						1667
-L048		1.703	1.00	0.019	0.308	2082
-L049						2000
-L050		1.685	1.00	0.023	0.319	2099
-L051						2185
-1B-L041		1.724	1.05	0.019	0.332	2248
-L042						1773
-L043		1.716	1.06	0.017	0.295	2131
-L044						1692
-L045						2197
-L047						1982
-L048		1.675	0.93	0.019	0.229	1568
-L049						1568
-L050		1.697	0.93	0.027	0.251	1658
-L051						1283
Mean		1.705	1.02	0.020	0.292	1934
Std. dev.		0.019	0.05	0.003	0.036	277

TABLE 11-5 (Continued)

Specimen No.	Position and Orientation[a]	Density (g/cm^3)	Elastic Modulus on Second Loading (10^6 psi)	Permanent Set After First Loading (%)	Fracture Strain (%)	Ultimate Strength (psi)
6484-41-3A-L002A	MLC(||)	1.680	1.10	0.017	0.255	1966
-L002B						1882
-L003A						1912
-L005A		1.696	1.10	0.019	0.233	1808
-L005B						2092
-L006A		1.690	1.10	0.017	0.274	2090
-L006B						1648
-L008A		1.707	1.14	0.019	0.243	1920
-L008B						1752
-L009A						1792
-3B-L002A		1.696	1.09	0.016	0.193	1547
-L002B						1952
-L003A						1992
-L005A		1.695	1.06	0.020	0.190	1503
-L005B						1837
-L006A		1.702	1.12	0.020	0.272	2096
-L006B						1887
-L008A		1.683	1.07	0.018	0.232	1771
-L008B						1887
-L009A						2182
Mean		1.694	1.10	0.018	0.236	1876
Std. dev.		0.009	0.02	0.001	0.032	178
-3A-L011	MLC(⊥)	1.689				838
-L012						1573
-L013		1.694				718
-L014						759
-L015						1623
-L017						1638
-L018		1.696	1.01	0.020	0.299	2001
-L019						1862
-L020		1.706	1.02	0.022	0.285	1977
-L021						2047
-3B-L011		1.694				844
-L012						1338
-L013		1.692	0.97	0.021	0.240	1621
-L014						1792
-L015						1642
-L017						1548
-L018		1.696	0.98	0.024	0.184	1382
-L019						1832
-L020		1.704	1.00	0.013	0.195	1546
-L021						1722
Mean		1.696	1.00	0.020	0.241	1515
Std. dev.		0.006	0.02	0.004	0.052	417

[a] EC = end center, MLC = midlength center, EE = end edge, MLE = midlength edge.

TABLE 11-6
TENSILE PROPERTIES OF SO-818 GRAPHITE, LOT 1
Log 6484-21, density = 1.72 g/cm^3, 0.505-in.-diameter by 3.00-in.-long samples

Specimen No.	Position and Orientation[a]	Density (g/cm^3)	Elastic Modulus on Second Loading (10^6 psi)	Permanent Set After First Loading (%)	Fracture Strain (%)	Ultimate Strength (psi)
6484-21-1A-L001	EC(∥)	1.733	1.20	0.011	0.276	2334
-L004		1.727	1.15	0.010	0.250	2176
-L005		1.729	1.17	0.007	0.253	2236
-L009		1.719	1.15	0.008	0.268	2284
-1B-L011		1.710	1.12	0.011	0.271	2224
-L014		1.723	1.17	0.013	0.243	2134
-L015		1.725	1.18	0.013	0.282	2358
-L019		1.732	(b)	(b)	0.258	2241
Mean		1.725	1.16	0.010	0.263	2248
Std. dev.		0.007	0.02	0.002	0.014	75
-1A-L025	EC(⊥)	1.731	1.07	0.015	0.276	2113
-L026		1.732	1.10	0.014	0.260	2037
-L027		1.730	1.03	0.010	0.247	2007
-L030		1.729	1.06	0.017	0.232	1793
-1B-L037		1.730	1.08	0.014	0.280	2136
-L038		1.728	1.07	0.011	0.268	2102
-L039		1.731	1.03	0.010	0.289	2172
-L042		1.724	1.05	0.011	0.259	1942
Mean		1.729	1.06	0.013	0.251	2038
Std. dev.		0.002	0.02	0.003	0.035	124
-3A-L050	MLC(∥)[QLC][c]	1.736	1.17	0.012	0.265	2231
-L053		1.738	1.22	0.010	0.276	2318
-L054		1.740	1.18	0.010	0.281	2393
-L058		1.722	1.18	0.010	0.256	2223
-3B-L061		1.709	1.10	0.014	0.274	2147
-L064		1.733	1.17	0.013	0.273	2268
-L065		1.729	1.20	0.014	0.250	2127
-L069		1.737	1.25	0.011	0.273	2281
Mean		1.730	1.18	0.012	0.268	2248
Std. dev.		0.010	0.04	0.002	0.011	87
-3A-L079	MLC(⊥)[QLC][c]	1.733	1.10	0.015	0.276	2144
-L076		1.730	1.10	0.014	0.254	1993
-L077		1.730	1.10	0.012	0.292	2236
-L080		1.733	1.06	0.015	0.220	1744
-3B-L087		1.732	1.08	0.011	0.247	1948
-L088		1.733	1.10	0.015	0.271	2093
-L089		1.733	1.07	0.009	0.272	2094
-L092		1.720	1.05	0.013	0.269	1972
Mean		1.730	1.08	0.010	0.263	2028
Std. dev.		0.004	0.02	0.005	0.022	149

TABLE 11-6 (Continued)

Specimen No.	Position and Orientation[a]	Density (g/cm^3)	Elastic Modulus on Second Loading (10^6 psi)	Permanent Set After First Loading (%)	Fracture Strain (%)	Ultimate Strength (psi)
6484-21-1A-L101	EE(||)	1.722	1.17	0.010	0.274	2307
-L103		1.725	1.17	0.010	0.247	2208
-L105		1.723	1.18	0.009	0.274	2404
-L107		1.740	1.18	0.009	0.277	2395
-1B-L111		1.650	1.02	0.014	0.259	1966
-L112		1.719	1.12	0.015	0.299	2356
-L114		1.727	1.17	0.009	0.277	2354
-L116		1.753	1.23	0.012	0.276	2475
Mean		1.720	1.15	0.011	0.273	2308
Std. dev.		0.030	0.06	0.002	0.015	159
-1A-L125	EE(⊥)	1.754	(d)	(d)	(d)	(d)
-L126		1.735	1.05	0.011	0.270	2101
-L129		1.725	1.02	0.010	0.231	1775
-L130		1.723	1.03	0.011	0.234	1840
-1B-L142		1.739	0.97	0.010	0.250	1845
-L143		1.739	1.06	0.011	0.278	2116
-L146		1.694	1.03	0.007	0.253	1980
-L147		1.697	0.96	0.016	0.291	1944
Mean		1.726	1.02	0.011	0.258	1943
Std. dev.		0.021	0.04	0.003	0.022	132
-3A-L151	MLE(||)[QLE][c]	1.731	1.25	0.007	0.259	2354
-L153		1.743	(e)	(e)	(e)	2494
-L155		1.742	1.25	0.014	0.309	2697
-L157		1.764	1.27	0.008	0.310	2823
-3B-L161		1.670	1.08	0.011	0.268	2130
-L162		1.732	1.15	0.015	0.284	2329
-L164		1.731	1.18	0.015	0.272	2289
-L166		1.752	1.25	0.011	0.286	2564
Mean		1.732	1.20	0.012	0.284	2460
Std. dev.		0.025	0.07	0.003	0.020	229
-3A-L175	MLE(⊥)[QLE][c]	1.742	1.08	0.016	0.281	2170
-L176		1.746	1.11	0.016	0.283	2234
-L179		1.732	1.08	0.008	0.230	1894
-L180		1.731	1.07	0.013	0.260	2040
-3B-L193		1.750	1.10	0.019	0.266	2060
-L194		1.733	1.02	0.021	0.257	1945
-L197		1.681	0.99	0.012	0.244	1796
-L198		1.673	0.98	0.022	0.293	1960
Mean		1.723	1.05	0.016	0.264	2012
Std. dev.		0.029	0.05	0.005	0.021	144

[a] EC = end center, MLC = midlength center, EE = end edge, MLE = midlength edge, QLC = quarter-length center

[b] Not cycled.

[c] Logs 6484-21 and -22 of grade S0-818 are halves of a 68-in.-long extrusion (Airco Speer Log No. 2-18). The terms in brackets indicate locations in the parent extrusion.

[d] Improper cycle.

[e] Accidental breakage.

TABLE 11-7
TENSILE PROPERTIES OF SO-818 GRAPHITE, LOT 1
Log 6484-22, density = 1.71 g/cm^3, 0.505-in.-diameter by 3.00-in.-long samples

Specimen No.	Position and Orientation[a]	Density (g/cm^3)	Elastic Modulus on Second Loading (10^6 psi)	Permanent Set After First Loading (%)	Fracture Strain (%)	Ultimate Strength (psi)
6484-22-1A-L101	EE(∥)[MLE][b]	1.715	1.10	0.014	0.300	2318
-L103		1.701	1.03	0.017	0.276	2051
-L105		1.734	1.15	0.014	0.320	2639
-L107		1.739	1.18	0.011	0.320	2629
-1B-L111		1.741	1.23	0.014	0.262	2271
-L112		1.745	1.20	0.007	0.250	2282
-L114		1.740	1.20	0.007	0.280	2515
-L116		1.743	1.17	0.006	0.314	2689
Mean		1.732	1.16	0.011	0.290	2424
Std. dev.		0.016	0.06	0.004	0.027	226
-1A-L125	EE(⊥)[MLE][b]	1.732	1.06	0.017	0.294	2178
-L126		1.741	1.02	0.014	0.287	2167
-L129		1.705	0.98	0.019	0.271	1894
-L130		1.717	0.97	0.017	0.281	1936
-1B-L142		1.740	1.10	0.014	0.282	2145
-L143		1.741	1.08	0.013	0.219	1830
-L146		1.736	1.06	0.012	0.222	1742
-L147		1.739	1.03	0.019	0.294	2099
Mean		1.731	1.04	0.016	0.265	1999
Std. dev.		0.013	0.05	0.003	0.031	169
-1A-L001	EC(∥)[MLC][b]	1.737	1.20	0.010	0.248	2210
-L004		1.719	1.11	0.013	0.282	2230
-L005		1.726	1.15	0.015	0.260	2133
-L009		1.738	1.11	0.009	0.275	2337
-1B-L011		1.734	1.20	0.016	0.271	2246
-L014		1.737	1.20	0.011	0.260	2290
-L015		1.737	1.20	0.014	0.264	2291
-L019		1.741	1.20	0.013	0.272	2360
Mean		1.734	1.17	0.013	0.266	2262
Std. dev.		0.007	0.04	0.002	0.011	73
-1A-L025	EC(⊥)[MLC][b]	1.716	(c)	(c)	(c)	(c)
-L026		1.727	1.10	0.011	0.274	2141
-L027		1.731	1.10	0.014	0.281	2196
-L030		1.711	1.05	0.015	0.245	1871
-1B-L037		1.737	1.08	0.012	0.301	2340
-L038		1.740	1.10	0.015	0.269	2137
-L039		1.737	1.12	0.014	0.279	2179
-L042		1.737	1.06	0.013	0.294	2159
Mean		1.729	1.09	0.011	0.277	2146
Std. dev.		0.011	0.02	0.004	0.018	139

[a] EC = end center, MLC = midlength center, EE = end edge, MLE = midlength edge.

[b] Logs 6484-21 and -22 of grade SO-818 are halves of a 68-in.-long extrusion (Airco Speer Log No. 2-18). The terms in brackets indicate locations in the parent extrusion.

TABLE 11-8
IMPURITY CONTENT (IN PPM) OF GRAPHITES H-451 (LOT 426), TS-1240 (LOT 1), AND SO-818 (LOT 1)

Graphite and Sample No.	Position in Log[a]	Ash	B	Fe	V	Ti	S
(H-451: 6484-33)							
6484-33-3A-L082	MLC	<25	2.0	<1.0	<0.5	<1.0	<2.0
-3B-L094	MLC	<25	2.0	2.0	<0.5	<1.0	<2.0
-3A-L156	MLE	<25	4.0	10.0	<0.5	<1.0	<2.0
-3B-L165	MLE	<25	2.0	10.0	<0.5	<1.0	<2.0
-1A-L031	EC	<25	8.0	<1.0	<0.5	<1.0	<2.0
-1B-L043	EC	<25	2.0	<1.0	<0.5	<1.0	<2.0
-1A-L106	EE	<25	2.0	<1.0	<0.5	<1.0	<2.0
-1B-L115	EE	<25	2.0	<1.0	<0.5	<1.0	<2.0
Mean	Whole log	<25	3.0	<3.4	<0.5	<1.0	<2.0
(H-451: 6484-34)							
6484-34-3A-L082	MLC	<25	20.0	<1.0	<0.5	<1.0	<2.0
-3B-L094	MLC	<25	2.0	<1.0	<0.5	<1.0	<3.0
-3A-L156	MLE	<25	2.0	<1.0	<0.5	<1.0	<2.0
-3B-L165	MLE	<25	2.0	<1.0	<0.5	<1.0	<2.0
-1A-L031	EC	<25	2.0	10.0	<0.5	<1.0	<2.0
-1B-L043	EC	<25	4.0	40.0	<0.5	10.0	<2.0
-1A-L106	EE	<25	2.0	<1.0	<0.5	<1.0	<2.0
-1B-L115	EE	<25	4.0	4.0	<0.5	<1.0	<2.0
Mean	Whole log	25	4.75	<7.4	<0.5	<1.0	<2.1
(H-451: 6484-41)							
6484-41-3A-L016	MLC	40	1.0	<1.0	<0.5	<1.0	<1.0
-3B-L016	MLC	40	4.0	<1.0	<0.5	<1.0	<1.0
-3A-L036	MLE	34	1.0	<1.0	<0.5	<1.0	<1.0
-3B-L036	MLE	36	2.0	<1.0	<0.5	<1.0	<1.0
-1A-L016	EC	55	0.5	<1.0	<0.5	<1.0	<1.0
-1B-L016	EC	37	1.0	<1.0	<0.5	<1.0	<1.0
-1A-L036	EE	31	1.0	<1.0	<0.5	<1.0	<1.0
-1B-L036	EE	57	1.0	<1.0	<0.5	<1.0	<1.0
Mean	Whole log	41	<1.4	<1.0	<0.5	<1.0	<1.0

TABLE 11-8 (Continued)

Graphite and Sample No.	Position in Log[a]	Ash	B	Fe	V	Ti	S
(TS-1240: 6484-29)							
6484-29-3A-L082	MLC	250	0.5	40.0	40.0	20.0	2.0
-3B-L094	MLC	204	<0.5	40.0	40.0	20.0	4.0
-3A-L156	MLE	138	<0.5	10.0	20.0	8.0	12.0
-3B-L165	MLE	66	<0.5	40.0	40.0	20.0	8.5
-1A-L031	EC	125	<0.5	20.0	20.0	20.0	12.0
-1B-L043	EC	171	<0.5	10.0	8.0	8.0	8.0
-1A-L106	EE	102	<0.5	20.0	40.0	20.0	9.5
-1B-L115	EE	257	<0.5	10.0	20.0	10.0	5.0
Mean	Whole log	157	<0.5	23.7	28.5	15.7	7.6
(SO-818: 6484-21)							
6484-21-3A-L082	MLC(QLC)[b]	102	<0.5	<1.0	<0.5	<1.0	<1.0
-3B-L094	MLC(QLC)[b]	93	<0.5	<1.0	<0.5	<1.0	<1.0
-3A-L156	MLE(QLE)[b]	118	<0.5	<1.0	<0.5	<1.0	<1.0
-3B-L165	MLE(QLE)[b]	119	<0.5	<1.0	<0.5	<1.0	<1.0
-1A-L031	EC	102	<0.5	<1.0	<0.5	<1.0	<1.0
-1B-L043	EC	91	<0.5	<1.0	<0.5	<1.0	<1.0
-1A-L106	EE	74	<0.5	<1.0	<0.5	<1.0	<1.0
-1B-L115	EE	66	<0.5	<1.0	<0.5	<1.0	<1.0
Mean	Whole log	92	<0.5	<1.0	<0.5	<1.0	<1.0
(SO-818: 6464-22)							
6484-22-3A-L082	MLC(3QLC)[b]	48	<0.5	<1.0	<0.5	<1.0	<1.0
-3B-L094	MLC(3QLC)[b]	50	<0.5	<1.0	<0.5	<1.0	<1.0
-3A-L156	MLE(3QLE)[b]	47	<0.5	<1.0	<0.5	<1.0	<1.0
-3B-L165	MLE(3QLE)[b]	57	<0.5	<1.0	<0.5	<1.0	<1.0
-1A-L031	EC(MLC)[b]	50	<0.5	<1.0	<0.5	<1.0	<1.0
-1B-L043	EC(MLC)[b]	41	<0.5	<1.0	<0.5	<1.0	<1.0
-1A-L106	EE(MLC)[b]	41	<0.5	<1.0	<0.5	<1.0	<1.0
-1B-L115	EE(MLC)[b]	47	<0.5	<1.0	<0.5	<1.0	<1.0
Mean	Whole log	48	<0.5	<1.0	<0.5	<1.0	<1.0

[a] MLC = midlength center, EC = end center, MLE = midlength edge, EE = end edge, QLC = quarter-length center, QLE = quarter-length edge, 3QLC = three-quarter-length center, 3QLE = three-quarter-length edge.

[b] Logs 6484-21 and -22 of grade SO-818 are halves of a 68-in.-long extrusion (Airco Speer Log No. 2-18). The terms in brackets indicate locations in the parent extrusion.

TABLE 11-9
THERMAL EXPANSIVITY OF H-451 GRAPHITE, LOT 426
Log 6484-34, density = 1.71 g/cm^3

Specimen No.	Position and Orientation[a]	Mean Coefficient of Thermal Expansion, $\alpha \times 10^6$ °C^{-1} (22°-500°C)
6484-34-1A-L007A	EC(∥)	4.24
-L007B		4.32
-L010A		4.46
-L010B		4.22
-1B-L032A		4.31
-L032B		4.40
-L035A		4.24
-L035B		4.29
Mean		4.31
Std. dev.		0.08
-1A-L063A	EC(⊥)	5.02
-L063B		4.91
-L066A		4.50
-L066B		4.33
-1B-L073A		4.41
-L073B		4.36
-L076A		4.35
-L076B		4.52
Mean		4.55
Std. dev.		0.27
-1A-L052A	EE(∥)	3.88
-L052B		4.13
-L054A		4.07
-L054B		4.17
-1B-L057A		4.24
-L057B		4.19
-L059A		4.09
-L059B		4.25
Mean		4.13
Std. dev.		0.12
-1A-L081A	EE(⊥)	4.62
-L081B		4.52
-L083A		4.66
-L083B		4.75
-1B-L085A		4.70
-L085B		4.53
-L087A		4.52
-L087B		4.45
Mean		4.59
Std. dev.		0.10

TABLE 11-9 (Continued)

Specimen No.	Position and Orientation[a]	Mean Coefficient of Thermal Expansion, $\alpha \times 10^6$ °C^{-1} (22°-500°C)
6484-34-3A-L107A	MLC(||)	4.06
-L107B		4.13
-L110A		3.98
-L110B		4.31
-3B-L132A		4.03
-L132B		4.07
-L135A		4.13
-L135B		4.13
Mean		4.10
Std. dev.		0.10
-3A-L163A	MLC(⊥)	4.75
-L163B		4.47
-L166A		4.73
-L166B		4.72
-3B-L173A		4.88
-L173B		4.24
-L176A		4.68
-L176B		4.56
Mean		4.63
Std. dev.		0.20
-3A-L152A	MLE(||)	3.69
-L152B		4.08
-L154A		3.75
-L154B		3.88
-3B-L157A		4.21
-L157B		4.02
-L159A		3.70
-L159B		4.01
Mean		3.92
Std. dev.		0.19
-3A-L181A	MLE(⊥)	4.61
-L181B		4.63
-L183A		5.14
-L183B		4.66
-3B-L185A		4.79
-L185B		4.77
-L187A		4.61
-L187B		4.42
Mean		4.66
Std. dev.		0.25

[a] EC = end center, EE = end edge, MLC = midlength center, MLE = midlength edge.

TABLE 11-10
MEAN TEMPERATURES AND FLUENCES IN CAPSULE OG-2

Crucible No.	Fast Fluence x 10^{-21} (n/cm^2) (E > 0.18 MeV)	Thermal Fluence x 10^{-21} (n/cm^2)	Mean Operating Temperature (°C)	
			Centerline	Periphery
1	1.9	1.2	687	602
2	2.5	1.4	778	664
3	3.0	1.6	998	907
4	3.3	1.8	1251	1090
5	3.2	1.8	1387	1316
6	3.0	1.7	1080	937
7	2.8	1.5	997	907
8	2.4	1.2	934	835
9	1.9	0.9	830	752
10	1.3	0.6	640	580

TABLE 11-11
TENSILE PROPERTIES OF H-451 GRAPHITE SPECIMENS IRRADIATED IN CAPSULE OG-2
(All specimens midlength center location)

Specimen No.	Orientation	Crucible No.	Hole No.	Mean Irradiation Temperature (°C)	Fluence x 10^{-21} (n/cm^2) (E > 0.18 MeV)	Ultimate Tensile Strength (psi)	Strain at Failure (%)	Young's Modulus x 10^{-6} (psi)	Secant Modulus x 10^{-6} (psi)
T-173	Axial	10	24	590	2.9	2532	0.110	2.61	2.30
T-174			24			2589	0.138	2.35	1.88
T-175			25			2326	0.090	2.73	2.58
T-176			25			1775	0.097	2.21	1.83
T-177			26			2624	0.121	2.58	2.17
T-178			26			2861	0.123	2.84	2.33
T-179			27			2641	0.134	2.51	1.97
T-180			27			2496	0.117	2.50	2.13
Mean						2481	0.116	2.54	2.15
Std. dev.						±322	±0.017	±0.20	±0.25
T-155	Axial	7	10	950-970	5.9	2240	0.105	2.50	2.13
T-156			10	950-970		2822	0.130	2.70	2.17
T-157			22	890-920		3027	0.136	2.59	2.23
T-158			22			2877	0.127	2.74	2.27
T-159			23			2857	0.125	2.61	2.29
T-160			23			3004	0.150	2.28	2.00
T-161			24			2550	0.122	2.52	2.09
T-162			24			2835	0.145	2.43	1.96
Mean						2777	0.130	2.55	2.14
Std. dev.						±261	±0.014	±0.15	±0.12

TABLE 11-11 (Continued)

Specimen No.	Orientation	Crucible No.	Hole No.	Mean Irradiation Temperature (°C)	Fluence x 10^{-21} (n/cm^2) (E > 0.18 MeV)	Ultimate Tensile Strength (psi)	Strain at Failure (%)	Young's Modulus x 10^{-6} (psi)	Secant Modulus x 10^{-6} (psi)
T-181	Axial	--	--	--	0	1446	0.130	1.22	1.11
T-182						1630	0.230	1.02	0.71
T-183						1650	0.212	1.15	0.78
T-184						1589	0.169	1.17	0.94
T-185						1548	0.152	1.20	1.02
T-186						1731	0.211	1.23	0.82
T-187						1243	0.182	0.95	0.68
T-188						1609	0.187	1.17	0.86
T-190						1630	0.184	1.17	0.89
Mean						1564	0.184	1.14	0.87
Std. dev.						±135	±0.029	±0.09	±0.13
T-219	Radial	--	--	--	0	1589	0.210	0.97	0.76
T-220						1751	0.215	0.98	0.81
T-221						1874	0.252	1.02	0.74
T-222						1731	0.223	1.02	0.77
T-223						1650	0.210	0.94	0.79
T-224						2037	0.267	1.02	0.76
T-225						1283	0.172	0.97	0.75
T-226						1609	0.181	1.12	0.89
T-227						1853	0.241	1.06	0.77
T-228						1344	0.147	1.02	0.91
T-1						1446	0.227	0.92	0.64
T-2						1508	0.242	0.91	0.62
T-3						2220	0.342	1.03	0.65
T-5						1609	0.219	0.99	0.73
T-6						1562	0.214	1.08	0.73
Mean						1671	0.224	1.00	0.75
Std. dev.						±242	±0.043	±0.05	±0.08

TABLE 11-12
TENSILE PROPERTIES OF TS-1240 GRAPHITE SPECIMENS IRRADIATED IN CAPSULE OG-2
(All specimens midlength center location)

Specimen No.	Orientation	Crucible No.	Hole No.	Mean Irradiation Temperature (°C)	Fluence x 10^{-21} (n/cm^2) (E > 0.18 MeV)	Ultimate Tensile Strength (psi)	Strain at Failure (%)	Young's Modulus x 10^{-6} (psi)	Secant Modulus x 10^{-6} (psi)
T40105	Axial	10	10	620	1.3	1940	0.104	2.16	1.87
T40107			10			1426	0.116	1.34	1.23
T40109			11			1104	0.100	1.22	1.10
T40111			11			1492	0.096	1.99	1.55
T40113			12			2221	0.156	1.64	1.42
T40115			12			2528	0.148	1.93	1.71
T40117			13			2202	0.133	2.09	1.66
T40118			13			1653	--	1.54	--
T40119			14			1629	0.114	1.70	1.43
T40120			14			2246	0.167	1.57	1.34
Mean						1844	0.126	1.72	1.48
Std. dev.						±452	±0.026	±0.32	±0.24
T40069	Axial	9	28	765	1.9	1204	0.089	1.56	1.35
T40071			28			1981	0.140	1.62	1.42
T40073			29			2270	0.182	1.47	1.25
T40075			29			1964	0.127	1.78	1.55
T40077			30			2354	0.150	2.05	1.57
T40079			30			1822	0.122	1.67	1.49
T40081			31			2309	0.144	1.84	1.60
T40083			31			2516	0.163	1.81	1.54
T40085			32			2385	0.153	1.85	1.56
T40087			32			1895	0.143	1.58	1.32
Mean						2070	0.141	1.72	1.47
Std. dev.						±385	±0.025	±0.17	±0.12

TABLE 11-12 (Continued)

Specimen No.	Orientation	Crucible No.	Hole No.	Mean Irradiation Temperature (°C)	Fluence x 10^{-21} (n/cm^2) (E > 0.18 MeV)	Ultimate Tensile Strength (psi)	Strain at Failure (%)	Young's Modulus x 10^{-6} (psi)	Secant Modulus x 10^{-6} (psi)
T40129	Radial	9	12	805	1.9	2163	0.140	1.74	1.55
T40131			12			1940	0.113	1.88	1.72
T40133			13			1816	0.131	1.56	1.39
T40135			13			1899	0.168	1.33	1.13
T40137			14			2180	0.166	1.48	1.31
T40139			14			1181	0.138	0.99	0.86
T40141			15			2302	0.174	1.54	1.32
T40143			15			2100	0.144	1.62	1.46
T40145			16			1979	0.160	1.38	1.24
T40147(a)			16			1084(a)	0.194(a)	0.66(a)	0.56(a)
Mean						1951	0.148	1.50	1.33
Std. dev.						±327	±0.020	±0.26	±0.25

(a) Specimen flawed - excluded from averages.

TABLE 11-12 (Continued)

Specimen No.	Orientation	Crucible No.	Hole No.	Mean Irradiation Temperature (°C)	Fluence x 10^{-21} (n/cm^2) (E > 0.18 MeV)	Ultimate Tensile Strength (psi)	Strain at Failure (%)	Young's Modulus x 10^{-6} (psi)	Secant Modulus x 10^{-6} (psi)
3A-6B	Axial	--	--	--	0	1427	0.210	0.90	0.68
-7B						1711	0.270	0.95	0.63
-12B						2015	0.310	1.00	0.65
-13B						1896	0.320	0.90	0.59
-18B						1469	0.200	0.86	0.73
-19B						1406	0.285	0.69	0.49
-24B						1796	0.275	0.95	0.65
-25B						1691	0.250	1.00	0.68
-27B						1449	0.245	0.86	0.59
-28B						1672	0.265	0.90	0.63
3B-6B						1976	0.323	1.00	0.61
-7B						1670	0.245	1.00	0.68
-12B						1438	0.185	1.00	0.78
-13B						1141	0.145	0.95	0.79
-18B						1080	0.240	0.60	0.45
-19B						1283	0.190	0.86	0.68
-24B						1487	0.215	0.88	0.69
-25B						1569	0.295	0.90	0.53
-27B						1507	0.275	0.86	0.55
-28B						1731	0.335	0.86	0.52
Mean						1571	0.254	0.90	0.63
Std. dev.						±252	±0.051	±0.10	±0.09

TABLE 11-12 (Continued)

Specimen No.	Orientation	Crucible No.	Hole No.	Mean Irradiation Temperature (°C)	Fluence x 10^{-21} (n/cm^2) (E > 0.18 MeV)	Ultimate Tensile Strength (psi)	Strain at Failure (%)	Young's Modulus x 10^{-6} (psi)	Secant Modulus x 10^{-6} (psi)
3A-36B	Radial	--	--	--	0	957	0.140	--	0.68
-37B						1428	0.220	0.95	0.65
-42B						1367	0.205	1.00	0.67
-43B						1266	0.300	0.78	0.42
-48B						1388	0.245	0.72	0.57
-49B						1120	0.130	1.00	0.86
-54B						1450	0.210	0.90	0.69
-55B						1531	0.250	0.95	0.61
-60A						2400	0.350	1.06	0.69
-60B						1170	0.175	0.90	0.67
3B-36B						1448	0.330	0.75	0.44
-37B						958	0.165	--	0.58
-42B						1428	0.210	0.95	0.68
-43B						1287	0.195	0.88	0.66
-48B						1594	0.252	0.90	0.63
-49B						1491	0.255	0.95	0.58
-54B						1384	0.205	1.00	0.68
-55B						1428	0.233	0.91	0.61
-60A						1428	0.295	0.83	0.48
-60B						1144	0.255	0.68	0.45
Mean						1383	0.231	0.90	0.62
Std. dev.						±298	±0.058	±0.11	±0.11

APPENDIX

PROJECT REPORTS PUBLISHED DURING THE QUARTER

Kaae, J. L., "Irradiation-Induced Microstructural Changes in Isotropic Pyrolytic Carbons," General Atomic Company Report GA-A13162, April 11, 1975.

Wallroth, C. F., "Feasibility Study of the Dragon Reactor for HTGR Fuel Testing," ERDA Report GA-A13333, General Atomic Company, March 3, 1975.

Jensen, D. D., et al., "Planning Guide for Validation of Fission Product Transport Codes," ERDA Report GA-A13386, General Atomic Company, April 15, 1975.